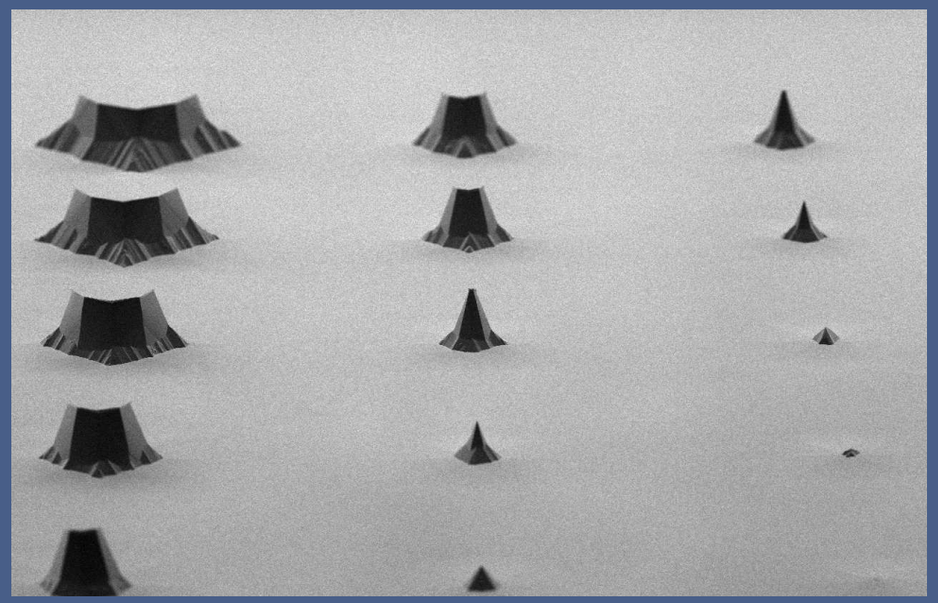

ISBN: 978-90-365-3024-8

Spin-Filter Scanning Tunneling Microscopy I. J. Vera Marún

Spin-Filter Scanning Tunneling Microscopy

A novel technique for the analysis of spin polarization on magnetic surfaces and spintronic devices

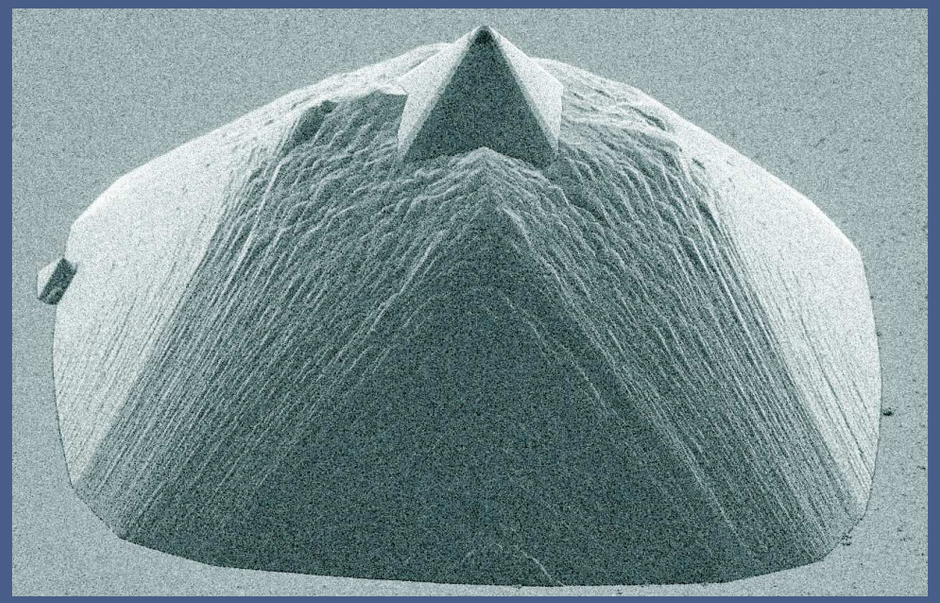

Iván Jesús Vera Marún

Spin-Filter Scanning Tunneling Microscopy

A novel technique for the analysis of spin polarization on magnetic surfaces and spintronic devices

Iván Jesús Vera Marún

GRADUATION COMMITTEE

CHAIRMAN & SECRETARY:	prof. dr. ir. A. J. Mouthaan	Univ. of Twente, EWI
PROMOTER:	prof. dr. P. J. Kelly	Univ. of Twente, TNW
ASSISTANT PROMOTER:	dr. R. Jansen	Univ. of Twente, EWI
MEMBERS:	prof. dr. M. C. Elwenspoek	Univ. of Twente, EWI
	prof. dr. ir. H. J. W. Zandvliet	Univ. of Twente, TNW
	prof. dr. H. J. M. Swagten	Eindhoven Univ. of Tech.
	prof. dr. J. Miltat	Univ. of Paris-Sud
	prof. dr. H.-J. Hug	Univ. of Basel

MESA+ Institute for Nanotechnology

University of Twente
The Netherlands

The research described in this thesis was carried out at the Nanoelectronics group of the MESA$^+$ Institute for Nanotechnology, University of Twente, the Netherlands. This research was funded by the "Nederlandse Organisatie voor Wetenschappelijk Onderzoek" (NWO), the Netherlands.

Typeset in LaTeX 2ε
Reference management in Zotero & BibTeX

Printed by Wöhrmann Print Service

ISBN: 978-90-365-3024-8
DOI: 10.3990/1.9789036530248

SPIN-FILTER SCANNING TUNNELING MICROSCOPY

A NOVEL TECHNIQUE FOR THE ANALYSIS OF SPIN POLARIZATION ON MAGNETIC SURFACES AND SPINTRONIC DEVICES

PROEFSCHRIFT

ter verkrijging van
de graad van doctor aan de Universiteit Twente,
op gezag van de rector magnificus,
prof. dr. H. Brinksma,
volgens besluit van het College voor Promoties
in het openbaar te verdedigen
op donderdag 20 mei 2010 om 15.00 uur

door

Iván Jesús Vera Marún

geboren op 1 oktober 1980

te Lechería, Venezuela

Dit proefschrift is goedgekeurd door

de promotor:	Prof. dr. P. J. Kelly
de assistent promotor:	Dr. R. Jansen

SPIN-FILTER SCANNING TUNNELING MICROSCOPY

A NOVEL TECHNIQUE FOR THE ANALYSIS OF SPIN POLARIZATION ON MAGNETIC SURFACES AND SPINTRONIC DEVICES

DISSERTATION

to obtain
the degree of doctor at the University of Twente,
on the authority of the rector magnificus,
prof. dr. H. Brinksma,
on account of the decision of the graduation committee,
to be publicly defended
on Thursday 20 May 2010 at 15.00 hrs

by

Iván Jesús Vera Marún

born on 1 October 1980

in Lechería, Venezuela

This dissertation is approved by

the promoter:	Prof. dr. P. J. Kelly
the assistant promoter:	Dr. R. Jansen

Dedicado a la presencia de Ana
y a la memoria de Ivonne

Contents

CHAPTER 1

Introduction

Nanotechnology encompasses the ability to observe and manipulate matter on the nanoscale. This thesis deals with the development of a technique for characterization of magnetic nanostructures, specifically in relation to spin-polarized transport. In this chapter we introduce background information on characterization of nanostructures, we outline the motivation for this thesis work and finally we give a description of the following chapters.

1.1 Scanning probe microscopy

Nanotechnology [1] is ubiquitous in current scientific and technical literature. When referring to the origins of nanotechnology most researchers mention the 1959 lecture by Richard Feynman [2]. There he described how the improvement of techniques to access the microscale and below could be revolutionary, especially regarding the mimicking of microbiological structures. Although highly referenced, Feynman's talk did not really start the boom of nanotechnology [3]. What really started it was the link between Feynman's ideas and new techniques for observation and manipulation on the nanoscale [4]. Such techniques began with the invention of the scanning tunneling microscope

(STM) in 1982 and its derivatives, which resulted in a Nobel prize just 5 years later [5].

STM showed the power of observing individual atoms on conducting surfaces and has allowed major developments in surface science. Visualization of atoms, at the apex of a tungsten field-emitter tip, had been already possible since the early 1950's using field-ion microscopy (FIM) [6]. The big difference when going from FIM to STM was the ability to interact locally with the atoms on the surface under study [7]. This opened the capability to create artificial nanostructures or direct chemical reactions atom by atom [8], transforming our perception of the mechanics of atomic structures [9].

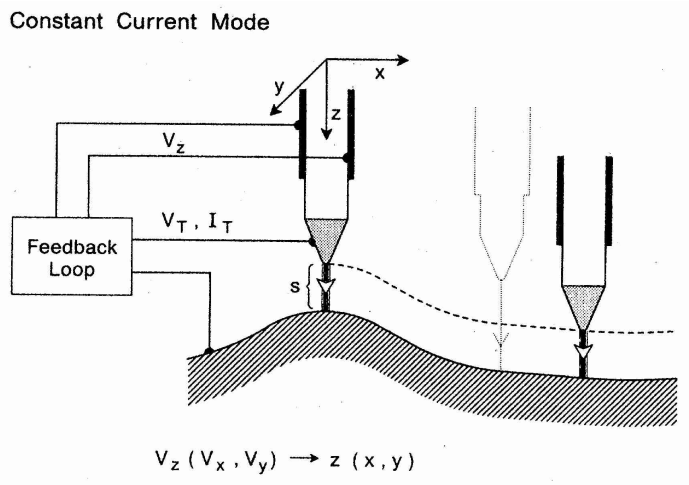

Figure 1.1. *Schematic of STM in constant current mode. The tip is scanned by sweeping V_X and V_Y in a raster-like fashion, whereas V_Z is modulated to keep the tunnel current I_T constant at fixed tip-sample bias V_T. Adapted from [5].*

The concept of STM is relatively simple [10]. It consists in scanning a conducting tip over a conducting surface as shown in Figure 1.1. A tip-sample bias V_T causes the tunneling of electrons between tip and sample when both are close enough to each other. The scanning action of the tip is performed by a piezoelectric actuator which can be precisely controlled, similar to a previous instrument called the topografiner [11]. The high resolution of the STM relies on the strong exponential dependence of the tunneling current on the tip-sample separation. When the tunnel current is kept constant by controlling the vertical position of the piezoelectrode with V_Z then this signal corresponds to the topographic picture of the surface. The key to the success of the STM to

access the atomic scale is the localized nature of the interaction between the sharp probe and the sample, effectively performing a local experiment at each sampled point during the raster scan. For a comprehensive description of STM we refer the reader to the book of Chen [12].

In the case of STM the interaction corresponds to the tunneling current, but the same approach can be used with any kind of near-field interaction. This is the principle of a group of techniques collectively called scanning probe microscopies [13]. A second revolution in surface science occurred when the measured interaction was the force between sample and tip. This is possible by using flexible cantilevers with sharp points as probes. The basic operation mode is to scan the probe while it exerts a constant force in contact with the sample. The force is proportional to the bending of the cantilever, which can be monitored by optical means. This operation mode is called (contact) atomic force microscopy (AFM) [14].

Advances in scanning probe techniques have been impressive. Variations of AFM can now produce atomic scale resolution comparable to that of STM, albeit with considerable difficulty [15]. By choosing appropriate probes, detectors and operation modes, one can measure different kind of forces between the probe and the sample. When the technique measures exchange interactions (repulsion), van der Waals, electrostatic or magnetic forces, it receives in each case a specific name, but the general scanning probe approach remains the same. Probes can be modified to be sharper or chemically selective, for example by attaching carbon nanotubes [16]. SPM offers the possibility to directly address and manipulate single molecules in order to measure their individual mechanical properties [17], a feat of considerable importance for biophysics [18].

The versatility of scanning probe microscopies to study and manipulate objects from the microscale down to the atomic scale is and will continue to be a major driving force towards establishing nanotechnology as an enabling technology that blurs the traditional barriers between scientific fields.

1.2 Why imaging magnetic nanostructures?

The field of magnetism has pervaded our lives since the introduction of the first magnetic hard disk drive in 1956, serving nowadays as the primary storage device for a myriad of applications [19]. In magnetic hard disk drives the

information is stored digitally as small magnetized regions called bits. A magnetic bit oriented in one direction may represent a '1' and an orientation in the opposite direction a '0'. The continuous reduction of critical feature sizes in magnetic data storage has allowed an exponential increase in the bit packing density, with present areal densities close to 1 Tb/in^2. As the technology downscales into the nanometer range there is a strong need to understand magnetic nanostructures. Therefore we require appropriate high-spatial-resolution characterization techniques.

From a scientific point of view, nanomagnetism is more than just an intermediate case between atomic scale magnetism and macroscopic magnetism. In the mesoscopic range there is a rich behavior of extrinsic properties like coercivity, remanence enhancement or nucleation modes which are highly geometry dependent [20]. The diversity of phenomena in nanomagnetism opens the door to several opportunities for applications, ranging from ultrastrong permanent magnets for energy efficient motors to biomagnetic sensors for medical applications [21].

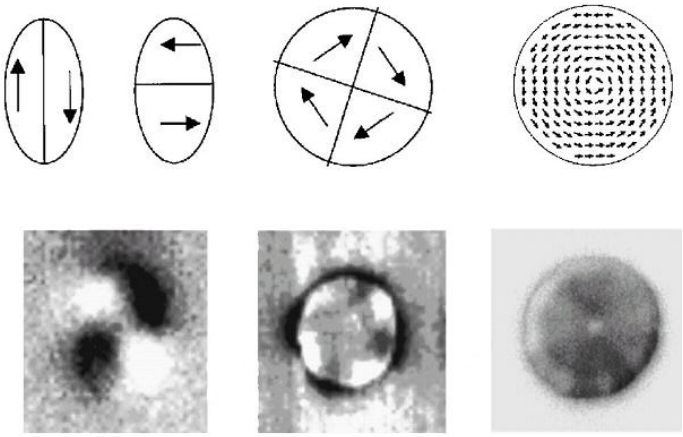

Figure 1.2. *Magnetic force microscopy images and suggested domain configuration for particles with different sizes and crystalline anisotropies. Left: elliptical particle with axes 150 and 450 nm made of a 50 nm thick epitaxial Co film. Center: circular particle with diameter 550 nm made of a 30 nm thick epitaxial (001)Fe film showing fourfold symmetry due to strong crystalline anisotropy. Right: circular particle with diameter 550 nm made of a 66 nm thick permalloy film showing a vortex state. Adapted from [22].*

A clear example of the importance of nanomagnetism is the case of patterned arrays of magnetic nanostructures. We consider circular magnetic dots

imaged with a variation of AFM called magnetic force microscopy (MFM) [23]. MFM detects the magnetic interaction between a magnetic sample and a probe with a thin magnetic coating. For dots with an in-plane easy axes and intermediate size (0.1 to 1 μm) the magnetic configuration is a vortex state, as shown in Figure 1.2. This state appears due to the balance of exchange and magnetostatic energies with the magnetization forming a flux closure except at the center where it shows a singularity pointing out-of-plane. Micromagnetic theory is a powerful tool to study magnetism at this scale [24]. If the dot is much larger it evolves into a multi-domain state, whereas if its size is decreased it shows a single-domain state. Such single-domain particles are interesting from the technological point of view. When their magnetization is oriented out-of-plane, as in Figure 1.3, they can form the basis of high-density perpendicular recording media. Out-of-plane magnetization can be realized in multilayer structures due to interface anisotropy [25, 26]. The direction of magnetization of a ferromagnetic material can also be controlled by shaping it into the form of a wire. Due to shape anisotropy the easy axis of magnetization is oriented along the wire axis [24].

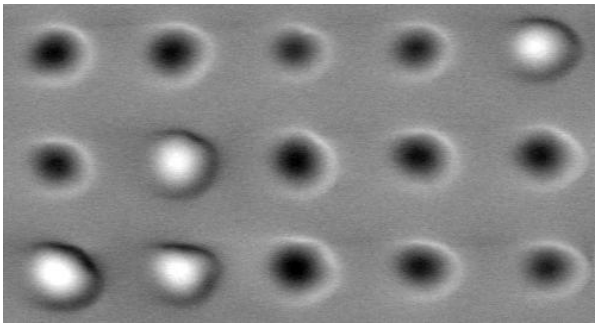

Figure 1.3. *Magnetic force microscopy of patterned media. Multilayer 20×(Co 5 Å/Pt 5 Å) dots with periodicity of 300 nm (diameter ≈ 140 nm) showing perpendicular single-domain state. Adapted from [27].*

The degree of electronic spin polarization is also a property that can be tailored in magnetic nanostructures [28]. This is relevant from the point of view of combining magnetism with electronics as it is occurring in the young field called spintronics (or magnetoelectronics) [29]. Here the spin of charge carriers is used as an extra degree of freedom to expand the capabilities of electronic devices such as magnetic memories, sensors and ultimately to develop new technologies like semiconductor electronics based on spin transport. The

interested reader is encouraged to check one of several thorough reviews on the subject [30, 31].

The initial thrust towards the study of spin-polarized transport came with the discovery of the giant magnetoresistance (GMR) effect in multilayers of alternating ferromagnetic metals and normal metals [32, 33]. The large resistance changes with magnetic field observed in this metallic structures opened the door to its rapid application in the read heads of magnetic hard disks, making it possible to keep up with the exponential increase in areal density [19]. The same GMR concept used in read heads has already proven its usefulness outside data storage applications. It is used to sense currents in conductors, monitor machinery (engine speed in automobiles), couple electrical systems, as displacement sensors and even to detect biological specimens [34]. The discovery of GMR, considering its large impact on modern technology, was recently recognized with a Nobel prize [35].

Spintronics promises a much larger technological impact than just providing GMR magnetic sensors or read heads. Completely new data storage systems are being developed which are based on arrays of magnetoresistive elements. Novel concepts include magnetic tunnel junctions (MTJs), propagation of domain walls in magnetic stripes, and switching via spin-transfer torque [36, 37]. The first commercial magnetic memory based on MTJ arrays was successfully introduced in 2006. Such magnetic random access memory (MRAM) combines the non-volatility, endurance and radiation resistance characteristic of magnetic materials together with fast access times and areal density approaching those of semiconductor memories [37]. Central to these developments is the use of magnetic nanostructures in the memory cells with typical lateral size below 100 nm.

The need for studying spin polarization becomes apparent when we consider the long-term goal of semiconductor spintronics [38]. Great effort has been placed on the development of devices that combine the electronic gain of a semiconductor transistor with the non-volatility of magnetic elements. The prototypical three-terminal spin transistor was proposed in 1990 [39]. This device has three main requirements: spin injection into a semiconductor, transport of spin information within the semiconductor, and detection of spin-dependent transmission [40]. Just the first requirement of efficient spin injection into a semiconductor has proven a hurdle. Fundamental obstacles to spin injection have been identified and solutions have been found in recent years [41, 42, 43]. Continuous progress has led to milestones such as

demonstration of all-electrical spin transport in semiconductors [44] and spin injection into silicon [45, 46]. Techniques to visualize and quantify the spin polarization of injected carriers are thus a must.

A future deployment of semiconductor spintronics where hybrid devices perform logic, communications and storage operations could have a profound impact on electronic systems. One example would be the broad use of reconfigurable electronics [47]. A direct approach to realize this is to have materials which are both magnetic and semiconducting. The prototypical ferromagnetic semiconductor is the diluted system $Ga_{1-x}Mn_xAs$, where the ferromagnetism is related to the carrier concentration, and many others are actively being studied [48]. The problems with these materials are their operation only at low temperature and the difficulty to prove that ferromagnetism is carrier-mediated. The latter happens because inhomogeneous magnetization in ferromagnetic semiconductors might arise due to inhomogeneous doping or formation of metallic ferromagnetic inclusions. Therefore careful characterization is required to understand the mechanism of ferromagnetism [49, 50]. A technique that can identify these inhomogeneities and quantify the spin polarization in the semiconducting matrix at the nanoscale would help to prove the existence of intrinsic and carrier-mediated ferromagnetism.

1.3 Motivation and thesis outline

Considering the examples given in the previous section it is clear that magnetic nanostructures matter a great deal for both scientific curiosity and practical interest. The advance of our understanding and control of magnetic nanostructures is directly tied to the development of appropriate magnetic microscopy methods. We can classify the imaging techniques in two groups according to the interaction mechanism between probe and sample, namely stray field mapping or magnetization mapping.

Among stray field mapping techniques the most widely used is MFM, followed by techniques using electron microscopes like Lorentz microscopy. The problem with field mapping is that the inversion of the information to obtain the magnetization of the sample is not unique [51]. For direct mapping of magnetization (or related properties) there are optical techniques like Kerr microscopy or x-ray based techniques like x-ray magnetic circular dichroism (XMCD) and electron beam based techniques like scanning electron micros-

copy with polarization analysis (SEMPA) [52]. Optical techniques stand out from the latter group due to their high temporal resolution for the study of spin dynamics [53] and XMCD is particularly powerful for element-specific imaging [54].

With regard to scanning probe techniques we have already mentioned that MFM has become the workhorse for imaging magnetic nanostructures. MFM has a truly general applicability as it senses the magnetostatic interaction between the ferromagnetic probe and sample. Despite steady progress on understanding and modeling MFM [51], the major drawback is its spatial resolution being limited in practice [55] to more than 10 nm [56].

According to micromagnetic theory [24] a vortex core in thin and soft ferromagnets has a width given by $2\sqrt{A/K_d}$, where A is the exchange stiffness and $K_d = \mu_0 M_s^2/2$ is the magnetostatic energy density [57]. For dots like those shown in Figure 1.2 this amounts to 9.9 nm for Co and 6.8 nm for Fe, below MFM resolution. Shifting from in-plane towards out-of-plane magnetized dots, as shown in Figure 1.3, is very relevant to present data storage hard disk drives using perpendicular magnetic recording [58]. As stated by its inventor [59] perpendicular magnetic recording is leading the way in data storage systems and is ultimately limited by the grain size of the magnetic medium, which is typically 5–10 nm. The resolution limit of MFM is a major drawback for its continued use as a workhorse for imaging modern day nanomagnetism.

It is important to note that magnetic imaging techniques which rely in sensing magnetic fields, like MFM, do not directly give information on the electronic spin polarization. For example, epitaxially grown lanthanum strontium manganese oxide (LSMO) nanowires possess a relatively small saturation magnetization M_s of 360 kA/m [60]. But LSMO is known to be a half-metal, which means its mobile electrons are nearly 100 % spin polarized [61]. A large spin polarization near Fermi level is a crucial requirement for many spin transport phenomena [30]. Therefore a technique that can measure spin polarization is relevant for characterization of spintronic properties of materials.

There are several scanning probe techniques with magnetic sensitivity which use magnetostatic forces, induced currents or magneto-optical effects [62]. There are also more specialized techniques that quantify magnetic flux or make use of magnetic resonance [63] which are alternatives in niche areas of application. But from all available scanning probe methods the STM-based techniques offer the highest resolution so far. This is demonstrated by the tremendous success of spin-polarized STM (SP-STM) to image magnetic

structure down to the atomic scale [64, 65]. More important, since STM is by definition a technique based on electron transport it gives access to the electronic structure of the sample [66].

Our focus is the development of a scanning probe technique for magnetic imaging highly relevant for spintronic nanostructures. Following the considerations above, we pursue in this work the goal of designing and implementing an STM-based technique to study magnetic surfaces. We set three requirements for such a technique. First, a high spatial resolution for magnetic imaging. Second, the ability to quantify the spin polarization near Fermi level on the surface of a conducting material. Third, general applicability without material restrictions like a specific electronic structure.

The thesis is structured as follows. In chapter 2 we give a short introduction to tunneling phenomena and show how it is used in present STM techniques with magnetic sensitivity. We argue that while these techniques have proven themselves capable of successful characterization of spin structures there is still a need for a generally applicable technique that can directly quantify spin polarization near Fermi level with high spatial resolution. So in chapter 3 we present the concept of our novel technique, spin-filter scanning tunneling microscopy (SF-STM). Next, in chapter 4 we describe the design and microfabrication process of multi-terminal probes consisting of a semiconductor/ferromagnet heterostructure, a key ingredient of our technique. In chapter 5 and chapter 6 we characterize the fabricated probes focusing on their geometrical, electrical, and magnetic properties. Finally, we present in chapter 7 the results of our preliminary experiments demonstrating the use of our microfabricated probes on magnetic surfaces, and assess the prospects of this novel technique.

References

[1] "National Nanotechnology Initiative FAQ". http://www.nano.gov/html/facts/faqs.html. [Cited on 1]

[2] R. P. Feynman. "There's plenty of room at the bottom". *California Institute of Technology Journal of Engineering and Science* **4** (2), 23–36 (1960). [Cited on 1]

[3] A. Junk and F. Riess. "From an idea to a vision: There's plenty of room at the bottom". *American Journal of Physics* **74** (9), 825–830 (2006). [Cited on 1]

[4] C. Toumey. "The man who understood the Feynman machine". *Nature Nanotechnology* **2** (1), 9–10 (2007). [Cited on 1]

[5] G. Binnig and H. Rohrer. "Scanning tunneling microscopy—from birth to adolescence". *Reviews of Modern Physics* **59** (3), 615–625 (1987). [Cited on 2]

[6] J. A. Panitz. "Field-ion microscopy-a review of basic principles and selected applications". *Journal of Physics E: Scientific Instruments* **15** (12), 1281 (1982). [Cited on 2]

[7] T. T. Tsong. "Fifty Years of Seeing Atoms". *Physics Today* **59** (3), 31 (2006). [Cited on 2]

[8] J. A. Stroscio and D. M. Eigler. "Atomic and Molecular Manipulation with the Scanning Tunneling Microscope". *Science* **254** (5036), 1319–1326 (1991). [Cited on 2]

[9] G. Binnig and H. Rohrer. "In touch with atoms". *Reviews of Modern Physics* **71** (2), S324 (1999). [Cited on 2]

[10] G. Binnig, H. Rohrer, C. Gerber, and E. Weibel. "Surface Studies by Scanning Tunneling Microscopy". *Physical Review Letters* **49** (1), 57 (1982). [Cited on 2]

[11] R. Young, J. Ward, and F. Scire. "The Topografiner: An Instrument for Measuring Surface Microtopography". *Review of Scientific Instruments* **43** (7), 999–1011 (1972). [Cited on 2]

[12] C. J. Chen. *Introduction to Scanning Tunneling Microscopy*. No. 64 in Monographs on the Physics and Chemistry of Materials (Oxford University Press, Oxford, 2007), 2nd edn. ISBN 978-0-19-921150-0. [Cited on 3]

[13] M. J. Brukman and D. A. Bonnell. "Probing physical properties at the nanoscale". *Physics Today* **61** (6), 36 (2008). [Cited on 3]

[14] G. Binnig, C. F. Quate, and C. Gerber. "Atomic Force Microscope". *Physical Review Letters* **56** (9), 930 (1986). [Cited on 3]

[15] F. J. Giessibl. "Advances in atomic force microscopy". *Reviews of Modern Physics* **75** (3), 949 (2003). [Cited on 3]

[16] J. H. Hafner, C. L. Cheung, A. T. Woolley, and C. M. Lieber. "Structural and functional imaging with carbon nanotube AFM probes". *Progress in Biophysics and Molecular Biology* **77** (1), 73–110 (2001). [Cited on 3]

[17] T. Hugel and M. Seitz. "The Study of Molecular Interactions by AFM Force Spectroscopy". *Macromolecular Rapid Communications* **22** (13), 989–1016 (2001). [Cited on 3]

[18] M. Rief and H. Grubmüller. "Force Spectroscopy of Single Biomolecules". *ChemPhysChem* **3** (3), 255–261 (2002). [Cited on 3]

[19] E. Grochowski and R. D. Halem. "Technological impact of magnetic hard disk drives on storage systems". *IBM Systems Journal* **42** (2), 338 (2003). [Cited on 3, 6]

[20] R. Skomski. "Nanomagnetics". *Journal of Physics: Condensed Matter* **15** (20), R841 (2003). [Cited on 4]

[21] S. D. Bader. "Colloquium: Opportunities in nanomagnetism". *Reviews of Modern Physics* **78** (1), 1–15 (2006). [Cited on 4]

[22] O. Kazakova, M. Hanson, P. Blomquist, and R. Wappling. "Arrays of epitaxial Co submicron particles: Critical size for single-domain formation and multidomain structures". *Journal of Applied Physics* **90** (5), 2440–2446 (2001). [Cited on 4]

[23] Y. Martin and H. K. Wickramasinghe. "Magnetic imaging by "force microscopy" with 1000 Å resolution". *Applied Physics Letters* **50** (20), 1455–1457 (1987). [Cited on 5]

[24] A. Hubert and R. Schäfer. *Magnetic Domains: The Analysis of Magnetic Microstructures* (Springer Berlin Heidelberg, 1998), corrected, 3rd printing 2009 edn. ISBN 978-3-540-64108-7. [Cited on 5, 8]

[25] M. T. Johnson, R. Jungblut, P. J. Kelly, and F. J. A. den Broeder. "Perpendicular magnetic anisotropy of multilayers: recent insights". *Journal of Magnetism and Magnetic Materials* **148** (1-2), 118–124 (1995). [Cited on 5]

[26] N. Nakajima, T. Koide, T. Shidara, H. Miyauchi, H. Fukutani, A. Fujimori, K. Iio, T. Katayama, M. Nývlt, and Y. Suzuki. "Perpendicular Magnetic Anisotropy Caused by Interfacial Hybridization via Enhanced Orbital Moment in Co/Pt Multilayers: Magnetic Circular X-Ray Dichroism Study". *Physical Review Letters* **81** (23), 5229 (1998). [Cited on 5]

[27] I. J. Vera-Marún. "Fabrication of nanomagnets using a hard mask scheme". 3rd report M.Sc. on nanotechnology, University of Twente (2005). [Cited on 5]

[28] F. J. Himpsel, K. N. Altmann, G. J. Mankey, J. E. Ortega, and D. Y. Petrovykh. "Electronic states in magnetic nanostructures". *Journal of Magnetism and Magnetic Materials* **200** (1-3), 456–469 (1999). [Cited on 5]

[29] S. A. Wolf, A. Y. Chtchelkanova, and D. M. Treger. "Spintronics - A retrospective and perspective". *IBM Journal of Research and Development* **50** (1), 101–110 (2006). [Cited on 5]

[30] I. Žutić, J. Fabian, and S. D. Sarma. "Spintronics: Fundamentals and applications". *Reviews of Modern Physics* **76** (2), 323 (2004). [Cited on 6, 8]

[31] J. Fabian, A. Matos-Abiague, C. Ertler, P. Stano, and I. Zutic. "Semiconductor Spintronics". *Acta Physica Slovaca* **57** (4&5), 565–907 (2007). Http://epub.uni-regensburg.de/7807/. [Cited on 6]

[32] M. N. Baibich, J. M. Broto, A. Fert, F. N. V. Dau, F. Petroff, P. Etienne, G. Creuzet, A. Friederich, and J. Chazelas. "Giant Magnetoresistance of (001)Fe/(001)Cr Magnetic Superlattices". *Physical Review Letters* **61** (21), 2472 (1988). [Cited on 6]

[33] G. Binasch, P. Grünberg, F. Saurenbach, and W. Zinn. "Enhanced magnetoresistance in layered magnetic structures with antiferromagnetic interlayer exchange". *Physical Review B* **39** (7), 4828 (1989). [Cited on 6]

[34] G. A. Prinz. "Magnetoelectronics applications". *Journal of Magnetism and Magnetic Materials* **200** (1-3), 57–68 (1999). [Cited on 6]

[35] S. M. Thompson. "The discovery, development and future of GMR: The Nobel Prize 2007". *Journal of Physics D: Applied Physics* **41** (9), 093001 (2008). [Cited on 6]

[36] S. Parkin, X. Jiang, C. Kaiser, A. Panchula, K. Roche, and M. Samant. "Magnetically engineered spintronic sensors and memory". *Proceedings of the IEEE* **91** (5), 661–680 (2003). [Cited on 6]

[37] C. Chappert, A. Fert, and F. N. V. Dau. "The emergence of spin electronics in data storage". *Nature Materials* **6** (11), 813–823 (2007). [Cited on 6]

[38] D. D. Awschalom and M. E. Flatte. "Challenges for semiconductor spintronics". *Nature Physics* **3** (3), 153–159 (2007). [Cited on 6]

[39] S. Datta and B. Das. "Electronic analog of the electro-optic modulator". *Applied Physics Letters* **56** (7), 665–667 (1990). [Cited on 6]

[40] B. Min. *Interface engineering of spin-tunnel contacts to silicon : towards silicon-based spintronic devices*. PhD thesis, University of Twente (2007). ISBN 978-90-365-2543-5. [Cited on 6]

[41] G. Schmidt, D. Ferrand, L. W. Molenkamp, A. T. Filip, and B. J. van Wees. "Fundamental obstacle for electrical spin injection from a ferromagnetic metal into a diffusive semiconductor". *Physical Review B* **62** (8), R4790 (2000). [Cited on 6]

[42] E. I. Rashba. "Theory of electrical spin injection: Tunnel contacts as a solution of the conductivity mismatch problem". *Physical Review B* **62** (24), R16267 (2000). [Cited on 6]

[43] B. Min, K. Motohashi, C. Lodder, and R. Jansen. "Tunable spin-tunnel contacts to silicon using low-work-function ferromagnets". *Nature Materials* **5** (10), 817–822 (2006). [Cited on 6]

[44] X. Lou, C. Adelmann, S. A. Crooker, E. S. Garlid, J. Zhang, K. S. M. Reddy, S. D. Flexner, C. J. Palmstrom, and P. A. Crowell. "Electrical detection of spin transport in lateral ferromagnet-semiconductor devices". *Nature Physics* **3** (3), 197–202 (2007). [Cited on 7]

[45] B. T. Jonker, G. Kioseoglou, A. T. Hanbicki, C. H. Li, and P. E. Thompson. "Electrical spin-injection into silicon from a ferromagnetic metal/tunnel barrier contact". *Nature Physics* **3** (8), 542–546 (2007). [Cited on 7]

[46] S. P. Dash, S. Sharma, R. S. Patel, M. P. de Jong, and R. Jansen. "Electrical creation of spin polarization in silicon at room temperature". *Nature* **462** (7272), 491–494 (2009). [Cited on 7]

[47] M. Tanaka. "Spintronics: recent progress and tomorrow's challenges". *Journal of Crystal Growth* **278** (1-4), 25–37 (2005). [Cited on 7]

[48] A. H. MacDonald, P. Schiffer, and N. Samarth. "Ferromagnetic semiconductors: moving beyond (Ga,Mn)As". *Nature Materials* **4** (3), 195–202 (2005). [Cited on 7]

[49] T. Fukumura, Y. Yamada, H. Toyosaki, T. Hasegawa, H. Koinuma, and M. Kawasaki. "Exploration of oxide-based diluted magnetic semiconductors toward transparent spintronics". *Applied Surface Science* **223** (1-3), 62–67 (2004). [Cited on 7]

[50] R. Ramaneti, J. C. Lodder, and R. Jansen. "Anomalous Hall effect in anatase Co:TiO_2 ferromagnetic semiconductor". *Applied Physics Letters* **91** (1), 012502–3 (2007). [Cited on 7]

[51] A. Thiaville, J. Miltat, and J. M. García. "Magnetic Force Microscopy: Images of Nanostructures and Contrast Modeling". In H. Hopster and H. P. Oepen (eds.), "Magnetic Microscopy of Nanostructures", No. XVIII in NanoScience and Technology, pp. 225–251 (Springer Berlin Heidelberg, 2005), 1st edn. ISBN 978-3-540-40186-5. [Cited on 7, 8]

[52] R. Allenspach, M. Stampanoni, and A. Bischof. "Magnetic domains in thin epitaxial Co/Au(111) films". *Physical Review Letters* **65** (26), 3344 (1990). [Cited on 8]

[53] J. Li, M. Lee, W. He, B. Redeker, A. Remhof, E. Amaladass, C. Hassel, and T. Eimuller. "Magnetic imaging with femtosecond temporal resolution". *Review of Scientific Instruments* **80** (7), 073703–5 (2009). [Cited on 8]

[54] M. R. Freeman and B. C. Choi. "Advances in Magnetic Microscopy". *Science* **294** (5546), 1484–1488 (2001). [Cited on 8]

[55] L. Abelmann, A. van den Bos, and C. Lodder. "Magnetic Force Microscopy-Towards Higher Resolution". In H. Hopster and H. P. Oepen (eds.), "Magnetic Microscopy of Nanostructures", No. XVIII in NanoScience and Technology, pp. 253–283 (Springer Berlin Heidelberg, 2005), 1st edn. ISBN 978-3-540-40186-5. [Cited on 8]

[56] M. R. Koblischka, U. Hartmann, and T. Sulzbach. "Improving the lateral resolution of the MFM technique to the 10 nm range". *Journal of Magnetism and Magnetic Materials* **272-276** (Part 3), 2138–2140 (2004). [Cited on 8]

[57] A. Wachowiak, J. Wiebe, M. Bode, O. Pietzsch, M. Morgenstern, and R. Wiesendanger. "Direct Observation of Internal Spin Structure of Magnetic Vortex Cores". *Science* **298** (5593), 577–580 (2002). [Cited on 8]

[58] S. Khizroev and D. Litvinov. "Perpendicular magnetic recording: Writing process". *Journal of Applied Physics* **95** (9), 4521–4537 (2004). [Cited on 8]

[59] S. Iwasaki. "Perpendicular magnetic recording —Its development and realization—". *Proceedings of the Japan Academy, Series B* **85** (2), 37–54 (2009). [Cited on 8]

[60] M. Mathews, R. Jansen, G. Rijnders, J. C. Lodder, and D. H. A. Blank. "Magnetic oxide nanowires with strain-controlled uniaxial magnetic anisotropy direction". *Physical Review B (Condensed Matter and Materials Physics)* **80** (6), 064408–7 (2009). [Cited on 8]

[61] A. Haghiri-Gosnet and J. Renard. "CMR manganites: physics, thin films and devices". *Journal of Physics D: Applied Physics* **36** (8), R127 (2003). [Cited on 8]

[62] U. Hartmann. "High-resolution magnetic imaging based on scanning probe techniques". *Journal of Magnetism and Magnetic Materials* **157-158**, 545–549 (1996). [Cited on 8]

[63] U. Hartmann. "Scanning Probe Methods for Magnetic Imaging". In H. Hopster and H. P. Oepen (eds.), "Magnetic Microscopy of Nanostructures", No. XVIII in NanoScience and Technology, pp. 285–307 (Springer Berlin Heidelberg, 2005), 1st edn. ISBN 978-3-540-40186-5. [Cited on 8]

[64] M. Bode. "Spin-polarized scanning tunnelling microscopy". *Reports on Progress in Physics* **66** (4), 523 (2003). [Cited on 9]

[65] M. Bode and R. Wiesendanger. "Spin-Polarized Scanning Tunneling Spectroscopy". In H. Hopster and H. P. Oepen (eds.), "Magnetic Microscopy of Nanostructures", No. XVIII in NanoScience and Technology, pp. 203–223 (Springer Berlin Heidelberg, 2005), 1st edn. ISBN 978-3-540-40186-5. [Cited on 9]

[66] H. J. W. Zandvliet and A. van Houselt. "Scanning Tunneling Spectroscopy". *Annual Review of Analytical Chemistry* **2**, 37–55 (2009). [Cited on 9]

CHAPTER 2

Magnetic imaging by scanning tunneling microscopy (STM)

We present a brief description of tunneling concepts as they evolved from solid state junctions and then introduce spin-dependent tunneling. We use these concepts to interpret scanning tunneling microscopy and describe how the most relevant STM-based techniques with spin sensitivity are used to study magnetic samples. We identify the need for a technique with practical and quantitative analysis of spin polarization.

2.1 Electron tunneling at a glance

The concept of tunneling "arises from the quantum-theory prediction that an initial state, prepared in one classically allowed region of configuration space, has a nonzero probability of penetrating through a classically forbidden region into a second classically allowed region" [1] as illustrated in Figure 2.1. Tunneling phenomena were one of the early successes of quantum mechanics. Its prediction and confirmation in a plethora of systems helped to establish the wave picture of matter. It is heavily applied in such diverse fields as atomic

physics (atomic field ionization), nuclear physics (alpha decay), and chemical reactions (molecular dissociation). In this section we restrict ourselves to discuss tunneling within the context of solid state physics. We focus on its application to tunnel junctions in order to understand STM.

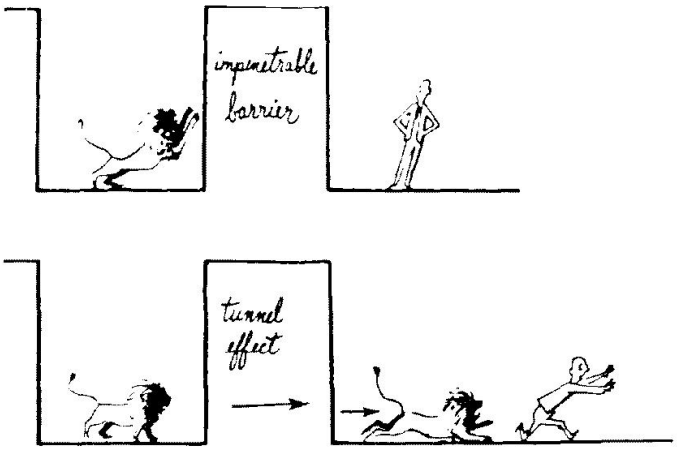

Figure 2.1. *Difference between classical theory and quantum theory by comparing a classically forbidden region with tunneling through a potential barrier. From [2].*

2.1.1 Basic description of tunneling

Two common ways to formulate the idea of tunneling are as a time-dependent initial-value problem or as a stationary-state problem. The stationary theory is by far the simplest and most used approach. In this theory the tunneling probability D is usually calculated by the Wentzel-Kramers-Brillouin (WKB) approximation [3]

$$D = \exp\left(-2\int_0^s \kappa \, \mathrm{d}s\right) \quad \text{with} \quad \kappa = \frac{\sqrt{2m\bar{\phi}}}{\hbar} \tag{2.1}$$

for an electron with mass m tunneling between two metallic electrodes through a potential barrier of thickness s and effective height $\bar{\phi}$. The quantity κ is the decay constant of the electron state within the barrier region. If we consider a rectangular tunnel barrier in the integration of Equation 2.1 we see that tunneling is characterized by an exponential decrease of the tunnel current with increasing barrier thickness or with the square root of the effective barrier

height. Tunneling is exquisitely sensitive to distance and to the energy of the electronic states involved, which is the reason of the high resolution of STM.

The stationary-state point of view has the advantage that it is applicable even for strong fields in which the tunnel probability cannot be treated as a perturbation. However, pioneering experiments by Giaever [4, 5], using solid state junctions with the structure normal metal/insulator/superconductor (NM/I/S), showed the appearance of the superconductor density of states (DOS) in the tunneling dI/dV spectra. This allowed the direct determination of the superconducting energy gap and called for a more refined description of tunneling. The WKB approach is heuristic, it cannot provide a logical and quantitative connection between tunneling conductance and the DOS.

The answer came in the form of the transfer Hamiltonian formalism by Bardeen [6, 7]. This can be viewed as a time-dependent formulation treating tunneling as a perturbation. We can now picture tunneling as arising due to the overlap within the tunnel barrier of the unperturbed electron wavefunctions corresponding to the conducting electrodes. It includes the many-body nature of tunneling in NM/I/S junctions and correctly predicted the appearance of the superconductor DOS. At a finite temperature the tunneling current I under an applied bias V can be represented as

$$\begin{aligned} I = \frac{2\pi e}{\hbar} \int_{-\infty}^{\infty} & [f(E_F - eV + \varepsilon) - f(E_F + \varepsilon)] \\ & \times [\rho_1(E_F - eV + \varepsilon)\rho_2(E_F + \varepsilon)] \, |M|^2 \, \mathrm{d}\varepsilon \end{aligned} \tag{2.2}$$

where $f(E)$ is the Fermi distribution function and the quantities $\rho_{1(2)}(E)$ are the density of states (DOS) of electrode 1(2), respectively. In this representation M is the average value of the matrix element $M(\Psi_1, \Psi_2)$ for tunneling between all states $\Psi_1(\Psi_2)$ of electrodes 1(2) whose energy lies in a small interval centered at ε. The theory does not use straightforward perturbation theory to obtain the tunneling matrix element M as it is based in several assumptions, but it has proven itself useful to interpret tunneling phenomena [8]. We will come back to the use of the transfer Hamiltonian formalism when discussing STM.

In practice, experimentalists often use fits to simple free-electron models based on stationary theory to parameterize experimental data [9, 10]. A widely used model is that of Simmons [9] which gives the tunnel current density J for a rectangular and symmetric tunnel barrier of height ϕ_0 under an applied bias V. At relatively low bias this expression can be reduced to a dependence of

the form $J = J_L(V + \beta V^3)$ as is commonly observed in experimental data. For moderate bias $eV < \phi_0$ the full expression is

$$J = J_0 \left\{ (\bar{\phi}) \exp\left[-\gamma \left(\bar{\phi}\right)^{\frac{1}{2}}\right] - (\bar{\phi} + eV) \exp\left[-\gamma \left(\bar{\phi} + eV\right)^{\frac{1}{2}}\right] \right\} \tag{2.3}$$

$$\text{with} \quad J_0 = \frac{e}{\hbar(2\pi s)^2} \quad , \quad \gamma = 2s\sqrt{\frac{2m}{\hbar^2}} \quad \text{and} \quad \bar{\phi} = \phi_0 - \frac{eV}{2}$$

2.1.2 Spin-dependent tunneling

Now we introduce the spin degree of freedom into tunneling. A second experimental breakthrough came with the work of Meservey and Tedrow [11] which dealt with the effect of high magnetic fields on junctions similar as those used by Giaever. They observed the splitting of the quasiparticle energy states in the superconducting electrode due to the applied magnetic field. For type 1 superconductors the DOS shows one peak at each edge of the energy gap. The splitting results in the dI/dV showing a DOS consisting of the addition of two shifted peaks per edge, each peak with opposite spin polarization. These peaks could act as a sort of analyzer for the spin-resolved contribution to tunneling from the other metallic electrode close to the Fermi level (within 1 meV).

By substituting the normal metal electrode by a ferromagnet (FM) they could indeed observe an asymmetry in the tunneling spectrum and quantify the degree of spin polarization of the ferromagnetic material using FM/I/S junctions [12]. We interpret the asymmetry as arising due to a difference in tunneling current for each spin component. If we consider the amount of tunneling electrons from the FM for majority (minority) spin $n_{\uparrow(\downarrow)}$ then the spin polarization of the tunneling current is defined as [13]

$$P \equiv \frac{n_\uparrow - n_\downarrow}{n_\uparrow + n_\downarrow} \tag{2.4}$$

where in principle it is understood as arising from the exchange-split DOS in the ferromagnet and considering tunneling as a spin-conserving process. Indeed, it was remarkable that the values of spin polarization obtained for several materials where in agreement with photoemission experiments on clean surfaces of these materials, even if the energy region sampled by each technique is different. This work unequivocally demonstrated spin-dependent tunneling in solid state devices. The polarization measured by the Meservey-Tedrow technique are usually taken as the standard for tunneling near Fermi level [14].

Still, there is a problem with directly relating the measured P to the FM total DOS: the values were positive for all $3d$ FM. If the fraction of tunneling electrons with majority spin is considered proportional to the fraction of majority-spin electrons in the FM DOS at Fermi level (and similarly for minority spin) then a negative P would be expected, in congruence with the negative P of the bulk DOS in Co. So we refer to the tunneling contribution $n_{\uparrow(\downarrow)}$ as an effective tunneling DOS. Stearns [15] offered a way out of this dilemma by considering the tunneling process to favor contributions from itinerant d_i electrons. $3d$ FM have localized d bands that have a strong negative P and high DOS at Fermi level, with a low group velocity. On the other hand s, p bands have a low DOS, compensated by a large group velocity. When the s, p bands hybridize with the d bands they can show a sizable exchange splitting while retaining a large group velocity near Fermi level. These electrons can be identified as the itinerant d_i electrons contributing to magnetoelectronic properties [16]. This points to the role of the tunnel barrier in determining the value and sign of spin polarization.

Stearns argument consists on disregarding the tunneling contribution of d electrons, since due to their localized nature their wavefunction decays rapidly within the tunnel barrier, and focus on the contribution from the more dispersive d_i electrons. The latter behave as nearly-free electrons so their DOS at Fermi level $\rho_{\uparrow(\downarrow)}$ is proportional to their Fermi wavevector $k_{\uparrow(\downarrow)}$. Taking the tunneling conductance to be proportional to the DOS we can substitute $n_{\uparrow(\downarrow)}$ with $k_{\uparrow(\downarrow)}$ in Equation 2.4. Following this analysis Stearns found positive P for Fe and Ni in agreement with the measured values with the Meservey-Tedrow technique. So spin polarized tunneling is dependent on specific electronic bands from the ferromagnet electrode (and also on the electronic properties of the barrier as we will discuss below).

A third experimental breakthrough was the observation of change in the tunneling resistance depending on the orientation (parallel or antiparallel) of two ferromagnetic electrodes in a $FM_1/I/FM_2$ tunnel junction [17, 18]. This tunneling magnetoresistance effect (TMR) is understood using a two-current model [19] where tunneling for each spin channel is considered independent. This approach is similar to the semi-phenomenological model of spin polarization used to interpret the Meservey-Tedrow technique. The difference is that instead of using a superconductor (in a high magnetic field) we have now a second ferromagnet with its exchange-split band structure acting as a spin analyzer. A majority electron tunneling out of FM_1 will enter into a majority

(minority) state in FM_2 if the electrodes are aligned parallel (antiparallel). With these assumptions we can obtain the conductances for each magnetic state $G_{P(AP)}$ and define the TMR effect as the change in resistance relative to the parallel state (optimistic definition)

$$G_P \propto n_\uparrow^1 n_\uparrow^2 + n_\downarrow^1 n_\downarrow^2 \quad \text{and} \quad G_{AP} \propto n_\uparrow^1 n_\downarrow^2 + n_\downarrow^1 n_\uparrow^2 \tag{2.5}$$

$$\text{TMR} \equiv \frac{G_P - G_{AP}}{G_{AP}} = \frac{R_{AP} - R_P}{R_P} = \frac{2P_1P_2}{1 - P_1P_2} \tag{2.6}$$

where P_i is the spin polarization due to each electrode. Equation 2.6 in conjunction with Equation 2.4 and assuming $n_{\uparrow(\downarrow)} \propto k_{\uparrow(\downarrow)}$ is usually referred to as Julliere model [17]. In a formal treatment of spin polarized tunneling by Slonczewski [20] (using still a free-electron approximation) it was shown that P depends on more factors than initially considered in Julliere model. The bottom line is that P_i does not depend only on the electronic structure of the electrode FM_i alone but we must consider it a description of the FM/I couple. Specifically, Slonczewski showed the height of the tunnel barrier affects the observed polarization. If the barrier's height is small it can decrease and even invert the sign of P, whereas when it is high the results approach Julliere's. Later work emphasized this notion of considering the spin polarization as an interface property [21].

A fourth experimental breakthrough came almost 20 years after Julliere's initial work on MTJs, when technological advances allowed the reliable fabrication of junctions showing large TMR response at room temperature [22, 23]. The use of good quality (though amorphous) Al_2O_3 tunnel barriers and flat electrodes exposed the basic behavior of MTJs in accordance with the previous model by Slonczewski[20]. In these FM_1/I/FM_2 there was agreement between measured TMR and the predicted TMR values using the spin polarization P_i obtained from the Meservey-Tedrow technique with FM/I/S structures. We must point out that this agreement is always present as long as the same barrier (amorphous Al_2O_3 in this instance) is used in both type of experiments, we will discuss barrier effects below. The early emergence of a basic picture of TMR and the technological achievements fueled a new wave of research around spin-dependent tunneling [24].

The current picture of TMR involves consideration of the detailed band structure of the FM and the barrier beyond that of free-electron models. Although the models of Julliere and Slonczewski seem to agree with experiment it was pointed out the limits of their application and the importance of electrode/

barrier electronic structure [25]. Detailed modeling of electronic transport from 3*d* FM in the ballistic regime by Tsymbal and Pettifor [26] remarked the role of covalent bonding at the FM/I interface on determining the orbital contribution to tunneling. By assuming only *s* bonding at the Co/Al_2O_3 they could correctly predict a positive spin polarization value, while introducing *p* and *d* bonding can readily decrease and change the sign of polarization. This dependence of *P* on interface chemistry was later observed experimentally [27]. According to theory [28] the usage of such an effective *P* can justify the application of Julliere model.

Further characterization of MTJs included experiments on tunneling bias and temperature dependence of TMR. Several processes introduce a decrease on polarization with increasing bias and temperature. Among these we consider intrinsic processes like spin-wave excitations of interface magnetism [29, 30, 31] and bias dependence due to the underlying band structure [32, 33, 34]. Extrinsic processes are usually related to the quality of the amorphous tunnel barrier, like spin-flip scattering due to barrier impurities [35] and multi-step tunneling via defects [36]. Theoretical calculations have also shown the effect of extrinsic factors including disorder in the electronic structure of the barrier [37] or disorder at the interfaces [38].

The convergence between theory and experiments recently increased after the development of epitaxial MTJs, notably those including MgO or $SrTiO_3$ barriers. These systems offer controllable interfaces, crystalline barriers with no defects and well defined electronic structure. Junctions using $SrTiO_3$ barriers exhibit a negative spin polarization of the $Co/SrTiO_3$ interface [39, 40]. Reliable measurement of this spin polarization is possible due to the use of LSMO as the other electrode. Since LSMO has nearly 100 % spin polarization [41] (half-metal) it acts as an ideal spin analyzer for the Co electrode [42, 43]. The half metallicity of LSMO is confirmed by MTJs with both electrodes made of LSMO which showed the highest TMR of 1800 % at low temperature [44]. The negative polarization of $Co/SrTiO_3$ is understood as arising due to the complex band structure of $SrTiO_3$ which is formed from localized 3*d* states of Ti that allows the efficient tunneling of minority *d* electrons from Co [45]. This is in contrast to the positive *P* found when using *sp*-bonded barriers like Al_2O_3 [14].

Indeed, in crystalline barriers the complex band structure causes the preferential tunneling of certain bands with specific symmetries. The most dramatic case is that of MgO barriers where large TMR values in excess of 200 % are ob-

servable at room temperature [46, 47]. The reliable fabrication of such devices have stimulated their development for industrial applications. Theoretically the large TMR in Fe/MgO/Fe is explained by considering the efficient transmission of *s* bands while the *d* bands decay rapidly within MgO [48, 49, 50]. The majority spin electrons in Fe, Co and Ni have more *s* character than the minority spin electrons, hence the large and positive TMR. This mechanism is consistent with the early arguments by Stearns for Al_2O_3 barriers [15].

In this section we have discussed a basic framework to rationalize spin-polarized tunneling in magnetic tunnel junctions. In practice we consider the degree of spin polarization P attributed to a certain ferromagnet/insulator interface as the relevant property determining the tunneling magnetoresistance (TMR) response. We relate these quantities within the framework of Julliere model. Since we are interested in developing a microscopy technique for measuring spin polarization of surfaces with possible technological applications (like TMR) we must choose a technique which is also based on tunneling. This is important because the definition of spin polarization depends on the transport phenomena under study [51]. Following these considerations the natural technique to consider is STM, which we discuss next.

2.2 Observing magnetism with STM

Interpretation of tunneling phenomena in STM uses the principles discussed in the previous section. Still, since early on it was clear that STM offered new possibilities when compared to planar solid state junctions [2]. An obvious difference is the local character of the microscope. Each pixel composing an STM image can be thought of as the result of a localized experiment between the apex of a sharp probe, ideally the very last atom of the probe, and a correspondingly small area of the sample. We can put the tunneling conductance G and the absolute tip-sample distance z on a quantitative ground by combining the WKB approximation for free-electron metals (Equation 2.1) and the Landauer theory of conductance [52]

$$G = G_0 \exp[-2\kappa(z - z_e)] \quad \text{with} \quad G_0 = \frac{e^2}{\pi\hbar} \approx 77.48\,\mu\text{S} \tag{2.7}$$

where z is defined as the vertical distance of the nucleus of the topmost tip atom with respect of the nucleus of the nearest atom from the sample. The

equilibrium tip-sample distance z_e with zero net force is where a single-atom contact is formed (about 2.5 Å). The tunnel barrier height $\bar{\phi}$ at low bias can be assumed to be equal to the metal work function, with values for typical materials in STM of 5 eV. Therefore we expect a tunneling distance $z - z_e$ of 5 Å at typical conductances of 1 GΩ. This distance has relevance regarding to how thick a barrier insulator could be deposited on top of a (ferro)magnet, while still being able to reliably operate an STM without making mechanical contact. For example, STM imaging on 2 two layers (5 Å) thick Al_2O_3 over a metal surface has proven successful [53].

A practical application of the transfer Hamiltonian formalism to STM experiments came with the introduction of the Tersoff-Hamann formula [54]. They modeled the electronic structure of the tip by radially symmetric wavefunctions, what is called s-wave tip states. In this case the tunneling matrix element M is proportional to the sample wavefunction at the location $\vec{r}_0$ of the center of curvature of the spherical tip $M \propto \Psi(\vec{r}_0)$. The result is that the tunneling current becomes proportional to the local density of states (LDOS) of the sample at the center of curvature of the tip $\rho_S(E, \vec{r}_0)$ [8]. Introducing this relationship into Equation 2.2 for the current and assuming that M does not depend on energy we obtain the following expression valid for low temperature

$$I \propto \int_0^{eV} \rho_T(E_F - eV + \varepsilon)\rho_S(E_F + \varepsilon, \vec{r}_0)\,\mathrm{d}\varepsilon \tag{2.8}$$

The latter equation represents an elementary model for interpreting scanning tunneling spectroscopy by relating the dynamic tunneling conductance G to the LDOS of the sample. Although the theory can be extended to more realistic tip states [55, 56] the present approach is very well applicable to tips made from nearly free-electron metals such as Au or Cu. In that case the DOS of the tip ρ_T is featureless and at moderate bias $G(V)$ can be considered to represent the LDOS of the sample alone

$$G(V) \equiv \frac{\mathrm{d}I}{\mathrm{d}V} \propto \rho_T \rho_S(E_F + eV, \vec{r}_0) \tag{2.9}$$

The Tersoff-Hamann formula provides a qualitatively correct interpretation of tunneling spectroscopy [57] and in many cases also a quantitative description of STM image resolution and corrugation amplitude [58]. We will come back to this subject in the following subsection.

Another difference between STM imaging of clean metal surfaces and solid tunnel junctions is the absence of a solid-state barrier. Most STM experiments

on magnetic surfaces are done under ultra high vacuum (UHV) conditions with freshly in-situ deposited metal films to avoid the influence of adsorbates and contamination. As we pointed out in subsection 2.1.2 the presence of a solid barrier has an influence in tunneling phenomena due to e.g. disorder, impurities or defects. These factors serve as scattering centers that change the momentum distribution of tunneling electrons contrary to the forward focused momenta expected for vacuum STM [59]. The absence of such factors result in a lower bias dependence of spin polarization [60].

Finally, the ability to change the width of the tunnel barrier by retracting the tip from the sample is probably the biggest difference from the case of a solid junction. By decreasing the width of the tunnel gap the spin polarization of the tunnel current can change. A increase of spin polarization at smaller tunnel was attributed to different decay constants κ of sp and d states [61], whereas a decrease of spin polarization at smaller widths has been attributed to a lower tunnel barrier height causing a decreased polarization according to Slonczewski's model [60], or spin-flip effects [62].

To apply the principles of spin-dependent tunneling acquired through research in solid junctions to the case of vacuum STM we must bear in mind the differences mentioned above. In general this would mean the absence of complications due to extrinsic effects in the tunnel barrier which allows the study of intrinsic tunneling phenomena.

2.2.1 Spin-polarized STM

The most successful STM-based technique to study surface magnetism is without a doubt spin-polarized scanning tunneling microscopy (SP-STM). For a comprehensive description of SP-STM and its modes of operation we refer the reader to a thorough review by Bode [63]. In short, SP-STM consists of using a tip with a magnetic surface FM_T to perform STM experiments on a magnetic sample FM_S. The resulting structure FM_T/vacuum/FM_S is in essence a MTJ. There are several modes of operation of SP-STM that can give information about the magnetic configuration of the sample. Below we focus on the most commonly used ones.

The first obvious way to use SP-STM is to scan the tip over the magnetic surface using the standard constant-current mode. This was first demonstrated by Wiesendanger et al. on the topological antiferromagnetic Cr(001) surface [64, 65]. In Cr(001) neighboring terraces separated by monatomic

steps are alternately magnetized in opposite directions. Given a constant gap width the tunneling conductance will be larger when the polarized tip and the Cr(001) terrace of the sample are aligned parallel and smaller when they are aligned antiparallel (see Equation 2.5). Since the STM is being operated in constant-current mode the feedback mechanism will adjust the gap width to achieve the set point tunnel current. The tunneling distance to a parallel terrace will then be larger than to an antiparallel one. This translates in alternating bi-valued step heights readily observable in the topographic scan measured with a magnetic tip, whereas a single-valued step height is measured for a non-magnetic tip.

The power of constant-current mode SP-STM to spatially resolve atomic-scale magnetism was shown by imaging the two-dimensional antiferromagnetic structure of a Mn monolayer on W(110) [66]. In this case the topographic STM image represents the magnetic superstructure of the sample rather than the real atomic topography, as long as a spin-sensitive tip is used. The fact that the magnetic contrast is so strong as to overcome the topographic corrugation is understood with the simple Tersoff-Hamann theory extended to include spin [67, 68]. Nevertheless, constant-current SP-STM is very challenging and limited when compared with other modes of operation. The main limitation is due to the use of the topographic signal to get magnetic information. It is possible to obtain magnetic images for atomic scale spin configurations (atomic scale STM alone is already challenging) but this mode is not useful to obtain information on nanoscale magnetic configuration [67]. Magnetic domains generally involve larger dimensions than atomic, and in this scale the small height variations due to spin-polarized tunneling (< 0.4 Å) are easily overshadowed by the usually larger topographic corrugation.

The most commonly used SP-STM mode of operation is that of spin-polarized scanning tunneling spectroscopy (SP-STS) [69]. This spectroscopic mode is an excellent technique for imaging nanoscale magnetism. In SP-STS a small bias modulation is superposed on the tunnel DC bias to obtain the dynamic conductance signal $\mathrm{d}I/\mathrm{d}V$ by using the lock-in technique. By expanding the Tersoff-Hamann model (Equation 2.8) with the two-current model of Julliere (Equation 2.6) we can account for spin-polarized tunneling.

Following Wortmann et al. [67] and Chen [52] Equation 2.9 is rewritten as

$$\frac{\mathrm{d}I}{\mathrm{d}V} \propto \rho_T \rho_S(E_F + eV, \vec{r}_0) \times (1 + P_T P_S(E_F + eV, \vec{r}_0)\cos(\theta) \tag{2.10}$$
$$\text{with} \quad \rho = \rho_\uparrow + \rho_\downarrow \quad \text{and} \quad P = \frac{\rho_\uparrow + \rho_\downarrow}{\rho_\uparrow - \rho_\downarrow}$$

where θ is the angle between the direction of spin polarization of the tip P_T and the direction of polarization of the sample P_S, and ρ is the non-spin-polarized DOS (LDOS) of the tip (sample). SP-STS has been successfully realized since it was first applied to study the surface of Gd(0001) thin films using Fe coated tips [70]. Gd(0001) exhibits a surface state exchange-split into a majority filled and an empty minority contribution. This characteristic makes Gd specially apt to demonstrate SP-STS operation.

The advantage of using a sample with a strong spin-polarized feature in its DOS is schematically shown in Figure 2.2. When the applied sample bias is changed to positive or negative values the empty or the filled sample states contribute to tunneling yielding peaks in the dynamic conductance $\mathrm{d}I/\mathrm{d}V$ spectrum close to the position of the surface state peaks. Several spectra can be acquired in different locations of the sample with each magnetic tip-sample alignment giving a slightly different spectrum, but it is more practical to scan the tip in constant-current mode while measuring the $\mathrm{d}I/\mathrm{d}V$ at the tunnel bias. The latter readily gives a map of $\mathrm{d}I/\mathrm{d}V$ at a single bias for the whole image much faster than taking spectra at each individual pixel.

The use of a spectroscopic signal helps in the separation of magnetic information from non-spin-polarized topographic contributions. To obtain the spin polarization of the sample two important assumptions are needed. First, the location of the exchange-split peaks are close enough to the Fermi level so that both spin parts can contribute to STS. Second, the spin polarization of the ferromagnetic tip is nearly constant in the energy range of interest. With these assumptions the asymmetry $A(V)$ observed in the dynamic conductance can be quantitatively related to the sample spin polarization

$$A(V) \equiv \frac{\mathrm{d}I/\mathrm{d}V_\uparrow - \mathrm{d}I/\mathrm{d}V_\downarrow}{\mathrm{d}I/\mathrm{d}V_\uparrow + \mathrm{d}I/\mathrm{d}V_\downarrow} \quad \text{and} \quad P_S(V) = \frac{A(V)}{P_T \cos\theta} \tag{2.11}$$

where $\mathrm{d}I/\mathrm{d}V_{\uparrow(\downarrow)}$ is the spectroscopic signal on sample domains with opposite magnetization and the angle θ is included to allow for a tip magnetization not collinear with the sample magnetization. Within this framework good

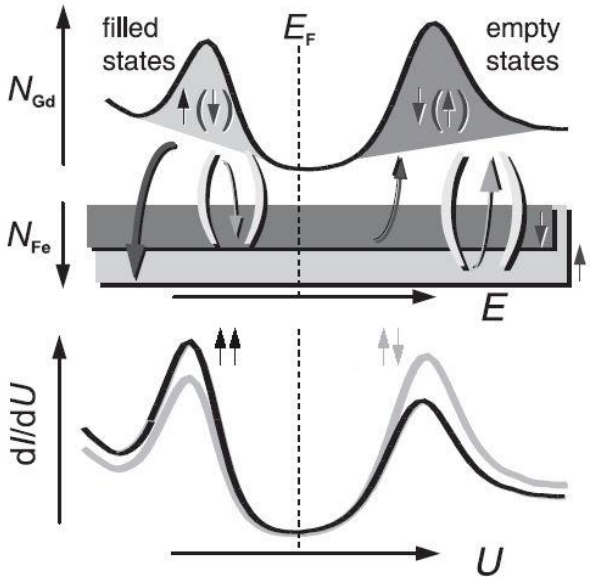

Figure 2.2. *Principle of SP-STS using a Gd(0001) sample with an exchange-split surface state and a magnetic Fe tip with constant spin polarization. Top: schematic of Gd and Fe spin-resolved DOS showing the tunneling contribution of each spin-channel when sample and tip magnetizations are aligned parallel (antiparallel). Bottom: Predicted dynamic conductance* $\mathrm{d}I/\mathrm{d}U$ *versus sample bias* U *showing reversal in signal contrast at the surface state peak positions upon reversal of sample magnetization. Adapted from [63].*

agreement between SP-STS experiments and photoemission data was found for Gd(0001) spin polarization [71].

The continuous success of SP-STS to reveal nanoscale magnetism is evidenced by its many achievements within the last ten years. Examples of observation of magnetic structure at high resolution includes domains in magnetic nanowires [72, 73], the magnetic structure of vortex cores in thin films [74] and even the (anti)ferromagnetic coupling of single magnetic adatoms on magnetic surfaces [75]. And there is also the possibility of manipulating the magnetic structure using the dipolar coupling due to the field from the tip (which can be avoided with antiferromagnetic tips [76]) or using current-induced switching [77].

We now discuss the quantitative analysis of spin polarization using the SP-STS. Even though SP-STS is appropriate for studying nanoscale magnetism, the spectroscopic nature of the technique makes the extraction of accurate

spin polarization difficult [78] and also limits the applicability to a wider range of material systems. A primary reason for these limitations is the need of strong spin-polarized features in the LDOS of the sample, as the exchange-split (surface) state of Gd(0001). If the material of interest has a constant LDOS and constant spin polarization there may not be any asymmetry visible in the $\mathrm{d}I/\mathrm{d}V$, contrary to what is known for solid-state MTJs. The main difference is the variable tunnel gap width in STM as explained in the following. The asymmetry from individual spectra for sample-tip (anti)parallel alignment gives a value of spin-polarization for different energies (Equation 2.11) but these spectra are taken at open-feedback condition. As mentioned above, practical use of SP-STS consists in scanning the tip at a fixed bias in closed feedback (i.e. constant current) while adding a small bias modulation. The tunneling distance is not governed by the LDOS but by the energy-integrated LDOS (ILDOS) [67]. If the ILDOS has a sizable spin-polarization the feedback would change the tunneling distance as for the case of the original constant-current SP-STM [64]. For antiparallel alignment the tunnel distance would be reduced, causing an effective increase in conductance, whereas the opposite would occur for parallel alignment. This effect from the spin-polarized ILDOS compensates the expected asymmetry at constant tunnel distance, leading to a strong reduction of the $\mathrm{d}I/\mathrm{d}V$ contrast [63]. On the other hand, if the ILDOS has a spin polarization with opposite sign to that of the LDOS then an increased apparent contrast is expected.

Therefore a large $\mathrm{d}I/\mathrm{d}V$ contrast that can offer an accurate picture of P_S can only be achieved if the ILDOS does not have a sizable spin polarization and we can assume a constant tunnel distance [78]. The minimum requirement for observing any contrast is to at least have different spin polarizations for LDOS and ILDOS but in this case an accurate value of P_S is not possible. This minimum requirement is not fulfilled when the sample has a constant spin polarization at all energies of interest which limits SP-STM applicability. This is the main reason why samples with strong LDOS features and enhanced tunnel bias are used in SP-STS. Unfortunately the same arguments are valid if tunneling is done at low bias to attempt to determine spin polarization at Fermi level. In this case both LDOS and ILDOS have similar spin polarization and the compensation mechanism just described also washes out the SP-STS contrast or may even invert it [79].

Another reason why the spectroscopic nature of the technique complicates image interpretation is that its dependence on small changes in spectroscopic

features makes it necessary to first get a detailed understanding of the spin-averaged electronic properties of the sample using non-magnetic tips. Only then can one assign $\mathrm{d}I/\mathrm{d}V$ asymmetry to magnetic effects. Due to contributions from non-spin-polarized electronic structure the interpretation of SP-STS images becomes even more complicated in the case of chemically inhomogeneous surfaces.

A related point of concern is the electronic structure and magnetization direction of the apex of the tip involved in tunneling. In STM the tip is very important (it is always half of the experiment). In general the energy dependence of the tip polarization cannot be neglected and Equation 2.11 is not directly applicable. Specially as the tip is made of magnetic material we can expect that the DOS is not constant. Therefore several tips must be used in order to account for changes in spectroscopic features from tip to tip. This also makes a reliable quantitative value of P_S more difficult [71] since P_T may not be well characterized. We also point out that $\mathrm{d}I/\mathrm{d}V$ measurements are mainly useful to find the empty density of states of the tip or sample, whereas for the occupied density of states the technique quickly looses sensitivity [80]. This invalidates Equation 2.10 for positive tip bias where the peaked distribution at the sample E_F is mainly probing the unoccupied states of the tip.

Apart from a different magnitude of P_T at the last atom of the tip, the magnetization direction is a critical factor determining sensitivity to out-of-plane or in-plane sample components. Complex magnetostatic configurations at the apex of tips with magnetic coating [81] introduce a large indeterminacy in the relative angle θ between the magnetizations of tip and sample. It is worth mentioning that SP-STS has also shown the capability of imaging both magnetization directions with the same tip by exploiting intra-atomic non-collinear magnetism in the tip [82]. So even with collinear bulk magnetizations of sample and tip there may be non-collinear components.

In conclusion, SP-STS is the technique of choice for nanoscale imaging of magnetic structures. It decouples topographic information that hinders the use of the original constant-current SP-STM mode and yields a great deal of information on the electronic structure of the sample. The main drawback is the strong convolution of magnetic information with (non-magnetic) electronic information which makes it difficult to get an accurate picture of the sample spin-polarization, specially close to Fermi level. Effects as the complex electronic structure of the tip P_T or the energy dependence of the tunneling matrix element M are usually ignored in the analysis of $\mathrm{d}I/\mathrm{d}V$ spectra. Therefore

a quantitative sample spin polarization requires a thorough comparison with detailed electronic structure calculations as pointed out by Yamada et al. [80] and proper characterization of the tip magnetic state. These are reasons for searching an alternative technique that can offer an accurate and generally applicable measurement of Fermi level spin polarization.

2.2.2 Ballistic electron magnetic microscopy

STM relies on the surface sensitivity of tunneling phenomena to get information from the topmost atoms of the sample. An interesting question is what happens with the injected carriers after they tunnel into the sample where they enter as hot electrons due to the applied tunneling bias V_T. After successive scattering events they loose their excess energy and eventually thermalize forming part of the current loop I_T between sample and tip. A different approach to STM is taken in ballistic electron emission microscopy (BEEM) where the energy-filtering properties of a metal-semiconductor Schottky barrier are used to remove a small part of the hot carriers from the metal and divert them via the semiconductor collector to a second electrical contact in the sample [83, 84]. Here we will give a brief description of the technique in order to understand the major differences relative to regular STM and how the magnetic counterpart of BEEM can be used to image magnetic nanostructures. For a thorough description of the transport processes involved in BEEM and related techniques we refer the reader to the extensive early review by Prietsch [85] and to more recent ones [86, 87, 88].

The basic configuration used in BEEM is shown in Figure 2.3. The sample consists of a semiconductor substrate with a thin metal film on top. This heterostructure leads to the formation of a Schottky energy barrier at the metal-semiconductor interface [89]. For moderate doping the Schottky barrier is wide enough to avoid tunneling through it and the transport is dominated by thermionic emission [90, 91]. The Schottky barrier prevents the transfer of electrons near the Fermi level of the metal into the semiconductor. If the tunneling bias V_T is less than the Schottky barrier height Φ_B the injected electrons do not have enough energy to enter into the semiconductor ($I_C = 0$). On the other hand, if $eV_T > \Phi_B$ then those electrons which have not undergone substantial scattering may fulfill the energy and momentum restrictions to enter into the semiconductor and contribute to I_C. This allows the investigation of the Schottky barrier corresponding to the buried metal-semiconductor interface [83,

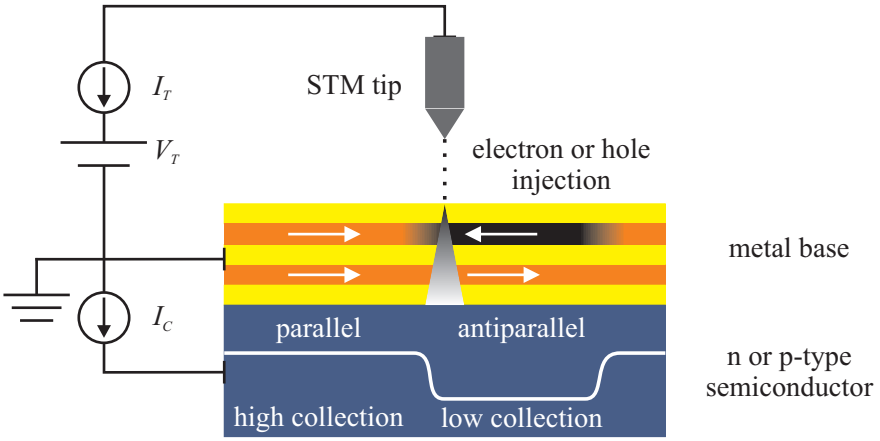

Figure 2.3. *Principle of ballistic electron magnetic microscopy. A metal-semiconductor Schottky diode is used as sample in BEEM. Individual contacts allow to measure the total tunnel current I_T and the ballistic part collected in the semiconductor I_C. In BEMM a magnetic spin-valve multilayer is used as the metal base. Spin-dependent filtering leads to an analogue of the optical polarizer-analyzer experiment.*

84] by monitoring the onset of I_C with increasing V_T.

In ballistic electron magnetic microscopy (BEMM) [92] the sensitivity of I_C to scattering processes in the metal base is combined with the spin dependence of hot-electron scattering in ferromagnetic metals by using a spin-valve structure as metal base (see Figure 2.3). The initially forward-focused and high-energy injected electrons undergo scattering as they progress into the base. These scattering processes remove electrons from the resulting collected signal I_C with a transmission probability that decays exponentially within the metal base with attenuation length λ. In ferromagnetic metals λ is spin dependent with majority spins being preferably transmitted ($\lambda_\uparrow > \lambda_\downarrow$) [93]. Consequently the relative magnetic alignment of the two ferromagnetic layers forming the spin valve leads to a larger I_C^P when both layers are parallel (smaller scattering) and a smaller I_C^{AP} when they are antiparallel (larger scattering), as shown in Figure 2.4. The relevant quantity measured in BEMM is the magnetocurrent MC defined as

$$\mathrm{MC} \equiv \frac{I_C^P - I_C^{AP}}{I_C^{AP}} \tag{2.12}$$

that due to the exponential spin filtering within the ferromagnets is commonly very large (MC $\approx$ 100–500 %). Therefore I_C gives information on the magnetic

state of the spin valve whereas the characteristic dependence on V_T is not substantially modified. A more detailed description of spin-dependent transport of hot electrons will be presented in the next chapter within the context of the goal of this thesis.

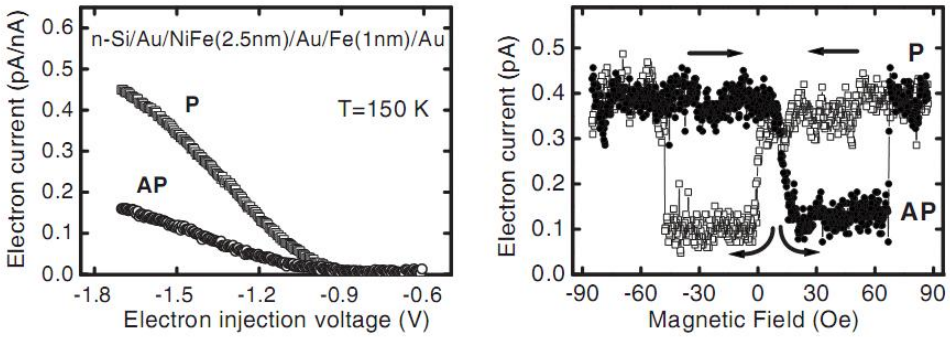

Figure 2.4. *Dependence of the collected electron current I_C on the magnetic configuration of the spin-valve base in BEMM. Left: I_C versus tip voltage for parallel (P) and antiparallel (AP) magnetic state, no signal is collected for $eV_T < \Phi_B = 0.8\,\mathrm{eV}$. Right: I_C versus magnetic field at fixed tip bias $V_T = -1.7\,\mathrm{V}$. Adapted from [94].*

Since its inception BEMM has demonstrated its power to study spin-dependent transport in magnetic nanostructures. Its usefulness range from the application as an imaging technique for magnetism in thin films [92] and nanostructures [95], acquisition of nanoscale hysteresis loops [96], up to studying fundamental processes of spin-dependent hot-electron transmission [93, 94]. Regarding the latter it is worth noticing that by using p-type semiconductor substrates it has also been possible to study spin-dependent transport of hot holes in a variant technique called ballistic hole magnetic microscopy (BHMM) [97, 98, 99, 100]. The complementary study of hot-hole transport gives insight into the spin dependence of electron-hole scattering processes in magnetic thin films [101].

The shape of the I_C vs V_T spectrum is determined by the energy and momentum distributions of the tunneling carriers plus the subsequent scattering processes within the metal and at the metal-semiconductor interface. Close to the onset of I_C it is normal to find a dependence of the transfer ratio α

$$\alpha = I_C/I_T \propto (eV_T - \Phi_B)^{\eta} \tag{2.13}$$

valid for a narrow energy window up to 0.3 eV above Φ_B, whereas for higher bias a (sub)linear dependence is observed [85]. The value of the exponent η

depends on the model used with the two most common values being $\eta = 2$ for the original Bell-Kaiser (BK) model [84] and $\eta = 2.5$ for the Ludeke-Prietsch (LP) model [102, 103]. The main assumptions on these models are the conservation of transverse momentum at the metal-semiconductor interface and energy-independent attenuation lengths. The former has been a topic of long debate [104, 105] with arguments both in favor [106] and against [107].

For Au/Si structures the BK model gives a better fit to experimental spectra than the LP model [85]. Since we will use Au/Si structures in this thesis we will only consider the BK model. It uses the framework of planar tunneling (similar as Equation 2.3) with the tunneling probability (Equation 2.1) depending only on the energy component E_x normal to the tunnel barrier. For the collector current two extra restrictions apply [87]. First, electrons must have enough energy to surmount the Schottky barrier so there is a minimum allowed energy E_x^{min}. Second, due to refraction at the metal-semiconductor interface there is a maximum allowed transverse energy E_t^{max} for collection, even if the electron energy is above the Schottky barrier. The obtained normalized collector current

$$\frac{I_C}{I_T} = R\frac{\int_{E_x^{min}}^{\infty} D(E_x)\int_0^{E_t^{max}}[f(E)-f(E+eV_T)]\,\mathrm{d}E_t\,\mathrm{d}E_x}{\int_0^{\infty} D(E_x)\int_0^{\infty}[f(E)-f(E+eV_T)]\,\mathrm{d}E_t\,\mathrm{d}E_x} \tag{2.14}$$

contains a parameter $R = T_{met}T_{int}$ considered energy independent for narrow enough energy range, that represents attenuation due to scattering within the metal base (T_{met}) and at the metal-semiconductor interface (T_{int}). Even though a planar tunneling framework is not strictly valid for STM [108] the BK model is very useful for parameterizing experimental data. A recent analytical form of the BK model by Thiaville et al. [109] has shown to properly fit spectra of Au/Si structures at extended energy ranges (more than 0.6 eV above Φ_B). Therefore we use the BK model to extract Schottky barrier heights and compare spectra in this thesis, with $\eta = 2$ (and $\eta = 4$ for operation in reverse mode [110]). More advanced models are considered in recent reviews [86, 87].

Imaging of spin-valve structures with BEMM has proven to achieve magnetic resolution better than 50 nm when collecting hot electrons [111] and better than 30 nm when collecting hot holes [98]. In these ballistic microscopies one loses spatial resolution from angular spread of the emitted carriers [112] which to first order is proportional to the thickness of the metal base. Since the sample must have an appropriate layered structure with a thickness large enough to induce contrast from spin-dependent scattering it is understandable the limited resolution achieved so far. On the other hand, the non-magnetic

BEEM technique has shown high resolution on the order of 1 nm [85, 104] and even atomic resolution for the case of surface-induced changes on the energy distribution of injected electrons [113].

We have discussed the main mechanism of electron transport in ballistic electron emission microscopy and how its magnetic counterpart BEMM can achieve magnetic contrast. But the magnetic imaging capabilities of BEMM only work when the sample consists of a special heterostructure. More important, the contrast mechanism in BEMM is the spin-dependent scattering of hot-carriers within the bulk of thin magnetic layers. This mechanism does not offer a way to quantify the spin-polarization near the Fermi level of those magnetic layers.

2.2.3 Alternative proposals

In the following we briefly discuss other STM-based and related imaging techniques used to study magnetic surfaces. We focus on their ability to image magnetic nanostructures and to measure the tunnel spin polarization of the sample.

There is another spectroscopic SP-STM operation mode by Wulfhekel et al. [114, 115, 116] where the modulation is achieved by alternating the direction of the tip magnetization $\vec{m}_T$ while assuming that the sample magnetization does not change. The local TMR effect is measured by recording $\mathrm{d}I/\mathrm{d}\vec{m}_T$ similar to the case of solid MTJs. This technique can get magnetic contrast without the need for different domains to be present in the same image (contrary to SP-STS) because one has control on the magnetization of the tip. Therefore it can provide magnetic information even if the sample is in a single-domain state. Another advantage is that it does not require knowledge of the spin-averaged electronic structure, since they only measure a spin-valve effect. On the other hand, one must be careful that the bulk tips used may generate too large stray fields, a problem that is avoided in SP-STS by the use of antiferromagnetic tips [76]. More relevant, the magnetization modulation in this technique requires proper deconvolution of magnetostriction effects in the tip which could add spurious contribution to the $\mathrm{d}I/\mathrm{d}\vec{m}_T$ signal. Even neglecting magnetostriction the presence of magnetic forces could also contribute to the current modulation $\mathrm{d}I/\mathrm{d}\vec{m}_T$. Compared with SP-STS this technique shares the same problems related to the indeterminacy of the electronic structure of the tip. It is worth to notice that magnetostrictive effects have indeed been harnessed to

image magnetic domains in Co dots with AFM using non-magnetic tips [117].

BEEM using a spin-polarized tip and a metal base made of a single ferromagnet was performed by Stollenwerk et al. [118]. Although it was not addressed in their work, that approach has the potential to measure the spin polarization of the tip by using the filtering effect of the magnetic base in the sample. This analysis would only happen at a single point at the tip apex. Therefore it is not possible any scanning or imaging of magnetic structure.

A great achievement for the study of atomic-scale magnetism in insulators came up with the realization of magnetic exchange force microscopy (MExFM) [119]. MExFM is a variation of non-contact AFM (NC-AFM) [120] using a magnetic tip. Such a technique is able to sense the short-range magnetic exchange force instead of the long-range magnetostatic force usually probed in MFM. NC-AFM with atomic resolution is notoriously difficult to achieve, so it is no wonder that more than 15 years had to pass to demonstrate MExFM after it was initially proposed [65]. MExFM can be applied to antiferromagnetic insulators which, similar to MFM, makes it capable of studying materials not apt for STM. The major problem of MExFM for nanoscale magnetism is that it shares the limitations of constant-current SP-STM, i.e. the impossibility to image magnetism on a scale larger than atomic due to its use of the topographic signal. Therefore its full potential is only realized by studying spin configurations as those found in antiferromagnetic surfaces. Furthermore, the interpretation of contrast formation in MExFM is still not fully understood [121]. Due to the absence of a quantitative link from MExFM contrast to spin-polarized transport this technique is not suited for our specific purpose of studying spintronic properties like spin polarization.

A different approach for STM-based magnetic microscopy is the use of non-spin-polarized tips. This line of research uses physical phenomena other than the usual TMR effect to study magnetic surfaces. The only STM-based technique we are aware of that has succeeded on imaging nanomagnetism with a non-magnetic tip is that of using spin-orbit coupling modifications of the sample LDOS by Bode et al. [122]. In this technique regular scanning tunneling spectroscopy with a non-magnetic tip can reveal the presence of domain walls because their electronic structure is different than that of domains. The major disadvantage is that it requires samples with a sizable effect of spin-orbit coupling on spectroscopic data. Since it relies in changes of the spin-averaged LDOS a measurement of spin polarization is not possible with this technique.

A combination of spin-polarized tunneling and optical techniques has been

studied by using GaAs tips [123, 124]. In this approach the GaAs tip is optically excited with circularly polarized light in order to create spin-polarized carriers. The polarization of the incident photons is modulated and the corresponding change in the tunneling current is monitored by the lock-in technique. Similar to SP-STS this technique as the potential to quantify the sample spin polarization. After several attempts a reliable magnetic contrast could not be unequivocally proved due to extrinsic dependence on the light polarization caused by purely optical effects given by the tunnel junction geometry that are hard to control [125]. Another magneto-optical effect (Faraday) was used to achieve magnetic contrast using a similar experimental setup [126] but in this case the resolution of 250 nm is optically limited and the contrast is not given by spin-dependent tunneling. We argue that the full potential of such GaAs tips is still to be demonstrated, as early experiments by Alvarado et al. [61, 127] using a GaAs sample and ferromagnetic tip (reversed geometry) were able to quantify the tunnel spin polarization. This early work in fact constituted the first demonstration of electrical spin injection into a semiconductor [128].

There is proposal of using a non-magnetic 2-terminal tip by Bruno [129, 130]. The concept is to use spin-orbit scattering within the tip to quantify the spin-asymmetry of conductance between the magnetic sample and one of the tip terminals. This approach is interesting but although experimental efforts have been put into its realization [131] this technique has not been demonstrated yet.

Finally, individual magnetic atoms can be studied in STM with non-magnetic tips by exploiting changes in the STS spectra due to the Kondo effect [132] or spin-flip effects [53]. In these cases imaging of nanoscale magnetic configurations is not possible and neither is quantifying spin polarization.

2.3 Conclusions

In this chapter we have presented a basic picture of electron tunneling in solid state systems and how this knowledge is transferred to the interpretation of vacuum tunneling in STM experiments. From fundamental relations between the tunnel current and the electronic properties of the electrodes and the tunnel barrier the concept of an effective tunneling DOS was developed. With the introduction of ferromagnetic electrodes possessing a spin-polarized DOS the field of magnetoelectronics took off from fundamental science up to the

technological application of magnetic tunnel junctions. It is this polarization which determines the characteristic phenomena of tunneling magnetoresistance and related spin-dependent phenomena.

Further developments on semiconductor spintronics and data storage systems render the study of spin polarization in nanostructures a major point of interest. The need for quantitative and high-resolution methods becomes apparent as traditional characterization techniques face fundamental limits for the study of such structures. The STM, with its atomic resolution and intrinsic capability to yield information on the electronic structure of magnetic samples comes forward as a method of choice to fulfill these needs. By applying the Tersoff-Hamann formula extended to include spin, it is understood how using a spin-polarized tip can yield magnetic contrast in SP-STM.

From all SP-STM operation modes the most successful to date is the spectroscopic one (SP-STS). This spectroscopic technique measures the asymmetry in the dynamic conductance for different alignments of tip and sample magnetizations in order to separate magnetic information from topographic information. Impressive images of nanoscale magnetism attest the applicability of SP-STS as a magnetic imaging technique. The spin polarization of the sample can also be quantified as demonstrated for the Gd(0001) surface. But this requires a previous knowledge of the electronic structure and magnetic configuration of the tip which complicates the quantitative interpretation of the data. The last atom of a magnetic tip can have a different magnetization direction than the assumed purely in- or out-of-plane which alters the magnetic contrast. More important is the structured DOS of magnetic tips, which require proper characterization of the sample using non-polarized tips in order to make a comparison. Finally, a major source of inaccuracy on the measured sample spin polarization is the adjustment of the tunneling distance by a sizable polarization in the integrated LDOS of the sample. This is a reason why better results are obtained with samples having strongly spin-polarized peaks in its DOS. Ideally we want a technique with the imaging capabilities of SP-STS but that is not limited to such specific samples. It is important to stress that all the other alternative STM-based methods discussed in the previous subsection lack the capability of giving a direct and reliable measure of spin polarization near Fermi level.

We have also discussed a rather different approach for magnetic imaging in BEMM. The (quasi)ballistic passage of hot carriers through spin-valve structures yields a direct map of the relative magnetic state due to the spin-

dependence of hot-electron scattering within the volume of ferromagnetic layers. Though the technique has a spatial resolution limited by the angular spread of the ballistic carriers, the interpretation of the relative contrast is indeed quite straightforward. All ferromagnets studied so far show a preferential transmission for majority electrons within their volume whereas minority spins are filtered out due to stronger scattering. So the major sample limitations is not so much the ferromagnetic material used but the special heterostructure required. It is not possible to measure the spin polarization near Fermi level of the magnetic layers in the spin valve. But this mechanism of spin filtering is promising for analysis of a spin-polarized tunnel current. We consider the possibility of using such spin-filtering effect in the next chapter.

References

[1] C. B. Duke. *Tunneling in Solids*. No. 10 in Solid State Physics (Academic Press, New York, 1969). ISBN 978-0-12-607770-4. [Cited on 15]

[2] D. Walmsley. "Pre-microscope tunnelling – Inspiration or constraint?" *Surface Science* **181** (1-2), 1–26 (1987). [Cited on 16, 22]

[3] S. Gasiorowicz. *Quantum physics* (Wiley, New York, 1974). ISBN 047129280X. [Cited on 16]

[4] I. Giaever. "Energy Gap in Superconductors Measured by Electron Tunneling". *Physical Review Letters* **5** (4), 147–148 (1960). [Cited on 17]

[5] I. Giaever and K. Megerle. "Study of Superconductors by Electron Tunneling". *Physical Review* **122** (4), 1101 (1961). [Cited on 17]

[6] J. Bardeen. "Tunnelling from a Many-Particle Point of View". *Physical Review Letters* **6** (2), 57–59 (1961). [Cited on 17]

[7] L. M. Falicov. "Quantum tunneling phenomena, John Bardeen, and the tunneling hamiltonian". *Journal of Superconductivity* **4** (5), 331–336 (1991). [Cited on 17]

[8] A. D. Gottlieb and L. Wesoloski. "Bardeen's tunnelling theory as applied to scanning tunnelling microscopy: a technical guide to the traditional interpretation". *Nanotechnology* **17** (8), R57 (2006). [Cited on 17, 23]

[9] J. G. Simmons. "Generalized Formula for the Electric Tunnel Effect between Similar Electrodes Separated by a Thin Insulating Film". *Journal of Applied Physics* **34** (6), 1793–1803 (1963). [Cited on 17]

[10] W. F. Brinkman, R. C. Dynes, and J. M. Rowell. "Tunneling Conductance of Asymmetrical Barriers". *Journal of Applied Physics* **41** (5), 1915–1921 (1970). [Cited on 17]

[11] R. Meservey, P. M. Tedrow, and P. Fulde. "Magnetic Field Splitting of the Quasiparticle States in Superconducting Aluminum Films". *Physical Review Letters* **25** (18), 1270 (1970). [Cited on 18]

[12] P. M. Tedrow and R. Meservey. "Spin-Dependent Tunneling into Ferromagnetic Nickel". *Physical Review Letters* **26** (4), 192 (1971). [Cited on 18]

[13] P. M. Tedrow and R. Meservey. "Spin Polarization of Electrons Tunneling from Films of Fe, Co, Ni, and Gd". *Physical Review B* **7** (1), 318 (1973). [Cited on 18]

[14] R. Meservey and P. M. Tedrow. "Spin-polarized electron tunneling". *Physics Reports* **238** (4), 173–243 (1994). [Cited on 18, 21]

[15] M. B. Stearns. "Simple explanation of tunneling spin-polarization of Fe, Co, Ni and its alloys". *Journal of Magnetism and Magnetic Materials* **5** (2), 167–171 (1977). [Cited on 19, 22]

[16] F. J. Himpsel, K. N. Altmann, G. J. Mankey, J. E. Ortega, and D. Y. Petrovykh. "Electronic states in magnetic nanostructures". *Journal of Magnetism and Magnetic Materials* **200** (1-3), 456–469 (1999). [Cited on 19]

[17] M. Julliere. "Tunneling between ferromagnetic films". *Physics Letters A* **54** (3), 225–226 (1975). [Cited on 19, 20]

[18] S. Maekawa and U. Gafvert. "Electron tunneling between ferromagnetic films". *Magnetics, IEEE Transactions on* **18** (2), 707–708 (1982). [Cited on 19]

[19] N. F. Mott. "The Electrical Conductivity of Transition Metals". *Proceedings of the Royal Society of London. Series A - Mathematical and Physical Sciences* **153** (880), 699–717 (1936). [Cited on 19]

[20] J. C. Slonczewski. "Conductance and exchange coupling of two ferromagnets separated by a tunneling barrier". *Physical Review B* **39** (10), 6995 (1989). [Cited on 20]

[21] J. Velev, P. Dowben, E. Tsymbal, S. Jenkins, and A. Caruso. "Interface effects in spin-polarized metal/insulator layered structures". *Surface Science Reports* **63** (9), 400–425 (2008). [Cited on 20]

[22] T. Miyazaki and N. Tezuka. "Giant magnetic tunneling effect in Fe/Al2O3/Fe junction". *Journal of Magnetism and Magnetic Materials* **139** (3), L231–L234 (1995). [Cited on 20]

[23] J. S. Moodera, L. R. Kinder, T. M. Wong, and R. Meservey. "Large Magnetoresistance at Room Temperature in Ferromagnetic Thin Film Tunnel Junctions". *Physical Review Letters* **74** (16), 3273 (1995). [Cited on 20]

[24] E. Y. Tsymbal, O. N. Mryasov, and P. R. LeClair. "Spin-dependent tunnelling in magnetic tunnel junctions". *Journal of Physics: Condensed Matter* **15** (4), R109 (2003). [Cited on 20]

[25] J. M. MacLaren, X. Zhang, and W. H. Butler. "Validity of the Julliere model of spin-dependent tunneling". *Physical Review B* **56** (18), 11827 (1997). [Cited on 21]

[26] E. Y. Tsymbal and D. G. Pettifor. "Modelling of spin-polarized electron tunnelling from 3d ferromagnets". *Journal of Physics: Condensed Matter* **9** (30), L411 (1997). [Cited on 21]

[27] M. Sharma, S. X. Wang, and J. H. Nickel. "Inversion of Spin Polarization and Tunneling Magnetoresistance in Spin-Dependent Tunneling Junctions". *Physical Review Letters* **82** (3), 616 (1999). [Cited on 21]

[28] K. D. Belashchenko, E. Y. Tsymbal, M. van Schilfgaarde, D. A. Stewart, I. I. Oleynik, and S. S. Jaswal. "Effect of interface bonding on spin-dependent tunneling from the oxidized Co surface". *Physical Review B* **69** (17), 174408 (2004). [Cited on 21]

[29] S. Zhang, P. M. Levy, A. C. Marley, and S. S. P. Parkin. "Quenching of Magnetoresistance by Hot Electrons in Magnetic Tunnel Junctions". *Physical Review Letters* **79** (19), 3744 (1997). [Cited on 21]

[30] J. S. Moodera, J. Nowak, and R. J. M. van de Veerdonk. "Interface Magnetism and Spin Wave Scattering in Ferromagnet-Insulator-Ferromagnet Tunnel Junctions". *Physical Review Letters* **80** (13), 2941 (1998). [Cited on 21]

[31] C. H. Shang, J. Nowak, R. Jansen, and J. S. Moodera. "Temperature dependence of magnetoresistance and surface magnetization in ferromagnetic tunnel junctions". *Physical Review B* **58** (6), R2917 (1998). [Cited on 21]

[32] A. H. Davis and J. M. MacLaren. "Spin dependent tunneling at finite bias". *Journal of Applied Physics* **87**, 5224–5226 (2000). [Cited on 21]

[33] P. LeClair, J. T. Kohlhepp, C. H. van de Vin, H. Wieldraaijer, H. J. M. Swagten, W. J. M. de Jonge, A. H. Davis, J. M. MacLaren, J. S. Moodera, and R. Jansen. "Band Structure and Density of States Effects in Co-Based Magnetic Tunnel Junctions". *Physical Review Letters* **88** (10), 107201 (2002). [Cited on 21]

[34] S. O. Valenzuela, D. J. Monsma, C. M. Marcus, V. Narayanamurti, and M. Tinkham. "Spin Polarized Tunneling at Finite Bias". *Physical Review Letters* **94** (19), 196601 (2005). [Cited on 21]

[35] R. Jansen and J. S. Moodera. "Influence of barrier impurities on the magnetoresistance in ferromagnetic tunnel junctions". In "The 7th joint MMM-intermag conference on magnetism and magnetic materials", vol. 83, pp. 6682–6684 (AIP, San Francisco, California (USA), 1998). [Cited on 21]

[36] J. Zhang and R. M. White. "Voltage dependence of magnetoresistance in spin dependent tunneling junctions". In "The 7th joint MMM-intermag conference on magnetism and magnetic materials", vol. 83, pp. 6512–6514 (AIP, San Francisco, California (USA), 1998). [Cited on 21]

[37] E. Y. Tsymbal and D. G. Pettifor. "Spin-polarized electron tunneling across a disordered insulator". *Physical Review B* **58** (1), 432 (1998). [Cited on 21]

[38] P. X. Xu, V. M. Karpan, K. Xia, M. Zwierzycki, I. Marushchenko, and P. J. Kelly. "Influence of roughness and disorder on tunneling magnetoresistance". *Physical Review B (Condensed Matter and Materials Physics)* **73** (18), 180402–4 (2006). [Cited on 21]

[39] J. M. D. Teresa, A. Barthélémy, A. Fert, J. P. Contour, R. Lyonnet, F. Montaigne, P. Seneor, and A. Vaurès. "Inverse Tunnel Magnetoresistance in Co/SrTiO3/La0.7Sr0.3MnO3: New Ideas on Spin-Polarized Tunneling". *Physical Review Letters* **82** (21), 4288 (1999). [Cited on 21]

[40] J. M. D. Teresa, A. Barthélémy, A. Fert, J. P. Contour, F. Montaigne, and P. Seneor. "Role of Metal-Oxide Interface in Determining the Spin Polarization of Magnetic Tunnel Junctions". *Science* **286** (5439), 507–509 (1999). [Cited on 21]

[41] A. Haghiri-Gosnet and J. Renard. "CMR manganites: physics, thin films and devices". *Journal of Physics D: Applied Physics* **36** (8), R127 (2003). [Cited on 21]

[42] M. Bowen, J. Maurice, A. Barthelemy, P. Prod'homme, E. Jacquet, J. Contour, D. Imhoff, and C. Colliex. "Bias-crafted magnetic tunnel junctions with bistable spin-dependent states". *Applied Physics Letters* **89** (10), 103517–3 (2006). [Cited on 21]

[43] I. J. Vera-Marún, F. M. Postma, J. C. Lodder, and R. Jansen. "Tunneling magnetoresistance with positive and negative sign in La0.67Sr0.33MnO3/SrTiO3/Co junctions". *Physical Review B (Condensed Matter and Materials Physics)* **76** (6), 064426–5 (2007). [Cited on 21]

[44] M. Bowen, M. Bibes, A. Barthélémy, J. Contour, A. Anane, Y. Lemaître, and A. Fert. "Nearly total spin polarization in La[sub 2/3]Sr[sub 1/3]MnO[sub 3] from tunneling experiments". *Applied Physics Letters* **82** (2), 233–235 (2003). [Cited on 21]

[45] J. P. Velev, K. D. Belashchenko, D. A. Stewart, M. van Schilfgaarde, S. S. Jaswal, and E. Y. Tsymbal. "Negative Spin Polarization and Large Tunneling Magnetoresistance in Epitaxial Co|SrTiO3|Co Magnetic Tunnel Junctions". *Physical Review Letters* **95** (21), 216601 (2005). [Cited on 21]

[46] S. S. P. Parkin, C. Kaiser, A. Panchula, P. M. Rice, B. Hughes, M. Samant, and S. Yang. "Giant tunnelling magnetoresistance at room temperature with MgO (100) tunnel barriers". *Nature Materials* **3** (12), 862–867 (2004). [Cited on 22]

[47] S. Yuasa, T. Nagahama, A. Fukushima, Y. Suzuki, and K. Ando. "Giant room-temperature magnetoresistance in single-crystal Fe/MgO/Fe magnetic tunnel junctions". *Nature Materials* **3** (12), 868–871 (2004). [Cited on 22]

[48] J. Mathon and A. Umerski. "Theory of tunneling magnetoresistance of an epitaxial Fe/MgO/Fe(001) junction". *Physical Review B* **63** (22), 220403 (2001). [Cited on 22]

[49] W. H. Butler, X. Zhang, T. C. Schulthess, and J. M. MacLaren. "Spin-dependent tunneling conductance of Fe|MgO|Fe sandwiches". *Physical Review B* **63** (5), 054416 (2001). [Cited on 22]

[50] K. D. Belashchenko, J. Velev, and E. Y. Tsymbal. "Effect of interface states on spin-dependent tunneling in Fe/MgO/Fe tunnel junctions". *Physical Review B* **72** (14), 140404 (2005). [Cited on 22]

[51] I. I. Mazin. "How to Define and Calculate the Degree of Spin Polarization in Ferromagnets". *Physical Review Letters* **83** (7), 1427 (1999). [Cited on 22]

[52] C. J. Chen. *Introduction to Scanning Tunneling Microscopy*. No. 64 in Monographs on the Physics and Chemistry of Materials (Oxford University Press, Oxford, 2007), 2nd edn. ISBN 978-0-19-921150-0. [Cited on 22, 26]

[53] A. J. Heinrich, J. A. Gupta, C. P. Lutz, and D. M. Eigler. "Single-Atom Spin-Flip Spectroscopy". *Science* **306** (5695), 466–469 (2004). [Cited on 23, 36]

[54] J. Tersoff and D. R. Hamann. "Theory of the scanning tunneling microscope". *Physical Review B* **31** (2), 805 (1985). [Cited on 23]

[55] C. J. Chen. "Origin of atomic resolution on metal surfaces in scanning tunneling microscopy". *Physical Review Letters* **65** (4), 448 (1990). [Cited on 23]

[56] C. J. Chen. "Tunneling matrix elements in three-dimensional space: The derivative rule and the sum rule". *Physical Review B* **42** (14), 8841 (1990). [Cited on 23]

[57] N. D. Lang. "Spectroscopy of single atoms in the scanning tunneling microscope". *Physical Review B* **34** (8), 5947 (1986). [Cited on 23]

[58] Y. Kuk, P. J. Silverman, and H. Q. Nguyen. "Study of metal surfaces by scanning tunneling microscopy with field ion microscopy". *Journal of Vacuum Science & Technology A: Vacuum, Surfaces, and Films* **6** (2), 524–528 (1988). [Cited on 23]

[59] R. Jansen, T. Banerjee, B. G. Park, and J. C. Lodder. "Probing momentum distributions in magnetic tunnel junctions via hot-electron decay". *Applied Physics Letters* **90** (19), 192503–3 (2007). [Cited on 24]

[60] W. Wulfhekel, H. F. Ding, and J. Kirschner. "Tunneling magnetoresistance through a vacuum gap". *Journal of Magnetism and Magnetic Materials* **242-245** (Part 1), 47–52 (2002). [Cited on 24]

[61] S. F. Alvarado. "Tunneling Potential Barrier Dependence of Electron Spin Polarization". *Physical Review Letters* **75** (3), 513 (1995). [Cited on 24, 36]

[62] M. V. Rastei and J. P. Bucher. "Spin polarized tunnelling investigation of nanometre Co clusters by means of a Ni bulk tip". *Journal of Physics: Condensed Matter* **18** (50), L619 (2006). [Cited on 24]

[63] M. Bode. "Spin-polarized scanning tunnelling microscopy". *Reports on Progress in Physics* **66** (4), 523 (2003). [Cited on 24, 27, 28]

[64] R. Wiesendanger, H. Güntherodt, G. Güntherodt, R. J. Gambino, and R. Ruf. "Observation of vacuum tunneling of spin-polarized electrons with the scanning tunneling microscope". *Physical Review Letters* **65** (2), 247 (1990). [Cited on 24, 28]

[65] R. Wiesendanger, D. Burgler, G. Tarrach, A. Wadas, D. Brodbeck, H. Guntherodt, G. Guntherodt, R. J. Gambino, and R. Ruf. "Vacuum tunneling of spin-polarized electrons detected by scanning tunneling microscopy". In "Fifth international conference on scanning tunneling microscopy/spectroscopy", vol. 9, pp. 519–524 (AVS, Boston, Massachusetts (USA), 1991). [Cited on 24, 35]

[66] S. Heinze, M. Bode, A. Kubetzka, O. Pietzsch, X. Nie, S. Blugel, and R. Wiesendanger. "Real-Space Imaging of Two-Dimensional Antiferromagnetism on the Atomic Scale". *Science* **288** (5472), 1805–1808 (2000). [Cited on 25]

[67] D. Wortmann, S. Heinze, P. Kurz, G. Bihlmayer, and S. Blügel. "Resolving Complex Atomic-Scale Spin Structures by Spin-Polarized Scanning Tunneling Microscopy". *Physical Review Letters* **86** (18), 4132 (2001). [Cited on 25, 26, 28]

[68] S. Heinze. "Simulation of spin-polarized scanning tunneling microscopy images of nanoscale non-collinear magnetic structures". *Applied Physics A: Materials Science & Processing* **85** (4), 407–414 (2006). [Cited on 25]

[69] M. Bode and R. Wiesendanger. "Spin-Polarized Scanning Tunneling Spectroscopy". In H. Hopster and H. P. Oepen (eds.), "Magnetic Microscopy of Nanostructures", No. XVIII in NanoScience and Technology, pp. 203–223 (Springer Berlin Heidelberg, 2005), 1st edn. ISBN 978-3-540-40186-5. [Cited on 25]

[70] M. Bode, M. Getzlaff, and R. Wiesendanger. "Spin-Polarized Vacuum Tunneling into the Exchange-Split Surface State of Gd(0001)". *Physical Review Letters* **81** (19), 4256 (1998). [Cited on 26]

[71] M. Bode, M. Dreyer, M. Getzlaff, M. Kleiber, A. Wadas, and R. Wiesendanger. "Recent progress in high-resolution magnetic imaging using scanning probe techniques". *Journal of Physics: Condensed Matter* **11** (48), 9387–9402 (1999). [Cited on 27, 29]

[72] O. Pietzsch, A. Kubetzka, M. Bode, and R. Wiesendanger. "Observation of Magnetic Hysteresis at the Nanometer Scale by Spin-Polarized Scanning Tunneling Spectroscopy". *Science* **292** (5524), 2053–2056 (2001). [Cited on 27]

[73] E. Y. Vedmedenko, A. Kubetzka, K. von Bergmann, O. Pietzsch, M. Bode, J. Kirschner, H. P. Oepen, and R. Wiesendanger. "Domain Wall Orientation in Magnetic Nanowires". *Physical Review Letters* **92** (7), 077207 (2004). [Cited on 27]

[74] A. Wachowiak, J. Wiebe, M. Bode, O. Pietzsch, M. Morgenstern, and R. Wiesendanger. "Direct Observation of Internal Spin Structure of Magnetic Vortex Cores". *Science* **298** (5593), 577–580 (2002). [Cited on 27]

[75] Y. Yayon, V. W. Brar, L. Senapati, S. C. Erwin, and M. F. Crommie. "Observing Spin Polarization of Individual Magnetic Adatoms". *Physical Review Letters* **99** (6), 067202–4 (2007). [Cited on 27]

[76] A. Kubetzka, M. Bode, O. Pietzsch, and R. Wiesendanger. "Spin-Polarized Scanning Tunneling Microscopy with Antiferromagnetic Probe Tips". *Physical Review Letters* **88** (5), 057201 (2002). [Cited on 27, 34]

[77] S. Krause, L. Berbil-Bautista, G. Herzog, M. Bode, and R. Wiesendanger. "Current-Induced Magnetization Switching with a Spin-Polarized Scanning Tunneling Microscope". *Science* **317** (5844), 1537–1540 (2007). [Cited on 27]

[78] A. Kubetzka, O. Pietzsch, M. Bode, and R. Wiesendanger. "Determining the spin polarization of surfaces by spin-polarized scanning tunneling spectroscopy". *Applied Physics A: Materials Science & Processing* **76** (6), 873–877 (2003). [Cited on 28]

[79] M. Kleiber, M. Bode, R. Ravlić, and R. Wiesendanger. "Topology-Induced Spin Frustrations at the Cr(001) Surface Studied by Spin-Polarized Scanning Tunneling Spectroscopy". *Physical Review Letters* **85** (21), 4606 (2000). [Cited on 28]

[80] T. Yamada, A. V. de Parga, M. Bischoff, T. Mizoguchi, and H. van Kempen. "Evaluation of sample spin-polarization from spin-polarized scanning tunneling spectroscopy experiments". *Microscopy Research and Technique* **66** (2-3), 93–104 (2005). [Cited on 29, 30]

[81] S. L. Tomlinson and A. N. Farley. "Micromagnetic model for magnetic force microscopy tips". In "The 41st annual conference on magnetism and magnetic materials", vol. 81, pp. 5029–5031 (AIP, Atlanta, Georgia (USA), 1997). [Cited on 29]

[82] M. Bode, O. Pietzsch, A. Kubetzka, S. Heinze, and R. Wiesendanger. "Experimental Evidence for Intra-Atomic Noncollinear Magnetism at Thin Film Probe Tips". *Physical Review Letters* **86** (10), 2142 (2001). [Cited on 29]

[83] W. J. Kaiser and L. D. Bell. "Direct investigation of subsurface interface electronic structure by ballistic-electron-emission microscopy". *Physical Review Letters* **60** (14), 1406 (1988). [Cited on 30]

[84] L. D. Bell and W. J. Kaiser. "Observation of Interface Band Structure by Ballistic-Electron-Emission Microscopy". *Physical Review Letters* **61** (20), 2368 (1988). [Cited on 30, 31, 33]

[85] M. Prietsch. "Ballistic-electron emission microscopy (BEEM): studies of metal/semiconductor interfaces with nanometer resolution". *Physics Reports* **253** (4), 163–233 (1995). [Cited on 30, 32, 33, 34]

[86] V. Narayanamurti and M. Kozhevnikov. "BEEM imaging and spectroscopy of buried structures in semiconductors". *Physics Reports* **349** (6), 447–514 (2001). [Cited on 30, 33]

[87] J. Smoliner, D. Rakoczy, and M. Kast. "Hot electron spectroscopy and microscopy". *Reports on Progress in Physics* **67** (10), 1863–1914 (2004). [Cited on 30, 33]

[88] W. Yi, A. Stollenwerk, and V. Narayanamurti. "Ballistic electron microscopy and spectroscopy of metal and semiconductor nanostructures". *Surface Science Reports* **64** (5), 169–190 (2009). [Cited on 30]

[89] R. T. Tung. "Recent advances in Schottky barrier concepts". *Materials Science and Engineering: R: Reports* **35** (1-3), 1–138 (2001). [Cited on 30]

[90] C. R. Crowell and S. M. Sze. "Current transport in metal-semiconductor barriers". *Solid-State Electronics* **9** (11-12), 1035–1048 (1966). [Cited on 30]

[91] S. M. Sze and K. K. Ng. *Physics of semiconductor devices* (John Wiley and Sons, 2007), 3rd edn. ISBN 978-0-471-14323-9. [Cited on 30]

[92] W. H. Rippard and R. A. Buhrman. "Ballistic electron magnetic microscopy: Imaging magnetic domains with nanometer resolution". *Applied Physics Letters* **75** (7), 1001–1003 (1999). [Cited on 31, 32]

[93] W. H. Rippard and R. A. Buhrman. "Spin-Dependent Hot Electron Transport in Co/Cu Thin Films". *Physical Review Letters* **84** (5), 971–974 (2000). [Cited on 31, 32]

[94] T. Banerjee, J. C. Lodder, and R. Jansen. "Origin of the spin-asymmetry of hot-electron transmission in Fe". *Physical Review B (Condensed Matter and Materials Physics)* **76** (14), 140407–4 (2007). [Cited on 32]

[95] W. H. Rippard, A. C. Perrella, P. Chalsani, F. J. Albert, J. A. Katine, and R. A. Buhrman. "Observation of magnetization reversal of thin-film permalloy nanostructures using ballistic electron magnetic microscopy". *Applied Physics Letters* **77** (9), 1357–1359 (2000). [Cited on 32]

[96] E. Haq, H. Gokcan, T. Banerjee, F. M. Postma, M. H. Siekman, R. Jansen, and J. C. Lodder. "Nanoscale magnetic hysteresis of $Ni_{80}Fe_{20}$/Au/Co trilayers using ballistic electron magnetic microscopy". *Journal of Applied Physics* **95**, 6930–6932 (2004). [Cited on 32]

[97] T. Banerjee, E. Haq, M. H. Siekman, J. C. Lodder, and R. Jansen. "Spin Filtering of Hot Holes in a Metallic Ferromagnet". *Physical Review Letters* **94** (2), 027204 (2005). [Cited on 32]

[98] E. Haq, T. Banerjee, M. H. Siekman, J. C. Lodder, and R. Jansen. "Ballistic hole magnetic microscopy". *Applied Physics Letters* **86** (8), 082502–3 (2005). [Cited on 32, 33]

[99] T. Banerjee, E. Haq, M. Siekman, J. Lodder, and R. Jansen. "Ballistic hole emission microscopy on metal-semiconductor interfaces". *Magnetics, IEEE Transactions on* **41** (10), 2642–2644 (2005). [Cited on 32]

[100] E. Haq, T. Banerjee, M. H. Siekman, J. C. Lodder, and R. Jansen. "Excitation and spin-transport of hot holes in ballistic hole magnetic microscopy". *Applied Physics Letters* **88** (24), 242501–3 (2006). [Cited on 32]

[101] E. ul Haq. *Nanoscale spin-dependent transport of electrons and holes in Si-ferromagnet structures*. PhD thesis, University of Twente (2005). ISBN 90-365-2241-2. [Cited on 32]

[102] R. Ludeke and M. Prietsch. "Ballistic electron emission spectroscopy of noble metal–GaP(110) interfaces". *Journal of Vacuum Science & Technology A: Vacuum, Surfaces, and Films* **9** (3), 885–890 (1991). [Cited on 33]

[103] M. Prietsch and R. Ludeke. "Ballistic-electron-emission microscopy and spectroscopy of GaP(110)-metal interfaces". *Physical Review Letters* **66** (19), 2511 (1991). [Cited on 33]

[104] F. J. Garcia-Vidal, P. L. de Andres, and F. Flores. "Elastic Scattering and the Lateral Resolution of Ballistic Electron Emission Microscopy: Focusing Effects on the Au/Si Interface". *Physical Review Letters* **76** (5), 807 (1996). [Cited on 33, 34]

[105] M. K. Weilmeier, W. H. Rippard, and R. A. Buhrman. "Ballistic electron transport through Au(111)/Si(111) and Au(111)/Si(100) interfaces". *Physical Review B* **59** (4), R2521 (1999). [Cited on 33]

[106] L. D. Bell. "Evidence of Momentum Conservation at a Nonepitaxial Metal/Semiconductor Interface Using Ballistic Electron Emission Microscopy". *Physical Review Letters* **77** (18), 3893 (1996). [Cited on 33]

[107] R. Ludeke and A. Bauer. "Hot electron scattering processes in metal films and at metal-semiconductor interfaces". *Physical Review Letters* **71** (11), 1760 (1993). [Cited on 33]

[108] I. Appelbaum, R. Sheth, I. Shalish, K. J. Russell, and V. Narayanamurti. "Experimental test of the planar tunneling model for ballistic electron emission spectroscopy". *Physical Review B* **67** (15), 155307 (2003). [Cited on 33]

[109] A. Thiaville, F. Caud, C. Vouille, and J. Miltat. "BEEM spectra of various Au-Si samples and their analysis". *The European Physical Journal B - Condensed Matter and Complex Systems* **55** (1), 29–36 (2007). [Cited on 33]

[110] L. D. Bell, M. H. Hecht, W. J. Kaiser, and L. C. Davis. "Direct spectroscopy of electron and hole scattering". *Physical Review Letters* **64** (22), 2679 (1990). [Cited on 33]

[111] A. Kaidatzis, S. Rohart, A. Thiaville, and J. Miltat. "Hot electron transport and a quantitative study of ballistic electron magnetic imaging on Co/Cu multilayers". *Physical Review B (Condensed Matter and Materials Physics)* **78** (17), 174426–10 (2008). [Cited on 33]

[112] M. R. Freeman and B. C. Choi. "Advances in Magnetic Microscopy". *Science* **294** (5546), 1484–1488 (2001). [Cited on 33]

[113] H. Sirringhaus, E. Y. Lee, and H. von Känel. "Atomic-Scale Variations of the Tunneling Distribution in a Scanning Tunneling Microscope Observed by Ballistic-Electron-Emission Microscopy". *Physical Review Letters* **74** (20), 3999 (1995). [Cited on 34]

[114] W. Wulfhekel and J. Kirschner. "Spin-polarized scanning tunneling microscopy on ferromagnets". *Applied Physics Letters* **75** (13), 1944–1946 (1999). [Cited on 34]

[115] H. F. Ding, W. Wulfhekel, and J. Kirschner. "Ultra sharp domain walls in the closure domain pattern of Co(0001)". *EPL (Europhysics Letters)* **57** (1), 100 (2002). [Cited on 34]

[116] U. Schlickum, W. Wulfhekel, and J. Kirschner. "Spin-polarized scanning tunneling microscope for imaging the in-plane magnetization". *Applied Physics Letters* **83** (10), 2016–2018 (2003). [Cited on 34]

[117] J. Wittborn, K. V. Rao, J. Nogues, and I. K. Schuller. "Magnetic domain and domain-wall imaging of submicron Co dots by probing the magnetostrictive response using atomic force microscopy". *Applied Physics Letters* **76** (20), 2931–2933 (2000). [Cited on 35]

[118] A. J. Stollenwerk, M. R. Krause, J. J. Garramone, E. J. Spadafora, and V. P. LaBella. "Measuring spin dependent hot electron transport through a metal-semiconductor interface using spin-polarized ballistic electron emission microscopy". *Physical Review B (Condensed Matter and Materials Physics)* **76** (19), 195311–5 (2007). [Cited on 35]

[119] U. Kaiser, A. Schwarz, and R. Wiesendanger. "Magnetic exchange force microscopy with atomic resolution". *Nature* **446** (7135), 522–525 (2007). [Cited on 35]

[120] F. J. Giessibl. "Advances in atomic force microscopy". *Reviews of Modern Physics* **75** (3), 949 (2003). [Cited on 35]

[121] A. Schwarz, U. Kaiser, and R. Wiesendanger. "Towards an understanding of the atomic scale magnetic contrast formation in NC-AFM: a tip material dependent MExFM study on NiO(001)". *Nanotechnology* **20** (26), 264017 (2009). [Cited on 35]

[122] M. Bode, A. Kubetzka, S. Heinze, O. Pietzsch, R. Wiesendanger, M. Heide, X. Nie, G. Bihlmayer, and S. Blügel. "Spin-orbit induced local band structure variations revealed by scanning tunnelling spectroscopy". *Journal of Physics: Condensed Matter* **15** (5), S679 (2003). [Cited on 35]

[123] R. Jansen, M. C. M. M. van der Wielen, M. W. J. Prins, D. L. Abraham, and H. van Kempen. "Progress toward spin-sensitive scanning tunneling microscopy using optical orientation in GaAs". In "The 1993 international conference on scanning tunneling microscopy", vol. 12, pp. 2133–2135 (AVS, Beijing, China, 1994). [Cited on 36]

[124] M. W. J. Prins, R. Jansen, and H. van Kempen. "Spin-polarized tunneling with GaAs tips in scanning tunneling microscopy". *Physical Review B* **53** (12), 8105 (1996). [Cited on 36]

[125] R. Jansen, R. Schad, and H. van Kempen. "Optical effects in spin-polarized scanning tunneling microscopy with GaAs probes". *Journal of Magnetism and Magnetic Materials* **198-199**, 668–670 (1999). [Cited on 36]

[126] M. W. J. Prins, R. H. M. Groeneveld, D. L. Abraham, H. van Kempen, and H. W. van Kesteren. "Near-field magneto-optical imaging in scanning tunneling microscopy". *Applied Physics Letters* **66** (9), 1141–1143 (1995). [Cited on 36]

[127] S. F. Alvarado and P. Renaud. "Observation of spin-polarized-electron tunneling from a ferromagnet into GaAs". *Physical Review Letters* **68** (9), 1387 (1992). [Cited on 36]

[128] S. F. Alvarado and R. Jansen. "Private communication" (2008). [Cited on 36]

[129] P. Bruno. "Magnetic Scanning Tunneling Microscopy with a Two-Terminal Nonmagnetic Tip". *Physical Review Letters* **79** (23), 4593 (1997). [Cited on 36]

[130] T. P. Pareek and P. Bruno. "Magnetic scanning tunneling microscopy with a two-terminal nonmagnetic tip: Quantitative results". *Physical Review B* **63** (16), 165424 (2001). [Cited on 36]

[131] D. Kobayashi, Y. Mita, T. Shibata, T. Bourouina, and H. Fujita. "Batch bulk-micromachined high-precision metal-on-insulator microspires and their application to scanning tunneling microscopy". *Journal of Micromechanics and Microengineering* **14** (9), S76 (2004). [Cited on 36]

[132] V. Madhavan, W. Chen, T. Jamneala, M. F. Crommie, and N. S. Wingreen. "Tunneling into a Single Magnetic Atom: Spectroscopic Evidence of the Kondo Resonance". *Science* **280** (5363), 567–569 (1998). [Cited on 36]

CHAPTER 3

Concept of spin-filter STM (SF-STM)

We introduce a new technique to study magnetic nanostructures: spin-filter scanning tunneling microscopy. We describe the principle of the technique, which is based on spin-polarized tunneling and subsequent analysis of the spin polarization in a multi-terminal semiconductor/ferromagnet probe tip. We show that this approach has the capability of yielding a quantitative measurement of surface spin polarization with high spatial resolution. We also describe our modified STM instrumentation in order to perform this novel operation mode.

3.1 The SF-STM technique

In the previous chapter we presented an overview of STM-based techniques for magnetic microscopy. The most successful technique is without a doubt SP-STM, specifically the differential conductivity (SP-STS) operation mode [1]. SP-STM has allowed the study of nanoscale magnetism in great detail for a variety of sample surfaces including bulk samples, thin films and nanostructures. As we discussed in section 2.2 there is a need to develop a different technique capable of measuring directly and quantitatively the sample spin polarization

at the Fermi level and with high (ideally atomic) resolution. From the large range of microscopy techniques available (not only STM-based) with magnetic sensitivity there is still no technique that can fulfill this need in a practical and generally applicable fashion [2], in the sense of not requiring specific materials with features in the DOS or complex heterostructures. The quantification of sample spin polarization related to tunneling phenomena is fundamental for the advance of spintronic devices and applications [3].

Here we propose a novel technique, spin-filter scanning tunneling microscopy (SF-STM) [4]. As in SP-STM, this new technique relies on spin-polarized tunneling between tip and sample to extract magnetic information from surfaces. The difference is that in SF-STM the spin analysis occurs within the tip in a semiconductor/ferromagnet heterostructure, i.e. *after tunneling*. The novel tip design consists of a top metallic surface where tunneling takes place, followed by a semiconductor/ferromagnet heterostructure in which transmission is spin dependent. As shown in Figure 3.1 there are two separate contacts to the tip, one to the metallic surface, the other to the semiconductor. The first contact to the tip establishes the electrical circuit for the tunneling current I_T between sample and tip. The second contact to the tip allows the measurement of the current I_C collected in the semiconductor. Magnetic contrast is provided by the DC measurement of I_C which acts as an information channel independent of the tunneling current, as described below.

The spin sensitivity of SF-STM relies on spin filtering of non-equilibrium electrons in a ferromagnet. This phenomenon is also used, but in a different way, in another STM-based technique discussed in subsection 2.2.2, namely ballistic electron magnetic microscopy (BEMM) [5, 6] and also on solid-state devices like the spin-valve transistor (SVT) [7, 8, 9] and the magnetic-tunnel transistor (MTT) [10, 11]. As explained in chapter 2, with BEMM one cannot quantify the tunnel spin polarization from the sample, whereas solid state devices offer no means of obtaining spatially-resolved information. In the following we explain the operating principle of SF-STM and show that our technique can achieve both feats.

The operation of SF-STM is schematically depicted in Figure 3.2. Electrons from the surface of a magnetic sample tunnel into the SF-STM probe due to a negative bias V_T applied to the sample. These tunneling electrons originate from near the Fermi level of the sample and are spin-polarized if the sample surface is magnetic. Notice that the tip surface need not be polarized for I_T to have a spin polarization and since the spin analysis occurs within the tip

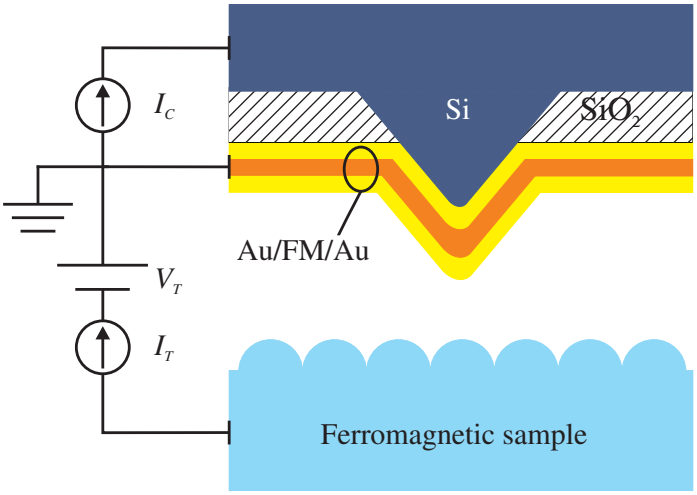

Figure 3.1. *Schematic of tip-sample configuration used for SF-STM. A bias V_T is applied between the magnetic sample and the metal layer stack on the tip, resulting in a spin-polarized tunneling current I_T. A small portion of the carriers is able to transmit the normal metals and the ferromagnetic layer of the tip, cross the semiconductor/metal interface, and enter the semiconductor, forming the collector current I_C. The magnitude of I_C is dependent on the spin polarization of the sample because the transmission from the ferromagnetic metal into the silicon is spin-dependent. The semiconductor/metal contact is defined only at the apex of the tip via SiO_2 isolation of the rest of the structure.*

there is absolutely no need for a spin polarized tip surface. The electrons enter states at an energy of eV_T above the Fermi level of the tip metal, and subsequently suffer elastic and inelastic scattering during transport through the metal stack. A ferromagnetic layer in this stack causes the scattering in the tip to be spin-dependent, with usually stronger attenuation of minority-spin electrons [12]. After scattering in the metal stack some electrons can reach the semiconductor/metal interface with the proper energy and momentum required to overcome the Schottky barrier at this interface and be collected into the semiconductor [13], forming the collector current I_C. Collection at the semiconductor/metal interface can be approximately described as in BEEM. No magnetic material is necessary at this interface, so we can use non-magnetic metals like Au to form a high-quality Schottky barrier.

I_C depends on the relative alignment of the magnetization of the sample and the ferromagnetic layer in the tip, in analogy with the prototypical polarizer-analyzer optical experiment [6]. More precisely, the magnetocurrent

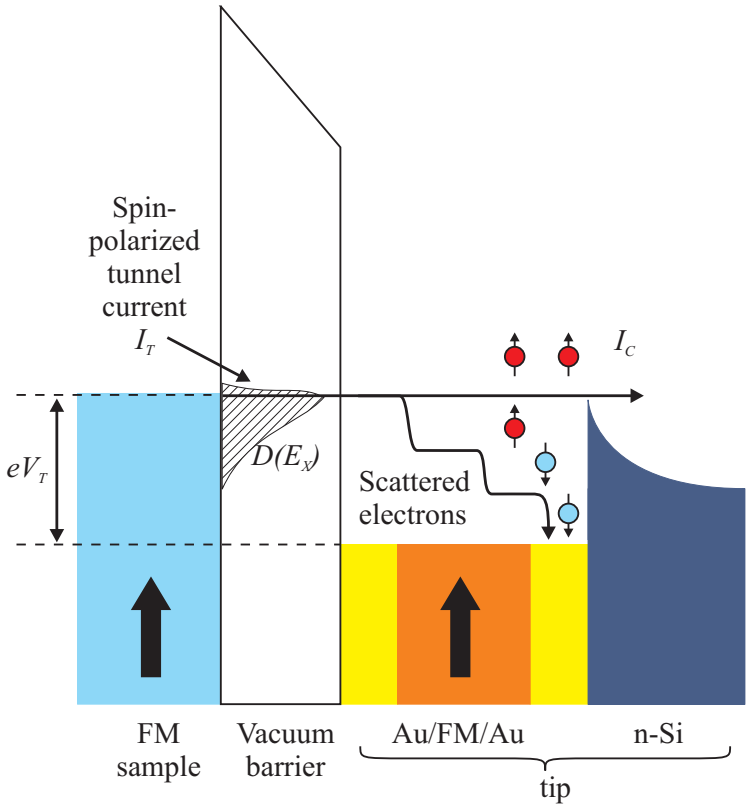

Figure 3.2. *Energy diagram of the tip-sample configuration for SF-STM. Spin-polarized electrons tunnel from the Fermi level of the magnetic sample (with energy distribution $D(E_x)$) to states above the Fermi level in the metallic layer of the tip. Due to spin-dependent scattering in the ferromagnetic thin film in the tip, one spin orientation will be more strongly attenuated. Therefore the collected signal I_C provides information on the sample spin polarization. Measuring the value of I_C for different relative alignment (parallel or antiparallel) of sample and tip magnetization allows quantitative determination of the spin polarization of I_T.*

MC $\equiv (I_C^P - I_C^{AP})/I_C^{AP}$ (Equation 2.12) or relative change in I_C between parallel and antiparallel states of sample and tip is proportional to (i) the tunnel spin polarization near the Fermi level of the sample, and (ii) the spin asymmetry of the electron transmission through the magnetic layer in the tip. As shown before for MTTs [14, 15] the latter can be made close to unity (as will be described in the next section), allowing quantitative determination of the sample spin polarization. However, since in SF-STM the I_T originates from an atomic scale region of the sample, high resolution quantitative magnetic imaging becomes

possible, while effectively decoupling topographic information (contained in the magnitude of I_T) from the spin information.

3.2 Spin-dependent transport in SF-STM

In this section we will describe how the tunnel spin polarization can be obtained from the collected current I_C. First, we discuss spin-dependent transport of non-equilibrium electrons through metallic structures having a ferromagnetic layer. Then we include the collection of these electrons in a semiconductor and show how this current carries information from the initial spin polarization from a ferromagnetic tunnel emitter. Finally, we consider the validity of this analysis including the energy resolution and experimental conditions.

The filtering of non-equilibrium electrons in semiconductor/metal heterostructures at energies above the Fermi level of the metal base is a powerful mechanism to study the dynamics of electrons in metals. A ferromagnet acts as an electron emitter with a distribution peaked close to its Fermi level. By varying the voltage applied between the emitter and the metal base we can study the scattering properties for a broad range of energies of the base. This approach to study the hot-electron transport within the base used in SVT, MTT and BEMM, bridges the energy range other techniques are not able to probe. For example, time- and spin-resolved two-photon photoemission is limited in practice to energies up to 1.1 eV above the Fermi level [16], whereas photoemission and electron transmission techniques can only probe energies higher than the metal work function [17]. For an account of electron dynamics in metals and related techniques we refer the reader to the review by Zhukov and Chulkov [18].

Hot-electron transport within a ferromagnet can be described by semi-empirical approximations of the Boltzmann equation [19]. In its simplest 1D form the ballistic transmission through a metal layer reduces to an exponential decay of the form $T = \exp(-t/\lambda_{eff})$ [7], with t equal to the thickness of the metal layer and λ_{eff} the effective attenuation length given by considering all scattering processes (elastic and inelastic) using Matthiessen's rule [20]. This means that the transmission will depend on the properties of the metal layers introduced in the base, including its interfaces. Let's consider the structure Au/FM/Au depicted in Figure 3.2. After tunneling the electrons must traverse the first Au layer, then the Au/FM interface, the FM layer, the second interface

and the second Au layer, until they reach the semiconductor/metal interface. These contributions are included in the transmission probability within the metal base (T_B) and are spin dependent due to the presence of the FM layer. We can express T_B for each spin-channel as

$$\begin{aligned} T_B^{\uparrow} &= \exp\left(-\frac{t_{Au}}{\lambda_{Au}}\right)\Gamma_{Au/FM}^{\uparrow}\exp\left(-\frac{t_{FM}}{\lambda_{FM}^{\uparrow}}\right)\Gamma_{FM/Au}^{\uparrow} \\ T_B^{\downarrow} &= \exp\left(-\frac{t_{Au}}{\lambda_{Au}}\right)\Gamma_{Au/FM}^{\downarrow}\exp\left(-\frac{t_{FM}}{\lambda_{FM}^{\downarrow}}\right)\Gamma_{FM/Au}^{\downarrow} \end{aligned} \tag{3.1}$$

where t_{Au} is the sum of the thicknesses of both Au layers, t_{FM} the thickness of the ferromagnet in the base, and the factors Γ represent interface transmission [14]. The main contribution to spin-asymmetry in T_B is given by volume attenuation within the ferromagnetic film due to a spin-dependent λ_{FM}. The asymmetry is normally attributed to electron-electron interactions taking into account the band structure of $3d$ transition metals [12, 16, 17]. It is argued that from all possible spin-dependent mechanisms the main responsible for the asymmetry in λ_{FM} is spontaneous spin-wave emission within the volume of the ferromagnetic layer [21, 22]. On the other hand, contribution to spin asymmetry at energies above E_F due to interfaces is less important than at E_F and only a small asymmetry in Γ of up to 20 % has been observed [12, 22, 23, 24]. Good fits to data can be obtained using $\Gamma^{\uparrow} = \Gamma^{\downarrow}$.

Now we discuss the collection of spin-filtered electrons in a semiconductor and show how these carry information from the initial spin polarization from a ferromagnetic tunnel emitter. We follow the framework used in solid-state MTT devices as presented in the review by Jansen [14]. We use the two-current model presented in the previous chapter together with the principles of hot-electron spin filtering in order to obtain an expression that directly relates the tunnel spin polarization (P_E) from the sample to the observed magnetocurrent (MC). We note that the principle of measurement of polarization is similar to that of MTTs with a ferromagnetic emitter and is well established by now [15, 23, 25, 26]. It is important to emphasize that while the electrons within the probe transport as hot carriers within the base, they originate from near the Fermi level (E_F) of the sample. So the information is related to $P_E(E_F)$. We discuss this point in detail later.

We begin by considering spin-polarized tunneling between emitter (sample) and base (tip). Each metallic surface has an associated (energy-dependent)

tunnel spin polarization according to $P \equiv (n_\uparrow - n_\downarrow)/(n_\uparrow + n_\downarrow)$ (Equation 2.4). The terms $n_{\uparrow,\downarrow}$ are the effective tunneling DOS for each spin channel, which the tunnel current I_T is proportional to. Next we address the collector current I_C. We have already given a description of the transfer ratio $\alpha = I_C/I_T$ using the Bell-Kaiser model in Equation 2.14 where the parameter $R = T_B T_{int}$ represents attenuation due to scattering within the metal base (T_B) and at the metal-semiconductor interface (T_{int}). In the Bell-Kaiser model T_{int} is energy-independent and since we are using Si/Au interfaces we can also consider it independent of spin. Therefore the only spin dependence is given by the ferromagnetic layer in the metal base affecting T_B. This framework works well for Si collectors which do not show band structure effects in MTTs [27, 28].

To obtain I_C we must now multiply each spin channel in I_T by the corresponding ballistic transmission factor of the semiconductor/metal heterostructure. In the derivation of I_C we leave out both T_{int} and the energy and momentum requirements at the Schottky barrier as they determine the shape of the collection spectrum but do not describe the spin dependence, and focus solely on T_B. Within the two-current model the collector signal for parallel and for antiparallel alignment of the magnetic sample and base is given by

$$I_C^P \propto n_\uparrow^E n_\uparrow^B T_B^\uparrow + n_\downarrow^E n_\downarrow^B T_B^\downarrow \quad \text{and} \quad I_C^{AP} \propto n_\uparrow^E n_\downarrow^B T_B^\downarrow + n_\downarrow^E n_\uparrow^B T_B^\uparrow \tag{3.2}$$

where we have also included the spin-dependent tunneling contribution n^B associated to the tip surface. As we mentioned in the previous section, there is no need for a spin-polarized tip in SF-STM. We can cover the FM filter in the probe with a non-magnetic layer like Au, so $n_\uparrow^B = n_\downarrow^B$. This is beneficial since the noble metal cap offers increased protection against oxidation and contamination, and ultimately may allow for fabrication of the SF-STM probe outside of the STM chamber followed by ex-situ transfer to the STM.

With the previous expressions for I_C we obtain the magnetocurrent as

$$\mathrm{MC} = \frac{2P_E P_B^*}{1 - P_E P_B^*} \quad \text{with} \quad P_B^* = \frac{n_\uparrow^B T_B^\uparrow - n_\downarrow^B T_B^\downarrow}{n_\uparrow^B T_B^\uparrow + n_\downarrow^B T_B^\downarrow} \tag{3.3}$$

where P_B^* is a renormalized polarization of the base [14] consisting of a combination of tunneling factors (n^B) and hot-electron transmission factors (Γ, λ) and therefore must not be confused with the regular tunnel spin polarization of the base P_B. Two important observations are deduced from the last expression. First, the measurable parameter MC is directly related to the quantity of interest

P_E and to an unrelated parameter P_B^* that represents spin-dependent transmission properties of the ferromagnetic base. Second, as the main contribution to P_B^* comes from the spin-asymmetry of $\exp(-t_{FM}/\lambda_{FM})$, for a sufficiently thick ferromagnet the value of P_B^* always saturates to 1 for $\lambda_{FM}^{\uparrow} > \lambda_{FM}^{\downarrow}$. By using thick enough spin filters the details of spin-dependent scattering in the probe become irrelevant and we have $\mathrm{MC} = 2P_E/(1-P_E)$. This immediately yields a *quantitative* value for P_E by measuring the MC.

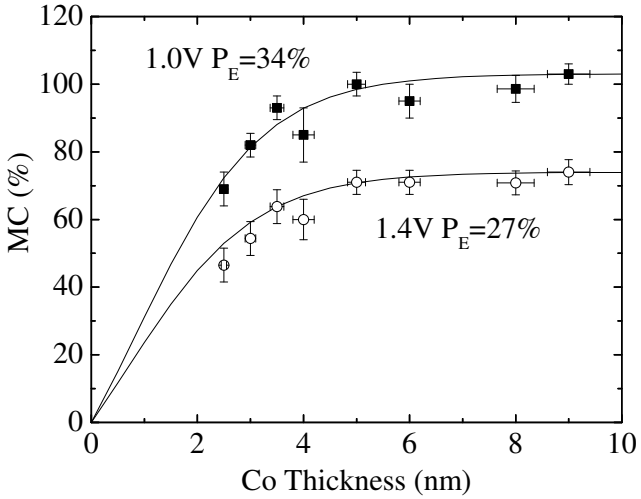

Figure 3.3. *Magnetocurrent as a function of ferromagnetic base thickness at an emitter bias of 1.0 and 1.4 eV in a MTT with the structure $Ni_{80}Fe_{20}/Al_2O_3$/Co/Au/n-type Si. Solid lines are fits for determination of the spin-asymmetry in the Co base attenuation length using Equation 3.3. The resulting emitter polarization P_E is displayed for each bias. Adapted from [15].*

The validity of this approach towards determination of P_E is demonstrated by the MTT results of Park et al. [15] as shown in Figure 3.3. The magnetocurrent depends on the thickness of the Co spin filter in the metal base. For too thin Co almost no filtering occurs within the volume of the ferromagnet ($t_{Co} \ll \lambda_{\uparrow(\downarrow)}$), so the transmission T_B shows little spin dependence. For increasing Co thickness the MC increases accordingly, until it saturates at $t_{Co} \approx 5\,\mathrm{nm}$. This corresponds to the case where all minority spins are filtered out ($t_{Co} \gg \lambda_{\downarrow}$) and only majority spins are collected, so $T_B^{\uparrow} \gg T_B^{\downarrow}$ or $P_B^* \approx 1$. For this MTT the data is properly fitted with constant attenuation lengths for Co $\lambda_{\uparrow} = 7\,\mathrm{nm}$ and $\lambda_{\downarrow} = 1\,\mathrm{nm}$. The corresponding polarization of 34 % is comparable with

the spin polarization values obtained from TMR measurements of MTJs at low bias, validating this approach.

A point of discussion is the energy dependence of the observed spin polarization as shown in Figure 3.3. When the tunnel bias is increased from 1.0 eV to 1.4 eV the polarization decreases from 34 % down to 27 %. If we consider *all* tunneling electrons from the emitter to originate strictly from E_F then, according to Equation 3.3, at large Co thickness we do not expect any variation in polarization with bias. There would be a bias dependent polarization only for lower thickness when energy-dependent attenuation lengths $\lambda_{\uparrow(\downarrow)}$ are considered. In reality the tunneling electrons originate *mostly* from E_F with a decaying contribution at lower energies given by the energy dependence of the tunneling matrix elements. In the WKB approximation the energy distribution $D(E_x)$ (see Figure 3.2) of the tunneling current has an exponential dependence given by Equation 2.1. This contribution is peaked at E_F and is characterized by the energy width $\Delta E_{1/2}$ where the tunneling probability decays to half (or alternatively $\Delta E_{1/e} \approx 1.4\Delta E_{1/2}$). Within the formalism of planar tunneling the distribution for typical STM operation conditions amounts to $\Delta E_{1/2} \approx 0.35$ eV [13, 29]. But more detailed calculations using single atom tips have shown narrower distributions. For example, for a tunnel distance $s = 15$ Å the distribution has $\Delta E_{1/2} = 0.12$ eV, whereas for $s = 4.5$ Å and 1 V tunnel bias it has $\Delta E_{1/2} = 0.28$ eV [30, 31]. The latter conditions are closer to those used in our experiments, so we consider $\Delta E_{1/2} = 0.3$ eV. As shown in Figure 3.3 the application of a large bias of 1 V to the emitter does not invalidate the measurement of polarization near the Fermi level.

Now we can understand the bias dependence of P_E by considering a emitter with a FM/I interface having a decreasing spin polarization for electrons tunneling from states below E_F. When $eV_T = \Phi_B + \varepsilon$ and $\varepsilon < \Delta E_{1/2}$ the Schottky barrier imposes a sharp cutoff, so only electrons within a range ε below E_F contribute to I_C. The practical rule is that when we operate at a tunnel bias just above the Schottky barrier height ($\varepsilon \approx 0$) then our measured P_E would be that corresponding at E_F. So $P_E(E_F)$ is the value obtained at collection threshold. At higher tunnel bias more electrons below E_F can be collected, ultimately limited by the tunnel distribution $D(E_x)$. Therefore the polarization P_E extracted from the measured MC at each bias using Equation 3.3 is regarded as an *effective* spin polarization, mostly representative of $P_E(E_F)$ and less so for energies down to 0.3 eV below E_F. The actual spin polarization of the emitter for specific energies within this 0.3 eV interval can be extracted by

deconvolution with the tunnel distribution $D(E_x)$, as shown for the MTT case [15]. For thickness below that required for saturation of the MC then an accurate value for P_E can still be obtained if there is knowledge of the corresponding spin-dependent attenuation lengths in the ferromagnet filter.

In the present framework a basic assumption is the application of the two-current model without the explicit consideration of spin-mixing scattering processes within the metal stack in the probe. A possible contributor to this effect are the normal-metal/ferromagnet interfaces. The interfaces may have a very small contribution to spin-mixing but this is usually negligible and only observable when dealing with very high MC (> 1000 %) in MTTs with a thick spin-valve base [32]. Another source may be scattering processes within the volume of the metal layers. Hot electron scattering by thermal spin-wave absorption and emission may also induce a small spin-mixing near room temperature, but it is negligible at low temperatures (< 150 K) [21, 27] and it is negligible even at room temperature for ferromagnets like Co with a large Curie temperature [22, 25]. Since most of our measurements were done at 100 K we do not include in the analysis of spin polarization spin-flip scattering, as this is usually not done for modeling [28]. The specific implementation of the spin-analysis principle presented in this section in the SF-STM probe geometry is discussed in chapter 4.

3.3 Instrumentation for SF-STM

There are several requirements for the implementation of SF-STM. The most crucial component in order to realize SF-STM is the multi-terminal semiconductor/ferromagnet probe tip. We will address the design and fabrication of SF-STM probes separately in the following chapter. Other requirements are related to other components of the STM system and external instrumentation. We proceed to describe these in the following.

We use a variable temperature, ultra-high vacuum system: UHV 300 STM from RHK Technology. This system is an updated version of a similar system previously used in our group for BEMM experiments [33]. We briefly mention the main characteristics while focusing on the modifications performed. The whole system rests on a steel frame placed over a commercial vibration control system. Originally the STM system consists of two parts: load lock and STM chamber. The load lock is equipped with a turbomolecular pump in

order to load samples or tips into the STM chamber without interrupting vacuum. During (un)loading there is a temporary rise in pressure up to the low 10^{-8} mbar range in the STM chamber. The STM chamber is equipped with ion and sublimation pumps which are able to keep the system pressure in the 10^{-10} mbar range. The STM setup is of the Besocke type (or beetle) with the scanning head (including the tip holder) standing directly on top of the sample holder. This design allows for effective temperature compensation and immunity to vibration [29].

Collected spin-filtered signals from SF-STM probes impose similar requirements on the probe side as those imposed by BEEM on the sample side [13]. The first one is to have two independent electrical contacts, one to bias the metal coating of the probe (usually grounded) and the other one to the Si to extract the collected current I_C. The second requirement is the need for very low noise electrical connections for I_C.

To satisfy the first requirement we must specify how to mount and contact our multi-terminal probes. In our system that would have meant the inclusion of a second, independent electrical path to the scan head running down to the tip holder. This was certainly possible, but it included some substantial modifications to the scan head and tip insert at the end of the scanning piezoelectric tube [34]. The scan head is the most delicate and fundamental part of our system so we decided to take a simpler and more flexible approach. The STM system already incorporated independent contacts to the sample holder, similar to those used for contacting BEEM samples. Therefore in this work we make use of such contacts by placing our multi-terminal probes in the sample holder of the STM. Since the sample only requires one electrical contact we mount the sample in the tip holder and use the single contact offered by the tip holder. So our operation of SF-STM involves interchanging of the sample and probe locations in the STM setup, as schematically shown in Figure 3.4. The SF-STM probes are fabricated on Si wafers cut into squares of 6.5 mm that fit into our modified STM sample holders. The two independent contacts to the SF-STM probe are made in a non-permanent way so the Si squares containing the probes can be easily mounted and removed from the holder without undergoing any damage. The (magnetic) samples are mounted on homemade STM tip holders that are able to accommodate surfaces up to 1 mm wide. Of course, regular STM tip holders with inserted PtIr wire acting as sharp tips can still be used.

For the realization of the second requirement we optimized the electrical

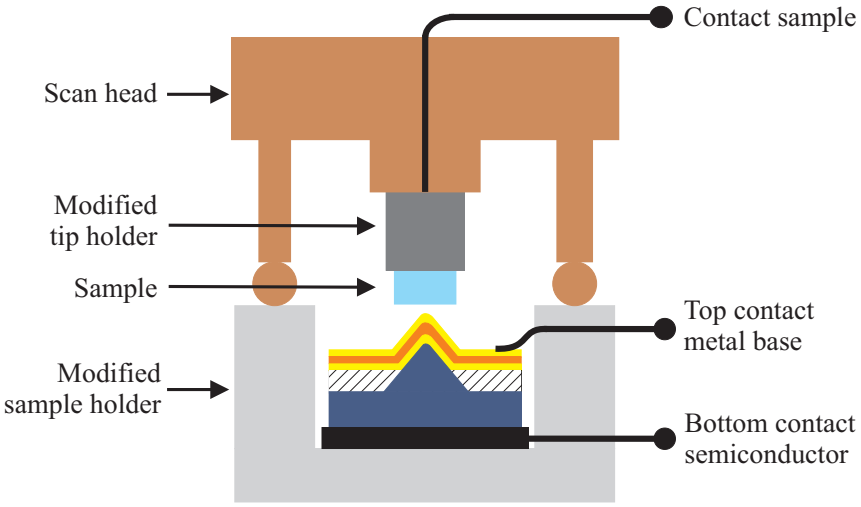

Figure 3.4. *Schematic of SF-STM operation in our STM system with the regular location of probe and sample exchanged. The sample holder is modified to allow for mounting of our microfabricated chips containing the SF-STM probes. Specially designed tip holders allow mounting of flat conducting samples about 1 mm wide.*

wiring to the semiconductor contact of the SF-STM probe in order to reduce noise and interference signals as much as possible. This is necessary due to the typically low magnitude of the collected current. For semiconductor/metal structures including a thin ferromagnetic layer it is common to observe transfer ratios of $\alpha = I_C/I_T \lesssim 1 \times 10^{-3}$ [33] which results in practical I_C signals in the pA range. After reducing the noise level by decreasing the distance of wiring to the preamplifier and using proper shielding, we identified the main source of noise to be interference due to inductive pickup. Using twisted wire proved to limit the dominant 50 Hz interference down to 0.02 pA peak-to-peak (pk-pk) when the power supply for application of magnetic field is switched off and 0.05 pA pk-pk when it is switched on. Proper averaging decreases this periodic interference. Therefore we can measure collection signals with a precision well below 0.1 pA. We use a dedicated high-gain preamplifier (Stanford Research SR570) for measuring I_C. The high gain used of $\approx 10^{11}$V/A thus means that small bandwidths of 10 Hz limit the speed of data acquisition.

We are also interested in applying magnetic fields in order to control the magnetic state of the sample and the probe. For application of magnetic field in the STM we use homemade Helmholtz coils placed outside the UHV system. The two Helmholtz coils are wrapped around the STM chamber in order to

provide a homogeneous magnetic field oriented parallel to the surface plane of the sample at the location of the STM assembly. We use commercially available bipolar power supplies to feed DC current into the Helmholtz coils at both polarities and with smooth transition through zero field (necessary for measurement of field sweeps). We calibrated the Helmholtz coils by measuring the magnetic field with a Hall probe located at the sample position (accessible with the UHV chamber open) obtaining a linear relationship of 23.8 Oe/A. The power supply is controlled by the same software controlling the rest of the STM instrumentation. We can draw a maximum current of 6 A from the power supplies so we are limited to maximum fields of 140 Oe. Therefore in the present setup we can study the magnetic switching of only soft magnetic materials. The choice for using external Helmholtz coils is given by the design constraints of our setup. Recent commercial designs offer the possibility of higher fields up to 1 T [35].

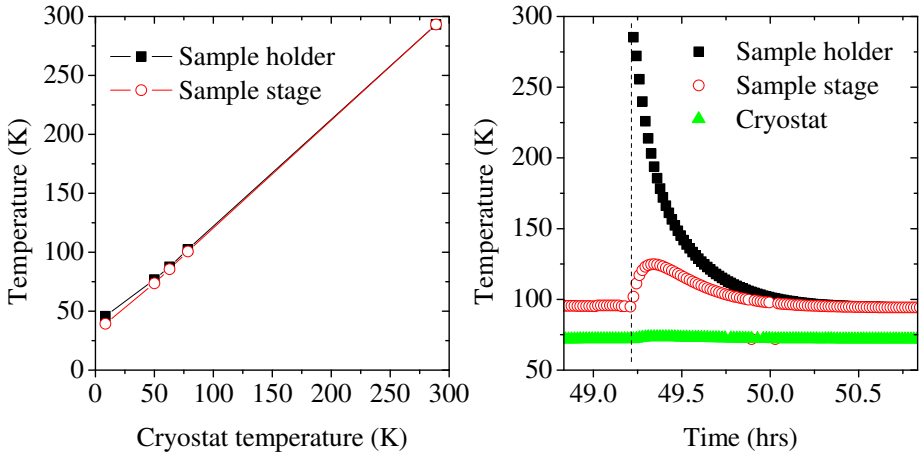

Figure 3.5. *Temperature monitoring using three independent sensors at the locations of the cryostat, the STM stage and at the sample holder (same location where SF-STM probes are mounted). Left: calibration of low-temperature operation using liquid He. Right: transient response after insertion of a sample holder at room temperature into a previously cooled down STM stage using liquid* N_2.

A consequence of measuring small signals from Schottky diodes is the possible need for low-temperature operation. This need is determined by the electrical properties of the diode: Schottky barrier height, area of the semiconductor/metal interface, and (edge) defects causing leakage currents [13]. Our system has the capability of performing variable temperature experiments

through the use of a flow cryostat thermally connected to the STM sample stage and a heater element wrapped around the cryostat. We point out that the tip holder (which holds the magnetic sample) is not directly cooled, but the SF-STM probe is. Therefore when we operate at low temperature we actually cool down only our probes. We can use either N_2 or He as cryogenic fluids. We have calibrated our system by installing low-temperature (diode) sensors at the location of the cryostat and in the STM sample stage. Since the sample holder rests over the sample stage during STM operation, it is clear that measuring the temperature of the stage should give a good indication of the sample holder temperature. To confirm this we have made use of the capability for independent electrical contacts in our modified sample holder to load a temperature sensor mounted at the exact same location where the SF-STM probes are also mounted. This procedure permits an accurate determination of the probe temperature and thermal transients, as shown in Figure 3.5. By controlling the flow of liquid N_2 we have demonstrated operation at 100 K for 10 consecutive days. We emphasize that depending on the probe characteristics it may not be required to operate at low temperature so our technique can in principle be used at room temperature.

Table 3.1. *Deposition of thin Co films in our STM system characterized by AFM and x-ray diffraction. The film thickness shows a linear relationship with the ion flux from the evaporator. Smooth films with low root mean square (rms) roughness are grown on SiO_2 substrates to be used as flat samples. Alternatively they can be grown over microfabricated SF-STM probes.*

Location	Flux (nA)	Time (min)	Thickness (nm)	Rate (Å/s)	rms (nm)
Flat sample	50	31.0	28.0	0.15	0.36
	150	9.0	23.2	0.43	0.32
	300	5.0	27.5	0.92	0.86
SF-STM probe	150	6.0	32.1	0.89	0.27

A final major modification to our system consists on the design and addition of a deposition chamber. Since we are interested on the study of metallic magnetic surfaces it is mandatory to work with clean and unoxidized samples. Contamination by adsorbate species or oxidation can impede the detection of spin-polarization from the sample [1]. Our deposition chamber is connected via an UHV gate valve to the main STM chamber. It includes a dedicated turbomolecular pump, a transfer arm and a wire type electron-gun evaporator. Having a dedicated pump and gate valve allows the renewal of evaporation

material without interrupting the vacuum of the STM chamber. The evaporator contains an ion-flux monitor that we use to estimate the deposition rate of magnetic material after proper calibration. This is shown in Table 3.1 for Co which we use as our test magnetic material. Both sample and tip holders can be transferred to the deposition chamber. This permits the in-situ deposition of thin magnetic films to act as flat samples and also the possibility to deposit in-situ thin magnetic layers on SF-STM probes.

3.4 Conclusions

We have presented the concept of a new STM-based technique to study the spin polarization of magnetic surfaces near the Fermi level. The technique, spin-filter scanning tunneling microscopy (SF-STM), is based on spin-polarized tunneling from a magnetic sample and subsequent spin analysis after tunneling within a multi-terminal semiconductor/ferromagnet tip. The principle of spin analysis in the probe relies on the spin-dependent transmission of hot electrons through thin ferromagnetic layers and on the energy-filtering capabilities of semiconductor/metal Schottky barriers. An independent electrical contact to the SF-STM probe, through which the current collected in the semiconductor is measured, offers an information channel decoupled from the tunneling signal which is kept at a constant value. The surface of the SF-STM probe does not need to be spin-polarized making the tunnel process itself not dependent on the magnetic state of the sample. In this way the novel technique provides a proper separation of magnetic information from topographic or non-spin-polarized electronic contributions.

Spin-dependent transport within our multi-terminal probes is rationalized using a similar framework as that used to describe transport in solid-state devices like the magnetic tunnel transistor. Using this description for spin-filtering within the probes together with spin-polarized tunneling we have presented expressions that relate the tunnel spin polarization from a magnetic sample to the relative change in collected signal (magnetocurrent) when the magnetizations of sample and probe are in parallel and antiparallel configurations. The significance of such expressions relies in the opportunity to extract quantitative values of tunnel spin polarization from the magnetocurrent and the spin-dependent transmission properties of the probe, all of which can be experimentally determined. Remarkably, for a thick enough spin-filter

layer the details of its spin-dependent transmission become irrelevant and we can get a direct quantitative measure of spin polarization from the observed magnetocurrent alone: $\mathrm{MC} = 2P_E/(1-P_E)$.

The ability of quantifying tunnel spin polarization near the Fermi level without any strong dependence on the electronic structure of the sample is an advantage of the technique here described over the well-established SP-STM. On the other hand, the foreseen spatial resolution of SF-STM is the same as that of (SP-)STM techniques, namely atomic. This is because the source of spin polarized electrons is the atomic scale contact to the sample, contrary to the other STM-based technique that uses spin-filtering of hot electrons (BEMM) where angular spread of the electron beam compromises spatial resolution. We have also presented a first approach towards the realization of SF-STM by modifying a standard STM UHV system. SF-STM shows the promise of a new and complementary technique to study transport in spintronic materials and devices.

References

[1] M. Bode. "Spin-polarized scanning tunnelling microscopy". *Reports on Progress in Physics* **66** (4), 523 (2003). [Cited on 49, 62]

[2] R. Allenspach. "Magnetic imaging (Tutorial)". In "Joint European Magnetic Symposia", (Dublin, 2008). [Cited on 50]

[3] I. Žutić, J. Fabian, and S. D. Sarma. "Spintronics: Fundamentals and applications". *Reviews of Modern Physics* **76** (2), 323 (2004). [Cited on 50]

[4] I. J. Vera-Marún and R. Jansen. "Multiterminal semiconductor/ferromagnet probes for spin-filter scanning tunneling microscopy". *Journal of Applied Physics* **105**, 07D520–3 (2009). [Cited on 50]

[5] W. J. Kaiser and L. D. Bell. "Direct investigation of subsurface interface electronic structure by ballistic-electron-emission microscopy". *Physical Review Letters* **60** (14), 1406 (1988). [Cited on 50]

[6] W. H. Rippard and R. A. Buhrman. "Ballistic electron magnetic microscopy: Imaging magnetic domains with nanometer resolution". *Applied Physics Letters* **75** (7), 1001–1003 (1999). [Cited on 50, 51]

[7] D. J. Monsma, J. C. Lodder, T. J. A. Popma, and B. Dieny. "Perpendicular Hot Electron Spin-Valve Effect in a New Magnetic Field Sensor: The Spin-Valve Transistor". *Physical Review Letters* **74** (26), 5260 (1995). [Cited on 50, 53]

[8] D. J. Monsma, R. Vlutters, and J. C. Lodder. "Room Temperature-Operating Spin-Valve Transistors Formed by Vacuum Bonding". *Science* **281** (5375), 407–409 (1998). [Cited on 50]

[9] D. J. Monsma. *The spin-valve transistor*. PhD thesis, University of Twente (1998). ISBN 90-365-1049-X. [Cited on 50]

[10] K. Mizushima, T. Kinno, T. Yamauchi, and K. Tanaka. "Energy-dependent hot electron transport across a spin-valve". *Magnetics, IEEE Transactions on* **33** (5), 3500–3504 (1997). [Cited on 50]

[11] K. Mizushima, T. Kinno, K. Tanaka, and T. Yamauchi. "Strong increase of the effective polarization of the tunnel current in Fe/AlOx/Al junctions with decreasing Fe layer thickness". *Physical Review B* **58** (8), 4660 (1998). [Cited on 50]

[12] W. H. Rippard and R. A. Buhrman. "Spin-Dependent Hot Electron Transport in Co/Cu Thin Films". *Physical Review Letters* **84** (5), 971–974 (2000). [Cited on 51, 54]

[13] M. Prietsch. "Ballistic-electron emission microscopy (BEEM): studies of metal/semiconductor interfaces with nanometer resolution". *Physics Reports* **253** (4), 163–233 (1995). [Cited on 51, 57, 59, 61]

[14] R. Jansen. "The spin-valve transistor: a review and outlook". *Journal of Physics D: Applied Physics* **36** (19), R289 (2003). [Cited on 52, 54, 55]

[15] B. G. Park, T. Banerjee, J. C. Lodder, and R. Jansen. "Tunnel Spin Polarization Versus Energy for Clean and Doped Al_2O_3 Barriers". *Physical Review Letters* **99** (21), 217206–4 (2007). [Cited on 52, 54, 56, 58]

[16] M. Aeschlimann, M. Bauer, S. Pawlik, W. Weber, R. Burgermeister, D. Oberli, and H. C. Siegmann. "Ultrafast Spin-Dependent Electron Dynamics in fcc Co". *Physical Review Letters* **79** (25), 5158 (1997). [Cited on 53, 54]

[17] D. Oberli, R. Burgermeister, S. Riesen, W. Weber, and H. C. Siegmann. "Total Scattering Cross Section and Spin Motion of Low Energy Electrons Passing through a Ferromagnet". *Physical Review Letters* **81** (19), 4228 (1998). [Cited on 53, 54]

[18] V. P. Zhukov and E. V. Chulkov. "The femtosecond dynamics of electrons in metals". *Physics-Uspekhi* **52** (2), 105–136 (2009). [Cited on 53]

[19] R. Vlutters, O. M. J. van 't Erve, R. Jansen, S. D. Kim, J. C. Lodder, A. Vedyayev, and B. Dieny. "Modeling of spin-dependent hot-electron transport in the spin-valve transistor". *Physical Review B* **65** (2), 024416 (2001). [Cited on 53]

[20] N. W. Ashcroft and N. D. Mermin. *Solid State Physics* (Holt, Rinehart and Winston, New York, 1976), 1 edn. ISBN 0030839939. [Cited on 53]

[21] R. Jansen, P. S. A. Kumar, O. M. J. van't Erve, R. Vlutters, P. de Haan, and J. C. Lodder. "Thermal Spin-Wave Scattering in Hot-Electron Magnetotransport Across a Spin Valve". *Physical Review Letters* **85** (15), 3277 (2000). [Cited on 54, 58]

[22] R. Vlutters, O. M. J. van 't Erve, S. D. Kim, R. Jansen, and J. C. Lodder. "Interface, Volume, and Thermal Attenuation of Hot-Electron Spins in Ni80Fe20 and Co". *Physical Review Letters* **88** (2), 027202 (2001). [Cited on 54, 58]

[23] S. van Dijken, X. Jiang, and S. S. P. Parkin. "Spin-dependent hot electron transport in Ni81Fe19 and Co84Fe16 films on GaAs(001)". *Physical Review B* **66** (9), 094417 (2002). [Cited on 54]

[24] S. van Dijken, X. Jiang, and S. S. P. Parkin. "Comparison of magnetocurrent and transfer ratio in magnetic tunnel transistors with spin-valve bases containing Cu and Au spacer layers". *Applied Physics Letters* **82** (5), 775–777 (2003). [Cited on 54]

[25] B. G. Park, T. Banerjee, B. C. Min, J. G. M. Sanderink, J. C. Lodder, and R. Jansen. "Temperature dependence of magnetocurrent in a magnetic tunnel transistor". *Journal of Applied Physics* **98** (10), 103701–4 (2005). [Cited on 54, 58]

[26] B. G. Park, T. Banerjee, B. C. Min, J. C. Lodder, and R. Jansen. "Tunnel spin polarization of $Ni_{80}Fe_{20}/SiO_2$ probed with a magnetic tunnel transistor". *Physical Review B (Condensed Matter and Materials Physics)* **73** (17), 172402–4 (2006). [Cited on 54]

[27] S. van Dijken, X. Jiang, and S. S. P. Parkin. "Nonmonotonic Bias Voltage Dependence of the Magnetocurrent in GaAs-Based Magnetic Tunnel Transistors". *Physical Review Letters* **90** (19), 197203 (2003). [Cited on 55, 58]

[28] X. Jiang, S. van Dijken, R. Wang, and S. S. P. Parkin. "Bias voltage dependence of magnetocurrent in magnetic tunnel transistors". *Physical Review B* **69** (1), 014413 (2004). [Cited on 55, 58]

[29] C. J. Chen. *Introduction to Scanning Tunneling Microscopy*. No. 64 in Monographs on the Physics and Chemistry of Materials (Oxford University Press, Oxford, 2007), 2nd edn. ISBN 978-0-19-921150-0. [Cited on 57, 59]

[30] N. D. Lang, A. Yacoby, and Y. Imry. "Theory of a single-atom point source for electrons". *Physical Review Letters* **63** (14), 1499 (1989). [Cited on 57]

[31] R. Ludeke and A. Bauer. "Hot electron scattering processes in metal films and at metal-semiconductor interfaces". *Physical Review Letters* **71** (11), 1760 (1993). [Cited on 57]

[32] S. van Dijken, X. Jiang, and S. S. P. Parkin. "Giant magnetocurrent exceeding 3400% in magnetic tunnel transistors with spin-valve base layers". *Applied Physics Letters* **83** (5), 951–953 (2003). [Cited on 58]

[33] E. ul Haq. *Nanoscale spin-dependent transport of electrons and holes in Si-ferromagnet structures*. PhD thesis, University of Twente (2005). ISBN 90-365-2241-2. [Cited on 58, 60]

[34] Z. Wang. "Private communication with CTO of RHK Technology" (2008). [Cited on 59]

[35] "RHK Expands Nanotech Research Capability through Variable Magnetics, by RHK Technology - physicsworld.com". http://physicsworld.com/cws/product/P000010152 (2009). [Cited on 61]

CHAPTER 4

Design & fabrication of SF-STM probes

We describe the design and fabrication of multi-terminal semiconductor/ferromagnet probes for the realization of spin-filter scanning tunneling microscopy. We devise a microfabrication process based on anisotropic wet etching and local oxidation of silicon. Characterizing the formation of the tip after each process step allows to controllably obtain probes having a (sub-micron) semiconductor/ferromagnet heterostructure localized at the apex of the tip.

4.1 Probe design

In the previous chapter we presented a framework to analyze the spin-dependent transmission properties of our multi-terminal probes. This semi-empirical framework is well established for solid-state devices (see section 3.2). In practice the operation conditions of our novel technique are different than those of solid-state devices. For example, due to the very local nature of the tunneling process in SF-STM we can not arbitrarily increase the collection signal by increasing the tunnel junction area. Therefore the magnitude of the collected

signal in the semiconductor becomes a matter of concern. Furthermore, the geometry of the semiconductor/metal heterostructure must be different than the usual planar geometry of solid-state devices. These and other considerations must be taken into account for the design of successful SF-STM probes. In this first section we address these issues and establish design rules to be used during the fabrication of the probes.

A major point of interest is the usage of the observable magnetocurrent (MC) to quantitatively extract the tunnel spin polarization P_S of a magnetic sample. It was stated that when the metal base of the probe contains a thick enough ferromagnet (FM) then the collected current I_C originates mostly from the majority spin channel and almost no minority spins are transmitted. Under these assumptions the heterostructure acts as a perfect spin filter with a renormalized base polarization $P_B^* = 1$ which according to Equation 3.3 yields

$$\mathrm{MC} = \frac{2P_S}{1-P_S} \quad \Longrightarrow \quad P_S = \frac{\mathrm{MC}}{2+\mathrm{MC}} \tag{4.1}$$

where the details of spin-dependent transmission in the probe are absent. This is the ideal regime because we can directly calculate P_S from the measured MC without the need of any other physical quantity. But using a very thick spin filter has the disadvantage of decreasing the magnitude of I_C due to the exponential decay of ballistic transmission with FM thickness. SF-STM operation dictates tunnel currents of up to a few nA which limits I_C to the pA regime. A way to increase I_C is to increase the tunnel bias V_T well above the Schottky barrier height Φ_B. Increasing V_T yields larger I_C while reducing the energy resolution to about 0.3 eV. But V_T cannot be increased indefinitely because we sacrifice tunnel gap stability or we may even induce tip/sample changes, so we limit V_T to practical values of 1.0–2.0 V.

We must find an optimum thickness that balances a large relative signal MC (increasing the validity of Equation 4.1) with a large magnitude of the absolute signal ($I_C^P - I_C^{AP}$). To address this issue we need to analyze the intermediate thickness regime, where the MC value is determined by the spin-dependent attenuation length in the spin filter. To guide us in this analysis we present a compilation of experimental effective attenuation lengths λ in Table 4.1.

We observe that λ is much larger for noble metals like Au or Cu than for typical ferromagnets. Using a metal stack of Au/FM/Au thus means that most of the scattering occurs within the ferromagnet alone. The inclusion of both noble metal layers is necessary for two reasons. First, having Au as a

seed layer over the Si substrate yields a better quality Schottky interface while increasing the collection properties of the heterostructure [1, 2, 3]. Second, a capping Au layer protects the underlying ferromagnet from oxidation and contamination. Previous similar structures capped with Au have not shown any decrease in collection characteristics between UHV in-situ deposited samples and those exposed for several hours to ambient conditions prior BEMM measurements [4]. Since we perform ex-situ transfer of the SF-STM probes to our STM chamber we require the capping layer.

Table 4.1. *Compilation of (spin-dependent) attenuation lengths in relevant metals.*

Material	Technique	$\lambda_{\uparrow,\downarrow}$ (nm)	Energy (eV)	Reference
Co	BEMM	2.1, 0.8	1.5	Rippard et al. [5]
	BEMM	2.4, —	1.5	Rippard et al. [4]
	BEMM	3.3, 1.1	1.5	Kaidatzis et al. [6]
	BEEM	3.4, < 1	1.4	Jansen et al. [7]
	MTT	6.7, < 1	1.4	Jansen et al. [7]
	MTT	7, 1	1.0–1.4	Park et al. [8]
$Co_{84}Fe_{16}$	MTT	5.0, 0.9	1.4	van Dijken et al. [9]
$Ni_{80}Fe_{20}$	SVT	4.3, 1.0	0.9	Vlutters et al. [10]
$Ni_{81}Fe_{19}$	MTT	6.7, 1.3	1.4	van Dijken et al. [9]
Fe	BEMM	1.5, 0.4	1.2–1.6	Banerjee et al. [11]
Au	BEEM	13	1.0	Bell [12]
	BEEM	24–28	1.2	Weilmeier et al. [13]
Cu	BEEM	37.5	0.9	Garramone et al. [14]
	MTT	10.5	1.4	van Dijken et al. [3]

For the case of ferromagnetic metals we must consider both majority ($\lambda_\uparrow$) and minority ($\lambda_\downarrow$) attenuation lengths. Experiments where the energy of the hot electrons can be varied, like MTT and BEMM (BEEM), have shown a rather weak dependence with energy. We focus on the range 1.2–1.7 eV where a good balance of collection signal level and magnetic contrast is usually obtained in BEMM [6, 15]. From the compilation above we conclude that $\lambda_\downarrow$ is about 1 nm for typical ferromagnets like Co or $Ni_{80}Fe_{20}$.

Interestingly for $\lambda_\uparrow$ there is a clear difference between the values obtained by MTT and BEMM techniques. As evidenced for the case of Co, $\lambda_\uparrow$ extracted from MTT devices is approximately twice the value of that from BEMM measurements [7]. This discrepancy has been attributed to the broader momentum

distribution of tunneling electrons caused by Al_2O_3 tunnel barriers in MTT opposite to a sharply focused distribution for vacuum tunneling in STM [7]. Since we use the same deposition system and conditions as that used by Jansen et al. we know that for our Co films $\lambda_\uparrow \gtrsim 3\,\text{nm}$. We remark that a similar difference is observed for $\lambda_\uparrow$ in NiFe alloys studied by SVT and MTT which may reflect the forward-focused character of the injected electrons in SVT devices [16]. So we also expect for $Ni_{80}Fe_{20}$ that $\lambda_\uparrow \gtrsim 3\,\text{nm}$. In the following we analyze the case of a ferromagnetic spin filter with $\lambda_\uparrow = 3\,\text{nm}$ and $\lambda_\downarrow = 1\,\text{nm}$. This is a conservative approach as any larger $\lambda_\uparrow$ or smaller $\lambda_\downarrow$ increases the spin-asymmetry and the validity of Equation 4.1.

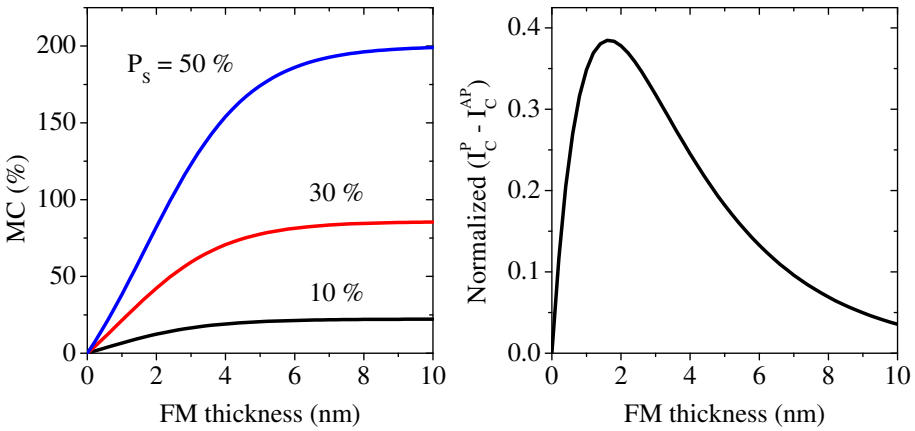

Figure 4.1. *Spin-dependent transport in SF-STM probes depending on thickness of the ferromagnetic spin-filter layer. Left: relative magnetic contrast for spin-polarized samples with P_S equal to 10 %, 30 % and 50 %. Right: normalized absolute magnetic contrast (see text). The spin filter has attenuation lengths of $\lambda_\uparrow = 3$ nm and $\lambda_\downarrow = 1$ nm.*

The analysis of the collection properties of SF-STM probes for intermediate thickness t_{FM} of the spin filter is shown in Figure 4.1. For the analysis we have used spin-independent interface attenuation factors $\Gamma^\uparrow = \Gamma^\downarrow$ and a spin-independent probe tunnel spin polarization ($n_\uparrow^B = n_\downarrow^B$) consistent with our Au/FM/Au metal base. We observe that the MC increases with increasing thickness of the spin filter. For $t_{FM} \approx 2\,\text{nm}$ the MC reaches half of its maximum value while it saturates for $t_{FM} > 5\,\text{nm}$, similarly as for MTTs (see Figure 3.3).

A different criteria for optimal t_{FM} is obtained when we look at the absolute magnetic contrast $I_C^P - I_C^{AP}$. The numerical value of this signal depends on several factors as shown in Equation 3.2. We can get a clear idea of the effect

of spin-dependent scattering within the volume of the spin filter by normalizing this signal with that expected for an ideal spin filter with $\lambda_{\downarrow} = 0$ and $\lambda_{\uparrow} = \infty$ ($P_B^* = 1$) while keeping all the other terms in Equation 3.1 the same [1, 17]. We observe that a maximum absolute contrast is obtained for $t_{FM} \approx 2\,\text{nm}$. At even larger thickness the signal decreases exponentially with a characteristic length of $\lambda_{\uparrow}$ because the ballistic current is dominated by majority electrons. For $t_{FM} \approx 5\,\text{nm}$ the signal is half of its possible maximum. At larger thickness the signal to noise ratio decreases which impairs the sensitivity of the technique. Therefore a thickness range of 2–5 nm seems to be an optimum choice.

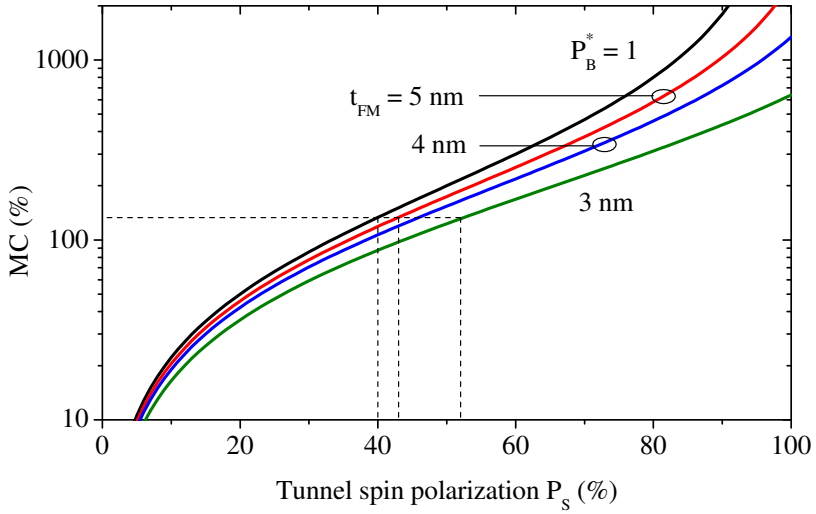

Figure 4.2. *Dependence of relative magnetic contrast on the tunnel spin polarization from the sample. The curves correspond to probes with a spin filter layer of thickness 3 nm, 4 nm, 5 nm or infinite ($P_B^* = 1$). The spin filter has attenuation lengths of $\lambda_{\uparrow} =$ 3 nm and $\lambda_{\downarrow} = 1$ nm.*

In Figure 4.2 we can visualize the impact of having a spin filter with intermediate thickness ($P_B^* < 1$) by plotting the dependence of the relative magnetic contrast on the sample tunnel spin polarization. For a perfect spin filter an observable MC of 133 % corresponds to a sample with 40 % spin polarization according to the simplified description of Equation 4.1. If we consider a 3 nm thick spin filter the same measured MC would correspond to a spin polarization of 52 % when we consider the more complete description given by Equation 3.3. The numerical discrepancy between both descriptions decreases by a factor of 4 if we consider a spin filter of 5 nm thickness for

which the same MC corresponds to a spin polarization of 43 %. In this regime of larger thickness the spin filter transmits mostly majority spins and the sample spin polarization can be approximated from the MC directly via Equation 4.1. The validity of this approximation increases for lower sample spin polarization. The bottom line is that with knowledge of the spin-dependent attenuation lengths it is possible to quantify the spin polarization from the MC for any thickness of the probe spin filter.

We can also use Figure 4.2 to identify the range of spin polarization values which can be accurately determined by SF-STM. Following on the arguments from the previous chapter we state that considering typical collection signals in the pA range and noise levels below 0.1 pA we expect a minimum detectable MC of about 10 % which corresponds to a 5 % sample spin polarization. On the other hand, previous MTT devices have shown a MC limited to about 1300 % due to scattering at the interfaces of the metal stack [18] which meant a polarization limited to 86 %. We remark that in that case a full spin-valve structure was used which has double the amount of interfaces than the case of a single ferromagnet filter for SF-STM probes. Moreover, in that MTT case the metals were deposited using magnetron sputtering which is expected to produce more intermixing at the interfaces than for evaporation (which we use in this work). Therefore we argue that with SF-STM it is possible to quantify sample spin polarization within the range of 5–90 %.

The foregoing analysis is based on the current knowledge of ballistic spin filtering in semiconductor/metal heterostructures with a planar geometry. Still, SF-STM probes should not have a completely planar apex as this would prevent the attainment of high spatial resolution. A way out of this dilemma is to give a radius of curvature to the apex that is small enough such that it can be used as an imaging probe but much larger than the thickness of the metal layers such that locally the interface can be considered flat as shown in Figure 4.3. This approach makes valid the previous analysis and also provides for a semiconductor/metal Schottky diode with similar properties as for the planar case. Since the thickness of the metal layer stack is about 10 nm we argue that a radius of curvature larger than 500 nm should suffice. On the other hand, a high spatial resolution typical for STM can be readily achieved by considering the intrinsic roughness of the probe metal surface due to the polycrystalline nature of the grown metal films. The topmost metal cluster constitutes the tunneling area and provides high spatial resolution, similarly to SP-STM tips [19]. Moreover, since the topmost layer is a noble metal the small

cluster would not produce a sizable magnetic field at the tunneling location which is an issue in SP-STM tips when using thin ferromagnetic coatings [20]. We also expect that having a smooth apex with large radius of curvature should help to attain a better defined in-plane magnetization direction similarly to planar solid state devices or BEMM samples.

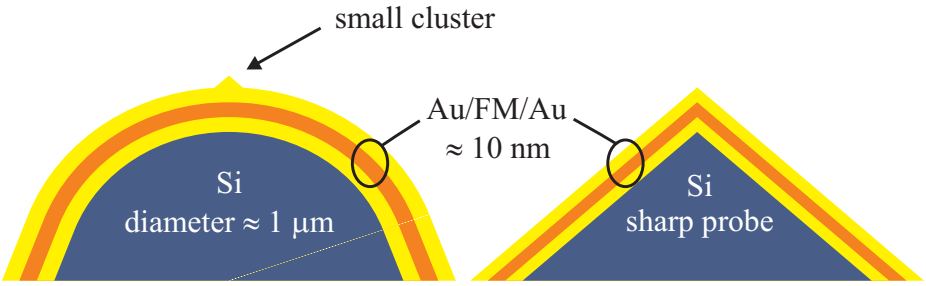

Figure 4.3. *Geometry at the apex of SF-STM probes. Left: a rounded apex with a radius of curvature much larger than the metal film thickness permits the analysis of spin-dependent transport using a planar framework. A small metal cluster provides high spatial resolution. Right: a completely sharp probe may not be optimal to achieve proper collection at the semiconductor and a well defined magnetization at the apex.*

The noise present in the collected signal I_C is also related to the geometry of the probe via the area of the Schottky diode. The input-voltage noise of the current amplifier and the Johnson noise in the Schottky diode will create a corresponding noise in the collected current signal similarly to the case of BEEM samples [21]. For a sizable noise the current signal would be rectified by the diode giving raise to a large offset in the signal (or leakage current). The way to decrease this noise is to increase the resistance of the Schottky diode (R_{diode}). For our instrumentation optimal values correspond to $R_{diode} \gtrsim 1\,\mathrm{G\Omega}$ because then the noise is limited by the amplifier electronics for the collection channel [15]. During SF-STM operation we do not apply a bias difference between the metal overlayer in the probe and the semiconductor contact so the resistance of the Schottky diode is that at zero bias $R_{diode} = \mathrm{d}V/\mathrm{d}I|_{V=0}$. Using the model of thermionic emission for the Schottky diode [22] and considering $\Phi_B = 0.8\,\mathrm{eV}$ for Si/Au we obtain a resistance larger than $1\,\mathrm{G\Omega}$ at room temperature for circular diodes with diameter below $120\,\mu\mathrm{m}$. Limiting the semiconductor/metal area is thus fundamental to achieve an accurate measurement of spin polarization at room temperature [23]. For diodes with lower resistance we can operate at a lower probe temperature since R_{diode} increases with decreasing temperature.

4.2 Probe microfabrication

In this section we describe the process developed for fabrication of SF-STM probes. We begin with a general description of the microfabrication steps involved in converting a Si wafer into a set of chips, each containing (several) SF-STM probes. Next, we proceed to discuss in detail some of the important steps, including experiments performed during the development of the fabrication process. We present results characterizing the state of the probes after certain fabrication steps and discuss our process within the context of previous work.

A schematic representation of important steps during the fabrication of SF-STM probes is shown in Figure 4.4. A more complete process flow diagram showing the main steps and alternative processing pathways is shown in Figure 4.5. In the following we refer the reader to these two figures during our general description of the fabrication process.

For the realization of SF-STM we have fabricated probes in the form of silicon double pyramids terminated with (sub-)micrometer Schottky diodes serving as the active elements for tunneling and spin filtering [24], as schematically shown in Figure 4.4. The double pyramid structure was chosen for two reasons. First, there is the need for a large and high-aspect-ratio probe, to be able to approach a flat sample while allowing for a small deviation of the tip-sample alignment (see the geometry of our STM setup in Figure 3.4). Second, the apex of the probe must have a small area where the semiconductor/metal interface is defined, resulting in a diode contact with a high resistance $R_{diode} \gtrsim 1\,\mathrm{G\Omega}$. This is required to obtain a sufficient signal to noise ratio to detect I_C [21], as discussed in section 4.1. Both requirements are most easily achieved by first etching a large bottom pyramid that provides a probe with sufficient height and aspect ratio, and then in a more controlled way a small pyramid on top where we can define the semiconductor/metal interface. A similar approach has been previously followed for the fabrication of near-field scanning optical microscopy (NSOM) probes [25].

The probes are made from n-type silicon (100) substrates with resistivity of 1–10 Ω cm (phosphorus doping $\approx 10^{15}\,\mathrm{cm^{-3}}$). The process starts with formation of a thin pad oxide (SiO_2) by dry oxidation at 950 °C and deposition of a stoichiometric silicon nitride (Si_3N_4) layer by low pressure chemical vapor deposition (LPCVD), followed by a short one hour anneal in N_2 atmosphere at 1150 °C to release residual stress [26]. A circular pattern of $\geq 10\,\mu\mathrm{m}$ diameter

is defined in the top nitride layer by photolithography and reactive ion etching (RIE). The gas mixture used in RIE was CHF_3:O_2 = 5:1. This nitride pattern serves as a mask to define the small pyramid later in the process. A pattern of <110> oriented openings in the nitride is also defined by RIE on the backside of the wafer. These openings are later used as break lines to easily separate the wafer into individual chips near the end of the process.

Then a thick 1 µm oxide is grown by wet thermal oxidation at 1150 °C and patterned in a larger concentric circle ($\geq$ 100 µm diameter) by a second photolithographic step using buffered HF (BHF). This thick oxide mask is used to define the large bottom pyramid having a height of 120 µm and a top mesa structure less than 50 µm wide, by anisotropic wet etching of silicon in a hot solution of potassium hydroxide (KOH) [27]. Then the remaining oxide mask is removed and the nitride mask is used to define the smaller top pyramid also in KOH solution, with a height of about 15 µm. The small pyramid has a top area less than 1 µm wide capped by the nitride mask, as shown by scanning electron microscopy (SEM) in Figure 4.10b. The mesa structure formed by the large bottom pyramid must not be too wide, to assure that the tunneling contact between probe and sample occurs at the apex of the small top pyramid and not at the edge of the mesa [28].

Next, the structure is again thermally oxidized to produce a SiO_2 electrical isolation layer everywhere except in the top area of the small pyramid, where the nitride cap prevents oxidation as in standard local oxidation of silicon (LOCOS) [29, 30]. During this process the top silicon apex becomes rounded due to formation of the so called oxide bird's beaks, in a geometry similar to fully-recessed LOCOS [31]. We remark that this step is performed using dry oxidation at 1100 °C up to a thickness of 300 nm, contrary to standard LOCOS where wet oxidation is used. This step is important for achieving a proper radius of curvature at the apex of the SF-STM probe, as shown later by atomic force microscopy (AFM) profiles (see Figure 4.12).

After LOCOS there are two possible process pathways, as depicted in Figure 4.5. The main differences between the two are given below. A more detailed explanation is presented later in this section.

1. The first process pathway is the easiest. It includes the removal of the nitride cap in hot phosphoric acid (85 % H_3PO_4 at 160 °C) followed by oxide removal to expose the Si surface at the apex of the probe. The amount of removed oxide must be more than the pad oxide thickness, also the oxide beaks in the vicinity of the Si apex must be removed,

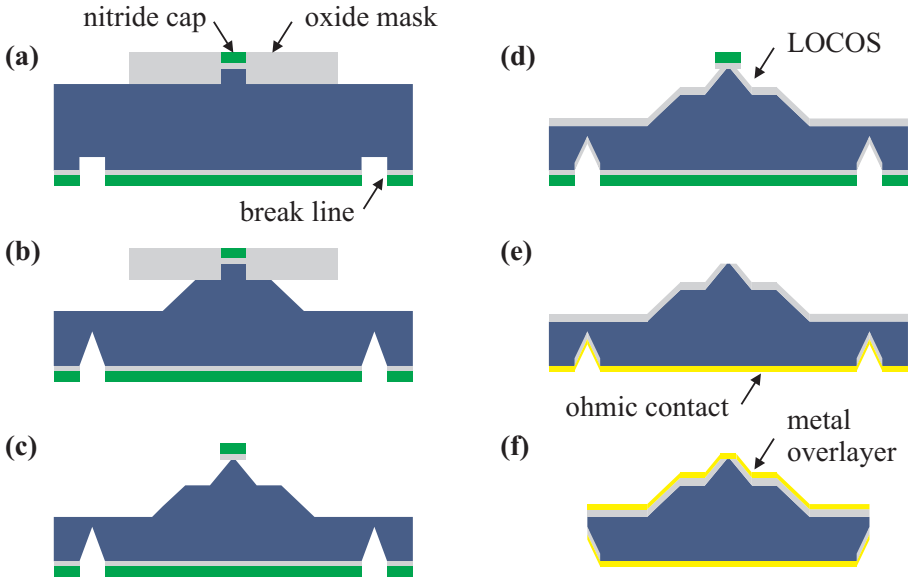

Figure 4.4. *Schematic of representative steps during fabrication of SF-STM probes. (a) After growth and patterning of the oxide and nitride masks. (b) Formation of large bottom pyramid using the oxide mask. (c) Formation of small top pyramid using nitride mask. (d) Growth of isolation oxide for LOCOS at apex. (e) Deposition of ohmic contact on rear surface of Si substrate. (f) Deposition of top metal overlayer for spin filter on separated chip. These steps correspond to the blocks having a thick edge as shown in Figure 4.5.*

otherwise the oxide beaks would be the highest point of the probe and tunneling would not take place at the Si/metal diode. But the removed oxide must also be considerably less than that grown during LOCOS (300 nm), otherwise the electrical isolation would be lost everywhere else on the pyramid. Therefore this pathway yields an exposed Si surface with similar size as that of the small pyramid area in direct contact with the nitride cap (from several micrometers down to sub-micrometer) but with the Si/SiO_2 edge quite close to the apex and a limited isolation thickness. Using this pathway we fabricated pyramidal metal-semiconductor structures on which we performed STM/BEEM experiments (see chapter 5).

2. The second process pathway is more elaborate. Besides the cap and oxide removal steps from the first pathway, it also includes the sputtering of extra SiO_2 (500 nm) and other steps (RIE, growth of sacrificial oxide)

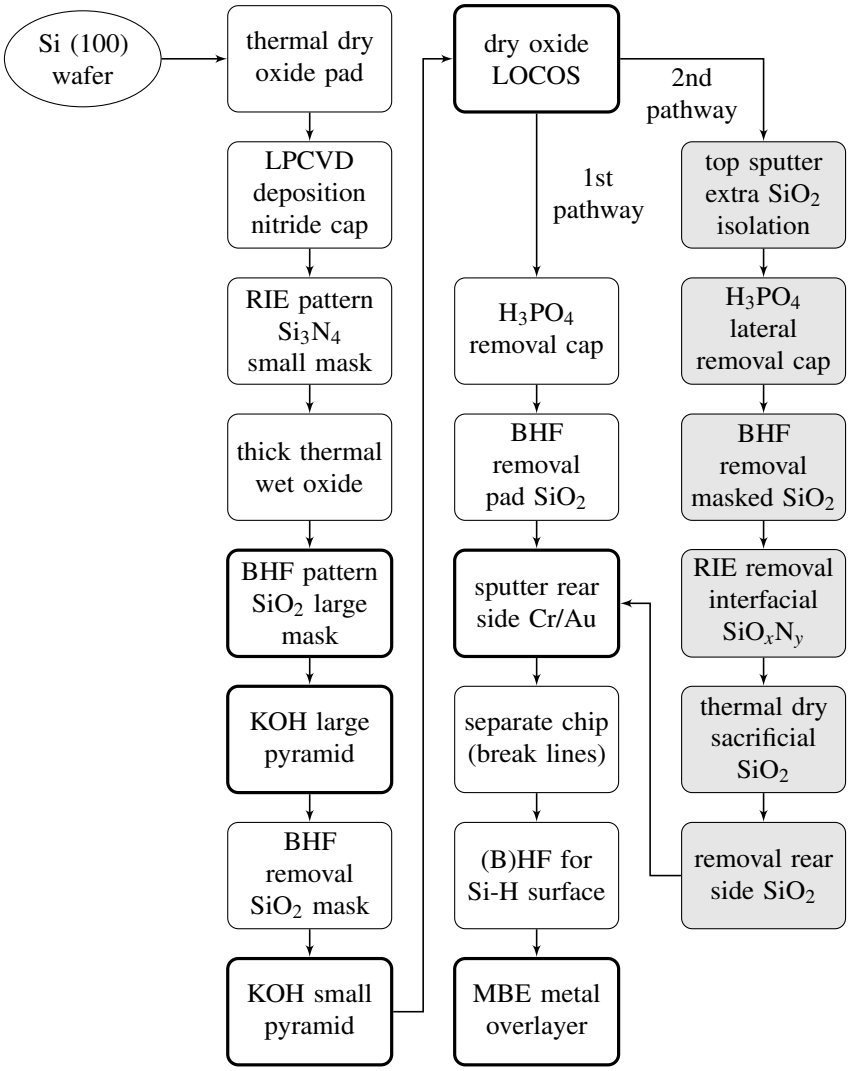

Figure 4.5. *Process flow diagram indicating the main microfabrication steps for SF-STM probes. Two pathways to achieve a locally exposed Si apex are shown. The second pathway (including the gray-filled steps) results in sharp probes without any oxide near the apex, but it can not produce structures with a wide flat apex. The steps with a thick edge correspond to those schematically shown in Figure 4.4.*

to ensure that the apex surface consists of clean and smooth exposed Si. The sputtered oxide on the wafer frontside is a key step because it changes the probe in two significant ways. First, it adds a thicker electrical isolation, so its thickness is no longer limited to the LOCOS

oxide thinned down after exposure of the Si apex. Second, it allows the removal of all the oxide shadow masked by the projection of the circular nitride cap, so there are no beaks or Si/SiO_2 edges close to the apex (see Figure 4.14). A more detailed description of these steps will be given later in this section. Using this pathway we successfully fabricated SF-STM probes for imaging of metallic surfaces (see chapter 6).

The rear side of the wafer serves as the ohmic contact to the semiconductor. For this purpose the oxide present at the rear side is removed in BHF, followed by sputtering of Cr/Au on the rear side. This low resistance electrical contact spans the complete rear surface of the semiconductor chip.

At this stage the probes are almost fully structured, except for the metal overlayer which serves as the top electrical contact and spin filter. Before the deposition of this overlayer the wafer is separated into individual chips (see Figure 4.6) using the break lines formed on the backside during the KOH etch of the double pyramid. These lines are oriented along <110> directions where the Si wafer is easily cleaved. The depth of the break lines is determined by the width of the pattern opened in the nitride rear side layer (300 µm) since etching in KOH results in grooves limited by {111} planes [32]. The reason we use this approach instead of standard dicing saw is to avoid the formation of large amounts of particles and debris. Once the double pyramid is formed it is prone to mechanical damage if the wafer is placed upside down on a hard surface.

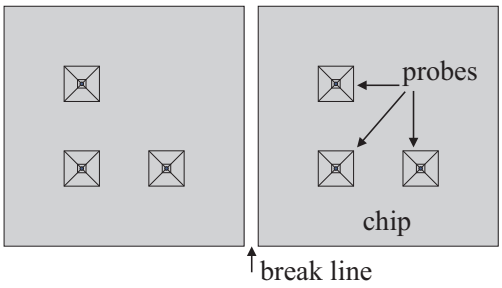

Figure 4.6. *Schematic of chips separated from a wafer using the break lines. There are three SF-STM probes within each chip. A sample can be positioned over each probe one at a time. This design facilitates STM experiments because if a probe is damaged, another probe can be tested without the need of loading a new chip.*

The last step is a HF dip to remove any (native) oxide from the top Si area and to cover the probe with the metal overlayer using a molecular beam

epitaxy (MBE) system at a pressure of 10^{-10} mbar. The previous separation of the wafer into individual chips allows the deposition of different layer stacks on each chip. The layer stack includes first a gold layer of ca. 10 nm to create a high-quality interface with the silicon of 0.8 eV Schottky barrier height, then the thin (ca. 5 nm) ferromagnet for spin-dependent filtering and finally a thin gold cap layer (ca. 5 nm) that provides an inert surface to allow ex-situ tip transfer to the SF-STM system. This layer stack was discussed in more detail in section 4.1.

The fabrication process described above was carefully monitored using several characterization tools like optical microscopy, SEM, AFM, stylus profilometry, ellipsometry and x-ray diffraction. In this way each process step was kept under control, leading to reproducible results. We measured etch rates for all relevant combinations of etchants and materials in good agreement with published micromachining data [33]. In the following, we proceed to describe in more detail some of the important fabrication steps.

4.2.1 Anisotropic wet etch of pyramidal structures

The importance of anisotropic etching technology for the semiconductor industry was realized since early on [32]. Anisotropic wet etching of silicon was initially studied using water-amine complexing agents, like ethylenediamine, pyrochatecol and water (EDP) [34]. Technologically speaking, the use of KOH mixtures are favoured versus organic baths like EDP and tetramethylammonium hydroxide (TMAH), because the organic etchants are problematic from the point of view of health issues and disposal costs of used baths [35]. In our cleanroom facilities KOH-based etchants are used as standard baths, so we have based our fabrication process on KOH. There are differences between KOH and organic etchants, e.g. KOH etchants do not show a strong dependence on etchant circulation whereas TMAH does, but both show variations in etch rate and anisotropy depending on the concentration and temperature of the bath [36]. There are still some advantages to the use of organic etchants, like a relative lower etch rate of SiO_2 and the absence of mobile K ions that get introduced into the SiO_2 and might damage electrical circuits [36]. We deal with the issue of K ions by performing a clean in a mixture of HCl, H_2O_2 and water (RCA-2).

During the initial development of our fabrication process we used a KOH-water etch of 25 % KOH by weight at 75 °C. This composition is close to the

maximum etch rate along <001> (≈ 1 µm/min). Due to reasons to be explained later, we changed to a similar solution with isopropyl alcohol (IPA) added up to saturation (250 mL IPA per 1 L water). A main difference between these solutions are the relative etch rates r_{lmn} for characteristic {lmn} planes. For KOH (without IPA) the relative etch rates are $r_{110} > r_{100} > r_{111}$, whereas for KOH with IPA (KOH-IPA) and EDP they are $r_{100} > r_{110} > r_{111}$ [37]. The presence of IPA in KOH etches produces more regular surfaces and reduces the generation and adhesion of hydrogen (H_2) bubbles [35], a process which can be described at an atomistic level [38].

Initial studies on the anisotropic etching of silicon in alkaline solutions dealt with the effect of substrate orientation and doping, leading to a proposed electrochemical model [39, 40]. Later work combined electrochemistry studies with the high spatial resolution of STM to characterize in-situ the surface chemistry and morphology during the etching process, resulting in the understanding of anisotropic etching as a step-flow process [41, 42]. This shows how STM is actively used to better understand basic semiconductor processes which have a high technological impact, whereas we attempt in this work to use such processes to further develope STM. From those in-situ STM observations of anisotropic etching a step-flow model has been developed which can predict the structure of convex corner undercutting in Si by KOH etching [43, 44], as encountered in the formation of pyramidal structures. Nevertheless, we must remark that the mechanism of wet chemical etching of Si in alkaline solutions is still a debated subject [44]. Since we are interested in characterizing the morphology of our SF-STM probes we present below a discussion of undercutting of convex corners and the resulting bevelling planes in Si pyramidal structures.

Corner undercutting in anisotropic wet etch

Anisotropic etching of Si using a convex shaped mask leads to formation of pyramidal structures. As mentioned above, when a mask edge is oriented along a <110> direction the result is a slow etching {111} plane (tilt of 54.75°) which for practical purposes acts as an etch stop. But even if the edges of a convex mask are oriented along <110> an undercutting process occurs at the corner, leading to the appearance of fast etching planes. The nature of these bevelling planes has been a subject of debate with several conflicting reports. To make the matter clearer we will refer in the following to all planes relative

to a substrate with a (001) surface. Two previous works give an account of this uncertain situation. Bean [32] observed {133} planes for KOH-IPA. On the other hand, Wu and Ko [45] observed {122} planes for both KOH-IPA and EDP, arguing against Bean. They mention both sets of planes result in octagonal apexes that are alike, determined by the intersection of these planes with the (001) surface. The octagons have similar alternating angles and only differ in their orientation, as shown in Figure 4.7a.

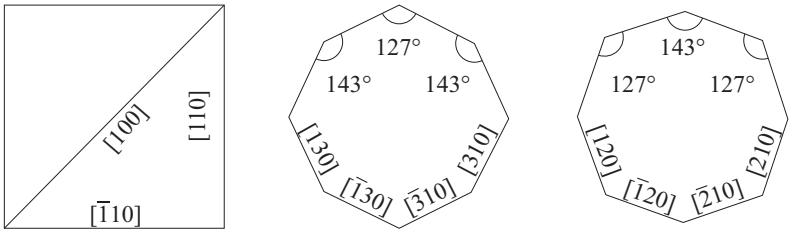

(a) *Important orientations in anisotropic wet etching of Si (001). The wafer flat is oriented along <110> and masks aligned along these orientations result in the appearance of slow-etching {111} planes. Due to convex corner undercutting below an etch mask other planes appear until they form an octagonal apex with sides typically oriented along <130> or <120>.*

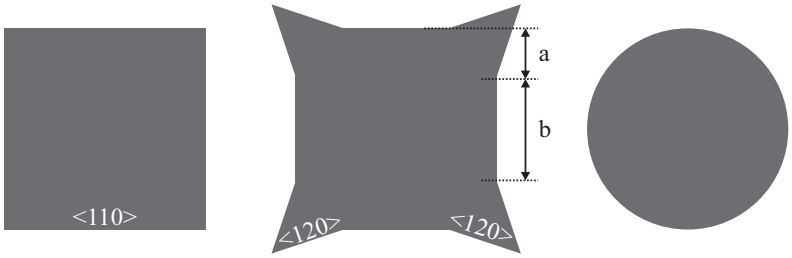

(b) *Shape of masks tested for etching Si pyramids. Square masks oriented along <110> initially lead to {111} planes but eventually suffer corner undercut. Corner compensation pattern (2a/(2a+b) = 50 % shown here) leads to a retardation of corner undercut. Circular masks are quickly undercut but offer more reproducibility from wafer to wafer.*

Figure 4.7. *Intersection of typical bevelling planes with (001) and etch masks used during anisotropic wet etching of Si.*

Wu and Ko [45] mention that when etching a concave surface the limiting shape is bounded by the slowest-etching planes, whereas for a convex surface (like a mesa) the shape is bounded by the fastest-etching planes. They also presented a mask compensation pattern by the addition of angles bounded

by <120> orientations to the convex corners of square mask paterns whose edges were parallel to the <110> orientations. After formation of the octagonal apex due to corner undercut, the octagon decreases its size as determined by the etch rates of the corresponding bevelling planes. A way to delay this corner undercut and the subsequent narrowing of the apex is by the use of such compensation patterns. We have used this approach for designing etch masks, as shown in Figure 4.7b. If one rotates these masks by 45° such that the sides of the square are aligned with <100> directions, then the compensation triangles would be now oriented in the <130> directions [27]. Both are fast etching directions with similar orientations, so a <120> compensation should work independent of the exact orientation of the bevelling planes. Ultimately, we chose for circular etch masks. These circular masks yield more reproducible results than square masks because of two reasons. First, they are insensitive to the exact alignment of the pattern with the crystallographic axis of the substrate. Second, for practical purposes their pattern can be perfectly transferred into the mask, something impossible for small (10 µm) square masks using standard photolithography.

For the sake of completeness we list other relevant reports on determination of bevelling planes. Puers and Sansen [46] obtained {122} crystal planes for KOH-IPA, whereas for KOH without IPA they observed intersects with (001) at <130> directions. Offereins et al. [47] argued that for KOH without IPA they obtain {411} planes. Trujillo and Hunt [48] observed {133} planes for KOH-IPA. Backlund and Rosengren [27] used masks with squares aligned in the <100> directions and observed the formation of {011} planes using KOH-IPA, whereas {133} planes were formed with EDP. Tan et al. [49] studied the transformation of etch hillock defects created in KOH-IPA from the original {567} planes into {133} planes, consistent with the occurrence of {133} planes during undercutting of convex corners. Tran et al. [50] observed {122} planes using KOH without IPA and EDP. Chung et al. [51] pointed out that EDP produced pyramids with {122} planes, whereas KOH without IPA produced pyramids with initially {133} planes which later break down into highly vertical {311} planes. This observation of a progression of planes has been observed in other studies, for example by Wilke et al. [52] who argue that the planes in pyramids formed by KOH without IPA follow a progression from nearly vertical planes down to {362} planes with an octagonal apex oriented along <120> directions. Following the discussion above on formation of pyramidal Si structures we present below the characterization of our probes

fabricated using KOH etch without IPA and KOH-IPA.

Pyramids formed by KOH without IPA

Initial experiments were performed using a KOH solution without IPA and square masks with several degrees of corner compensation, as those presented in Figure 4.7b. We studied the effect of mask size and amount of corner compensation on the resulting pyramidal structure. One example of such experiments is presented in Figure 4.8. For a fixed etch time the undercut at the corners of SiO_2 masks resulted on Si pyramids with different widths of their top mesa structures. These mesas were intended to serve as the substrate were the top small pyramid would be formed. The cases were a zero value is shown correspond to a complete narrowing of the octagonal apex resulting in sharp pyramids which lost their top oxide or nitride masks.

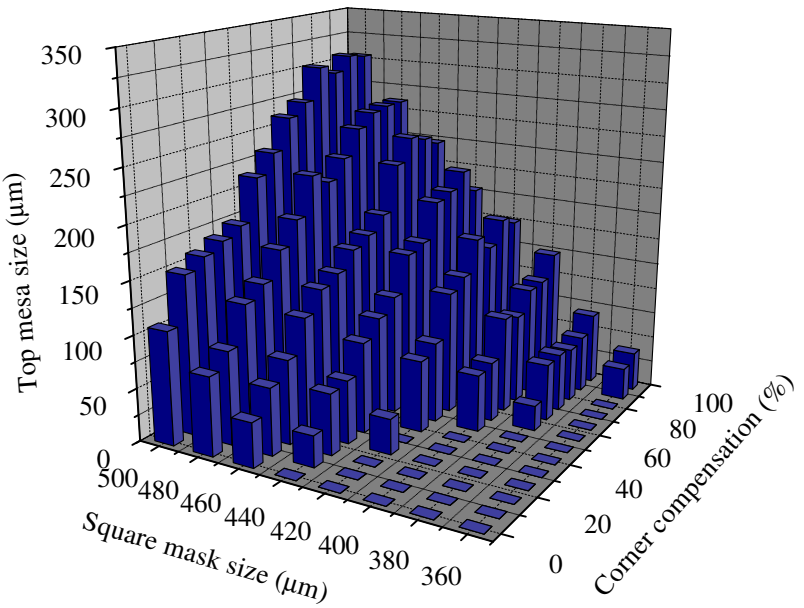

Figure 4.8. *Effect of square mask size and amount of corner compensation on top mesa width along <110> for large pyramids etched 3 h in KOH without IPA.*

As mentioned above we decided later to use only circular masks for the formation of both large and small pyramids. Their insensitivity to alignment

with the substrate crystal structure or to the resolution of the photolithography process (to define sharp corners) yielded reproducible results for pyramid formation over the whole wafer, their homogeneity only limited by the small gradient on etch rate found on the KOH bath in our cleanroom. SEM images of the obtained pyramidal structures are shown in Figure 4.9. Our results for KOH without IPA using square masks agree well with those of Wilke et al. [52], both in the evolution of the mesa width versus time (not shown here) and in the appearance of highly vertical {362} planes (tilt of 73.4°) forming the sides of the pyramids as determined by analysis of SEM images. For the detailed analysis of SEM images we refer the reader to previous work in our group [53].

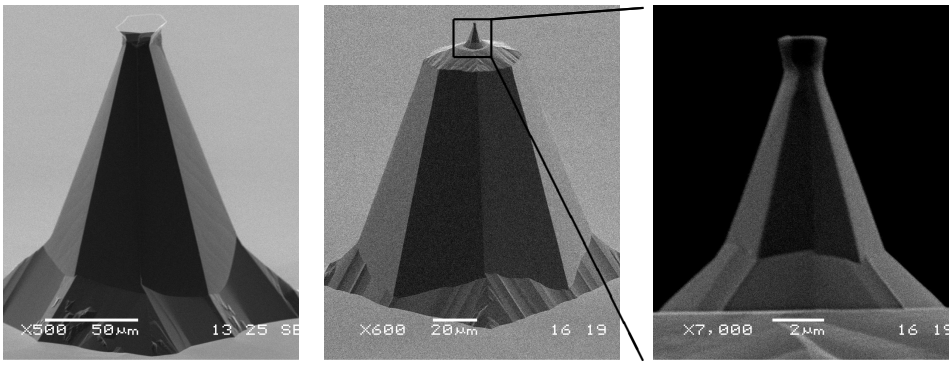

(a) *(b)* *(c)*

Figure 4.9. *SEM characterization of the SF-STM tip morphology formed by anisotropic wet etching of Si using KOH solution (without IPA). (a) Single large pyramid showing negative slope edge at the apex. (b) Complete double pyramid showing removal of the negative slope edge of the large pyramid due to the second etching for formation of the small top pyramid. (c) Zoom into top small pyramid from (b) showing also a negative slope edge at its apex.*

Corner undercut and further decrease of the octagonal apex occurs quite fast in KOH without IPA. After octagon formation its width decreases at a typical rate of 3–4 µm/min, too fast to controllably form a 1 µm wide apex. Still, the main reason to stop using KOH without IPA was the occurrence of negative sloped planes near the apex, as shown in Figure 4.9a. This phenomenon has been observed previously [51, 52] and there is recent interest in its simulation [54]. The negative slope is a problem for our SF-STM probes because it prevents the continuous coating of the probe with metal layers due to

shadowing effects, specially when evaporation is used for the metal overlayer. This problem creates a lack of electrical contact to the metal layer stack just at the apex because the clip for electrical contact is located far away on the substrate of the chip (see Figure 3.4). We tried to overcome this issue in several ways.

1. Using sputtering instead of evaporation for a less directional metal deposition. The initial Au layer could be sputtered with formation of a good electrical contact to the exposed Si at the apex, but this only worked for thick Au films of more than 40 nm. Such a thick layer is detrimental to the transmission of hot electrons in the metal overlayer and the magnitude of the collected signal in the Si, so this is not a workable solution.

2. Removing the negative sloped planes at the large bottom pyramid by a sufficiently long KOH etch (> 10 min) during formation of the small top pyramid. Since the oxide mask is previously removed this approach indeed removes the negative sloped planes at the large pyramid, as shown in Figure 4.9b. But the small top pyramid also developed negative sloped planes at its apex (see Figure 4.9c), so this is not a solution either. The negative sloped planes are formed even though the pyramid was only 10 µm high, contrary to the interpretation of Wilke et al. [52].

So we decided to change the etch system due to the issues encountered with the formation of pyramids in KOH. We found a straightforward alternative in the addition of IPA to the present solution, which we describe next.

Pyramids formed by KOH-IPA

Addition of IPA up to saturation of a 25 % KOH etch at 75 °C led to solving most of the issues encountered with the original KOH without IPA. The major issue solved was the negative sloped planes. A full SF-STM probe fabricated with KOH-IPA is shown in Figure 4.10a without any negative sloped planes. We remark that formation of individual pyramids resulted in smooth sidewalls and no negative sloped planes whatsoever, independent of the size of the pyramid. The texture observed near the top mesa of the large bottom pyramid in Figure 4.10a appears only after the second KOH-IPA etch for formation of the small top pyramid. This texture was no problem for achieving a proper electrical contact to the metal overlayer at the apex of the probe. Furthermore,

the less steep sidewalls compared with the pyramids formed in KOH without IPA result in a thicker metal coating.

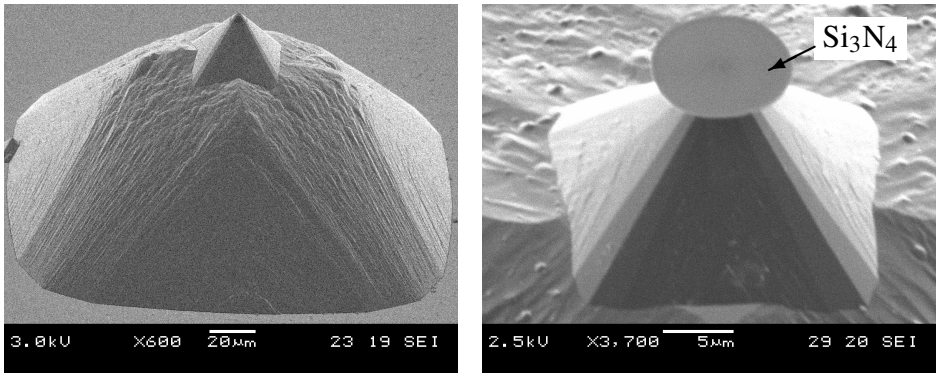

(a) *(b)*

Figure 4.10. *SEM characterization of the SF-STM tip morphology formed by anisotropic wet etching of Si using KOH-IPA solution. (a) Complete double pyramid. (b) Small top pyramid before removal of the Si_3N_4 mask, visible as the circular disc on the top of the pyramid.*

The addition of IPA causes a slight decrease in etch rate along the substrate normal down to about 0.75 µm/min. But it has a larger effect on other fast etching directions making the etch less agressive. The pyramid morphology is clearly seen in Figure 4.10b, just after formation of a small pyramid and before removal of the circular nitride mask. Close to the apex the bevelling planes are very smooth. We will show later in section 4.3 that the planes intersecting the nitride mask are {133} planes (tilt of 46.51°). Further away from the apex the pyramid looks almost square, with the {133} planes only visible at the edges of the square bottom. The sides of the square bottom are close to {111} planes, though each side might be resolved into two similarly oriented planes like {567} [49]. For pyramids with a short etch time (apex similar size as circular mask) the {133} planes are dominant and the pyramid looks octagonal. Our KOH-IPA results with {133} planes agree with previous work [32, 48, 49].

Another issue improved by the use of KOH-IPA is the slower undercutting and further narrowing of the octagonal apex. The lateral decrease of the apex in KOH-IPA occurs at a rate of about 0.35 µm/min, ten times slower than for KOH without IPA. Therefore a KOH-IPA etch offers a better control during formation of the sub-micrometer apex, as shown in Figure 4.11. The width of

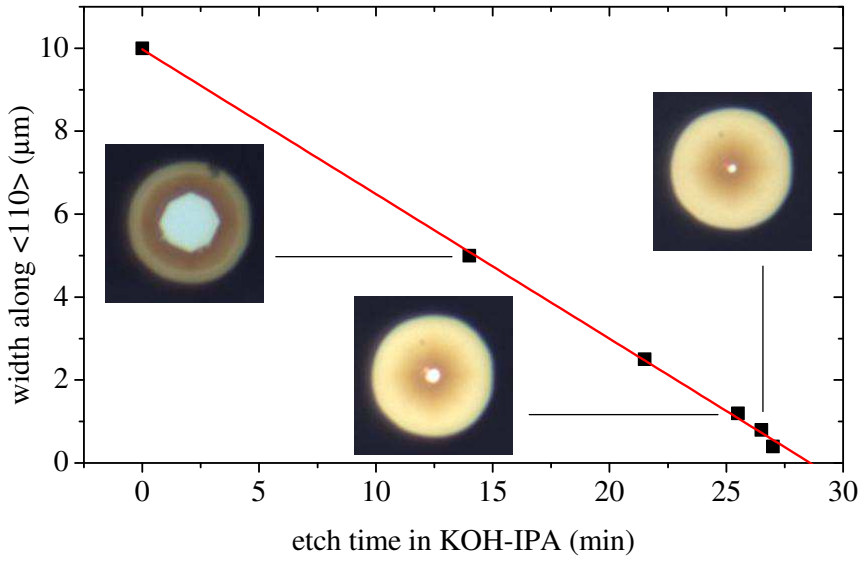

Figure 4.11. *Formation of the small top pyramid using KOH-IPA wet etch. The width of the apex along <110> decreases with a rate of 0.35 µm/min. The data point at 0 min corresponds to the edge of the nitride mask. The insets are optical images showing the Si_3N_4 mask as the 10 µm circular disc on the top of the pyramid and the octagonal shape of the apex visible through the transparent mask.*

the square base of the pyramid increases at a rate of 0.7 µm/min, consistent with the two rates mentioned above and the nearly {111} sidewalls.

4.2.2 Local oxidation of Silicon (LOCOS)

After structuring of the double pyramid the next step is the thermal oxidation in which the isolation oxide is formed everywhere except at the apex where the pyramid is in direct contact with the nitride cap. This step corresponds to a LOCOS process because the nitride layer acts as an oxidation mask. LOCOS has a general use in semiconductor industry [29]. For a review of LOCOS and related modern isolation techniques we refer the reader to Smeys [55].

A basic LOCOS pattern consists of a nitride layer acting as oxidation mask on top of a thin pad oxide that relieves the stress from the nitride layer, protecting the underlying silicon from mechanical damage. During thermal oxidation the free Si surface is oxidized up to a certain nominal oxide thickness,

whereas at the edges of the LOCOS pattern the oxide growth is limited by the nitride. The grown oxide gets thinner when going from the edge into the LOCOS pattern up to a certain effective distance L_{bb} beyond which there is no oxidation below the nitride layer. This encroachment of the oxide at the pattern edge is what is called the bird's beak, its geometry determines how effective is the local isolation technique. We use this oxide encroachment for definition of a rounded probe apex by making the octagonal apex in KOH etching narrow enough so that the bird's beaks on opposite edges barely touch, as shown in Figure 4.12. In this way we can obtain a diameter of about 1 µm at the apex.

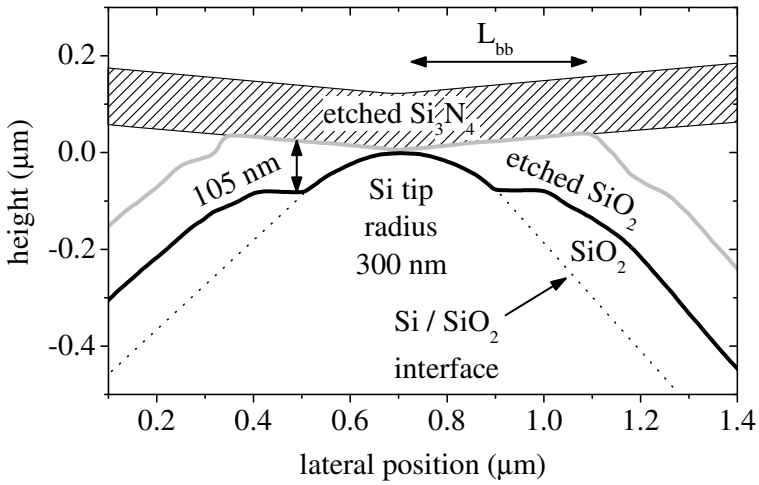

Figure 4.12. *AFM profiles of a SF-STM tip apex just after removal of the Si_3N_4 mask and thin SiO_2 pad (light-gray profile) and after further removal of 105 nm of SiO_2 to expose the sub-micrometer Si surface (thick black profile). Dotted lines represent the expected Si/SiO_2 interface on the oxidized walls of the pyramid. The removed Si_3N_4 cap is schematically shown by the dashed structure above the tip.*

The LOCOS profile near the edge of the pattern is sensitive to the properties of the pad oxide and nitride layers and to the oxidation process itself. The pad oxide is formed by dry oxidation and we have calibrated our oxidation process to achieve any desired oxide thickness according to the Deal-Grove model [56]. The thickness of the nitride layer is easily controlled by the fixed deposition rate of LPCVD Si_3N_4. The general behavior is that a thicker pad oxide allows more oxidant species to diffuse into the pattern leading to wider bird's beaks, whereas a thicker nitride resists more the bending caused by the

grown oxide leading to shorter bird's beaks. We present a detailed description of LOCOS profiles in section 4.3.

An important aspect of our LOCOS step is the use of dry oxidation, as opposed to wet oxidation in standard LOCOS. The choice of dry LOCOS is due to several reasons. We are interested in obtaining a clean Si surface on top of which to define good quality Si/Au Schottky interfaces. Nevertheless, wet oxidation has shown to form hard-to-remove oxynitrides at the Si/SiO_2 interface near the bird's beak edge, leading to the phenomenon of gate oxide thinning [30, 57]. Similar nitridation phenomena has also been observed through a too thin nitride [58, 59]. The oxynitride formation is related to the presence of water, so it is avoided by using dry LOCOS. It is shown in semiconductor technology that the use of dry oxidation decreases process complexity while reducing gate oxide thinning [60] and field oxide thinning [61] effects.

Now we discuss the thicknesses of the oxide and nitride layers. We fabricated LOCOS structures with pad oxide thickness within the range of 5–50 nm, consistent with most LOCOS literature. The nitride thickness was limited to the 100–200 nm range because of several considerations. When the nitride cap was much thinner than 100 nm it was not rigid enough to keep its circular shape after formation of the small pyramid, resulting in flexible films that bended towards the pyramid [53]. Besides, thin layers result on nitridation of the Si/SiO_2 interface as mentioned above. On the other hand, nitride layers thicker than 200 nm may create considerable damage to the underlying Si substrate due to stress [58, 60]. We will show later in chapter 5 that a 200 nm nitride used in the first process pathway is enough to prevent formation of oxynitride at the Si/SiO_2 interface, whereas in chapter 6 we will show that a 120 nm nitride can result in working structures when the extra RIE and sacrificial oxidation steps from the second process pathway are included.

The temperature of 1100 °C during dry LOCOS is also important. Such a high temperature helps to reduce stress-induced defects in the bird's beak area, due to the viscous flow of SiO_2 at high temperature [60]. A high oxidation temperature also reduces the length of the bird's beak (together with a thin pad oxide) [60, 62] which is convenient from the point of view of achieving a probe with a small radius of curvature.

We conclude this discussion on LOCOS by noting that the initial thickness of the nitride layer is not the same as the one present during the LOCOS step. For an initial thickness of 120 nm the measured thickness after LOCOS goes down to 80–85 nm. This is due to the oxidation of ca. 30 nm Si_3N_4 during

the thermal growth of 1 µm wet oxide [63] that is used as mask for the large pyramid, plus the later removal of this mask in BHF.

4.2.3 Cap removal and Si exposure

After LOCOS we proceed to remove the nitride cap and the underlying pad oxide in order to expose the Si at the apex. This Si surface will be later covered with the metal overlayer, marking the end of the fabrication of our SF-STM probes. Our fabrication process has a bifurcation into two pathways just after the LOCOS step, as shown in Figure 4.5. The process of cap removal is dependent on the pathway followed.

In the first process pathway the cap removal occurs relatively fast because the phosphoric acid etch can access the nitride cap from above, as shown in Figure 4.13a. Considering a nitride thickness of 120 nm this case corresponds to an etch time of about 40 min. The underlying oxide acts as an effective etch stop in phosphoric acid with a measured Si_3N_4/SiO_2 selectivity of S = 15–25. Exposure of the Si apex is then achieved by removal of the pad oxide and the bird's beaks in BHF. The resulting structure is that shown in the thick black profile of Figure 4.12. The isolation oxide is considerably reduced due to the required BHF etch. This affects the reliability of the semiconductor/metal diodes if the isolation is thinner in some locations. Indeed, we observed a reduced growth of thermal oxide at the foot of the pyramids by transmission electron microscopy (TEM) due to stress effects [64]. Besides, the Si/SiO_2 edge defining the area of the Si surface is too close to the apex. This proximity introduces the need of a good alignment between probe and sample in order to tunnel to the Si/metal apex of the probe instead of to the SiO_2/metal sides.

In the second process pathway the cap removal occurs in a different fashion. The phosphoric acid etchant cannot access the nitride cap from above due to the top sputtered oxide just after LOCOS. The sputtered oxide thickness used was 500 nm, followed by a short 30 min anneal at 1100 °C that improved its etch-resistant property up to the level of a thermally grown oxide. Therefore the cap removal must proceed from below and then laterally towards the center of the apex, as shown in Figure 4.13b. This increases the time for cap removal up to 4–6 h for a 1 µm wide apex. After cap removal, the exposure of the Si apex in BHF is also performed in a different fashion for the second process pathway. Now a longer BHF etch can remove all the LOCOS oxide below the projection of the former cap while retaining a thick isolation oxide anywhere

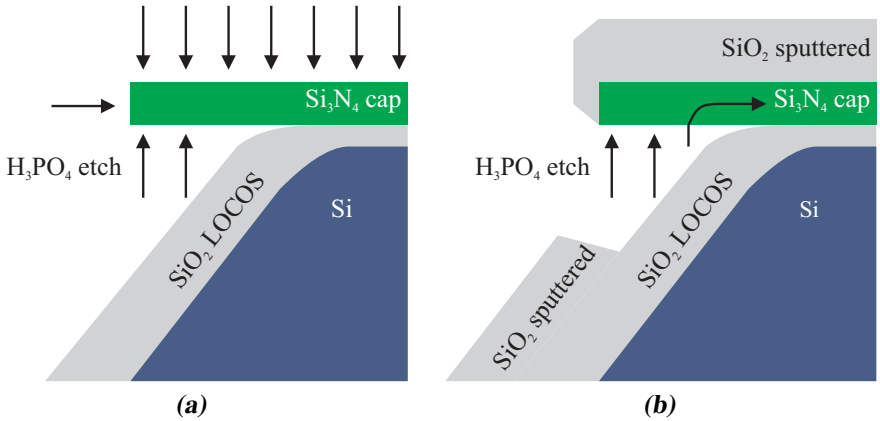

Figure 4.13. *Schematic of removal of the Si_3N_4 cap in hot H_3PO_4 solution for the two investigated process pathways (see Figure 4.5). (a) In the first process pathway, the cap is readily removed by the isotropic etch from the top until the underlying pad oxide is reached. (b) In the second process pathway, the sputtered SiO_2 prevents the etching of the cap from the top so the etch proceeds laterally towards the center of the apex.*

else, as shown in Figure 4.14. Besides, since there is no oxide right next to the apex (at least within 4 μm) the probe-sample alignment is less critical in order to tunnel into the Si/metal area. The size of the exposed Si area is determined by the size of the cap nitride and the geometry of the small pyramid.

Two other process steps were also introduced in the second pathway to ensure that the final surface at the apex consisted in clean Si and not other materials like silicon oxynitride as discussed in subsection 4.2.2. These are a short RIE step and growth of sacrificial oxide. RIE for less than 2 min is an effective step for removal of oxynitrides due to its selectivity for both Si_3N_4 and SiO_2 materials [59]. We observed similar etch rates in RIE for Si_3N_4 and SiO_2 with a 5–6 times slower etch rate for Si. Next we performed a standard wafer cleaning followed by thermal growth of a sacrificial 80 nm dry oxide. Sacrificial oxidation serves to regenerate the Si/SiO_2 interface [57, 58, 59] such that further oxide removal results in a good quality Si surface. The prevision of taking these extra steps will be confirmed by the results presented later in chapter 5.

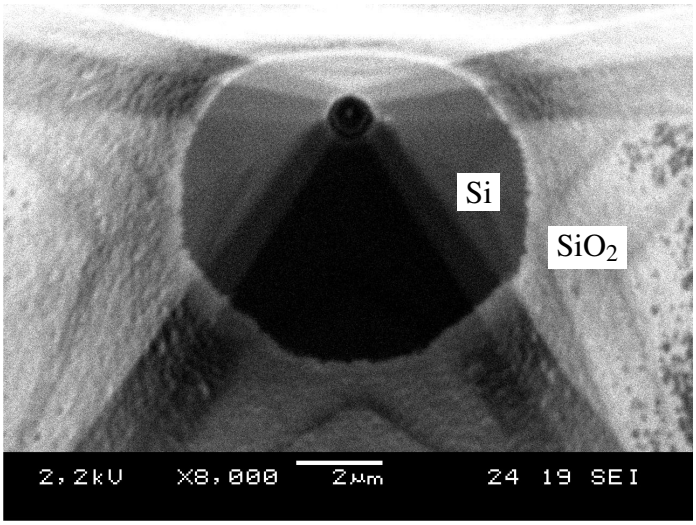

Figure 4.14. *SEM image of a SF-STM probe fabricated using the second process pathway shown in Figure 4.5, just after BHF removal of the SiO_2 (from LOCOS) masked by the Si_3N_4 cap. During previous sputtering of SiO_2 the cap acts as a shadow mask, its projection is visible as an 8 µm diameter Si/SiO_2 edge. The inner area of the circle shows the exposed Si surface of the top of the small pyramid where no SiO_2 is present at all. The rest of the probe is still fully covered with SiO_2.*

4.2.4 Related tip fabrication methods

Here we discuss previous relevant work for fabrication of silicon pyramids as scanning probes or field emitters. Besides anisotropic silicon etchants there are also diffusion controlled [65] isotropic etchants, the more common are mixtures of HF, HNO_3 and water (NWH) [66]. Previous work on fabrication of silicon field emission pyramids have combined both isotropic and anisotropic etchants for achieving high aspect ratio tips with a sharp apex. For example, Trujillo and Hunt [48] used KOH-IPA to fabricate field emission points with an apex of 200 nm radius of curvature, then a following NWH isotropic etch reduced the radius of curvature to 60 nm. They even performed a final low-temperature dry oxidation resulting in a radius of curvature < 5 nm. A similar approach to fabricate field emission devices used a two step etching with KOH (without IPA) and NWH [51]. These approaches point out the use of anisotropic etch to define the bulk structure of the pyramid with a large aspect ratio and sufficient height, whereas isotropic etching is later used for sharpening of the apex. Such a process is not applicable to our purpose of defining a small Schottky diode at

the top in a controlled manner, as the isotropic sharpening occurs after loss of the etch mask. A possibility for only using isotropic etch could be the approach of Bale and Palmer [28] where a small tip is fabricated on top of a large mesa, all done using photoresist masks and isotropic RIE. The latter approach is similar to our double pyramid structure and is indeed less reliable as it depends on the specific shape of thick photoresist patterns.

For definition of small Schottky diodes at the apex of a probe we refer to literature on fabrication of near-field scanning optical microscopy (NSOM) probes because they require such a structure. An approach for fabrication of NSOM probes using only isotropic etchants was presented by Davis et al. [67, 68]. They obtained pyramids with Schottky diodes about 2 µm wide and sub-micrometer regions without metal at the apex. These probes are not appropriate for our purposes because they are very low (5 µm height) and the apex is very sharp (< 50 nm). We found a better match to our requirements in the work of Chelly et al. [25] on fabrication of pyramid-shaped silicon photodetectors. They formed double pyramid structures by anisotropic wet etch and a sub-micrometer Schottky diode at its apex rounded using LOCOS. This approach partially suited our needs and is similar to our first process pathway. Still, we needed to introduce changes in the morphology of the pyramids to use them for STM. Furthermore, we had to deviate from their approach with the steps introduced in the second process pathway in order to meet the geometrical and electrical requirements for SF-STM probes.

4.3 Atomic force microscopy to monitor fabrication of probes

In the previous section we presented the fabrication process for SF-STM probes. The geometry of the probe is defined by the formation of the double pyramid structure by anisotropic etching of silicon and further LOCOS at the apex. In STM the most important aspect of a probe is its apex so a proper characterization of the LOCOS profile is necessary. We showed such a characterization in Figure 4.12 by AFM imaging after different fabrication steps. The result was a rounded apex with a sub-micrometer radius of curvature. To achieve that result it was necessary to first monitor the fabrication process in order to understand how the process steps and variation of process parameters influence the LOCOS profile. This AFM analysis of SF-STM probes is shown

in this section.

The topology of LOCOS at the apex of SF-STM probes is quite different than for planar structures. Before the LOCOS oxidation step planar structures have a flat silicon surface that continues beyond the nitride pattern, whereas in our structures the silicon surface is interrupted by bevelling planes. Our structures have a resemblance to the topology of fully recessed LOCOS which has profiles previously parameterized by Bassous [31]. In fully recessed LOCOS the Si surface outside of the nitride pattern is recessed by a thickness comparable to half of the LOCOS oxide thickness. On the other hand, our bevelling planes extend down the LOCOS pattern for several micrometers and can be considered as semi-infinite for practical purposes. Furthermore, previous characterization of fully recessed structures focus on wet LOCOS whereas we use dry LOCOS. To the best of our knowledge there is no previous experimental data characterizing dry LOCOS on structures like the SF-STM probes presented in this work.

Basic modelling gives insight on the effect of process parameters on LOCOS profiles [62] but getting accurate results from simulation is challenging. Part of the difficulty is due to stress effects on the oxidation process, as evidenced by pioneering work on two-dimensional oxidation [69, 70]. Later refinements [71, 72] allowed better numerical agreement with previous two-dimensional experimental data [31, 70]. Though modern implementation of simulators can give an account of advanced isolation techniques [73], even nowadays it is required to use analytical tools [74] with limited applicability as a fallback for simulating oxidation of three-dimensional sharp structures [75, 76]. Therefore we took an experimental approach as a guide in the fabrication of SF-STM probes.

The choice of AFM as a practical characterization tool for the apex of SF-STM probes is straightforward. AFM is superior than SEM for obtaining topographic information with nanometer resolution. Besides, three-dimensional sharp structures with cylindrical symmetry are not appropriate for TEM. Techniques like SEM or TEM only become useful for two-dimensional structures like line-shaped LOCOS patterns. We have studied LOCOS patterns aligned along <110> directions by TEM. Such patterns have {111} sidewalls and result in LOCOS profiles similar to those taken through the flat sides of the octagonal apex. AFM imaging results on topographic profiles that match the TEM observations (see Figure 4.15).

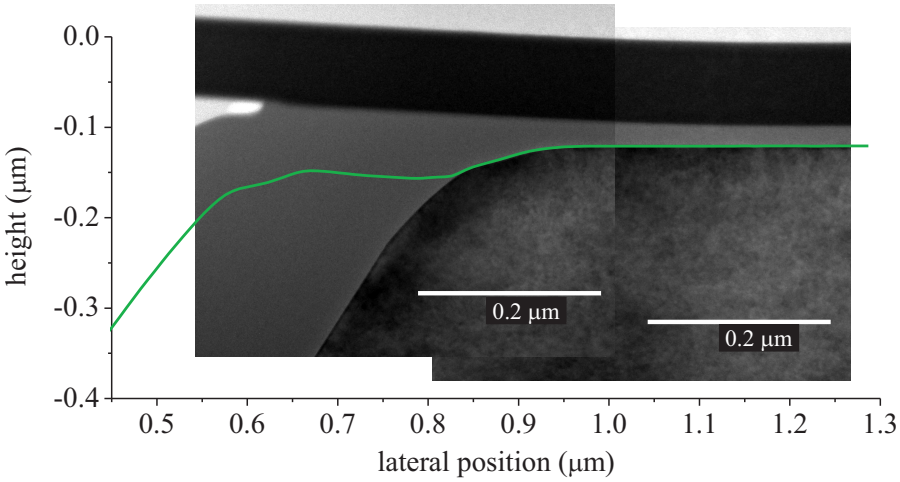

Figure 4.15. *TEM imaging at the edge of a line shaped LOCOS pattern after undergoing same processing as that for SF-STM probes and superimposed AFM topographic profile. The TEM image was taken after LOCOS. The AFM profile was taken after removal of the cap and enough oxide to expose the silicon apex.*

4.3.1 Topography of pyramidal apex

For obtaining topographical images of the SF-STM probes we use AFM. This approach is practical because the AFM probes consist of much sharper Si pyramids than the ones present in SF-STM probes leading to minimal convolution effects. Typical images of a SF-STM probe fabricated following the second process pathway are shown in Figure 4.16.

Just after removal of the nitride cap the apex still shows a clear octagonal shape limited by smooth and well defined bevelling planes, as shown in Figure 4.16a. The octagon has inner angles consistent with having its sides oriented along <130> directions (see Figure 4.7a). A full description of the bevelling planes is achieved by calculating the distribution of normal vectors to the AFM image and comparing it with low-index planes typically found in anisotropic etching of silicon. The result of this analysis is shown in Figure 4.17 which leads us to conclude that the probe apex is intersected by {133} planes, as mentioned previously in this chapter.

After oxide removal to expose the Si surface and the short RIE and sacrificial oxidation steps the resulting probe is shown in Figure 4.16b. At this stage this particular probe has a radius of curvature of 600 nm which is enough for high-resolution STM after coverage with the metal overlayer [19]. We can

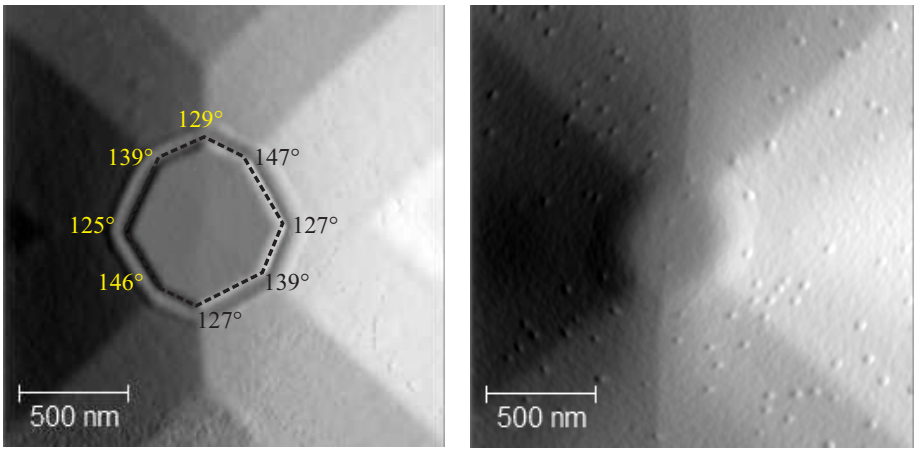

Figure 4.16. *AFM topographic images (horizontal gradient) of SF-STM probes fabricated using the second process pathway shown in Figure 4.5. The initial layer thicknesses were 50 nm pad oxide and 120 nm nitride. (a) Probe after cap removal in H_3PO_4. The octagonal apex is delineated by a dotted curve with the inner angles indicated. (b) Same probe after growth of a 80 nm dry SiO_2 for regeneration of the Si/SiO_2 interface. The resulting radius of curvature is 600 nm.*

compare this result with the radius of curvature of 300 nm for the probe shown in Figure 4.12. The main reasons for the larger radius of curvature is the use of a thicker pad oxide (50 nm versus 5 nm) and also possibly the RIE step.

4.3.2 Parameterization of LOCOS profile

We extract topographic profiles from AFM images of SF-STM structures to analyze the LOCOS topology. We used images from each structure under study at two distinct fabrication steps: after removal of the nitride cap and then after removal of some oxide just enough to expose the Si surface at the apex. The profiles corresponding to each step are plotted together, using the images to keep proper registry between both profiles. For this analysis the structures are fabricated following the first process pathway, i.e. without sputtering of oxide after LOCOS. This is done to keep at a minimum the etch time in phosphoric acid during the cap removal step, such that the amount of oxide removed during this step is ca. 10 nm outside of the apex (within the apex the amount of oxide removed is negligible). In this way the first profile represents the oxide

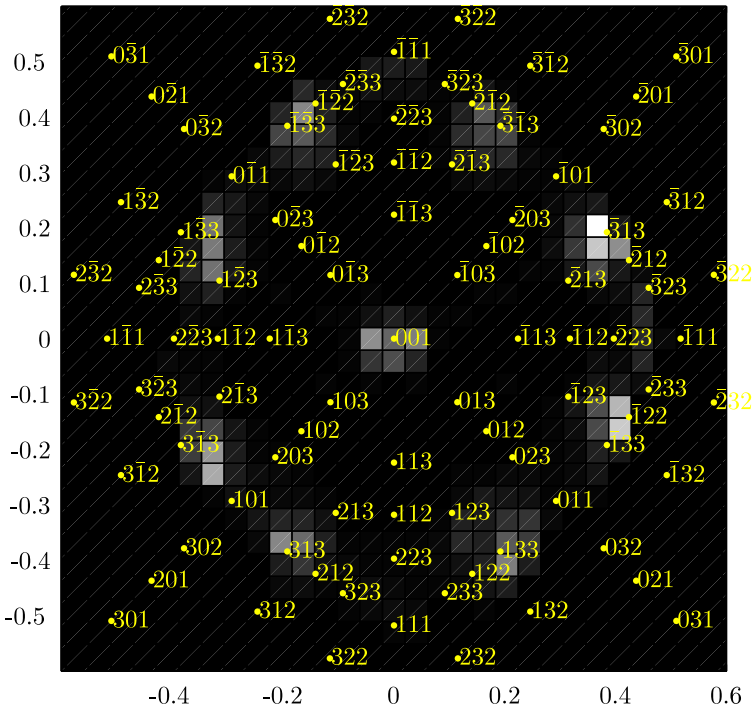

Figure 4.17. *Stereographic projection of the distribution of normal vectors to the topographic AFM image shown in Figure 4.16a. The directions [lmn] up to Miller index 3 are also shown. A best match is found for <133> directions.*

topology formed during LOCOS, whereas the second profile represents the underlying silicon. We remark that the information obtained this way is also relevant for probes fabricated with the second process pathway.

To allow the parameterization of each bird's beak the structures had their octagonal apex wider than for the case of forming a fully rounded apex. The definition of the parameters describing the LOCOS topology is schematically shown in Figure 4.18 superimposed to the AFM profiles after cap removal (black line) and after oxide removal (red line). We observe two kinds of bird's beaks depending on the initial thickness of the pad oxide (t_{pad}). For pad oxides above certain thickness $t_{pad} > 20\,\text{nm}$ the profiles appear as expected. From the profile after cap removal we obtain the bird's beak height H_{bb} (measured from the Si/SiO_2 interface) and the bird's beak length L_{bb} (measured from the beak top up to the beak edge, i.e. reaching the height of the pad oxide within 0.5 nm). Since we know the thickness t_{ox} of the LOCOS oxide we can locate

the underlying Si/SiO_2 at the sidewall and from there estimate the position of the former Si corner of the apex (before LOCOS). The distance from this Si corner to the beak edge is named L_{corner}.

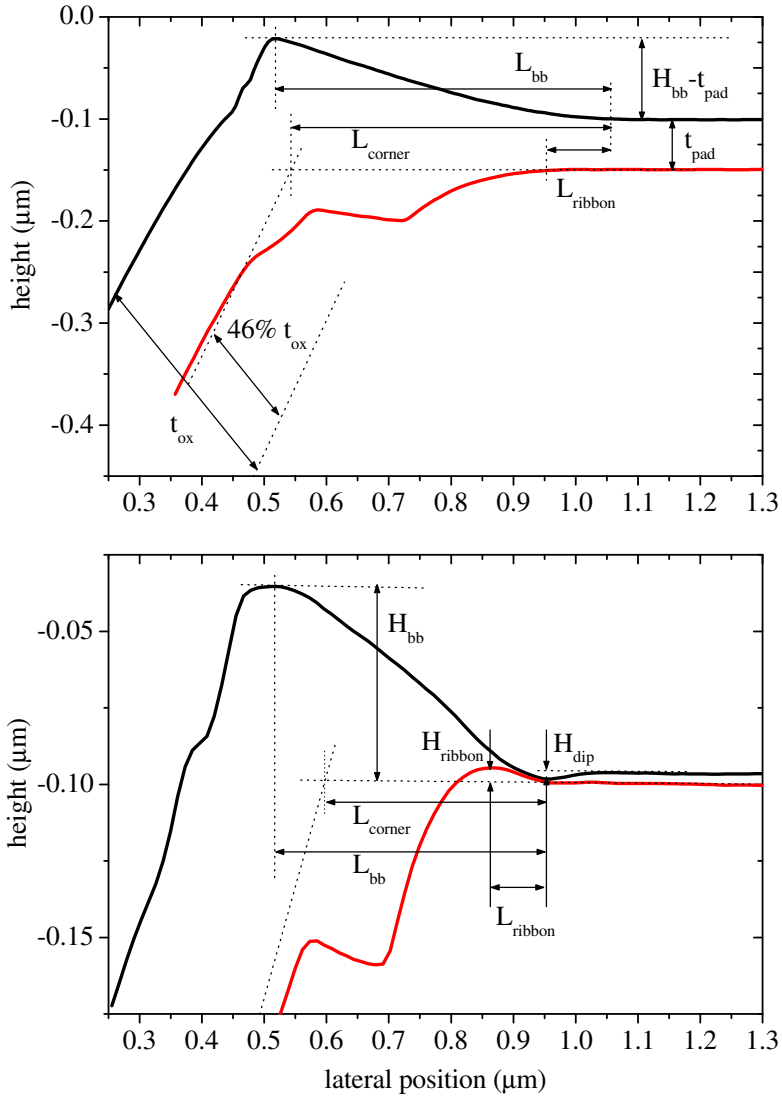

Figure 4.18. *Definition of parameters for analysis of LOCOS at the apex of pyramidal structures (see text). Top: expected profile when a sufficiently thick pad oxide is used (t_{pad} = 50 nm). Bottom: anomalous profile for too thin pad oxide (t_{pad} = 10 nm).*

The profile after oxide removal reveals the flat silicon surface at the center

of the apex and the downturn located near the beak edge. It is significant that the downturn does not occur exactly at the beak edge as would be expected. We name L_{ribbon} this difference in the position of the beak edge when located by the upturn in oxide versus when it is located by the downturn in the silicon, because it seems there is a ribbon around the apex where the two do not coincide. In principle L_{ribbon} could be an artifact due to a blunt AFM tip. Our images demonstrate sharp AFM tips and L_{ribbon} proved to be rather consistent for many different AFM tips and SF-STM probes. Such an observable difference is visible in Figure 4.15 and is indeed apparent in other TEM images of LOCOS structures with receded and vertical sidewalls [77]. Therefore we consider that L_{ribbon} is not an imaging artifact.

In Figure 4.18 a different kind of bird's beak is seen when the pad oxide is thinner. For $t_{pad} < 20$ nm an anomalous feature is present at the beak edge. In the profile just after cap removal there is now a dip with a depth H_{dip} relative to the pad oxide surface. We redefine L_{bb} to cover up to this dip for this kind of beak. Furthermore, in the profile after oxide removal there is an elevation of height H_{ribbon} at the place where we expected to see a downturn. This anomalous elevation is above the level of the silicon surface. It should have been composed by oxide and therefore removed. A region within the pad oxide that is hard to remove in BHF may indicate formation of silicon oxynitride, as seen at the beak edge in wet LOCOS [30, 57]. Since we use dry LOCOS we do not expect this to be the case [60]. The anomalous feature may also be a defect due to stress. Large tensile stress at the bird's beak edge due to bending of the nitride mask has been observed by micro-Raman spectroscopy [78, 79] and x-ray diffraction imaging [80] which can generate defects or even break the pad oxide there. This tensile stress may be related to the anomalous profile.

The defined parameters were measured for several pad oxide thicknesses. A set of relevant parameters is presented in Figure 4.19. We include data for two different profile directions: profiles taken through the flat edges of the octagonal apex (filled symbols) and profiles taken through the corners of the octagon (open symbols). For thicker pad oxides the height and length of the bird's beak increase whereas the anomalous parameters reduce to zero. Also the bird's beaks are wider and higher at the corners of the octagon, consistent with an increased oxidant concentration at the corners [75].

We can now use the parameter values to find an optimum phase space for fabrication of SF-STM probes. For this we follow the design guidelines discussed in the previous section. Namely, we want to have the opposite

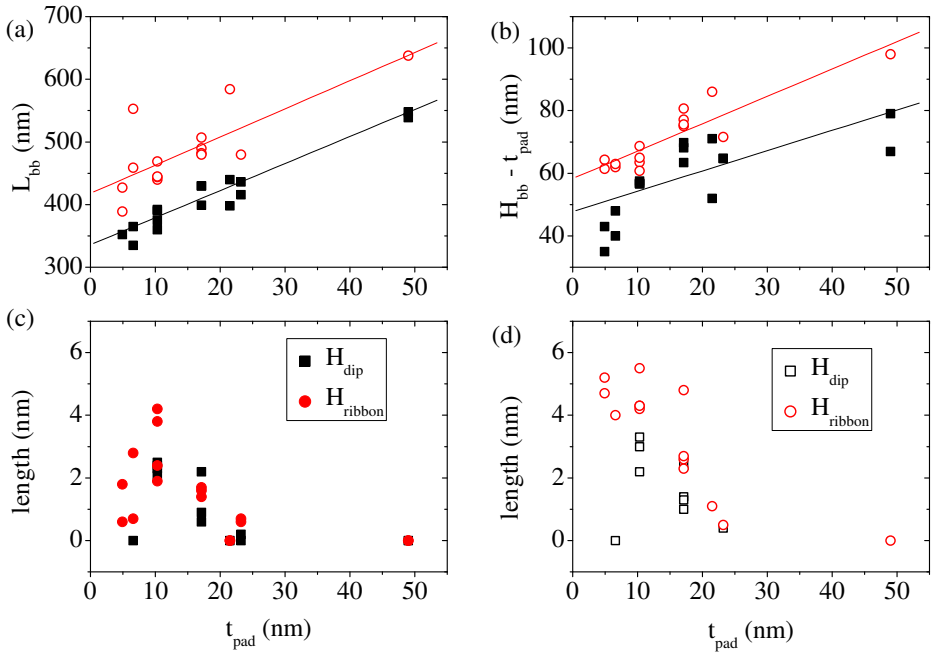

Figure 4.19. *Measured values of parameters for analysis of LOCOS at the apex of pyramidal structures, as defined in Figure 4.18. In (a) and (b) are shown the length and height of the bird's beak, respectively. In (c) and (d) are shown the anomalous features observed for thin pad oxides. Filled symbols are for AFM profiles taken through the flat sides of the octagonal apex, open symbols for profiles taken through the corners. For all cases a Si_3N_4 cap of 120 nm was initially grown and the LOCOS was carried out at 1100 °C up to a 300 nm dry oxide thickness.*

edges of the bird's beak slightly merging in order to achieve a rounded apex. Considering the width of the Si apex during formation of the small pyramid then we need to achieve a width equal to $2 \times (L_{corner} - L_{ribbon})$. This design guideline is shown in Figure 4.20.

The analysis is also useful for design of the pad oxide thickness when the second process pathway is used to fabricate SF-STM probes. Due to the lateral etch process (see Figure 4.13b) a long etch time in H_3PO_4 is needed to fully remove the cap. If the pad oxide is too thin this may lead to complete removal of the pad oxide and further attack of the underlying silicon. Therefore, there is a minimum required pad thickness to withstand the cap removal. Since the cap removal takes place with an ideal width of the apex *after* LOCOS of $2 \times (L_{bb} - L_{ribbon})$ the rule of thumb is that this width must be narrower than a

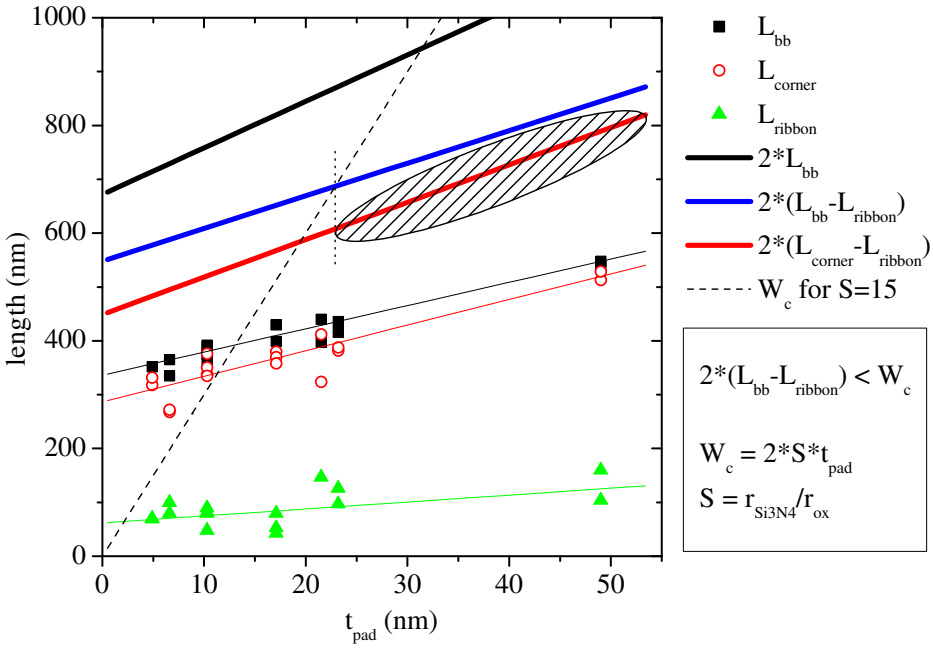

Figure 4.20. *Analysis of LOCOS at the apex of pyramidal structures for fabrication of rounded SF-STM probes, as suggested by the parameters extracted from AFM profiles taken through the flat sides of the octagonal apex. A rounded probe is obtained when the bird's beaks merge. Furthermore, using the second process pathway the cap is etched from the sides (see Figure 4.13) which imposes a maximum width W_c of the apex in order to prevent etching the underlying Si surface in H_3PO_4.*

critical length W_c that depends on pad oxide thickness and etch selectivity (S). As shown in Figure 4.20, for a typical value $S = 15$ the condition is met only for $t_{pad} > 24$ nm. The result is that during formation of the small pyramid in KOH etch (see Figure 4.11) one should aim for an apex width defined by the hatched region in Figure 4.20. So for a pad oxide of 50 nm we need to form a small pyramid with an 800 nm wide apex.

Formation of a probe too far away from this ideal phase space invariably results in attack of the silicon during the cap removal step, as shown for a 3 µm probe fabricated following the second process pathway in Figure 4.21. The sloped apex is a result of the etch rates in phosphoric acid ($Si_3N_4 \approx 3$ nm/min, $SiO_2 = 0.18$ nm/min) and similar etch rates for Si and SiO_2 [33].

Finally, we may also consider the case of making the apex too narrow. A too narrow apex results in oxide punch-through [81] which means that the

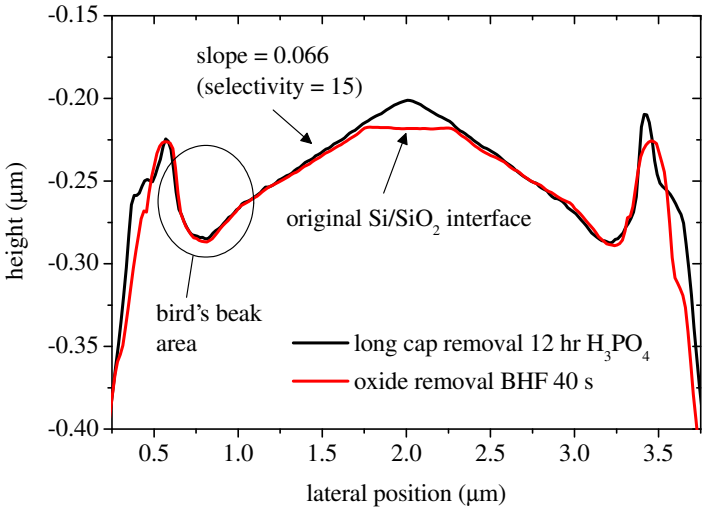

Figure 4.21. *AFM profiles for a SF-STM probe fabricated using the second process pathway, showing the effect of applying a too long H_3PO_4 etch for cap removal due to a wide 3 µm apex. After 12 h etch in the apex becomes slanted. The slope is equal to the inverse of the Si_3N_4/SiO_2 selectivity, assuming similar etch rates for Si and SiO_2. After SiO_2 removal the center area still exposes the underlying Si/SiO_2 interface. The continuity of the slope in the previous profile confirms the assumption.*

beaks merge too much. This increases the oxide thickness below the nitride cap considerably and may cause the apex to loose its curvature. Besides, when the first process pathway is used the need to remove much more oxide to expose the silicon leads to a reduced isolation oxide or even to its total loss. Ultimately, a too narrow apex is mechanically fragile and does not withstand the fabrication process.

4.4 Conclusions

We have presented the design and fabrication of multi-terminal semiconductor/ferromagnet probes for the realization of a new STM-based technique (SF-STM) to study spin polarization of magnetic surfaces near the Fermi level. The technique is based on spin-polarized tunneling from a magnetic sample and spin analysis after tunneling within the SF-STM probe.

The design of SF-STM probes deals with the central subject of analysis of spin polarization via the magnetocurrent MC or relative change in the collected

ballistic signal I_C in the semiconductor for parallel and antiparallel magnetic alignment between sample and probe. The relationship between MC and spin polarization is dependent on the thickness of the spin filter in the probe. A thicker spin filter layer results in larger MC at the expense of a decreased absolute signal. Therefore we have analyzed the ballistic transmission properties of the probes for several common spin-filtering materials used in solid-state devices. The more stringent operation conditions for STM as compared to solid-state devices lead us to design the probe with an optimum spin filter that balances the magnitude of absolute and relative signals, while discussing the quantitative relationship to sample spin polarization. We also discussed STM specific considerations like operation energy, different transmission properties, geometry of the spin analyzer and noise. The result is a design capable of quantitative spin analysis with STM spatial resolution within a range of 5–90 % sample spin polarization using robust materials with well known electronic properties.

Furthermore we developed a fabrication process for SF-STM probes in a highly parallel fashion using standard microfabrication facilities. The probes are fabricated in the form of silicon double pyramids terminated with (sub-) micrometer Schottky diodes serving as the active elements for tunneling and spin filtering. The double pyramid structure is formed by anisotropic wet etching of silicon in a process optimized for the fabrication of probes with a large aspect ratio and good control of the apex dimension. A 1 µm radius of curvature is readily achieved by a special local oxidation of silicon process occurring just at the apex of the probe. This process also allows the definition of the (sub-)micrometer Schottky diode area in a controllable manner. Our fabrication process is flexible with alternative pathways developed for specific probe requirements. Through careful analysis of each fabrication step we obtain reproducible and well characterized probes with geometrical properties apt for the realization of SF-STM. In the following chapters we will study the electrical properties of the probes.

Control of the apex morphology required the initial study of local oxidation of silicon on unconventional three-dimensional sharp structures. For this purpose we performed a detailed study of the apex profile during the different fabrication process steps using atomic force microscopy (AFM). Monitoring the fabrication process with AFM offered a practical access to study the apex-rounding process. A parameterization of the local oxidation topology allowed the finding of optimum fabrication parameters, identification of issues and

finally led us to the establishment of clear rules to achieve the desired probe morphology. The fabrication presented in this chapter shows the way for the following inclusion of these probes in STM experiments.

References

[1] O. M. J. van 't Erve, R. Vlutters, P. S. A. Kumar, S. D. Kim, F. M. Postma, R. Jansen, and J. C. Lodder. "Transfer ratio of the spin-valve transistor". *Applied Physics Letters* **80** (20), 3787–3789 (2002). [Cited on 71, 73]

[2] S. van Dijken, X. Jiang, and S. S. P. Parkin. "Comparison of magnetocurrent and transfer ratio in magnetic tunnel transistors with spin-valve bases containing Cu and Au spacer layers". *Applied Physics Letters* **82** (5), 775–777 (2003). [Cited on 71]

[3] S. van Dijken, X. Jiang, and S. S. P. Parkin. "The influence of nonmagnetic seed layers on the magnetotransport properties of magnetic tunnel transistors with a silicon collector". *Journal of Applied Physics* **97** (4), 043712–8 (2005). [Cited on 71]

[4] W. H. Rippard, A. C. Perrella, and R. A. Buhrman. "Ballistic current transport studies of ferromagnetic multilayer films and tunnel junctions (invited)". *Journal of Applied Physics* **89**, 6642–6646 (2001). [Cited on 71]

[5] W. H. Rippard and R. A. Buhrman. "Spin-Dependent Hot Electron Transport in Co/Cu Thin Films". *Physical Review Letters* **84** (5), 971–974 (2000). [Cited on 71]

[6] A. Kaidatzis, S. Rohart, A. Thiaville, and J. Miltat. "Hot electron transport and a quantitative study of ballistic electron magnetic imaging on Co/Cu multilayers". *Physical Review B (Condensed Matter and Materials Physics)* **78** (17), 174426–10 (2008). [Cited on 71]

[7] R. Jansen, T. Banerjee, B. G. Park, and J. C. Lodder. "Probing momentum distributions in magnetic tunnel junctions via hot-electron decay". *Applied Physics Letters* **90** (19), 192503–3 (2007). [Cited on 71, 72]

[8] B. G. Park, T. Banerjee, J. C. Lodder, and R. Jansen. "Tunnel Spin Polarization Versus Energy for Clean and Doped Al_2O_3 Barriers". *Physical Review Letters* **99** (21), 217206–4 (2007). [Cited on 71]

[9] S. van Dijken, X. Jiang, and S. S. P. Parkin. "Spin-dependent hot electron transport in Ni81Fe19 and Co84Fe16 films on GaAs(001)". *Physical Review B* **66** (9), 094417 (2002). [Cited on 71]

[10] R. Vlutters, O. M. J. van 't Erve, S. D. Kim, R. Jansen, and J. C. Lodder. "Interface, Volume, and Thermal Attenuation of Hot-Electron Spins in Ni80Fe20 and Co". *Physical Review Letters* **88** (2), 027202 (2001). [Cited on 71]

[11] T. Banerjee, J. C. Lodder, and R. Jansen. "Origin of the spin-asymmetry of hot-electron transmission in Fe". *Physical Review B (Condensed Matter and Materials Physics)* **76** (14), 140407–4 (2007). [Cited on 71]

[12] L. D. Bell. "Evidence of Momentum Conservation at a Nonepitaxial Metal/Semiconductor Interface Using Ballistic Electron Emission Microscopy". *Physical Review Letters* **77** (18), 3893 (1996). [Cited on 71]

[13] M. K. Weilmeier, W. H. Rippard, and R. A. Buhrman. "Ballistic electron transport through Au(111)/Si(111) and Au(111)/Si(100) interfaces". *Physical Review B* **59** (4), R2521 (1999). [Cited on 71]

[14] J. J. Garramone, J. R. Abel, I. L. Sitnitsky, L. Zhao, I. Appelbaum, and V. P. LaBella. "Electron Transport Metrology: Ballistic Electron Emission Microscopy Studies of Hot Electron Scattering in Copper". In "2009 International Conference on Frontiers of Characterization and Metrology for Nanoelectronics", (Albany, New York, 2009). [Cited on 71]

[15] E. ul Haq. *Nanoscale spin-dependent transport of electrons and holes in Si-ferromagnet structures*. PhD thesis, University of Twente (2005). ISBN 90-365-2241-2. [Cited on 71, 75]

[16] R. Vlutters, O. M. J. van 't Erve, R. Jansen, S. D. Kim, J. C. Lodder, A. Vedyayev, and B. Dieny. "Modeling of spin-dependent hot-electron transport in the spin-valve transistor". *Physical Review B* **65** (2), 024416 (2001). [Cited on 72]

[17] D. J. Monsma, R. Vlutters, and J. C. Lodder. "Room Temperature-Operating Spin-Valve Transistors Formed by Vacuum Bonding". *Science* **281** (5375), 407–409 (1998). [Cited on 73]

[18] S. van Dijken, X. Jiang, and S. S. P. Parkin. "Giant magnetocurrent exceeding 3400% in magnetic tunnel transistors with spin-valve base layers". *Applied Physics Letters* **83** (5), 951–953 (2003). [Cited on 74]

[19] M. Bode. "Spin-polarized scanning tunnelling microscopy". *Reports on Progress in Physics* **66** (4), 523 (2003). [Cited on 74, 97]

[20] A. Kubetzka, M. Bode, O. Pietzsch, and R. Wiesendanger. "Spin-Polarized Scanning Tunneling Microscopy with Antiferromagnetic Probe Tips". *Physical Review Letters* **88** (5), 057201 (2002). [Cited on 75]

[21] M. Prietsch. "Ballistic-electron emission microscopy (BEEM): studies of metal/semiconductor interfaces with nanometer resolution". *Physics Reports* **253** (4), 163–233 (1995). [Cited on 75, 76]

[22] S. M. Sze and K. K. Ng. *Physics of semiconductor devices* (John Wiley and Sons, 2007), 3rd edn. ISBN 978-0-471-14323-9. [Cited on 75]

[23] B. G. Park, T. Banerjee, B. C. Min, J. G. M. Sanderink, J. C. Lodder, and R. Jansen. "Temperature dependence of magnetocurrent in a magnetic tunnel transistor". *Journal of Applied Physics* **98** (10), 103701–4 (2005). [Cited on 75]

[24] I. J. Vera-Marún and R. Jansen. "Multiterminal semiconductor/ferromagnet probes for spin-filter scanning tunneling microscopy". *Journal of Applied Physics* **105**, 07D520–3 (2009). [Cited on 76]

[25] R. Chelly, Y. Cohen, A. Sa'ar, and J. Shappir. "Pyramid-shaped silicon photodetector with subwavelength aperture [for NSOM]". *Electron Devices, IEEE Transactions on* **49** (6), 986–990 (2002). [Cited on 76, 95]

[26] S. Isomae, Y. Tamaki, A. Yajima, M. Nanba, and M. Maki. "Dislocation Generation at Si_3N_4 Film Edges on Silicon Substrates and Viscoelastic Behavior of SiO_2 Films". *Journal of The Electrochemical Society* **126** (6), 1014–1019 (1979). [Cited on 76]

[27] Y. Backlund and L. Rosengren. "New shapes in (100) Si using KOH and EDP etches". *Journal of Micromechanics and Microengineering* **2** (2), 75 (1992). [Cited on 77, 84]

[28] M. Bale and R. E. Palmer. "Microfabrication of silicon tip structures for multiple-probe scanning tunneling microscopy". *Journal of Vacuum Science & Technology B: Microelectronics and Nanometer Structures* **20** (1), 364–369 (2002). [Cited on 77, 95]

[29] J. A. Appels, E. Kooi, M. M. Paffen, J. J. H. Schatorjé, and W. H. C. G. Verkuylen. "Local oxidation of silicon and its application in semiconductor-device technology". *Philips Research Reports* **25** (2), 118–132 (1970). [Cited on 77, 89]

[30] E. Kooi, J. G. van Lierop, and J. A. Appels. "Formation of Silicon Nitride at a Si-SiO_2 Interface during Local Oxidation of Silicon and during Heat-Treatment of Oxidized Silicon in NH_3 Gas". *Journal of The Electrochemical Society* **123** (7), 1117–1120 (1976). [Cited on 77, 91, 101]

[31] E. Bassous, H. N. Yu, and V. Maniscalco. "Topology of Silicon Structures with Recessed SiO_2". *Journal of The Electrochemical Society* **123** (11), 1729–1737 (1976). [Cited on 77, 96]

[32] K. Bean. "Anisotropic etching of silicon". *Electron Devices, IEEE Transactions on* **25** (10), 1185–1193 (1978). [Cited on 80, 81, 83, 88]

[33] K. Williams, K. Gupta, and M. Wasilik. "Etch rates for micromachining processing-Part II". *Microelectromechanical Systems, Journal of* **12** (6), 761–778 (2003). [Cited on 81, 103]

[34] R. M. Finne and D. L. Klein. "A Water-Amine-Complexing Agent System for Etching Silicon". *Journal of The Electrochemical Society* **114** (9), 965–970 (1967). [Cited on 81]

[35] S. A. Campbell, K. Cooper, L. Dixon, R. Earwaker, S. N. Port, and D. J. Schiffrin. "Inhibition of pyramid formation in the etching of Si p(100) in aqueous potassium hydroxide-isopropanol". *Journal of Micromechanics and Microengineering* **5** (3), 209 (1995). [Cited on 81, 82]

[36] M. Shikida, K. Sato, K. Tokoro, and D. Uchikawa. "Differences in anisotropic etching properties of KOH and TMAH solutions". *Sensors and Actuators A: Physical* **80** (2), 179–188 (2000). [Cited on 81]

[37] S. Chang and D. B. Hicks. "The formation of microbridges on (100)-oriented silicon". *Journal of Micromechanics and Microengineering* **1** (1), 25 (1991). [Cited on 82]

[38] I. Zubel and M. Kramkowska. "Etch rates and morphology of silicon (h k l) surfaces etched in KOH and KOH saturated with isopropanol solutions". *Sensors and Actuators A: Physical* **115** (2-3), 549–556 (2004). [Cited on 82]

[39] H. Seidel, L. Csepregi, A. Heuberger, and H. Baumgartel. "Anisotropic Etching of Crystalline Silicon in Alkaline Solutions I. Orientation Dependence and Behavior of Passivation Layers". *Journal of The Electrochemical Society* **137** (11), 3612–3626 (1990). [Cited on 82]

[40] H. Seidel, L. Csepregi, A. Heuberger, and H. Baumgartel. "Anisotropic Etching of Crystalline Silicon in Alkaline Solutions II. Influence of Dopants". *Journal of The Electrochemical Society* **137** (11), 3626–3632 (1990). [Cited on 82]

[41] P. Allongue, V. Costa-Kieling, and H. Gerischer. "Etching of Silicon in NaOH Solutions I. In Situ Scanning Tunneling Microscopic Investigation of n-Si(111)". *Journal of The Electrochemical Society* **140** (4), 1009 (1993). [Cited on 82]

[42] P. Allongue, V. Costa-Kieling, and H. Gerischer. "Etching of Silicon in NaOH Solutions II. Electrochemical Studies of n-Si(111) and (100) and Mechanism of the Dissolution". *Journal of The Electrochemical Society* **140** (4), 1018 (1993). [Cited on 82]

[43] H. Schroder, E. Obermeier, A. Horn, and G. Wachutka. "Convex corner undercutting of 100 silicon in anisotropic KOH etching: the new step-flow model of 3-D structuring and first simulation results". *Microelectromechanical Systems, Journal of* **10** (1), 88–97 (2001). [Cited on 82]

[44] E. van Veenendaal, A. J. Nijdam, J. van Suchtelen, K. Sato, J. G. E. Gardeniers, W. J. P. van Enckevort, and M. Elwenspoek. "Simulation of anisotropic wet chemical etching using a physical model". *Sensors and Actuators A: Physical* **84** (3), 324–329 (2000). [Cited on 82]

[45] X. Wu and W. H. Ko. "Compensating corner undercutting in anisotropic etching of (100) silicon". *Sensors and Actuators* **18** (2), 207–215 (1989). [Cited on 83]

[46] B. Puers and W. Sansen. "Compensation structures for convex corner micromachining in silicon". *Sensors and Actuators A: Physical* **23** (1-3), 1036–1041 (1990). [Cited on 84]

[47] H. L. Offereins, K. Kühl, and H. Sandmaier. "Methods for the fabrication of convex corners in anisotropic etching of (100) silicon in aqueous KOH". *Sensors and Actuators A: Physical* **25** (1-3), 9–13 (1990). [Cited on 84]

[48] J. T. Trujillo and C. E. Hunt. "Fabrication of silicon field emission points for vacuum microelectronics by wet chemical etching". *Semiconductor Science and Technology* **6** (3), 223 (1991). [Cited on 84, 88, 94]

[49] S. Tan, M. Reed, H. Han, and R. Boudreau. "Morphology of etch hillock defects created during anisotropic etching of silicon". *Journal of Micromechanics and Microengineering* **4** (3), 147 (1994). [Cited on 84, 88]

[50] E. Tran, E. S. Kim, and S. Y. Lee. "Fabrication of mesas and octagonal cones in silicon by wet chemical etching". *Journal of Micromechanics and Microengineering* **5** (3), 251 (1995). [Cited on 84]

[51] I. J. Chung, D. B. Murfett, A. Hariz, and M. R. Haskard. "Fabrication of high aspect ratio silicon micro-tips for field emission devices". *Journal of Materials Science* **32** (18), 4999–5003 (1997). [Cited on 84, 86, 94]

[52] N. Wilke, M. L. Reed, and A. Morrissey. "The evolution from convex corner undercut towards microneedle formation: theory and experimental verification". *Journal of Micromechanics and Microengineering* **16** (4), 808 (2006). [Cited on 84, 86, 87]

[53] W. W. Koelmans. *Multi-terminal tips for spin-polarized scanning tunneling microscopy*. Master thesis, University of Twente (2006). [Cited on 86, 91]

[54] M. Chahoud. "Etching simulation of negative sloped planes at convex mask corners in Si". *Sensors and Actuators A: Physical* **117** (2), 356–363 (2005). [Cited on 86]

[55] P. Smeys. *Local Oxidation Of Silicon for Isolation*. PhD thesis, Stanford University (1996). [Cited on 89]

[56] B. E. Deal and A. S. Grove. "General Relationship for the Thermal Oxidation of Silicon". *Journal of Applied Physics* **36** (12), 3770–3778 (1965). [Cited on 90]

[57] T. A. Shankoff, T. T. Sheng, S. E. Haszko, R. B. Marcus, and T. E. Smith. "Bird's Beak Configuration and Elimination of Gate Oxide Thinning Produced during Selective Oxidation". *Journal of The Electrochemical Society* **127** (1), 216–222 (1980). [Cited on 91, 93, 101]

[58] O. Nakajima, N. Shiono, S. Hashimoto, and C. Hashimoto. "Defects in a Gate Oxide Grown after the LOCOS Process". *Japanese Journal of Applied Physics* **18**, 943–951 (1979). [Cited on 91, 93]

[59] M. Itsumi and F. Kiyosumi. "Identification and Elimination of Gate Oxide Defect Origin Produced during Selective Field Oxidation". *Journal of The Electrochemical Society* **129** (4), 800 (1982). [Cited on 91, 93]

[60] P. Bellutti, M. Boscardin, G. Soncini, M. Zen, and N. Zorzi. "DW-LOCOS: a convenient VLSI isolation technique". *Semiconductor Science and Technology* **10** (12), 1700 (1995). [Cited on 91, 101]

[61] P. Bellutti and M. Zen. "Oxide Growth Effects in Micron and Submicron Field Regions". *Journal of The Electrochemical Society* **143** (9), 2953–2957 (1996). [Cited on 91]

[62] T. C. Wu, W. T. Stacy, and K. N. Ritz. "The Influence of the LOCOS Processing Parameters on the Shape of the Bird's Beak Structure". *Journal of The Electrochemical Society* **130** (7), 1563–1566 (1983). [Cited on 91, 96]

[63] T. Enomoto, R. Ando, H. Morita, and H. Nakayama. "Thermal Oxidation Rate of a Si3N4 Film and Its Masking Effect against Oxidation of Silicon". *Japanese Journal of Applied Physics* **17**, 1049–1058 (1978). [Cited on 92]

[64] P. Sutardja, Y. Shacham-Diamand, and W. Oldham. "Simulation of stress effects on reaction kinetics and oxidant diffusion in silicon oxidation". In "Electron Devices Meeting, 1986 International", vol. 32, pp. 526–529 (1986). [Cited on 92]

[65] V. B. Svetovoy, J. W. Berenschot, and M. C. Elwenspoek. "Precise Test of the Diffusion-Controlled Wet Isotropic Etching of Silicon via Circular Mask Openings". *Journal of The Electrochemical Society* **153** (9), C641–C647 (2006). [Cited on 94]

[66] B. Schwartz and H. Robbins. "Chemical Etching of Silicon III. A Temperature Study in the Acid System". *Journal of The Electrochemical Society* **108** (4), 365–372 (1961). [Cited on 94]

[67] R. C. Davis, C. C. Williams, and P. Neuzil. "Micromachined submicrometer photodiode for scanning probe microscopy". *Applied Physics Letters* **66** (18), 2309–2311 (1995). [Cited on 95]

[68] R. C. Davis, C. C. Williams, and P. Neuzil. "Optical intensity mapping on the nanometer scale by near-field photodetection optical microscopy". *Optics Letters* **21** (7), 447–449 (1996). [Cited on 95]

[69] D. Kao, J. McVittie, W. Nix, and K. Saraswat. "Two-dimensional thermal oxidation of silicon—I. Experiments". *Electron Devices, IEEE Transactions on* **34** (5), 1008–1017 (1987). [Cited on 96]

[70] D. Kao, J. McVittie, W. Nix, and K. Saraswat. "Two-dimensional thermal oxidation of silicon. II. Modeling stress effects in wet oxides". *Electron Devices, IEEE Transactions on* **35** (1), 25–37 (1988). [Cited on 96]

[71] P. Sutardja and W. Oldham. "Modeling of stress effects in silicon oxidation". *Electron Devices, IEEE Transactions on* **36** (11), 2415–2421 (1989). [Cited on 96]

[72] P. Griffin and C. Rafferty. "A viscous nitride model for nitride/oxide isolation structures". In "Electron Devices Meeting, 1990. IEDM '90. Technical Digest., International", pp. 741–744 (1990). ISBN 0163-1918. [Cited on 96]

[73] V. Senez, D. Collard, P. Ferreira, and B. Baccus. "Two-dimensional simulation of local oxidation of silicon: calibrated viscoelastic flow analysis". *Electron Devices, IEEE Transactions on* **43** (5), 720–731 (1996). [Cited on 96]

[74] N. Guillemot, G. Pananakakis, and P. Chenevier. "A new analytical model of the "Bird's beak"". *Electron Devices, IEEE Transactions on* **34** (5), 1033–1038 (1987). [Cited on 96]

[75] H. Park, P. Smeys, Z. Sahul, K. Saraswat, R. Dutton, and H. Hwang. "Quasi-three-dimensional modeling of sub-micron LOCOS structures". *Semiconductor Manufacturing, IEEE Transactions on* **8** (4), 390–401 (1995). [Cited on 96, 101]

[76] V. Agache, R. Ringot, P. Bigotte, V. Senez, B. Legrand, L. Buchaillot, and D. Collard. "Modeling and experimental validation of sharpening mechanism based on thermal oxidation for fabrication of ultra-sharp silicon nanotips". *Nanotechnology, IEEE Transactions on* **4** (5), 548–556 (2005). [Cited on 96]

[77] B. Dietrich, V. Bukalo, A. Fischer, K. F. Dombrowski, E. Bugiel, B. Kuck, and H. H. Richter. "Raman-spectroscopic determination of inhomogeneous stress in submicron silicon devices". *Applied Physics Letters* **82** (8), 1176–1178 (2003). [Cited on 101]

[78] I. D. Wolf, J. Vanhellemont, A. Romano-Rodriguez, H. Norstrom, and H. E. Maes. "Micro-Raman study of stress distribution in local isolation structures and correlation with transmission electron microscopy". *Journal of Applied Physics* **71** (2), 898–906 (1992). [Cited on 101]

[79] I. D. Wolf, H. Norstrom, and H. E. Maes. "Process-induced mechanical stress in isolation structures studied by micro-Raman spectroscopy". *Journal of Applied Physics* **74** (7), 4490–4500 (1993). [Cited on 101]

[80] S. D. Fonzo, W. Jark, S. Lagomarsino, C. Giannini, L. D. Caro, A. Cedola, and M. Muller. "Non-destructive determination of local strain with 100-nanometre spatial resolution". *Nature* **403** (6770), 638–640 (2000). [Cited on 101]

[81] P. Kenkare, J. Pfiester, J. Hayden, R. Subrahmanyan, R. Hegde, and V. Kaushik. "Sensitivity of field isolation profiles to active pattern". In "Electron Devices Meeting, 1993. IEDM '93. Technical Digest., International", pp. 479–482 (1993). ISBN 0163-1918. [Cited on 103]

CHAPTER 5

Electrical characterization of pyramidal semiconductor/metal structures

We present the electrical characterization of semiconductor/metal diodes formed at the apex of pyramidal structures by a local oxidation of silicon (LOCOS) process. Ballistic electron emission microscopy is used to study the hot-electron transmission at the semiconductor/metal interface which shows to be sensitive to the details of the fabrication process. Elemental mapping of the heterostructure indicates nitridation of the silicon surface. Further elimination of this oxynitride results in proper hot-electron transmission. This knowledge is relevant for the fabrication of novel semiconductor/ferromagnet probes for spin-filter scanning tunneling microscopy.

5.1 Electrical characterization of diodes

The study of semiconductors/metal interfaces has been an interesting subject for several decades due to its rich physics [1, 2, 3, 4] and its direct relevance

for semiconductor devices [5]. This is still an active subject providing a deeper understanding of the Schottky energy barrier present at those interfaces [6]. More recently, Schottky barriers have been used as energy filters in spintronic devices such as the spin-valve transistor [7]. Within the latter context we study the electrical transport through pyramidal semiconductor/metal structures for the realization of spin-filter scanning tunneling microscopy (SF-STM).

In SF-STM a two-terminal probe is used to quantify the tunnel spin polarization of a magnetic surface with high spatial resolution (see chapter 3 for a description of SF-STM). The probes consist of a Si double pyramid with a semiconductor/metal heterostructure at the apex, where the spin polarization of the tunnel current is analyzed. In this chapter we study similar structures, with two main differences. First, the apex is not fully rounded but it is an extended flat surface. Second, the metal overlayer only contains Au without any ferromagnetic spin filter. These differences allow us to easily characterize the Schottky diode, since we can reliably measure the diode area and even perform STM experiments locally at the apex.

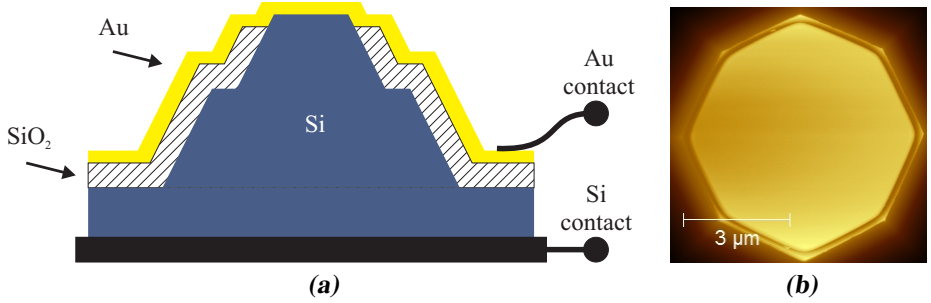

Figure 5.1. *Geometry of semiconductor/metal pyramidal structures. (a) Schematic of a pyramidal structure. The apex contains the active Si/Au area whereas the sidewalls are still isolated by oxide. (b) AFM image showing the octagonal apex from one Si/Au diode having an effective diameter of 6 µm.*

The pyramidal structure is schematically shown in Figure 5.1a. The n-type Si/Au diode is defined at the apex by use of a local oxidation of silicon (LOCOS) process, as described in section 4.2. Here we specifically use the first process pathway shown in Figure 4.5 because we want to obtain a flat apex wider than a few micrometers. The area of the apex is determined by optical microscopy or by atomic force microscopy (AFM), as shown in Figure 5.1b.

We start the electrical characterization of our pyramidal structures by measuring the two-terminal $I-V$ curve of the semiconductor/metal diodes at

room temperature, using the contact to the top metal overlayer and the ohmic contact to the silicon on the rear side of the chip. Each silicon chip contains three pyramidal structures with nominally the same apex size, so we measure three identical diodes in parallel (see Figure 4.6). These measurements yield $I-V$ curves such as those shown in Figure 5.2. The rectifying behavior is consistent with Schottky diodes.

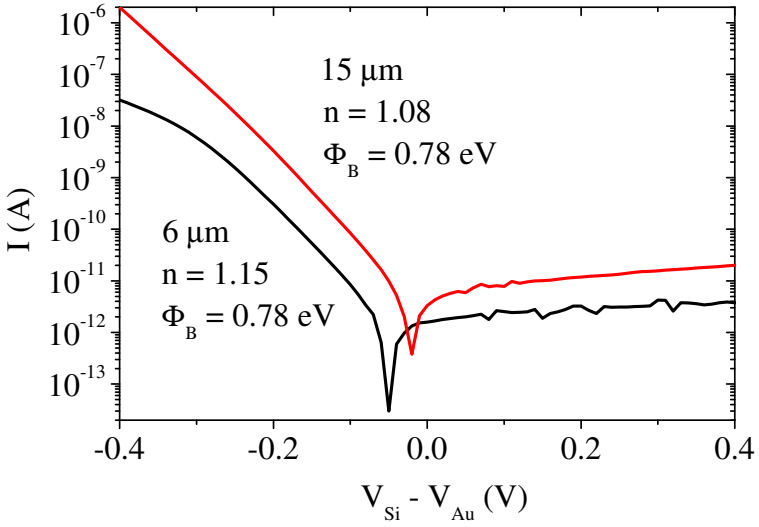

Figure 5.2. *Electrical transport of semiconductor/metal pyramidal structures. Two-terminal $I-V$ curves for chips containing pyramids with a Si/Au effective diameter of 6 µm (black) and 15 µm (red). The parameters extracted with the thermionic emission model are also shown. For both chips the initial LOCOS layer thicknesses were 20 nm pad oxide and 120 nm nitride.*

The forward-bias characteristic of the $I-V$ curves shows an exponential behavior. We fit this exponential part using the thermionic emission model [5] to extract the Schottky barrier height (Φ_B) and the ideality factor (n),

$$I = aA^{**}T^2 \exp\left(-\frac{\Phi_B}{k_B T}\right)\left[\exp\left(\frac{eV}{nk_B T}\right) - 1\right] \tag{5.1}$$

where a is the area of the semiconductor/metal interface, A^{**} the reduced effective Richardson constant (1.1×10^6 A m^{-2} K^{-2} for n-type Si), k_B the Boltzmann constant and T the absolute temperature. The result of fitting the $I-V$ curves of several pyramidal structures is shown in Figure 5.3. Besides a spread on the extracted parameters it is observed that the typical values are

Φ_B =0.77–0.80 eV and n =1.04–1.25, indicating that indeed thermionic emission is the dominant transport mechanism. The area of the pyramid apex did not show to have a strong influence on the $I-V$ characteristics. Furthermore, the zero-bias resistance of the diodes are usually in excess of 1 GΩ which indicates the feasibility of using similar structures for magnetic imaging at room temperature via the newly proposed technique (see section 4.1).

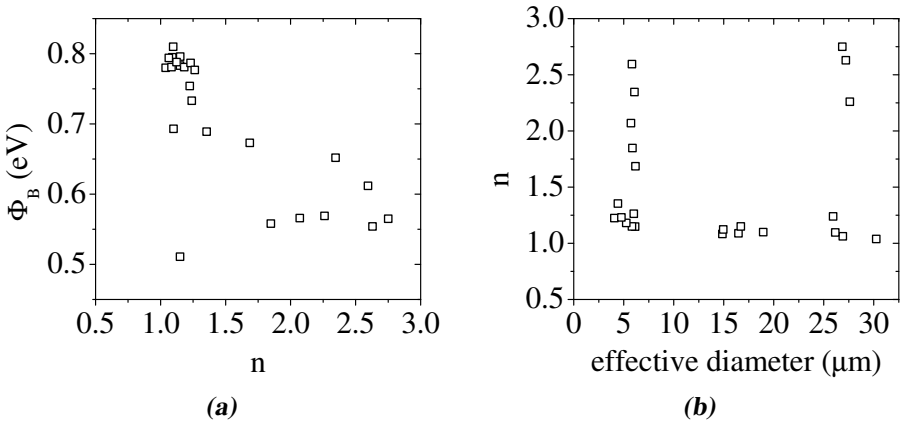

Figure 5.3. *Analysis of diode $I-V$ curves from pyramidal structures by using the thermionic emission model. (a) Two parameters are extracted from each $I-V$ curve, namely the Schottky barrier height (Φ_B) and the ideality factor (n). (b) The extraction of nearly ideal parameters ($\Phi_B \approx 0.8$ eV and $n \approx 1.1$) is not dependent on diode size.*

LOCOS involves the definition of two layers prior to the growth of the thick isolation oxide. These layers are a thin pad oxide and a nitride cap. The pad oxide serves to relieve the stress from the nitride layer and that appearing during the growth of the isolation oxide. The nitride cap acts as an oxidation mask and serves to define the area at the apex for the Si/Au diode. For the present study we initially investigated relatively thin nitrides of 120 nm with pad oxides of 20 nm or 50 nm. Later we also studied thicker nitrides of 200 nm with pad oxides of 50 nm. The analysis of all these structures is included in Figure 5.3. For a detailed discussion of LOCOS and the use of these layer thicknesses we refer the reader to subsection 4.2.2. The main point is that there was no apparent correlation between the different LOCOS layer thicknesses used and the Schottky diode parameters extracted from the two-terminal measurements.

The spread on the extracted parameters may be related to piercing of the isolation oxide while mounting the silicon chips on the STM sample holder

(this issue was improved in a later design), to the presence of an inhomogeneous Schottky barrier height [8, 9] or to edge effects [10]. We will show in the following sections by STM experiments that the Schottky barrier height showed to be homogeneous across the apex area.

Finally, we mention that the series resistance of the Si pyramid has only a minor effect on the $I-V$ curves. We estimate the resistance of the small top pyramid to be less than 100 kΩ for an apex with a diameter greater than 1 µm at room temperature for our 1–10 Ω cm n-type Si [11, 12].

5.2 STM study of electron transmission

We continue the electrical characterization of our pyramids by studying the ballistic transport through the Si/Au heterostructure. This is important because the SF-STM technique relies on spin filtering of ballistic electrons going through the metal overlayer, over the Schottky barrier, and finally being collected in the semiconductor (see chapter 3). For this characterization we tunnel from an STM tip to the pyramid apex and perform ballistic electron emission microscopy (BEEM) on it at room temperature, as shown in Figure 5.4.

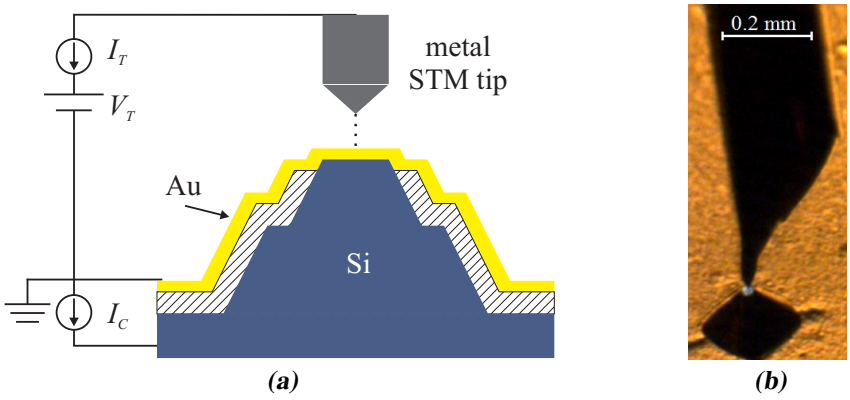

Figure 5.4. *Geometry for STM characterization of pyramidal Si/Au structures. (a) Schematic of a BEEM experiment on the apex of the pyramid. Only a part of the tunneling carriers injected into the pyramid are collected in the silicon and contribute to I_C. (b) Optical image of an STM tip scanning a pyramid with a 27 µm wide apex.*

BEEM is an STM-based technique used to study the ballistic transmission of electrons (or holes) through semiconductor/metal heterostructures [13, 14].

In BEEM hot carriers are injected via tunneling from an STM tip into the top metal layer of the heterostructure, where most carriers rapidly relax their energy in the metal and return through the electrical contact to this layer. Only those carriers which are able to transmit through the metal and be collected in the semiconductor are then measured via a second electrical contact to the semiconductor. The magnitude and energy dependence of the collected current (I_C) gives information about scattering processes in the heterostructure and about the height of the Schottky barrier [15]. We have discussed BEEM in subsection 2.2.2.

In our fabrication process we etch the native oxide on the pyramid apex using a 1 % HF solution. This produces an oxide-free Si(100)-H surface just prior deposition of the Au overlayer by evaporation in an ultra-high-vacuum (UHV) deposition system. Next, the chip containing the pyramidal Schottky diodes is exposed to air in order to be transferred to our UHV STM setup, where we perform the BEEM experiments.

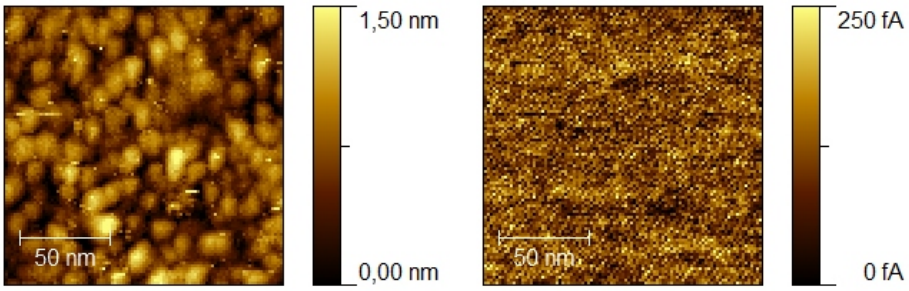

Figure 5.5. *Topographic (a) and collected current (b) images for BEEM on the apex of a pyramidal n-Si/Au (22 nm) structure using tunneling parameters of $V_T = -1.6$ V and $I_T = 4$ nA. The initial LOCOS layer thicknesses were 20 nm pad oxide and 120 nm nitride.*

We initially studied pyramidal structures fabricated using a LOCOS process with a relatively thin 120 nm nitride cap. A typical result of BEEM experiments on the apex of such a pyramidal Si/Au structure is shown in Figure 5.5. The STM topographic image shows a granular surface with a grain size of 10 nm and a small root mean square (rms) roughness of 0.3 nm. This topography is typical for our evaporated Au films with thicknesses of 10–25 nm. The collected current image shows a ballistic collection with an average value of

$I_C = 0.12 \pm 0.05$ pA at a tunnel bias of $V_T = -1.6$ V and $I_T = 4$ nA. Besides some minor contrast on the BEEM image due to the granular topography [15] we observe that the signal is low and close to the noise level of ± 0.05 pA typically found in our I_C channel.

We have also studied the energy dependence of the collected current by changing the tunnel voltage. Such $I_C - V_T$ spectrum for the same structure discussed above is shown in Figure 5.6. The BEEM spectrum is usually scaled by the tunneling current I_T in order to extract the transfer ratio $\alpha = I_C/I_T$ which does not depend on the tunneling current used [15]. We observe that BEEM spectra taken at a fixed tip location are consistent with the average values extracted from BEEM images. Furthermore, the Schottky barrier height of Si/Au structures can be extracted using the Bell-Kaiser (BK) model [14] which in its simplest form states a dependence of the transfer ratio $I_C/I_T \propto (eV_T - \Phi_B)^\eta$ with $\eta = 2$ (see Equation 2.13). Analysis with the BK model yields a Schottky barrier height of 1.13 eV.

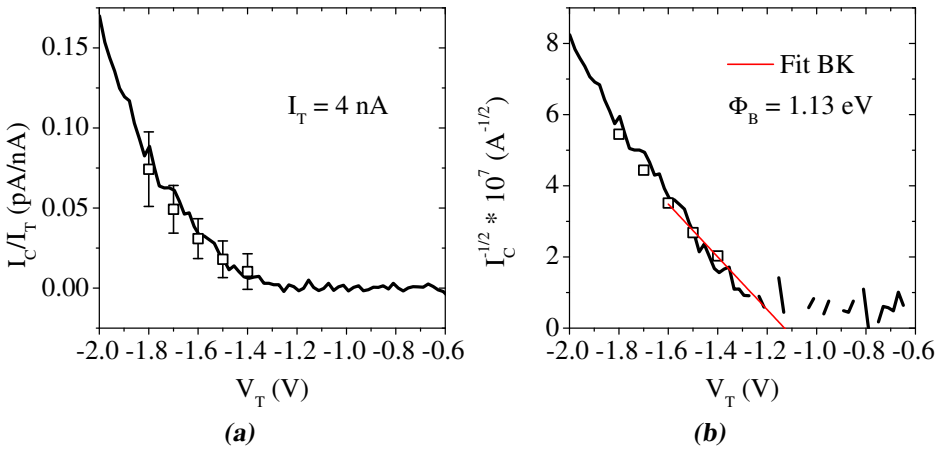

Figure 5.6. *Energy dependence of ballistic transmission for the pyramidal n-Si/Au (22 nm) structure imaged in Figure 5.5. (a) BEEM spectrum: black line is an average of four consecutive spectra taken at the same location, open squares are the statistical analysis of BEEM images. (b) Analysis of spectrum in (a) using the BK model.*

Low I_C signals and high Schottky barriers within the range of 1.1–1.3 eV were consistently observed for different pyramidal structures fabricated with thin 120 nm LOCOS nitride caps, independently of the thickness of the pad oxide (20 or 50 nm). This observation is in contrast with BEEM literature on n-Si (100)/Au structures which show a typical Φ_B of 0.8 eV and transfer ratios

of α =3–5 pA/nA at 1.2 eV for 22 nm Au [16, 17]. Not only do our structures show a 100 times lower transmission than that reported in the literature, but the Schottky barrier height we observe by BEEM is not consistent with the value of 0.8 eV that we extracted on the same structures by two-terminal $I-V$ curves in section 5.1.

The contradictory results from two-terminal diode $I-V$ curves and BEEM spectra can be reconciled by considering the presence of a thin tunnel barrier at the semiconductor/metal interface. For example, thin ($\approx$ 1 nm) Al_2O_3 tunnel barriers in metal-insulator-semiconductor (MIS) structures do not have a strong effect on the value of the Schottky barrier height extracted from two-terminal measurements [18]. On the other hand, similar AlO_x tunnel barriers have a strong influence on BEEM measurements resulting on $\approx$ 100 times lower collected current and an energy dependence given by the tunnel barrier height of 1.2 eV [19, 20]. Even thicker barriers (> 5 nm) made of Al_2O_3 or SiO_2 show a typical threshold tip energy of 4 eV [21, 22, 23, 24]. Therefore we infer that a thin tunnel barrier (or other form of strong scattering) may be present at the semiconductor/metal interface. We note that if such a barrier is present then the previous analysis using the BK model is not strictly correct. We already observed that we could fit almost all the spectrum with the BK model, contrary with its typical validity of up to 0.3 eV above Φ_B found for clean Si/Au systems [15]. Here the BK model just provides an indication of the height of the interfacial tunnel barrier.

5.3 Characterization of the Si interface

We have observed a decreased ballistic transmission on our pyramidal structures relative to the case of regular Si/Au BEEM samples. The low collected signals may be related to the presence of a (tunnel) barrier at the semiconductor/metal interface other than the Si/Au Schottky barrier. We remove the native oxide from the Si surface and perform the subsequent metal deposition using the same process and equipment which has shown to produce high-quality BEEM samples [25]. So the presence of contamination at the interface may be related to the processing specifically used for definition of our pyramidal Schottky structures.

The major difference between the fabrication of planar BEEM samples and our fabrication process for pyramidal structures is in the use of LOCOS to

obtain a Si exposed area located at their apex. We introduce a new material (Si_3N_4) and subsequent oxidation, annealing and wet etching steps. If the LOCOS layers are clean and well defined then no problems are expected since both the nitride and the pad oxide can be efficiently removed with selective chemical etches. On the other hand, a Si/SiO_2 interface with an uncertain composition may result in a surface different than Si(100)-H prior Au deposition. So we have studied the apex of our structures with transmission electron microscopy (TEM), as shown in Figure 5.7.

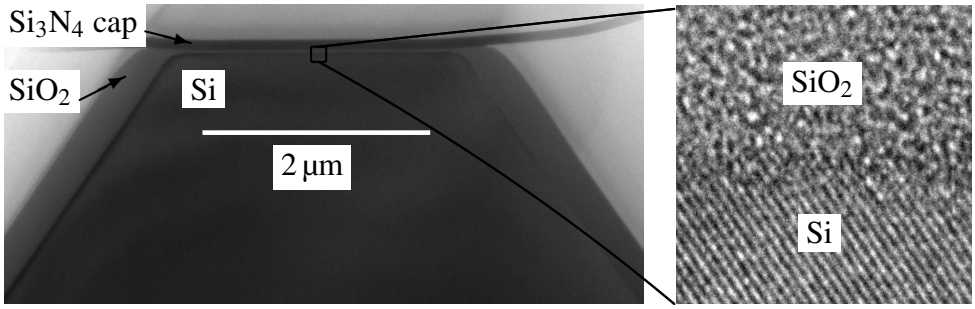

Figure 5.7. *TEM imaging of LOCOS structures. (a) The structure consists of a Si pyramid with sidewalls covered by insulation SiO_2 and an apex with the Si/SiO_2 pad/Si_3N_4 cap LOCOS stack. (b) High-resolution TEM image of the interface between the Si apex and the pad oxide.*

The LOCOS structures studied by TEM consist of <110> oriented lines instead of pyramids, due to the difficulty of studying the apex of three-dimensional pyramids by TEM. In this way the specimen could be thinned down to 0.4 times the mean free path [26] of the electron beam (about 150 nm in Si) [27]. Other than the geometry, the structures underwent the exact same processing as regular pyramidal structures just before removal of the nitride cap. High-resolution imaging of the Si/SiO_2 interface at the apex (see Figure 5.7b) does not show any indication for the presence of an interfacial layer.

The situation is different when we study the chemical composition of the structure with energy-filtered TEM (EFTEM) where spatial images of the distribution of a specific element are obtained via core-loss images using the three-window mapping technique [28]. EFTEM images are shown in Figure 5.8. Near the center of the apex we consistently observe the presence of nitrogen at the Si/SiO_2 interface, visible as a faint line indicated by the white

arrows in Figure 5.8c. Similar maps for oxygen and silicon (not shown) have the expected distribution along the depth of the LOCOS layer stack.

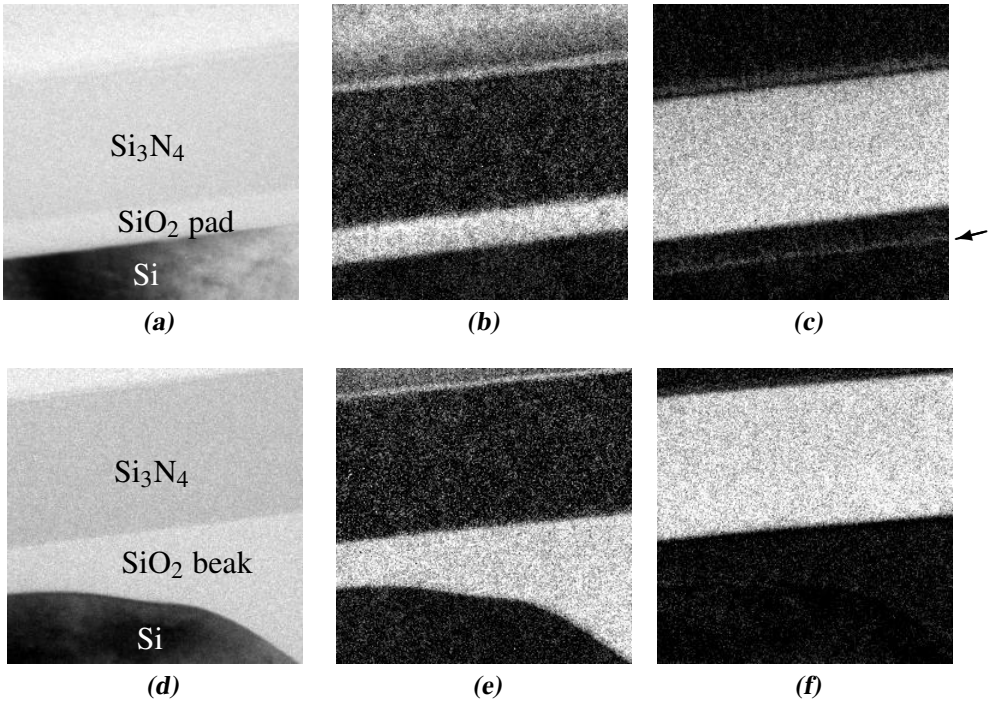

Figure 5.8. *EFTEM on apex of LOCOS structure shown in Figure 5.7. Unfiltered image near the center (a) and corresponding oxygen (b) and nitrogen (c) maps. Unfiltered image near the edge (d) and corresponding oxygen (e) and nitrogen (f) maps. All images are 180 nm wide.*

The observation of nitrogen at the Si/SiO_2 interface indicates the presence of a nitride compound, possibly silicon oxynitride (SiO_xN_y). If such an oxynitride is present at the interface then it will not be removed by the short 1 % HF dip aimed for removal of native oxide, because Si_3N_4 is more resistant to HF etch than SiO_2 [29]. After deposition of the Au overlayer we end up with a MIS structure with the oxynitride acting as tunnel barrier. The origin of this nitrogen is linked to the top Si_3N_4 layer used as oxidation mask. We used a dry-oxidation LOCOS process to avoid this kind of nitrogen accumulation at the Si/SiO_2 interface which is only found in wet LOCOS [30]. Therefore this accumulation must have occurred prior to the LOCOS dry oxidation step. We corroborate the latter by noting the absence of nitrogen accumulation near the

edges of the apex where the oxide bird's beak is grown, as shown in Figure 5.8f. The lack of nitrogen accumulation in the bird's beak is beneficial for the case of a fully rounded apex as used in SF-STM probes, to be discussed in chapter 6.

We have extracted elemental profiles from the EFTEM images near the center of the apex. The resulting profiles are shown in Figure 5.9a. Accumulation of nitrogen at the Si/SiO_2 interface is evident, with a signal amplitude 1/4 that from the Si_3N_4 and a width of about 3 nm. We note that the resolution of the three-window method is 1 nm [31] and since the signal intensity is based only on the core-loss spectra it is not fully quantitative. We have also extracted spatially resolved electron energy-loss spectra (EELS) by locally assembling a sequence of plural EFTEM images [27]. The EELS spectrum (not shown) at the Si/SiO_2 interface confirms the presence of SiO_xN_y.

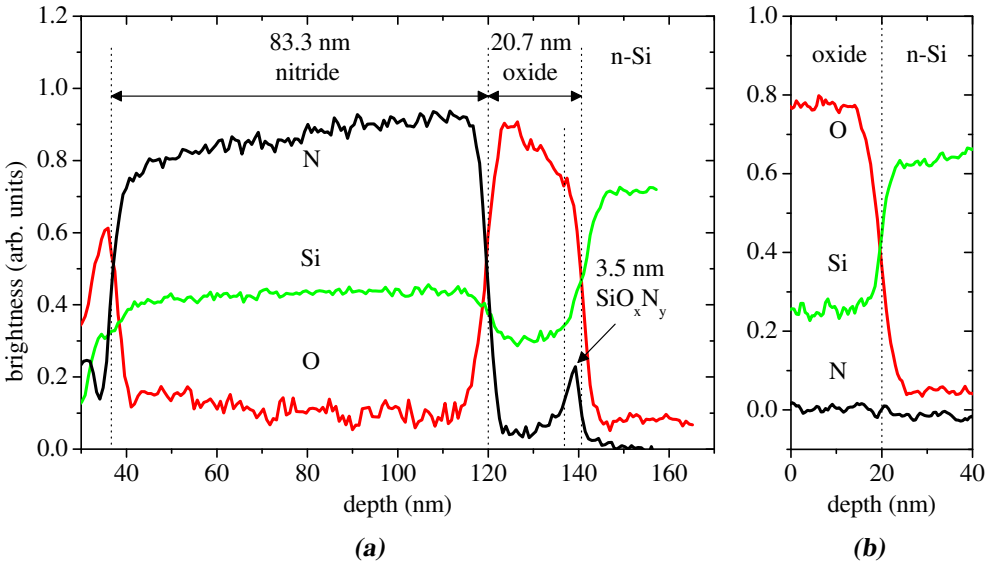

Figure 5.9. *Elemental profile of LOCOS structures. (a) Fully processed structure showing nitrogen accumulation at the Si/SiO_2 interface, same location as in Figure 5.8a. (b) LOCOS layer stack just after deposition of the top Si_3N_4, no nitrogen is detected at the Si/SiO_2 interface.*

Based on our fabrication process we did not expect the presence of nitrogen at the Si/SiO_2 interface since the pad oxide is thermally grown on a clean Si substrate using dry oxygen. The nitrogen accumulation at the interface resembles previous reports in literature of structures studied by EFTEM where

the pad oxide was exposed to NH_3 annealing [31, 32]. Other studies using x-ray photoelectron spectroscopy depth-profiling [33] or secondary ion mass spectrometry [34] had focused on similar nitrogen accumulation phenomena on N_2O grown oxynitrides. Our pad oxide is not intentionally nitrided in such ways.

The question arises as to whether the nitrogen gets accumulated during the growth of the top Si_3N_4 layer or during later oxidation/anneal steps. To rule out the appearance of nitrogen accumulation due to deposition of the top Si_3N_4 layer over the pad oxide we have also performed EFTEM on a LOCOS stack just after this step, prior to any further processing. In this case there is no indication of nitrogen at the Si/SiO_2 interface, as shown in Figure 5.9b. Therefore the nitrogen accumulation occurs during the subsequent steps.

We point out that the top nitride layer has a thickness of about 83 nm prior to its removal, contrary to the 120 nm thick layer initially deposited. As discussed in subsection 4.2.2 the nitride layer gets thinner during fabrication of the pyramidal structures, specially due to a wet thermal oxidation step used to grow a thick oxide mask for definition of pyramids by anisotropic etching. When a nitride is too thin it may not act as a proper oxidation mask and allow diffusion of NH_3 species formed at its surface during wet thermal oxidation [35]. If such species reach the pad oxide then they can easily end up at the Si/SiO_2 interface since the oxide is fairly transparent to NH_3 diffusion [30]. We conclude that the failure of the nitride mask during a long wet-oxidation step causes our pyramids to finally consist of a Si/SiO_xN_y/Au MIS structure, with its associated low ballistic transmission.

5.4 Improving the Si interface

We proceed to address the issue of reduced ballistic transmission in our Schottky pyramidal structures due to the presence of an oxynitride tunnel barrier remaining at the Si interface. There are two possible ways to proceed. We can either prevent the nitrogen accumulation at the interface or remove the oxynitride prior deposition of the Au overlayer. In this process optimization we kept the amount of changes from the first process pathway at a minimum (see chapter 4).

We first tried to remove the oxynitride using wet chemical etches of buffered HF (BHF), nitric acid (HNO_3), phosphoric acid (H_3PO_4) or suc-

cessive combinations thereof. In this approach we follow our original process up to removal of pad/native oxide by a short dip in 1 % HF. Then we introduce the wet chemical etch aimed to remove the oxynitride, and finally the pyramid is coated with the Au overlayer. We note that BHF is selective towards oxide and the extent of etching we can use is limited by the thickness of the oxide isolation in our structures, H_3PO_4 is selective towards nitride, whereas HNO_3 does not etch oxide or nitride and is usually used for cleaning off organics [29].

None of the wet chemical treatments yielded a proper ballistic electron transmission in our pyramidal structures. It is remarkable that even a 10 min treatment in 85 % H_3PO_4 at 160 °C did not improve the BEEM collected signal (see Figure 5.10a) since we found an etch rate of $\approx$ 3 nm/min for Si_3N_4. This is consistent with previous work studying the retardation of gate oxidation due to nitridation during wet LOCOS [35, 36]. The oxynitrides formed at the Si interface are notoriously difficult to remove.

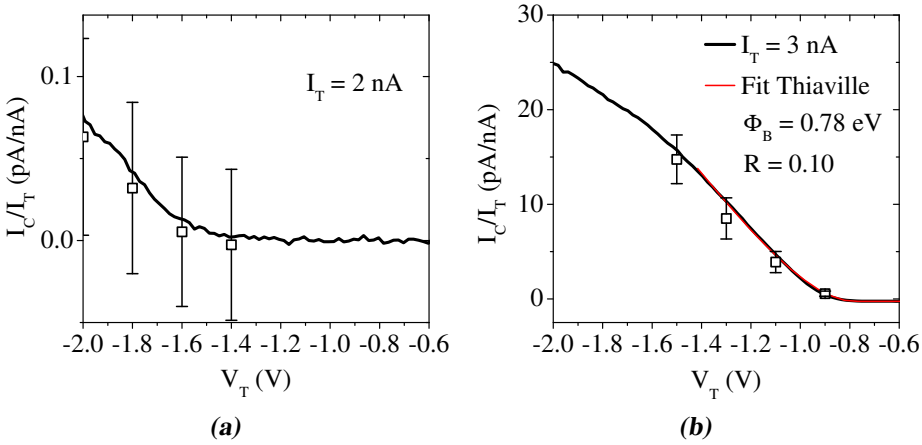

Figure 5.10. *(a) Low collection in n-Si/Au (15 nm) fabricated using a 120 nm thick nitride cap, with a treatment of 10 min H_3PO_4 prior Au deposition. (b) Proper collection in n-Si/Au (16 nm) fabricated using a 200 nm thick nitride cap. The spectrum is fitted up to -1.4 V using the analytical BK model by Thiaville et al. [37]. Open squares correspond to statistics from BEEM images. Note the different scales on the vertical axis of (a) and (b).*

Another approach is to prevent the appearance of oxynitride at the interface by changing our fabrication process. Nitridation of the Si interface usually occurs at the bird's beak edge [30] but it may also occur through a thin enough nitride by diffusion of NH_3 as discussed by Nakajima et al. [35]. Nakajima

et al. showed that a nitride mask thinner than 100 nm allows nitridation of the Si interface, whereas nitride layers of more than 200 nm also cause problems because of mechanical damage to the substrate. Therefore we have used a thicker nitride layer of 200 nm to obtain a clean Si/SiO_2 interface [35, 38]. There is no reason to increase the thickness of the pad oxide to values larger than the thicknesses of 20 nm and 50 nm previously used because SiO_2 is fairly transparent to NH_3 diffusion [30]. Still, since we now use a thicker nitride layer we only consider pads of 50 nm thick to prevent mechanical damage.

The resulting ballistic transmission for a pyramidal structure fabricated using a 200 nm thick nitride is shown in Figure 5.10b. There is an increased signal by two orders of magnitude and onset of collection for tip bias close to the height of the Si/Au Schottky barrier of 0.8 eV. A more detailed analysis of the BEEM spectrum is readily performed using an analytical version of the BK model developed by Thiaville et al. [37]. Such a fit is good for up to 0.6 eV above the threshold and yields two parameters (see Equation 2.14), representing the ballistic transmission within the metal base ($R = 0.10$) and the Schottky barrier height ($\Phi_B = 0.78$ eV). Fitting a simpler quadratic BK model [14] up to 0.3 eV above threshold also results in the same barrier height. The magnitude of $I_C = 7.5$ pA at 1.2 eV is in accordance with the literature, with transfer ratios of 4–7 pA/nA for n-Si(100)/Au (16 nm) [16, 17]. Therefore the use of a 200 nm thick nitride cap prevents the formation of the oxynitride at the Si interface resulting in a nearly ideal Si/Au Schottky interface.

The observation of proper BEEM spectra at room temperature on structures with a 200 nm nitride layer was reproducible. In Figure 5.11 we show the ballistic transmission for another Si/Au structure with similar collection properties. The collected signal I_C scales linearly with the tunneling current I_T. Collection in the silicon is observed for tunneling into the pyramidal structure with both electrons (BEEM) and holes in the so called reverse BEEM (R-BEEM) [39]. Proper hole transport in our SF-STM probes is also important, as the spin-dependent transport of holes has been shown to be useful for magnetic imaging and spintronics [40, 41, 42].

We also studied electron collection at the edge of the apex where the boundary between the Si/Au diode and the Si/SiO_2/Au isolated sidewall is located. In Figure 5.12a profiles taken along a scan line of the STM tip show the correlation between topographic and BEEM signal. When the tip is inside the Si/Au apex the collected signal is large and the topography shows a typical roughness of 1 nm. As the tip moves out of the apex and descends towards

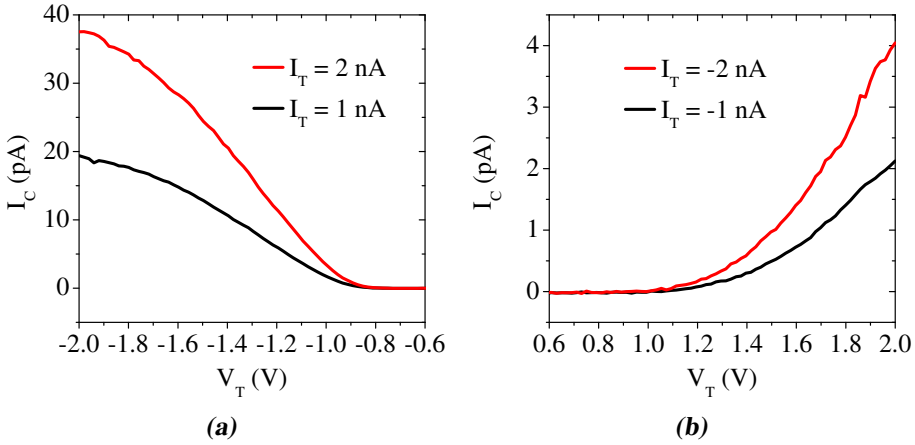

Figure 5.11. *BEEM (a) and R-BEEM (b) spectra on n-Si/Au (16 nm) pyramidal structure fabricated using a 200 nm thick nitride cap.*

the sidewall then tunneling takes place on top of the isolation oxide with no measurable collected signal in the semiconductor. The BEEM signal decreases smoothly in a transition region of about 50 nm wide until the edge of the isolation oxide is reached. BEEM spectra were also taken at different locations along the edge. As shown in Figure 5.12b spectra 1 and 2 are taken inside the Si/Au apex and both show similar collected signals, whereas spectrum 3 corresponds to the transition region and shows a reduced signal. Only the intensity of the BEEM signal decreases along the edge but the location of the energy threshold for ballistic collection is constant at 0.8 eV. This behavior is similar to that found for BEEM samples with a topographic gradient on the metal surface [43]. The fact that the Schottky barrier height does not change at the edge of the apex is relevant for the functioning of SF-STM probes with a fully rounded apex, to be presented in chapter 6.

The problem of low collected signals has thus been solved by using a thicker nitride layer within the LOCOS layer stack in order to prevent the nitridation of the Si/SiO_2 interface. The presence of a thin oxynitride SiO_xN_y tunnel barrier explains our observations. We note that the bandgap of bulk SiO_2 is ≈ 8.5 eV and is reduced for thin transition layers next to Si [44], whereas the bandgap of bulk Si_3N_4 is ≈ 4.5 eV [45]. One would expect to observe a barrier height close to half the bandgap. The observed reduced effective barrier height of 1.2 eV could then be related to its thickness $\lesssim 3$ nm remaining prior

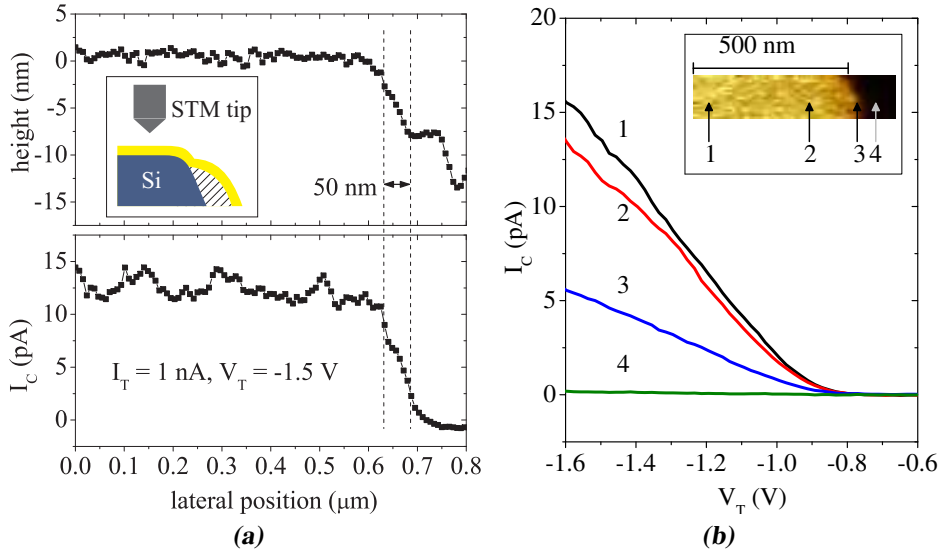

Figure 5.12. *BEEM at the edge of the apex of a pyramidal n-Si/Au (16 nm) structure fabricated using a 200 nm thick nitride cap. (a) Topographic and ballistic transmission profiles along a scan line. The inset shows a schematic representation of the experimental geometry. (b) BEEM spectra taken at different locations along the edge. The inset shows the location of each spectrum in a BEEM image of the edge of the apex.*

Au deposition, as previously observed for very thin Al_2O_3 barriers [20].

There are other options to remove the oxynitride layer present at the Si surface, other than the wet chemical etches tested in this chapter within the context of our first process pathway. For example, removal by reactive ion etching (RIE) [38] or by sacrificial oxidation [35, 36, 38] are effective methods to obtain a nitride-free Si surface. As explained in section 4.2 these methods are introduced into a second process pathway aimed for the fabrication of SF-STM probes, which have a rounded apex. In this way it is possible to achieve proper collection properties independent of the nitride layer thickness. The electrical properties of SF-STM probes will be the subject of chapter 6.

5.5 Conclusions

We have studied the electrical properties of silicon pyramidal structures with a Si/Au Schottky diode located at their apex having a size of a few micrometers

wide. Central to their electrical behavior is the fact that the localized diodes are fabricated using a LOCOS process. These structures with a flat apex serve as an intermediate case towards the study of SF-STM probes which have a fully rounded apex with a radius of curvature $\lesssim 1\,\mu m$.

The structures studied in this chapter, thanks to their wide apex, allow for the characterization of their Schottky barrier height via two-terminal $I-V$ diode curves and by performing STM experiments right at their apex. The two-terminal $I-V$ curves confirm that the transport is dominated by thermionic emission with a Schottky barrier height equal to the one found in literature for standard planar devices. On the contrary, STM experiments show that the ballistic transmission in these structures depends on the LOCOS process parameters. For pyramids with an initial LOCOS structure having a 120 nm nitride layer a small ballistic transmission and high barrier heights are extracted from BEEM spectra, indicating the presence of a tunnel barrier at the semiconductor/metal interface. The latter was confirmed by TEM analysis of the LOCOS layer stack where an oxynitride layer is observed at that interface. The two-terminal $I-V$, BEEM, and TEM data indicate that our pyramids are in fact MIS structures.

Optimization of the LOCOS process parameters allowed the increase of ballistic transmission in the pyramidal structures up to the same magnitude as that found in planar BEEM samples. Furthermore, the Schottky barrier height extracted from BEEM spectra now coincided with that from two-terminal $I-V$ curves and was equal to the literature values. The LOCOS parameter changed was the thickness of the nitride layer, which was increased to 200 nm. We attribute the result to an increased masking effect of the nitride layer during during a wet oxidation step in our fabrication process, thereby preventing the formation of the oxynitride at the Si interface.

The optimized structures with a ballistic transmission at room temperature comparable with that of high-quality BEEM samples demonstrate that we are able to fabricate three-dimensional structures with micrometer-sized Schottky diodes located at their apex without any degradation of the semiconductor/metal interface. Reproducible results, ballistic transport consistent with planar BEEM theory, and high-quality Schottky barriers down to the edge of the apex, were all requirements needed to be fulfilled prior the realization of SF-STM probes. Most importantly, the knowledge gained on the nitridation of the silicon surface and its effect on the ballistic transmission allow the design of a better fabrication process for SF-STM probes, which will be discussed in

the following chapter.

References

[1] C. R. Crowell and S. M. Sze. "Current transport in metal-semiconductor barriers". *Solid-State Electronics* **9** (11-12), 1035–1048 (1966). [Cited on 113]

[2] S. G. Louie, J. R. Chelikowsky, and M. L. Cohen. "Ionicity and the theory of Schottky barriers". *Physical Review B* **15** (4), 2154 (1977). [Cited on 113]

[3] J. Tersoff. "Schottky Barrier Heights and the Continuum of Gap States". *Physical Review Letters* **52** (6), 465 (1984). [Cited on 113]

[4] R. T. Tung. "Schottky-Barrier Formation at Single-Crystal Metal-Semiconductor Interfaces". *Physical Review Letters* **52** (6), 461 (1984). [Cited on 113]

[5] S. M. Sze and K. K. Ng. *Physics of semiconductor devices* (John Wiley and Sons, 2007), 3rd edn. ISBN 978-0-471-14323-9. [Cited on 114, 115]

[6] R. T. Tung. "Recent advances in Schottky barrier concepts". *Materials Science and Engineering: R: Reports* **35** (1-3), 1–138 (2001). [Cited on 114]

[7] R. Jansen. "The spin-valve transistor: a review and outlook". *Journal of Physics D: Applied Physics* **36** (19), R289 (2003). [Cited on 114]

[8] R. T. Tung. "Electron transport at metal-semiconductor interfaces: General theory". *Physical Review B* **45** (23), 13509 (1992). [Cited on 117]

[9] R. F. Schmitsdorf, T. U. Kampen, and W. Monch. "Explanation of the linear correlation between barrier heights and ideality factors of real metal-semiconductor contacts by laterally nonuniform Schottky barriers". *Journal of Vacuum Science & Technology B: Microelectronics and Nanometer Structures* **15** (4), 1221–1226 (1997). [Cited on 117]

[10] P. A. Tove. "Methods of avoiding edge effects on semiconductor diodes". *Journal of Physics D: Applied Physics* **15** (4), 517 (1982). [Cited on 117]

[11] J. D. Romano and R. H. Price. "The conical resistor conundrum: A potential solution". *American Journal of Physics* **64** (9), 1150–1153 (1996). [Cited on 117]

[12] M. W. Denhoff. "An accurate calculation of spreading resistance". *Journal of Physics D: Applied Physics* **39** (9), 1761 (2006). [Cited on 117]

[13] W. J. Kaiser and L. D. Bell. "Direct investigation of subsurface interface electronic structure by ballistic-electron-emission microscopy". *Physical Review Letters* **60** (14), 1406 (1988). [Cited on 117]

[14] L. D. Bell and W. J. Kaiser. "Observation of Interface Band Structure by Ballistic-Electron-Emission Microscopy". *Physical Review Letters* **61** (20), 2368 (1988). [Cited on 117, 119, 126]

[15] M. Prietsch. "Ballistic-electron emission microscopy (BEEM): studies of metal/semiconductor interfaces with nanometer resolution". *Physics Reports* **253** (4), 163–233 (1995). [Cited on 118, 119, 120]

[16] L. D. Bell. "Evidence of Momentum Conservation at a Nonepitaxial Metal/Semiconductor Interface Using Ballistic Electron Emission Microscopy". *Physical Review Letters* **77** (18), 3893 (1996). [Cited on 120, 126]

[17] M. K. Weilmeier, W. H. Rippard, and R. A. Buhrman. "Ballistic electron transport through Au(111)/Si(111) and Au(111)/Si(100) interfaces". *Physical Review B* **59** (4), R2521 (1999). [Cited on 120, 126]

[18] B. C. Min, J. C. Lodder, R. Jansen, and K. Motohashi. "Cobalt-Al_2O_3-silicon tunnel contacts for electrical spin injection into silicon". *Journal of Applied Physics* **99**, 08S701–3 (2006). [Cited on 120]

[19] W. H. Rippard, A. C. Perrella, and R. A. Buhrman. "Ballistic current transport studies of ferromagnetic multilayer films and tunnel junctions (invited)". *Journal of Applied Physics* **89**, 6642–6646 (2001). [Cited on 120]

[20] W. H. Rippard, A. C. Perrella, F. J. Albert, and R. A. Buhrman. "Ultrathin Aluminum Oxide Tunnel Barriers". *Physical Review Letters* **88** (4), 046805 (2002). [Cited on 120, 128]

[21] R. Ludeke, A. Bauer, and E. Cartier. "Hot electron transport in SiO2 probed with a scanning tunnel microscope". *Applied Physics Letters* **66** (6), 730–732 (1995). [Cited on 120]

[22] B. Kaczer and J. P. Pelz. "Ballistic-electron emission microscopy studies of charge trapping in SiO2". *Journal of Vacuum Science & Technology B: Microelectronics and Nanometer Structures* **14** (4), 2864–2871 (1996). [Cited on 120]

[23] H. J. Wen and R. Ludeke. "Investigation of existing defects and defect generation in device-grade SiO2 by ballistic electron emission spectroscopy". *Journal of Vacuum Science & Technology B: Microelectronics and Nanometer Structures* **15** (4), 1080–1088 (1997). [Cited on 120]

[24] R. Ludeke. "Electrical characterization of gate oxides by scanning probe microscopies". *Journal of Non-Crystalline Solids* **303** (1), 150–161 (2002). [Cited on 120]

[25] E. ul Haq. *Nanoscale spin-dependent transport of electrons and holes in Si-ferromagnet structures*. PhD thesis, University of Twente (2005). ISBN 90-365-2241-2. [Cited on 120]

[26] R. Egerton and S. Cheng. "Measurement of local thickness by electron energy-loss spectroscopy". *Ultramicroscopy* **21** (3), 231–244 (1987). [Cited on 121]

[27] K. Kimoto, T. Sekiguchi, and T. Aoyama. "Chemical shift mapping of Si L and K edges using spatially resolved EELS and energy-filtering TEM". *Journal of Electron Microscopy* **46** (5), 369–374 (1997). [Cited on 121, 123]

[28] R. D. Twesten. "Practical Aspects of EELS and EFTEM". EELS imaging and analysis school, Gatan, Inc., Pleasanton, CA. [Cited on 121]

[29] K. Williams, K. Gupta, and M. Wasilik. "Etch rates for micromachining processing-Part II". *Microelectromechanical Systems, Journal of* **12** (6), 761–778 (2003). [Cited on 122, 125]

[30] E. Kooi, J. G. van Lierop, and J. A. Appels. "Formation of Silicon Nitride at a Si-SiO_2 Interface during Local Oxidation of Silicon and during Heat-Treatment of Oxidized Silicon in NH_3 Gas". *Journal of The Electrochemical Society* **123** (7), 1117–1120 (1976). [Cited on 122, 124, 125, 126]

[31] T. Sekiguchi, K. Kimoto, T. Aoyama, and Y. Mitsui. "Nitrogen Distribution and Chemical Bonding State Analyses in Oxynitride Film by Spatially Resolved Electron Energy Loss Spectroscopy (EELS)". *Japanese Journal of Applied Physics* **37** (Part 2, No. 6B), L694–L696 (1998). [Cited on 123, 124]

[32] K. Kimoto, K. Kobayashi, T. Aoyama, and Y. Mitsui. "Analyses of composition and chemical shift of silicon oxynitride film using energy-filtering transmission electron microscope based spatially resolved electron energy loss spectroscopy". *Micron* **30** (2), 121–127 (1999). [Cited on 124]

[33] E. C. Carr and R. A. Buhrman. "Role of interfacial nitrogen in improving thin silicon oxides grown in N_2O". *Applied Physics Letters* **63** (1), 54–56 (1993). [Cited on 124]

[34] Y. Okada, P. J. Tobin, V. Lakhotia, W. A. Feil, S. A. Ajuria, and R. I. Hegde. "Relationship between growth conditions, nitrogen profile, and charge to breakdown of gate oxynitrides grown from pure N_2O". *Applied Physics Letters* **63** (2), 194–196 (1993). [Cited on 124]

[35] O. Nakajima, N. Shiono, S. Hashimoto, and C. Hashimoto. "Defects in a Gate Oxide Grown after the LOCOS Process". *Japanese Journal of Applied Physics* **18**, 943–951 (1979). [Cited on 124, 125, 126, 128]

[36] T. A. Shankoff, T. T. Sheng, S. E. Haszko, R. B. Marcus, and T. E. Smith. "Bird's Beak Configuration and Elimination of Gate Oxide Thinning Produced during Selective Oxidation". *Journal of The Electrochemical Society* **127** (1), 216–222 (1980). [Cited on 125, 128]

[37] A. Thiaville, F. Caud, C. Vouille, and J. Miltat. "BEEM spectra of various Au-Si samples and their analysis". *The European Physical Journal B - Condensed Matter and Complex Systems* **55** (1), 29–36 (2007). [Cited on 125, 126]

[38] M. Itsumi and F. Kiyosumi. "Identification and Elimination of Gate Oxide Defect Origin Produced during Selective Field Oxidation". *Journal of The Electrochemical Society* **129** (4), 800 (1982). [Cited on 126, 128]

[39] L. D. Bell, M. H. Hecht, W. J. Kaiser, and L. C. Davis. "Direct spectroscopy of electron and hole scattering". *Physical Review Letters* **64** (22), 2679 (1990). [Cited on 126]

[40] T. Banerjee, E. Haq, M. H. Siekman, J. C. Lodder, and R. Jansen. "Spin Filtering of Hot Holes in a Metallic Ferromagnet". *Physical Review Letters* **94** (2), 027204 (2005). [Cited on 126]

[41] E. Haq, T. Banerjee, M. H. Siekman, J. C. Lodder, and R. Jansen. "Ballistic hole magnetic microscopy". *Applied Physics Letters* **86** (8), 082502–3 (2005). [Cited on 126]

[42] E. Haq, T. Banerjee, M. H. Siekman, J. C. Lodder, and R. Jansen. "Excitation and spin-transport of hot holes in ballistic hole magnetic microscopy". *Applied Physics Letters* **88** (24), 242501–3 (2006). [Cited on 126]

[43] M. Prietsch and R. Ludeke. "Ballistic-electron-emission microscopy and spectroscopy of GaP(110)-metal interfaces". *Physical Review Letters* **66** (19), 2511 (1991). [Cited on 127]

[44] S. Markov, P. V. Sushko, S. Roy, C. Fiegna, E. Sangiorgi, A. L. Shluger, and A. Asenov. "Si-SiO2 interface band-gap transition - effects on MOS inversion layer". *physica status solidi (a)* **205** (6), 1290–1295 (2008). [Cited on 127]

[45] L. Giacomazzi and P. Umari. "First-principles investigation of electronic, structural, and vibrational properties of a-Si3N4". *Physical Review B (Condensed Matter and Materials Physics)* **80** (14), 144201–12 (2009). [Cited on 127]

CHAPTER 6

Properties of SF-STM probes

We study the properties of novel two-terminal semiconductor/ferromagnet probes necessary for the realization of spin-filter scanning tunneling microscopy. The probes are used in STM experiments to demonstrate their capability of performing imaging on metallic surfaces. The probe collector current, measured via the second terminal to the semiconductor, is used to evaluate the energy-filtering and transmission properties of ballistic electrons within the probes after tunneling has taken place. This work fulfills the basic requirements for using the probes for quantitative imaging of spin polarization.

6.1 Morphology and electrical properties

In chapter 3 we have discussed the concept of spin-filter scanning tunneling microscopy (SF-STM) a novel technique aimed at high-resolution and quantitative imaging of tunnel spin polarization (P_S) on the surface of a conducting sample. The basic element for the realization of SF-STM is a two-terminal semiconductor/ferromagnet probe operated as depicted in Figure 6.1. The first probe terminal to the metal overlayer acts as a regular contact to an STM tip for the tunnel current (I_T). The second probe terminal is an ohmic contact

to the semiconductor where the transmitted carriers are detected as a probe collector current (I_C). The spin-dependent energy filter formed by the semiconductor/ferromagnet Schottky heterostructure makes I_C an information channel sensitive to P_S and independent from sample topography. Therefore the success of SF-STM relies on achieving a spin-dependent energy filter, similar to that found in solid state devices [1], at the apex of an STM probe.

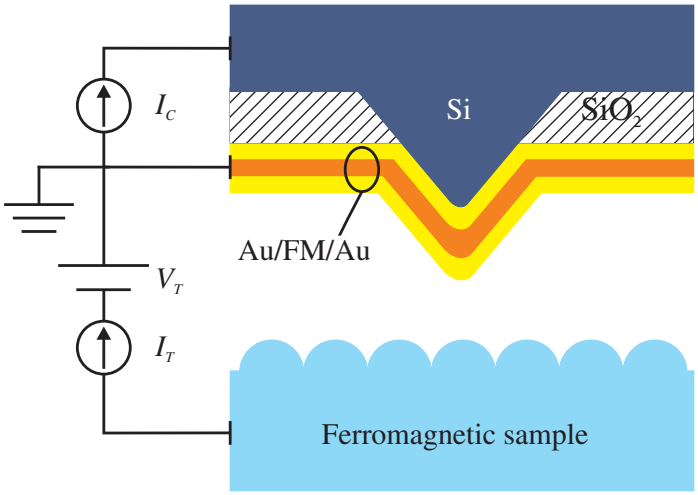

Figure 6.1. *Schematic of tip-sample configuration used for SF-STM. A bias V_T is applied between the magnetic sample and the metal layer stack on the tip, resulting in a spin-polarized tunneling current I_T. A small portion of the carriers is able to transmit the normal metals and the ferromagnetic layer of the tip, cross the semiconductor/metal interface, and enter the semiconductor, forming the collector current I_C. The magnitude of I_C is dependent on the spin polarization of the sample because the transmission from the ferromagnetic metal into the silicon is spin-dependent. The semiconductor/metal contact is defined only at the apex of the tip via SiO_2 isolation of the rest of the structure.*

In this chapter we study the properties of SF-STM probes and evaluate if they fulfill the basic requirements for successful SF-STM operation. For a complete description of the probe design and the considerations during the fabrication process we refer the reader to chapter 4. Here we focus on three main aspects of the probes. First, their morphology and macroscopic electrical properties are studied to determine if they can be used as STM probes with a (spin-dependent) energy filter at their apex. Second, the local electrical properties at the apex of the probes are directly studied by using them in actual STM experiments where the collection properties are determined by measuring

the energy dependence of the probe collector current I_C. Third, we briefly study the magnetostatics near the apex of the probe by imaging it with magnetic force microscopy (MFM) [2].

The SF-STM probes discussed here have a layer stack at their apex consisting of n-Si/Au (10–12 nm)/FM/Au (5 nm), where FM is a thin (2–5 nm) ferromagnetic layer of $Ni_{80}Fe_{20}$ or Co. The use of both normal metal and ferromagnetic layers and the corresponding thicknesses were discussed in section 4.1. The main reasons for such a layer stack are that the Si/Au interface offers a high-quality Schottky barrier, the Au surface allows for an inert probe which can be exposed to air, while the ferromagnet adds the spin sensitivity to the ballistic transmission of electrons through the metal overlayer and into the semiconductor.

The microfabrication process used for the SF-STM probes has a major influence on the ability to obtain a probe collector current when the probe scans a sample. In section 4.2 we introduced two process pathways we have used for fabrication of SF-STM probes. The first process pathway has the ability to yield probes with a sub-micrometer active Schottky area at the apex (active area refers to the area of the metal/semiconductor contact, not to the ”tunnel area”). The second process pathway only yields active areas which are several micrometer wide. In the following we discuss the main properties of probes fabricated using each of the two process pathways. Later in this chapter we will focus on probes fabricated with the second process pathway, since these were the only ones which showed satisfactory collection properties.

6.1.1 Sub-micrometer Schottky areas: first process pathway

We initially aimed for the realization of SF-STM probes with sub-micrometer active areas located at their apex. One of the reasons is that the noise in the probe collector current decreases for smaller Schottky diode areas due to the higher resistance (see section 4.1), similar to samples in ballistic electron emission microscopy (BEEM) [3]. For this reason we developed a first fabrication process pathway, schematically depicted in Figure 4.5. The resulting probes consist of a sub-micrometer area at the apex where the Si/Au diode is defined, closely surrounded by isolation oxide. An atomic force microscopy (AFM) image of such a probe is shown in Figure 6.2a.

We have previously studied the collection properties of similar structures fabricated using the first process pathway in chapter 5. The main difference

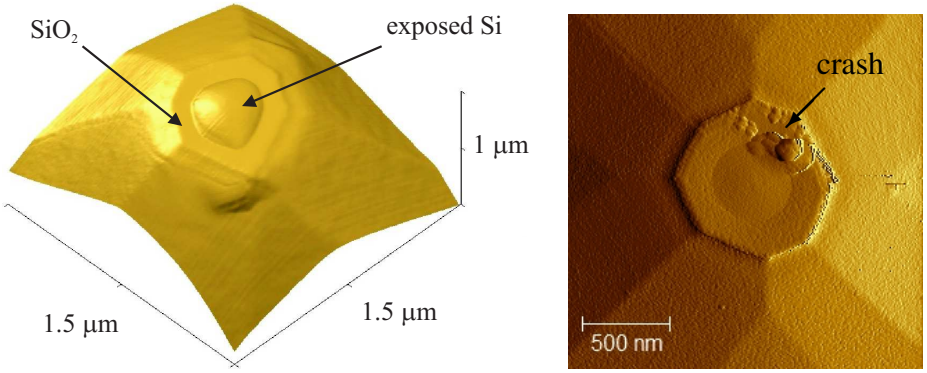

Figure 6.2. *AFM images of SF-STM probes fabricated using the first process pathway. (a) AFM image (perspective view) of a probe prior metal coating, topographic profiles were shown in Figure 4.12. (b) AFM image (amplitude) of a probe after STM experiments, showing the tunneling contact where it crashed the sample.*

is that those pyramidal structures consisted of a large and flat apex several micrometers wide, so they could not be used as probes for imaging purposes (in fact, we performed STM imaging on those structures using a conventional metal STM tip). On the other hand, the structures we consider here have a sub-micrometer-sized and rounded apex which can effectively be used as an imaging probe.

Despite the similar processing, the SF-STM probes with sub-micrometer apex did not show as good electrical properties as those structures from chapter 5. Low zero-bias two-terminal resistance of the Si/Au diode ($< 10\,\mathrm{M\Omega}$) prevented STM operation at room temperature due to a large noise in I_C. Therefore STM experiments, where the probe is scanned over a flat Au sample, where performed with the probe cooled down using liquid N_2 to a typical temperature of 95 K. Even if the noise was greatly reduced at low temperature, no reliable I_C signal was detected.

What could be the cause for the lack of probe collector current in probes with sub-micrometer active areas? One possibility is that the transmission within the spin-filter is too low due to a SiO_xN_y layer present at the semiconductor/metal interface, similar to that reported in chapter 5. This scenario is probably not correct for two reasons. First, we did not observe collection signal even for SF-STM probes fabricated with a thick (200 nm) nitride layer within the local oxidation of silicon layer stack, whereas these specifications

yielded working pyramidal structures in chapter 5. Second, the sharp SF-STM probes discussed here are formed by merging of the oxidation bird's beaks at the edges of the apex where we do not expect to have a SiO_xN_y layer, as observed in Figure 5.8f.

A probable cause is identified by performing AFM on SF-STM probes after they have been used in STM experiments. In every STM experiment, there is always the risk (which sometimes is an opportunity [4]) that the probe and sample come into contact with each other, namely a crash. If a crash happens then the metal coating of the SF-STM probe may be peeled off, a problem common to all STM-based techniques where probes are coated with thin films. We have imaged a probe after being crashed during STM imaging of a Au surface. As shown in Figure 6.2b the crashed probe seems to have contacted the sample at its oxide edge, instead of at the center of the active area. If tunneling takes place at the $Si/SiO_2/Au$ edge of the probe then no I_C signal can be expected as the hot electron cannot transmit the SiO_2 insulation layer. The impossibility of defining the isolation oxide edge far away from the active apex using the first process pathway and the typical alignment error of a few degrees while mounting our sample (see the geometry of the experiment in Figure 3.4) might very well explain the observations.

Strictly speaking, the reduced size of the diode at the apex should be taken into account when comparing these results to those of larger structures. Small-sized diodes have been shown to have a narrower depletion width that results in enhanced contribution of tunneling through the Schottky barrier relative to thermionic emission and therefore to a reduced zero-bias resistance [5, 6]. For our n-Si with doping $\approx 10^{15}\,\mathrm{cm}^{-3}$ we expect this effect to occur when the lateral radius of the diode is less than about 500 nm [6]. Our probe radius is indeed smaller than this characteristic length. This effect is expected to actually increase the probe collector signal due to the thinner Schottky barrier, not otherwise. Therefore this is not the reason for the lack of I_C. The study of transport in sub-micrometer Schottky contacts is indeed an interesting subject. For the purpose of our work we do not pursue this subject and proceed to focus only on probes fabricated using the second process pathway.

6.1.2 Several micrometers Schottky areas: second process pathway

In order to keep the edge of the SiO_2 isolation far away from the probe apex we introduced a second fabrication process pathway, which is more complex than the first one, as schematically depicted in Figure 4.5. The main differences are the sputtering of extra isolation oxide that yields a thicker isolation at the end of the process, treatment of the exposed Si surface with reactive ion etching (RIE) and sacrificial oxidation to rule out any remains of SiO_xN_y, and the final result of an active Si/Au area that spans the apex of the probe across a distance of several micrometers. For a detailed description of the second process pathway and the rationale behind it, we refer the reader to section 4.2.

The probes fabricated using the second process pathway are different than the structures discussed previously. Therefore we start by characterizing their macroscopic electrical behavior via two-terminal $I-V$ measurements of the resulting n-Si/Au Schottky diodes at room temperature. The $I-V$ curves show current rectification with an exponential bias dependence at forward bias consistent with the thermionic emission model [7]. The curves are properly fitted using Equation 5.1 with an ideality factor close to $n = 1.1$, as shown in Figure 6.3a. On the other hand, the measured Schottky barrier height is close to $\Phi_B = 0.5\,\text{eV}$, much lower than the literature value of $0.8\,\text{eV}$ for n-Si/Au planar diodes [3]. The extracted thermionic emission parameters from several SF-STM probes are summarized in Figure 6.3b.

The area of the active Schottky area in these probes was estimated from optical or scanning electron microscopy (SEM) images. A more detailed view of the probe morphology near the apex is obtained by AFM. As shown in Figure 6.4a the top few micrometers of the apex are free from isolation oxide. The latter is visible due to the rough surface of the sputtered oxide compared to the smooth surface of the exposed Si area. The size of the active area is determined by the $10\,\mu\text{m}$ wide circular Si_3N_4 cap used as a shadow mask during sputtering of the isolation oxide (for an image of the Si_3N_4 cap see Figure 4.10b). The absence of oxide near the apex prevents the issue of tunneling into an oxide-covered area from happening (observed for sub-micrometer probes), so these probes should be able to show a probe collector current.

Before the actual STM experiment, we note that even though the probes show proper rectifying $I-V$ curves the height of the Schottky barrier is lower

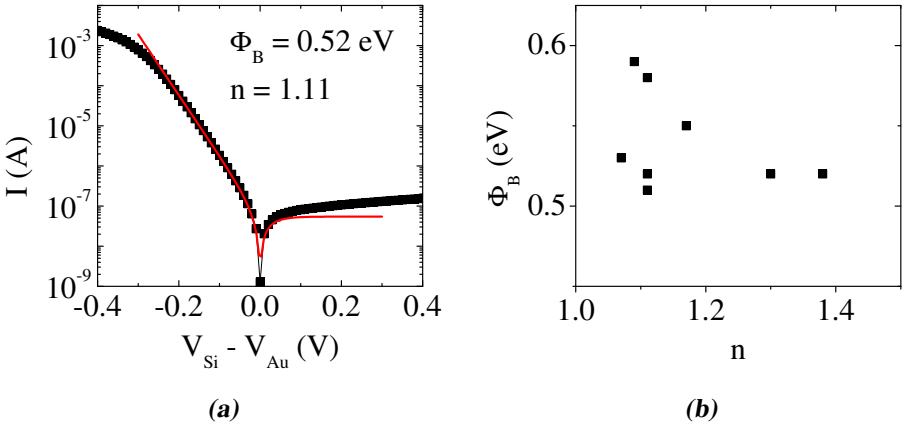

Figure 6.3. *Analysis of diode $I-V$ curves from SF-STM probes fabricated using the second process pathway. (a) Two parameters are extracted from each $I-V$ curve using a fit (red) based on the thermionic emission model, namely the Schottky barrier height (Φ_B) and the ideality factor (n). (b) Typical parameters are limited to ranges of 0.5–0.6 eV for Φ_B and 1.1–1.3 for n.*

than expected. This results in a zero-bias resistance close to 1 MΩ, which is too low for observation of I_C at room temperature. The latter is clear if we monitor the I_C channel even before tunneling takes place. Ideally, one would expect to measure no signal if there is no tunnel current I_T. In reality, due to the low resistance there is current noise in the channel. This noise gets rectified by the diode and results in a net offset in I_C. This offset is easily identified because it has a polarity opposite to the real I_C signal and is present even for $I_T = 0$. The magnitude of the I_C offset versus temperature is shown in Figure 6.4b. The probes show a typical room temperature offset of 10–200 pA. This noise is totally suppressed below 200 K because the diode resistance is increased exponentially at low temperature. At lower temperature the observed offset is mainly the intrinsic offset of our measurement electronics and can be safely subtracted from the data.

The cause for the lower Schottky barrier height as observed by two-terminal $I-V$ curves may be related to the morphology of the edge of the sputtered oxide. The extra oxide is sputtered over a previously grown thermal oxide, so in principle the Si/SiO_2 interface at the sidewalls of the pyramid is nearly ideal. However, when the oxide is thinned down (to remove the thermal oxide which was shadow masked by the nitride cap) the morphology of the

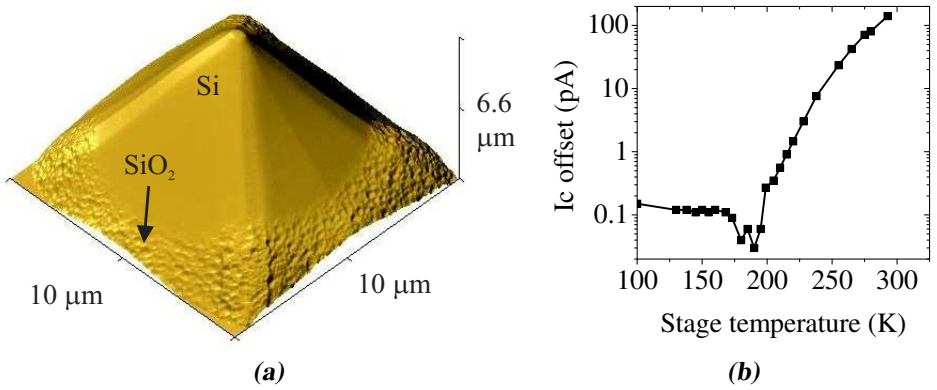

Figure 6.4. *(a) AFM image (perspective view) of SF-STM probe fabricated using the second process pathway, showing the SiO_2 edge. A zoomed-in image near the apex was shown in Figure 4.16b and a SEM image of a similar probe in Figure 4.14. (b) Offset in probe collector signal versus temperature during probe cool down.*

sputtered oxide is transferred to the underlying thermal oxide at its edge (the thinnest region). The result is an oxide edge with pinholes acting as small-sized Schottky diodes, which could show an increased conductance due to narrower Schottky barriers [5, 6]. Another possibility may be the presence of a reduced Schottky barrier height at the stepped sidewalls of the pyramid or their intersections. Even without pinholes, a rough oxide edge can produce field crowding and increased leakage currents [8] which may result in apparent lower Schottky barrier heights in $I-V$ curves. However, we note that Φ_B at the real apex is not reduced. This can be concluded from the collection properties of the probes in STM, as discussed in the next section.

Independently of the actual reason for the apparent lower Schottky barrier height, the fact that we can effectively reduce the noise by cooling down the probe with liquid N_2 to below 200 K allows us to proceed to use these probes for STM imaging and to evaluate their collection properties. Cooling the probe is by no means a limitation on the present capability of the technique, as the sample is not required to be cooled down. We will see in the following section that imaging of a sample at room temperature (with a cooled down probe) and detection of probe collector current is possible, yielding a Schottky barrier height at the apex tunnel contact equal to the literature value of $\Phi_B = 0.8\,\text{eV}$.

6.2 Imaging and collection properties

We proceed to use the SF-STM probes in STM experiments. The probes we focus on for the rest of this chapter are those fabricated using the second process pathway described in section 4.2. We use these probes to scan a metallic sample that consists of a 1 mm wide Si square with a thermally grown 1 µm oxide as the substrate, which is then coated by sputtering to result in a SiO_2/Cr (22 nm)/Au (75 nm) sample. The probe-sample configuration in our STM system was previously described in section 3.3. Our goal is to demonstrate the use of SF-STM probes for topographic imaging of the Au sample and simultaneous measurement of the probe collector current I_C.

The results for imaging a Au surface with a SF-STM probe are shown in Figure 6.5. The topographic image clearly shows the structure of the sputtered Au sample with a typical grain size of 10 nm and a root mean square roughness of 0.9 nm, whereas the simultaneously acquired probe collector image (see Figure 6.5b) shows a rather homogeneous signal of 1.9 pA on average. In order to better quantify the imaging results and account for the small offset present in the signal (due to our measurement electronics) we extracted the distribution of I_C from the image shown in Figure 6.5b and did the same for another image acquired at a tunnel bias (0.7 V) below the threshold for electron collection, which is 0.8 V for a n-Si/Au Schottky barrier. The latter gives an average signal of 0.7 pA that corresponds to the offset. The full energy dependence of the probe collector current is obtained by acquiring $I_C - V_T$ spectra where the tunnel bias is swept while the tunnel current I_T is kept at a constant value. This spectrum is similar to that obtained in BEEM [3] and can be described using the Bell-Kaiser (BK) model [9] previously presented in Equation 2.14. All spectra shown in this section are the average of 2–10 individual spectra taken at a fixed representative location. The results obtained from image analysis or from individual spectra are fully consistent, as shown in Figure 6.5d.

The results in Figure 6.5 demonstrate the successful detection of probe collector current I_C in a probe with a fully rounded apex. The collection spectrum has an onset of about 0.8 V. Therefore in these STM experiments we do not observe a reduced Schottky barrier height at the apex, opposite to the apparent 0.5 eV barrier extracted from two-terminal diode curves in the previous section. From an electrical point of view, we are able to fabricate probes that have all the properties required for SF-STM.

The principle of current collection in SF-STM probes was schematically

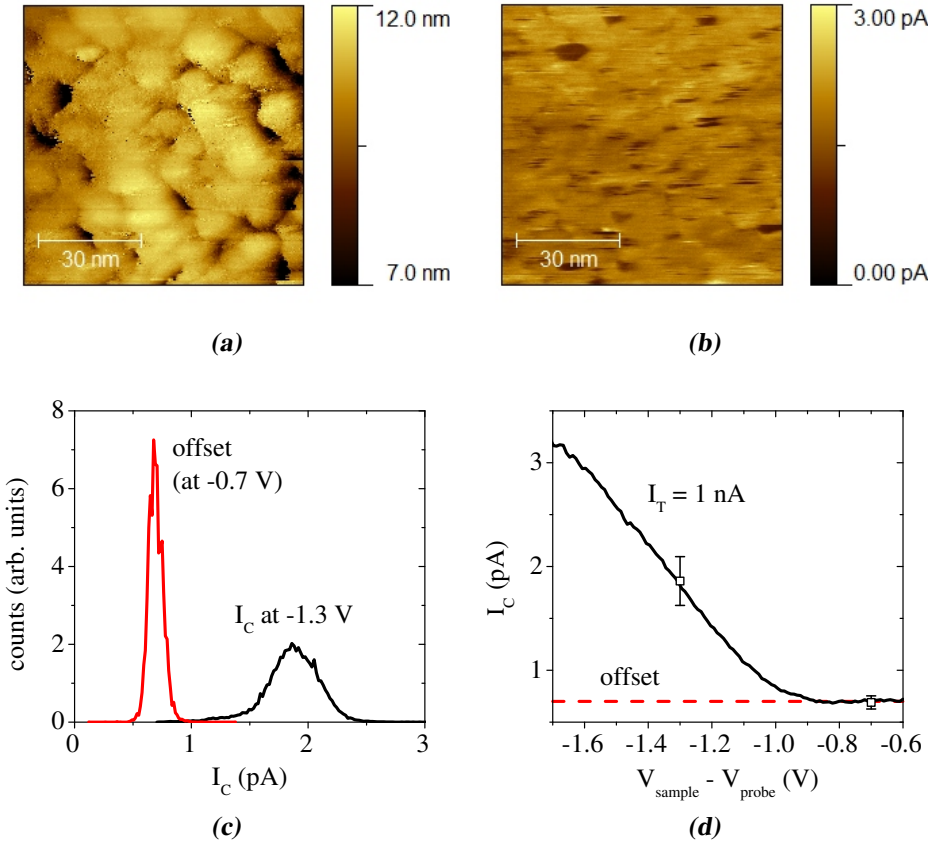

Figure 6.5. *Imaging of sputtered Au sample with a SF-STM probe. Simultaneously acquired topographic (a) and collector current (b) images taken with a SF-STM probe having a Au/$Ni_{80}Fe_{20}$ (2 nm)/Au spin filter at tunneling conditions of $V_T = 1.3$ V and $I_T = 1$ nA. (c) Distribution of probe collector current for the image shown in (b) and another image taken at 0.7 V tunnel bias. (d) Energy spectrum showing the dependence of probe collector current on tunnel bias together with the statistical results from (c) (open squares).*

depicted in Figure 3.2. The ballistic transmission through a metal layer reduces to an exponential decay of the form $T = \exp(-t/\lambda_{eff})$ [10], with t equal to the thickness of the metal layer and λ_{eff} the effective attenuation length given by considering all scattering processes. For a description of the full Au/FM/Au spin filter in our probes we use the formalism shown in Equation 3.1. Using these expressions we can compare our results with previous work. The probe

used in the experiments shown in Figure 6.5 has a ferromagnetic layer of 2 nm $Ni_{80}Fe_{20}$ with a transfer ratio of $I_T/I_C = 1.8$ pA/nA at 1.5 V (after subtraction of the offset). Previous work in our group [11, 12] showed that a planar BEEM sample with a similar layer stack where the $Ni_{80}Fe_{20}$ was 3 nm thick had a transfer ratio of 1.3 pA/nA at 1.5 V. If we assume similar attenuation lengths for both structures (and account for a 3 nm difference in Au thickness) then the results are consistent when the $Ni_{80}Fe_{20}$ attenuation length is $\lambda_{eff} \approx 2$ nm within this 2–3 nm thickness range. We have discussed reported spin-dependent values for λ_{eff} already in section 4.1 and indeed $\lambda_{\downarrow} < \lambda_{eff} < \lambda_{\uparrow}$ as expected.

We have studied the collection properties of SF-STM probes with different spin-filter layers. In Figure 6.6a we show spectra for probes with a thin layer of Co, $Ni_{80}Fe_{20}$, or no ferromagnet at all. All spectra show the typical shape similar to that observed in planar BEEM samples with a quadratic onset near 0.8 V and a (sub)linear bias dependence for higher bias [3]. In this case we are measuring the ballistic transmission of electrons after tunneling into the probe. So we are able to fabricate probes with nearly ideal Si/Au Schottky interfaces and proper ballistic transmission independently of the presence of a ferromagnetic layer to add spin sensitivity.

Interestingly, in Figure 6.6b we also observe collector signal for opposite bias polarity, namely for electron tunneling from probe to sample (or equivalently hole tunneling into the probe). This reverse-mode collection spectra measures the scattering of ballistic holes with conduction-band electrons, the latter may be excited to energies above the Schottky barrier height and in turn be collected into the semiconductor [13]. The signals are rather low, but the spectra are reproducible and scale linearly with the tunnel current. To the best of our knowledge there are no previous reports of such reverse ballistic collection for thin ferromagnetic films on n-Si.

Another interesting result is that obtained for probes that have only one sputtered Au layer, also shown in Figure 6.6. Besides regular use of evaporation we also considered sputtering as a deposition method to achieve more uniform and continuous metal coverage on the pyramidal probes due to its more isotropic nature. Contrary to previous work [14, 15] we observe nearly ideal collection properties for probes with a sputtered metal overlayer. The bias threshold and magnitude of both direct and reverse collection spectra is similar to that obtained for an evaporated Au layer on large pyramidal structures discussed in the previous chapter (see Figure 5.11). To be more quantitative, we fitted the collection spectrum for sputtered Au (20 nm) shown in Figure 6.6a

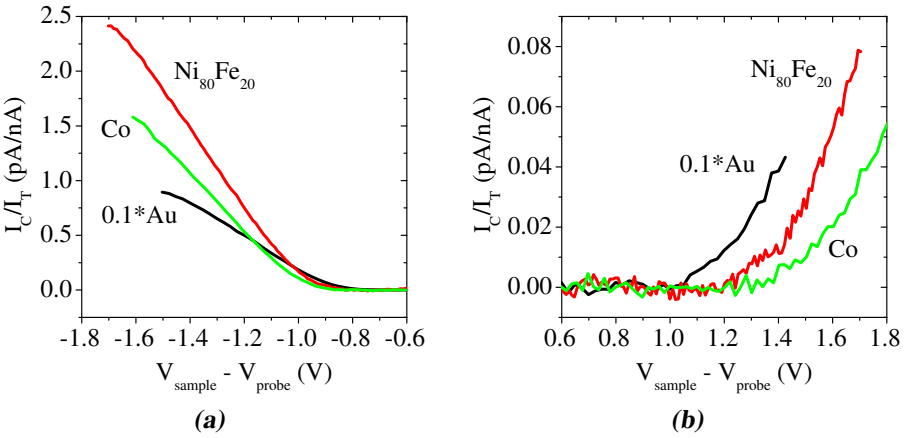

Figure 6.6. *Collection properties of SF-STM probes with different spin filters. (a) Collection spectra for electron tunneling into the SF-STM probe. (b) Reverse collection spectra for hole tunneling into the probe. The metal overlayers are evaporated Au/$Ni_{80}Fe_{20}$ (2 nm)/Au, evaporated Au/Co (2.5 nm)/Au, or sputtered Au (20 nm). The spectra for sputtered Au is divided by 10 for clearer presentation.*

with an analytical BK model developed by Thiaville et al. [15]. The fit is good up to a tunnel bias of 1.3 V (not shown) and yields two parameters: the ballistic transmission of the metal base $R = 0.06$ and the Schottky barrier height $\Phi_B = 0.75\,\text{eV}$. Now we compare these parameters with those obtained for an evaporated Au (16 nm) structure: $R = 0.10$ and $\Phi_B = 0.78\,\text{eV}$ (see Figure 5.10b). Both Schottky barriers have a similar height, with only a decrease of 30 meV for the sputtered case. To compare the transmission parameter R we must consider the slightly different Au thickness of the structures and the effective attenuation length of Au, $\lambda_{Au} = 13\,\text{nm}$ [16]. Starting from the result for evaporated Au (16 nm) we estimate a transmission parameter for a 20 nm thick film of $0.10 \times \exp[(16-20)/13] = 0.07$, consistent with the value of 0.06 obtained for the sputtered case.

The ability to prepare n-Si/Au interfaces via sputtering yielding nearly ideal ballistic transmission properties is technologically relevant. We may wonder why sputtering resulted in deteriorated properties in previous studies. Rippard et al. [14] observed a transmission lower by a factor of 2 for Co-Cu multilayers sputtered at 3 mTorr ($4 \cdot 10^{-3}$ mbar) Ar, whereas both sputtered and evaporated multilayers showed similar $\lambda_{Co} \approx 2.4\,\text{nm}$. They attributed the lower transmission to Co-Cu interface alloying. Since we have only used Au

for sputtering at $6.6 \cdot 10^{-3}$ mbar we cannot rule out this possibility for metal-metal interfaces, but at least we know that we do not observe such alloying at the Si/Au interface. In another study Thiaville et al. [15] reported for Au samples sputtered at a high pressure of 0.1 mbar Ar a transmission almost 30 times lower than for nearly ideal samples (attributed to a disordered Au film) and a lower Schottky barrier height of 0.62 eV (attributed to Si/Au interface alloying). The absence of both effects in our structures may be related to our lower sputtering Ar pressure.

To get a better understanding of the attenuation lengths present in the spin-filter we have prepared probes with different thicknesses of $Ni_{80}Fe_{20}$ within the range of 2–5 nm. After acquiring collection spectra for all the probes we obtained their transfer ratio I_C/I_T at a tunnel bias of $V_T = 1.4\,V$ and plotted it as a function of the ferromagnetic layer thickness. From the literature on transmission of hot electrons through thin metal films we know that the transmission decays exponentially with the thickness of the metal film (see section 4.1). As shown in Figure 6.7 the transmission decreases exponentially with increasing $Ni_{80}Fe_{20}$ thickness and can be fitted with a single effective attenuation length of $\lambda_{eff} = 2.4\,nm$. Because we only have three data points we must take the accuracy of the fit with caution. We note that the extracted effective attenuation length for $Ni_{80}Fe_{20}$ is similar to that found in previous BEEM studies on Co [17]. Furthermore, we also show data for a Co spin filter and for a spin filter consisting of a spin-valve structure $Ni_{80}Fe_{20}$/Au/Co. The Co data adjusts perfectly to the single exponential fit of the $Ni_{80}Fe_{20}$ data.

One could interpret the extracted attenuation length $\lambda_{eff} = 2.4\,nm$ as the majority attenuation length ($\lambda_\uparrow$) [14] for $Ni_{80}Fe_{20}$, since for large ferromagnet thickness the contribution of the spin channel with the largest attenuation length is dominant and this is the case for majority spins [17]. Still, one must be careful since at the beginning of the thickness range considered there is still a sizable contribution from minority spins in the probe collector current. The latter causes the extracted attenuation length to not be exactly $\lambda_\uparrow$ but to exhibit a value $\lambda_\downarrow < \lambda_{eff} \lesssim \lambda_\uparrow$. In section 4.1 we presented a discussion on spin-dependent attenuation lengths found in literature and considered values of $\lambda_\uparrow = 3\,nm$ and $\lambda_\downarrow = 1\,nm$ to be representative for the ferromagnetic films used in this work. To evaluate this assumption we have simulated the dependence of the total transmission of a SF-STM probe on the ferromagnet thickness using the attenuation lengths mentioned above. Then we have fitted this curve with a single exponential decay in the range 2–5 nm and obtained an effective

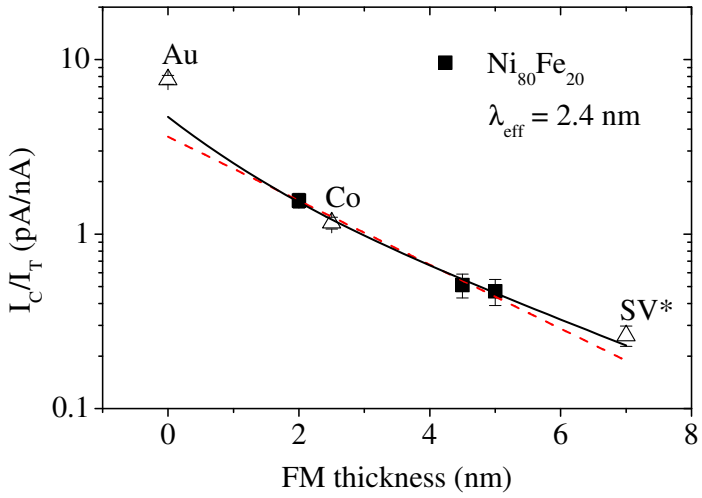

Figure 6.7. *Transfer ratio at V_T=1.4 V for SF-STM probes versus total thickness of ferromagnetic filter. Probes with a Au/$Ni_{80}Fe_{20}$ (2–5 nm)/Au spin filter (black squares) and fits using a single exponential decay with attenuation length λ_{eff} =2.4 nm (dashed red line) and a double exponential decay with attenuation lengths of 1 nm and 3 nm (black line). Open triangles also show data for probes with sputtered Au (20 nm), evaporated Au/Co (2.5 nm)/Au and a spin-valve structure Au/$Ni_{80}Fe_{20}$ (5 nm)/Au (8 nm)/Co (2 nm)/Au. The spin-valve data point SV* is corrected to account for the extra 8 nm of Au between the two ferromagnetic layers. Error bars correspond to the standard deviation of several probes per FM thickness.*

attenuation length of $\lambda_{eff} = 2.5\,\text{nm}$. Therefore our assumptions for majority and minority attenuation lengths are consistent with our data for $Ni_{80}Fe_{20}$. If we fit the simulated total transmission mentioned above to the $Ni_{80}Fe_{20}$ data we obtain a good fit to all probes with magnetic layers, including the probe with the spin-valve structure. Although we have a limited data set, the phenomenological framework developed in chapter 3 and the spin-dependent attenuation lengths used to guide us in designing the probes in section 4.1 do offer a consistent interpretation of the experimental results presented here.

6.3 MFM on probes

After the analysis presented in the previous sections we are now certain that the SF-STM probes can be used as imaging probes and that the basic electrical

requirements regarding the probe collection current and the spin-filter are satisfied. Therefore now we move on to the subject of the magnetization state at the apex of the probe. This is a difficult issue since one cannot use macroscopic magnetic measurements to study the magnetization just at the apex of the probe because the thin ferromagnetic filter is also deposited on the rest of the pyramidal probe and surrounding substrate. Furthermore, we are interested only in the properties of a small magnetic volume at the apex. For these reasons we have decided to perform an initial study of the probe magnetostatics using magnetic force microscopy (MFM).

We used MFM tips provided by SmartTip [18] (type SC-35-M). These are coated on only one side of the tip at the end of the cantilever with a 35 nm thick $Co_{80}Ni_{20}$ alloy. The result is tips with a well defined perpendicular magnetization. Here we discuss dynamic MFM imaging [2] of a SF-STM probe with a spin-filter containing a 5 nm thick $Ni_{80}Fe_{20}$ layer. The simultaneously obtained topographic and magnetic images of this SF-STM probe are shown in Figure 6.8. MFM images shown here are phase images, but operation yielding resonance frequency images gave similar results.

In all MFM images taken at the apex of SF-STM probes we have observed a concentric ring pattern centered at the apex. This pattern is not related to the topographic image or to any real magnetic signal. We have realized that it is an optical interference effect due to the laser light used for detection of the MFM tip oscillation. When the laser light also shines at the edges of the cantilever and the tip moves around the apex of the non-planar SF-STM probe such a pattern is expected. This interference makes it quite difficult to understand what part of the MFM image is actually related to the magnetism of the SF-STM probe. We have applied an in-plane magnetic field of up to 10 mT while imaging the SF-STM probes. From these experiments it is visible that the probe magnetic configuration responds to the applied field, but the actual magnetic image is still quite obscured. A way to sort out this problem is to calculate the difference between two MFM images at different magnetic states of the probe in order to get rid of the non-magnetic background. An image calculated using the MFM images for maximum applied field in opposite directions is shown in Figure 6.8e where the ring pattern has been removed. The dipole-like pattern is an indication that the magnetic state at the apex is addressable with moderate magnetic fields of similar magnitude as the ones we can apply in our modified STM system (up to 14 mT, see section 3.3).

Comparison of images at remanence and under applied field indicates that

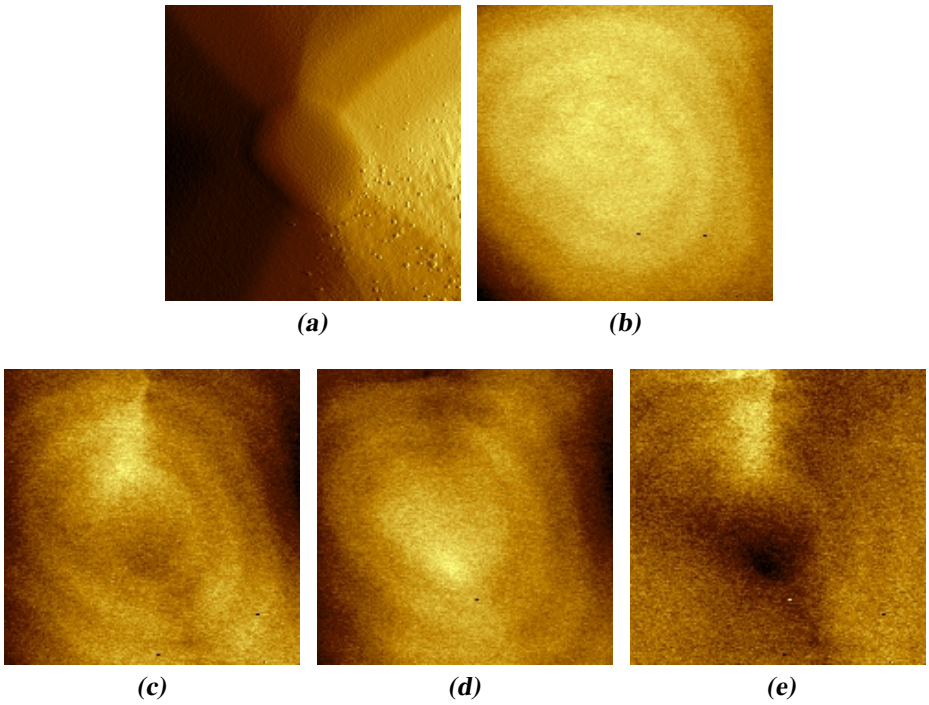

Figure 6.8. *MFM images (2.5 µm) of the apex of a SF-STM probe with $Ni_{80}Fe_{20}$ (5 nm) spin-filter. (a) Topographic (amplitude) image of the apex. (b)–(e) MFM (phase) images. (b) Probe at remanence. (c) Probe under applied in-plane 10 mT magnetic field pointing from top to bottom of the image. (d) Probe under applied magnetic field of opposite polarity to that from (c). (e) Calculated difference image from (c) and (d).*

the SF-STM probe has a low remanence. This is understood by assuming a preferred out-of-plane magnetization direction, contrary to the in-plane applied fields. This is not the desired behavior, as we expected that for very thin films and relatively blunt probes the magnetization of the magnetic coating would be oriented in plane. This way a direct comparison between previous work on planar magnetic BEEM samples and the behavior of SF-STM probes could be done. For example, we mention that in spin-polarized STM (SP-STM) [19, 20] a blunt probe coated with about 2 nm Fe is magnetized in-plane.

Besides the homogeneous MFM image at remanence shown in Figure 6.8 we have also observed formation of domain patterns and interaction between the MFM tip and the soft SF-STM probe resulting in changes of the MFM image. Quantitative methods to understand MFM imaging that resort to math-

ematical models and calibration of the MFM tips [21] or methods that rely on numerical simulations [22] become either invalid or computationally too expensive in this situation of a sample with a three-dimensional topography.

A more practical approach is to compare the SF-STM probe with an MFM tip. MFM tips have been studied for a long time in order to understand their magnetic configuration. Magnetic moments and relative magnetization direction due to applied fields has been studied by imaging current-carrying lines [23] and microscale loops [24, 25] with the MFM tip. We cannot use our probes for MFM imaging, but within this context it is reasonable to expect an out-of-plane probe magnetization as commonly found for MFM tips. The magnetization direction of MFM tips is sensitive to the uniformity of coverage on the pyramid faces and can form vortices [26]. Magnetic vortices are also formed on magnetically coated nanospheres [27] which can be compared with the blunt apex of our SF-STM probes. For a full description of the probe magnetization it may be required to also consider the effect of different angle of deposition on the faces of the pyramid [28, 29]. Clearly the magnetic state at the apex of the probe is an important matter because in SF-STM one is only sensitive to the properties of the tunneling contact at the apex. Control of the magnetization direction of the probes is an ongoing work.

6.4 Conclusions

We have studied the properties of two-terminal semiconductor/ferromagnet probes which are the cornerstone of spin-filter STM, a novel technique for quantitative imaging of tunnel spin polarization on magnetic surfaces. The probes have a rounded apex with a typical radius of curvature below 1 µm serving the double functionality of a tunnel contact for scanning the topography of a sample and an analysis device for measuring spin polarization. We have studied in detail the detection of probe collector current in the semiconductor, which is the signal used for the analysis of spin polarization.

Probes fabricated using two different processes were considered. A first process yielding probes where the semiconductor/ferromagnet Schottky diode is sub-micrometer and localized just at the apex. A second process yielding probes with a larger Schottky area covering the apex and a few micrometers around it. Only the second fabrication process resulted in working probes with a detectable probe collector current. So we decided to continue our work

focusing solely on probes fabricated using the second process pathway.

Macroscopic characterization of the Schottky diodes showed current rectification although not ideal properties. On the other hand, actual use of the probes in STM experiments demonstrated that the electrical properties of the probes are nearly ideal at the tunnel contact area. Both topographic imaging of a Au sample and detection of the probe collector current demonstrate that we have achieved the primary goal of defining a (spin-dependent) energy-filter at the rounded apex of an STM probe.

The collection properties of the probes were analyzed within the framework of ballistic transmission of electrons after tunneling into the probe. Properties like the Schottky barrier height, ballistic transmission, effective attenuation lengths within the spin-filter, proved to be consistent with the literature on ballistic emission microscopy and similar solid-state devices. The latter was true not only for evaporated metal layers, but also for sputtered ones which is a technologically relevant observation. Finally, the magnetization at the apex of the probe seems to be aligned out-of-plane similar to the case of magnetically coated MFM tips. After establishing the basic properties of the SF-STM probes in this work the next step is to perform the actual experiments with spin-polarized surfaces. The latter will be the subject of the next chapter.

References

[1] R. Jansen. "The spin-valve transistor: a review and outlook". *Journal of Physics D: Applied Physics* **36** (19), R289 (2003). [Cited on 136]

[2] A. Thiaville, J. Miltat, and J. M. García. "Magnetic Force Microscopy: Images of Nanostructures and Contrast Modeling". In H. Hopster and H. P. Oepen (eds.), "Magnetic Microscopy of Nanostructures", No. XVIII in NanoScience and Technology, pp. 225–251 (Springer Berlin Heidelberg, 2005), 1st edn. ISBN 978-3-540-40186-5. [Cited on 137, 149]

[3] M. Prietsch. "Ballistic-electron emission microscopy (BEEM): studies of metal/semiconductor interfaces with nanometer resolution". *Physics Reports* **253** (4), 163–233 (1995). [Cited on 137, 140, 143, 145]

[4] J. A. Stroscio and D. M. Eigler. "Atomic and Molecular Manipulation with the Scanning Tunneling Microscope". *Science* **254** (5036), 1319–1326 (1991). [Cited on 139]

[5] R. T. Tung. "Electron transport at metal-semiconductor interfaces: General theory". *Physical Review B* **45** (23), 13509 (1992). [Cited on 139, 142]

[6] G. D. J. Smit, S. Rogge, and T. M. Klapwijk. "Scaling of nano-Schottky-diodes". *Applied Physics Letters* **81** (20), 3852–3854 (2002). [Cited on 139, 142]

[7] S. M. Sze and K. K. Ng. *Physics of semiconductor devices* (John Wiley and Sons, 2007), 3rd edn. ISBN 978-0-471-14323-9. [Cited on 140]

[8] P. A. Tove. "Methods of avoiding edge effects on semiconductor diodes". *Journal of Physics D: Applied Physics* **15** (4), 517 (1982). [Cited on 142]

[9] L. D. Bell and W. J. Kaiser. "Observation of Interface Band Structure by Ballistic-Electron-Emission Microscopy". *Physical Review Letters* **61** (20), 2368 (1988). [Cited on 143]

[10] D. J. Monsma, J. C. Lodder, T. J. A. Popma, and B. Dieny. "Perpendicular Hot Electron Spin-Valve Effect in a New Magnetic Field Sensor: The Spin-Valve Transistor". *Physical Review Letters* **74** (26), 5260 (1995). [Cited on 144]

[11] E. Haq, H. Gokcan, T. Banerjee, F. M. Postma, M. H. Siekman, R. Jansen, and J. C. Lodder. "Nanoscale magnetic hysteresis of $Ni_{80}Fe_{20}$/Au/Co trilayers using ballistic electron magnetic microscopy". *Journal of Applied Physics* **95**, 6930–6932 (2004). [Cited on 145]

[12] E. ul Haq. *Nanoscale spin-dependent transport of electrons and holes in Si-ferromagnet structures*. PhD thesis, University of Twente (2005). ISBN 90-365-2241-2. [Cited on 145]

[13] L. D. Bell, M. H. Hecht, W. J. Kaiser, and L. C. Davis. "Direct spectroscopy of electron and hole scattering". *Physical Review Letters* **64** (22), 2679 (1990). [Cited on 145]

[14] W. H. Rippard, A. C. Perrella, and R. A. Buhrman. "Ballistic current transport studies of ferromagnetic multilayer films and tunnel junctions (invited)". *Journal of Applied Physics* **89**, 6642–6646 (2001). [Cited on 145, 146, 147]

[15] A. Thiaville, F. Caud, C. Vouille, and J. Miltat. "BEEM spectra of various Au-Si samples and their analysis". *The European Physical Journal B - Condensed Matter and Complex Systems* **55** (1), 29–36 (2007). [Cited on 145, 146, 147]

[16] L. D. Bell. "Evidence of Momentum Conservation at a Nonepitaxial Metal/Semiconductor Interface Using Ballistic Electron Emission Microscopy". *Physical Review Letters* **77** (18), 3893 (1996). [Cited on 146]

[17] W. H. Rippard and R. A. Buhrman. "Spin-Dependent Hot Electron Transport in Co/Cu Thin Films". *Physical Review Letters* **84** (5), 971–974 (2000). [Cited on 147]

[18] "SmartTip | Probe Solutions". http://www.smarttip.nl/en/home.php. [Cited on 149]

[19] M. Bode. "Spin-polarized scanning tunnelling microscopy". *Reports on Progress in Physics* **66** (4), 523 (2003). [Cited on 150]

[20] M. Bode and R. Wiesendanger. "Spin-Polarized Scanning Tunneling Spectroscopy". In H. Hopster and H. P. Oepen (eds.), "Magnetic Microscopy of Nanostructures", No. XVIII in NanoScience and Technology, pp. 203–223 (Springer Berlin Heidelberg, 2005), 1st edn. ISBN 978-3-540-40186-5. [Cited on 150]

[21] P. J. A. van Schendel, H. J. Hug, B. Stiefel, S. Martin, and H. Guntherodt. "A method for the calibration of magnetic force microscopy tips". *Journal of Applied Physics* **88** (1), 435–445 (2000). [Cited on 151]

[22] J. M. Garcia, A. Thiaville, J. Miltat, K. J. Kirk, J. N. Chapman, and F. Alouges. "Quantitative interpretation of magnetic force microscopy images from soft patterned elements". *Applied Physics Letters* **79** (5), 656–658 (2001). [Cited on 151]

[23] K. L. Babcock, V. B. Elings, J. Shi, D. D. Awschalom, and M. Dugas. "Field-dependence of microscopic probes in magnetic force microscopy". *Applied Physics Letters* **69** (5), 705–707 (1996). [Cited on 151]

[24] L. Kong and S. Y. Chou. "Quantification of magnetic force microscopy using a micronscale current ring". *Applied Physics Letters* **70** (15), 2043–2045 (1997). [Cited on 151]

[25] A. Carl, J. Lohau, S. Kirsch, and E. F. Wassermann. "Magnetization reversal and coercivity of magnetic-force microscopy tips". *Journal of Applied Physics* **89** (11), 6098–6104 (2001). [Cited on 151]

[26] S. L. Tomlinson and A. N. Farley. "Micromagnetic model for magnetic force microscopy tips". In "The 41st annual conference on magnetism and magnetic materials", vol. 81, pp. 5029–5031 (AIP, Atlanta, Georgia (USA), 1997). [Cited on 151]

[27] M. M. Soares, E. de Biasi, L. N. Coelho, M. C. dos Santos, F. S. de Menezes, M. Knobel, L. C. Sampaio, and F. Garcia. "Magnetic vortices in tridimensional nanomagnetic caps observed using transmission electron microscopy and magnetic force microscopy". *Physical Review B (Condensed Matter and Materials Physics)* **77** (22), 224405–7 (2008). [Cited on 151]

[28] A. Dirks and H. Leamy. "Columnar microstructure in vapor-deposited thin films". *Thin Solid Films* **47** (3), 219–233 (1977). [Cited on 151]

[29] J. M. Alameda, F. Carmona, F. H. Salas, L. M. Alvarez-Prado, R. Morales, and G. T. Pérez. "Effects of the initial stages of film growth on the magnetic anisotropy of obliquely-deposited cobalt thin films". *Journal of Magnetism and Magnetic Materials* **154** (2), 249–253 (1996). [Cited on 151]

CHAPTER 7

Imaging magnetic surfaces with SF-STM

We present experiments on imaging of magnetic surfaces with spin-filter scanning tunneling microscopy. Two-terminal probes featuring a semiconductor/ferromagnet heterostructure at their apex serve as spin-analyzers for the quantification of tunnel spin polarization. We demonstrate the use of these probes for imaging a ferromagnetic surface and evaluate their spin-filtering capabilities. This work sets the ground for further development of this promising imaging technique.

7.1 Background

Magnetic nanostructures are important for both scientific curiosity and practical interest [1]. Our understanding and control of magnetic nanostructures is directly tied to the development of appropriate magnetic microscopy methods. The degree of electronic spin polarization is a property that can be tailored in magnetic nanostructures [2] which is highly relevant for the young field of spintronics [3, 4]. The need for studying spin polarization becomes apparent

when we consider the long-term goal of semiconductor spintronics [5] where spin information is injected, transported, manipulated and detected in nano-electronic devices. Magnetic force microscopy (MFM) [6] has become the workhorse scanning probe technique for imaging magnetic nanostructures but its spatial resolution is limited in practice to more than 10 nm [7, 8] and it is unable to measure electronic properties like spin polarization. On the other hand, spin-polarized scanning tunneling microscopy (SP-STM) [9, 10] has direct access to the electronic properties of a sample with spin sensitivity but as discussed in subsection 2.2.1 the spectroscopic nature of the technique makes the quantitative determination of sample spin polarization difficult, specially close to the Fermi level.

Here we present the initial testing of a novel scanning probe microscopy technique aimed to the high-resolution imaging and quantitative analysis of sample tunnel spin polarization (P_S). The technique, called spin-filter scanning tunneling microscopy (SF-STM), should fulfill three requirements. First, a high spatial resolution for magnetic imaging. Second, the ability to quantify the spin polarization near Fermi level on the surface of a conducting material. Third, general applicability without material restrictions like a specific electronic structure. We introduced the principle of the technique in chapter 3, where we inferred its potential of fulfilling all the requirements aforementioned.

The basic element for the realization of SF-STM is a two-terminal semiconductor/ferromagnet probe operated as depicted in Figure 3.1. The technique is based on spin-polarized tunneling from a magnetic sample and subsequent spin analysis after tunneling within the multi-terminal semiconductor/ferromagnet probe. The principle of spin analysis in the probe relies on the spin-dependent transmission of hot electrons through thin ferromagnetic layers and on the energy-filtering capabilities of semiconductor/metal Schottky barriers, similar to solid state devices [11]. An independent electrical contact to the SF-STM probe, through which the current collected in the semiconductor (I_C) is measured, offers an information channel sensitive to P_S decoupled from topographic or non-spin-polarized electronic contributions.

In the following we will apply SF-STM probes to the imaging of magnetic samples with nominally spin-polarized surfaces. The probes have a layer stack at their apex consisting of n-Si/Au (10–12 nm)/FM/Au (5 nm) where FM is a thin (2–5 nm) ferromagnetic layer of $Ni_{80}Fe_{20}$ or Co, as described in chapter 4. These probes were successfully incorporated in STM experiments involving imaging of non-polarized Au surfaces in chapter 6. Here we study

the appearance of magnetic contrast in the probe collector current I_C, which is a measure of the local tunnel spin polarization of the magnetic sample under investigation. We note that the collector current data has a small offset corresponding to the measured I_C value for tunnel bias below the Schottky barrier height of n-Si/Au (0.8 eV). In this chapter we subtract this offset from the data for a clearer presentation.

Our SF-STM probes have already shown to have the proper electrical properties to yield a measurable probe collector current I_C corresponding to electron transmission within the semiconductor/metal heterostructure after tunneling from near the Fermi level of the sample. The final step in the development of SF-STM is to prove the spin-filtering properties of the probes. When the transmission within the probes is spin dependent one can quantify the tunnel spin polarization P_S of the sample from the relative change in I_C called magnetocurrent (MC). The magnetocurrent is based on the values of I_C for parallel and antiparallel relative magnetization between the magnetic sample and the thin ferromagnetic layer in the probe and is defined as $MC \equiv (I_C^P - I_C^{AP})/I_C^{AP}$ (Equation 2.12). The relationship between MC and P_S was explained in section 3.2 and for a thick enough ferromagnetic spin filter it takes the simple form $MC = 2P_S/(1-P_S)$. Hence a measurement of the MC allows the direct quantification of P_S.

7.2 Ex-situ Co/Al_2O_3 sample

A fundamental requirement for observing magnetocurrent is that the surface of the sample must have a detectable tunnel spin polarization ($P_S \neq 0$). From the discussion and numerical results in section 4.1 we concluded that a minimum spin polarization of at least 5 % should be detectable in our experimental setup. To obtain a spin polarized surface of a ferromagnetic metal one needs to avoid contamination by adsorbate species or oxidation [9]. For this reason most spin-sensitive STM experiments always use samples that are deposited in-situ or at least treated once loaded into the UHV environment.

At the beginning of our work we did not possess the equipment for in-situ deposition of samples or to perform sample treatment. We were forced to load already prepared samples exposed to air into the STM chamber so we could not use simple metallic ferromagnets as samples. A solution to this problem is to coat the magnetic surface with a thin oxide layer similar to the one used in

magnetic tunnel junctions (MTJs) [12]. If the thin oxide acts as a tunnel barrier then one is still able to measure the spin polarization from the underlying FM/oxide interface, as long as the layer is thin enough to allow reliable STM operation without crashing our probes into the oxide. For this experiment we chose to use Co as ferromagnet and Al_2O_3 as the tunnel barrier. This is a model system extensively used in MTJs. The Co/Al_2O_3 interface has a known tunnel spin polarization of $P_S \approx 30\,\%$ [13] determined on structures fabricated with the same deposition facilities we used in our cleanroom. Furthermore, Al_2O_3 is a rather inert surface that can be safely expose to air.

We are interested in keeping the thickness of the oxide as low as possible. If the SF-STM probe would crash into the oxide there is the risk that the metal overlayer of the probe would peel-off rendering the probe useless. Uniform Al_2O_3 barriers are prepared by first depositing a thin layer of Al and then oxidizing it. The Al thickness is very important: if it is too thin or too thick the P_S will be reduced from its optimum value and may not be detectable. This critical Al thickness depends on the oxidation method whether it is plasma or natural oxidation. MTJs studies have shown that for certain plasma conditions (fixed time) the optimum Al thickness is about 1.2 nm [14], whereas for natural oxidation it is about 0.7 nm [15]. In-situ time-resolved studies of natural oxidation of Al confirm that a fast Al oxidation in O_2 occurs up to a thickness of 0.7 nm [16]. Therefore we choose to form our Co/Al_2O_3 by natural oxidation. We cannot use a thinner oxide because our sample will be exposed to air before loading it into the STM chamber and we must avoid oxidation of the underlying Co.

The probe-sample configuration in our STM system was previously described in section 3.3. Our sample consist of a 1 mm wide Si square with a thermally grown 1 µm SiO_2, onto which we have evaporated the Co (15 nm)/Al (0.7 nm) bilayer in an UHV MBE system. We perform the initial oxidation within the MBE system using 10 Torr O_2 for 5 min and only after that we expose the sample to air in order to transfer it to our STM system. We observed probe collector current (see Figure 7.1a) with a magnitude consistent with our previous experiment on Au samples. But the tunneling was not reliable because the sample made contact with the oxide, as observed by the non-exponential decay in current-distance spectroscopy in Figure 7.1b. Certainly the resulting oxide was too thick to prevent the probe from crashing into it at our typical tunneling conditions. For these reasons we decided not to proceed further with these samples and modify our system for in-situ deposition of ferromagnets.

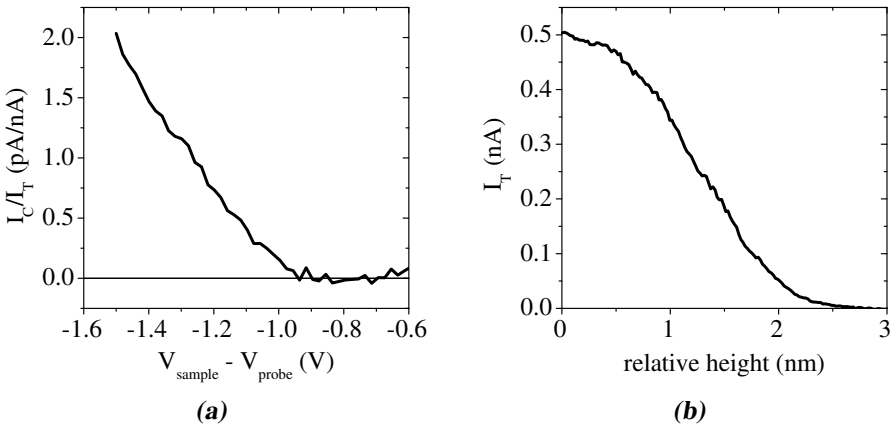

Figure 7.1. *SF-STM with a Au/$Ni_{80}Fe_{20}$ (2 nm)/Au spin filter in the probe, and a Co/Al_2O_3 sample. (a) Probe collector spectrum measured with a fixed tunnel current at I_T =0.5 nA. Note that negative tunnel bias corresponds to electrons tunneling from the Fermi level of the sample into the probe. (b) Tunnel current-distance spectrum at a tunnel bias of -1.2 V. Zero height corresponds to the set-point distance at I_T =0.5 nA. The probe was kept at 96 K.*

7.3 In-situ Co sample

We designed and assembled a deposition chamber connected to our main STM chamber in order to deposit fresh ferromagnetic metals in-situ prior to studying them with SF-STM without breaking vacuum. This modification to our STM system was described in section 3.3. In this way we can work with clean and unoxidized metallic magnetic surfaces. We use Si/SiO_2 substrates (as described in the previous section) onto which we deposit a thin ferromagnetic Co film. The deposition conditions and morphology of the films were properly characterized as shown in Table 3.1. Besides smooth surfaces we also need to test the magnetic properties of the samples. In our modified STM setup we can only apply in-plane magnetic fields of up to 140 Oe. So we need a sample of which we can modify its magnetic state at smaller fields. We characterized our Co samples ex-situ using a vector vibrating sample magnetometer model 10 of ADE technologies [17]. The magnetic characterization (see Figure 7.2) showed that our Co films are magnetized in-plane and have a small uniaxial anisotropy [18] but they are easily switched with low fields within the 10–20 Oe range. For the relatively thick films of 15–40 nm Co on SiO_2 that we

have used, the films have a stable switching with in-plane easy axis [19].

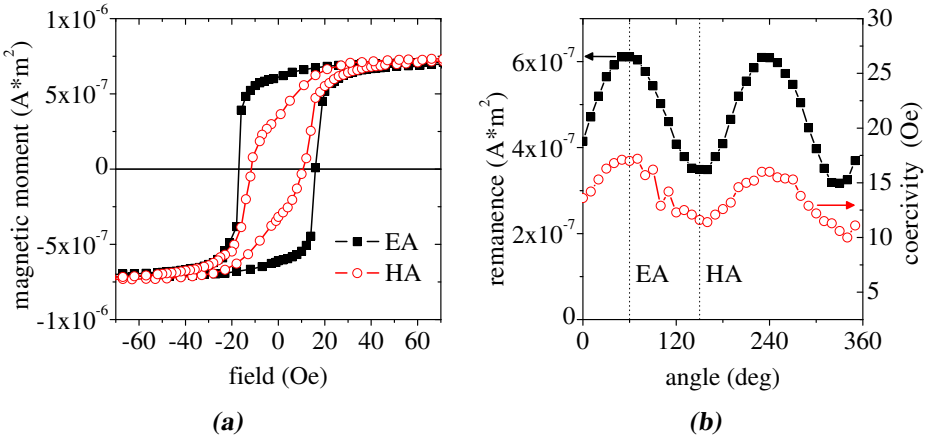

Figure 7.2. *Magnetic characterization of Co film deposited in our STM setup. (a) Magnetic moment versus applied field in two different in-plane directions. (b) Remanence and coercivity for in-plane field applied at different angles. In both figures the easy (EA) and hard (HA) axis are indicated. The sample is a 32 nm thick circular Co film with 5 mm diameter and a measured saturation magnetization of about 1200 kA/m.*

We chose Co as a model system to study spin polarization because it has been the subject of extensive theoretical and experimental work. Theory predicts that the spin polarization of Co in vacuum is negative ($P_S \approx -30\,\%$) due to a minority surface state below Fermi level [20]. Experimental work using SP-STM inferred a spin polarization of -23 % [21] but due to the inadequate normalization $(\mathrm{d}I/\mathrm{d}V)/(I/V)$ of tunnel spectra the spin polarization near Fermi level is not quantifiable by SP-STM [22]. Further theoretical work has also determined that the spin polarization of Co is negative, but can easily be changed to positive due to the effect of an oxygen layer [23] or to the presence of an Al_2O_3 oxide barrier [24, 25]. A similar effect of an oxygen layer has been predicted for Fe [26]. Therefore the sign of spin polarization observed in Co surfaces depends on the presence of oxygen inside the UHV chamber. We note that hydrogen may also change the sign of spin polarization because it quenches surface states in the Co surface [27].

We present the imaging of a fresh Co surface in Figure 7.3 using a similar SF-STM probe to that used previously for the Co/Al_2O_3 sample. The probe collector current I_C shows an energy dependence similar to the previous results for both Au (see chapter 6) and Co/Al_2O_3 surfaces, which demonstrates the

robustness of the I_C signal. Furthermore, the tunnel current-distance spectrum shows an exponential decrease in I_T with distance, from which we extracted typical tunnel barrier heights (ϕ_0) of 2–3.5 eV using Equation 2.7. The latter is in sharp contrast with the behavior observed for the Co/Al_2O_3 sample and is consistent with clean metallic surfaces [28]. From the topographic image of the Co surface we obtained a root mean square roughness of 0.34 nm that fits well the atomic force microscopy (AFM) characterization done ex-situ (see Table 3.1). The statistical analysis of the probe collector current image shows a single peaked distribution with an average value consistent with the individual energy spectrum. Next we studied the effect of an applied magnetic field on the probe collector current I_C. From in-plane magnetic field sweeps at constant tunneling conditions (current and bias) and at a fixed tip location we could not observe any clear magnetic dependence of I_C. Averaging several field loops only resulted in a constant I_C value (not shown).

The lack of magnetocurrent in the aforementioned experiment may be explained because of a too small magnetic contrast when using a 2 nm thick ferromagnetic spin filter within our SF-STM probes. The magnetocurrent increases with the thickness of the ferromagnetic spin filter as discussed in section 4.1. If the spin polarization of our Co sample is about 10 % we would expect a magnetocurrent of only 12 % for the ideal case when the sample and probe magnetizations can be made to align parallel and antiparallel to each other. A magnetocurrent of 12 % is close to the estimated detection limit of SF-STM.

Therefore we also investigated the use of a thicker spin filter. The results for using a probe with a 5 nm $Ni_{80}Fe_{20}$ spin filter are shown in Figure 7.4. Again we observe a probe collector current with a proper energy dependence that matches the statistics obtained from imaging. The statistical distribution of collector current for an image still shows a single peak, with little I_C contrast in the image (not shown). Nevertheless, when we performed magnetic field sweeps there was a small modulation of I_C showing a minimum for fields close to zero. Although the modulation was small, it was visible after averaging four field loops (each sweep direction is averaged separately). The issue is that the modulation was so small that it was obscured by the typical distribution observed in an image scan, as indicated by the arrows in Figure 7.4b. The field sweeps in Figure 7.4c show a small modulation in I_C but the lower I_C value also appears erratically at higher fields. A clear modulation of I_C was observed with other similar probe as shown in Figure 7.4d. Such a modulation was not

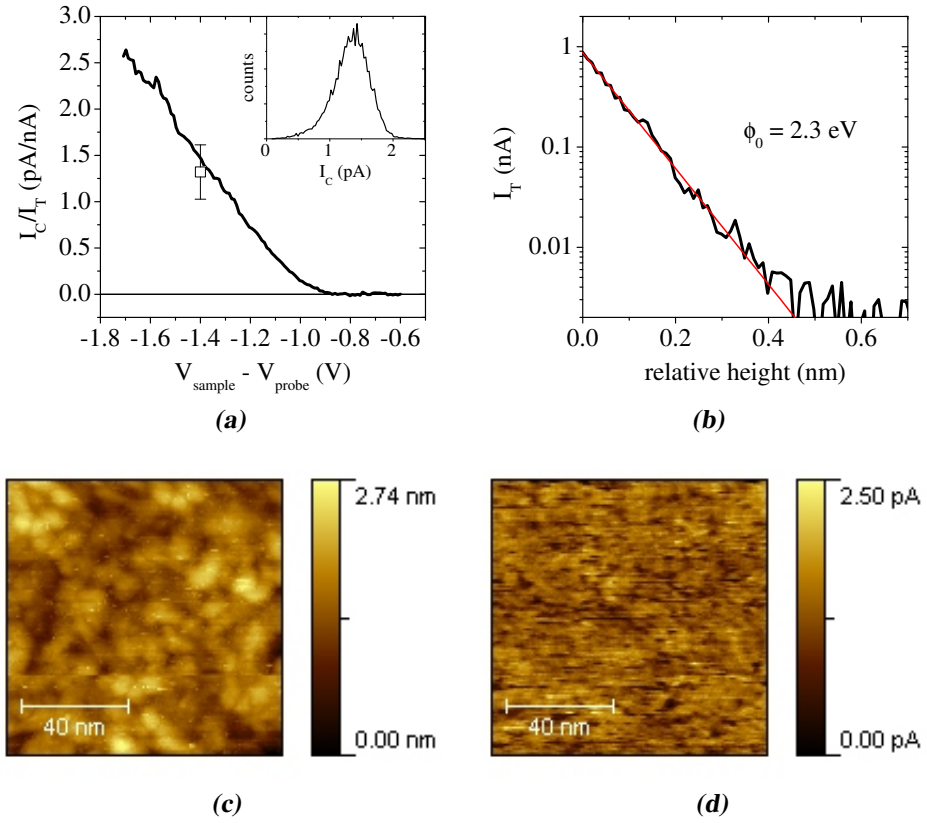

Figure 7.3. *SF-STM with a Au/$Ni_{80}Fe_{20}$ (2 nm)/Au spin filter in the probe, and a Co sample. (a) Probe collector spectrum. The square data point and the inset correspond to the distribution of probe collector current for the image shown in Figure 7.3d. (b) Tunnel current-distance spectrum at a tunnel bias of -1.2 V. Topographic (c) and collected I_C current (d) images taken using tunneling conditions of -1.4 V and 1 nA. The probe was kept at 96 K.*

related to drift of the probe or sample to a location with different collection properties due to the applied magnetic field, since the effect was reproducible and not depending on location.

From the results of probes with a 5 nm thick ferromagnet we could extract a positive magnetocurrent of 10–15 %, under the assumption that the small modulation is magnetic in origin. We also assume that parallel configuration occurs at high fields and antiparallel one at low fields. Using the calculations shown in Figure 4.2 this corresponds to a tunnel spin polarization P_S = 5–8 %.

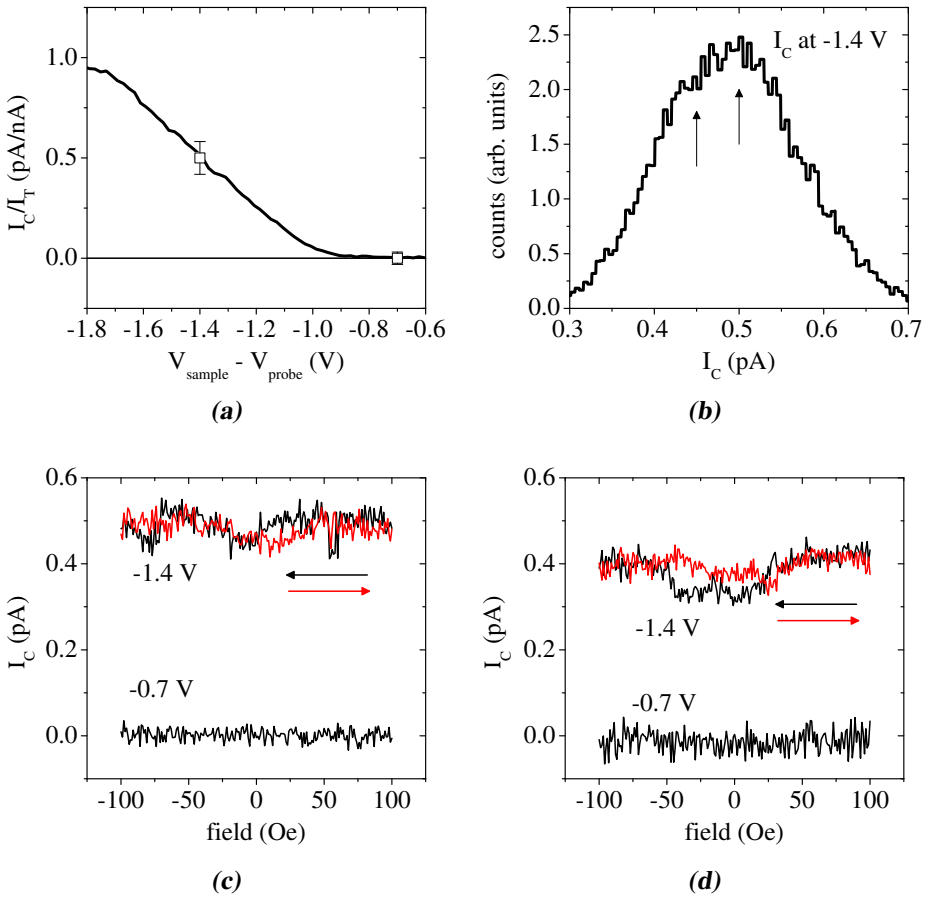

Figure 7.4. *SF-STM with a Au/$Ni_{80}Fe_{20}$ (5 nm)/Au spin filter in the probe, and a Co sample. (a) Probe collector spectrum. The square data points correspond to the distribution of probe collector current from images. (b) I_C distribution for an image acquired using tunneling conditions of -1.4 V and 1 nA. (c) Field sweeps using same probe and tunneling current as in (b) for tunnel bias of -1.4 V (same as (b)) and -0.7 V (reference). (d) Field sweep in another probe with similar spin filter layer stack. Field sweeps are averages from four field loops by averaging each sweep direction separately. The probes were kept at 95 K.*

The question arises as to why do we obtain such a low spin polarization? Furthermore, why is there little or no hysteresis in our field sweeps? We know the Co sample is easily switched with fields below 20 Oe but the magnetic state of the tip at the apex is not fully understood. From our previous MFM study

in section 6.3 it seemed that the probes have an out-of-plane magnetization at the apex. This would lead to a reduced magnetocurrent response due to the inability to reach a fully aligned antiparallel state. At this point one could even question the spin-filter capabilities of the SF-STM probes. Before further development of the probes we need to prove that they are able to act as spin filters, not only as carrier collectors and energy filters.

7.3.1 Probes with spin-valve metal overlayer

To prove the spin-filter capability of our SF-STM probes we have prepared probes that incorporate a spin valve within the metal overlayer. The structure of these probes is n-Si/Au/$Ni_{80}Fe_{20}$ (5 nm)/Au (8 nm)/Co (2 nm)/Au. Each magnetic layer acts as a spin filter and the total transmission of the structure depends on the relative alignment between the two. By changing the magnetic alignment between the layers in the spin valve the probe collector current I_C should also change, in analogy to the classical optical polarizer-analyzer experiment. This effect is used in ballistic electron magnetic microscopy [29] and in solid state devices like the spin-valve transistor [11]. In this way we can assert the spin-filter capabilities and examine the magnetic behavior of our probes without including extrinsic factors like the spin polarization or relative magnetic alignment of the sample.

As shown in Figure 7.5 the probes incorporating a spin valve can perform imaging of the Co surface equally well. The collector current images were homogeneous with no appreciable contrast. The major drawback is the reduced probe collector current due to the lower transmission of the thicker metal overlayer. On the other hand, applying magnetic field caused a strong modulation of the collector current by about a factor of two, as seen in Figure 7.5c. We observed a lower I_C for large positive fields, whereas a larger I_C was observed for large negative fields. The dependence of I_C on magnetic field was absent for the signal measured using a tunnel bias of -0.7 V, consistent with the lack of electron collection for energies below the n-Si/Au Schottky barrier height (0.8 eV). Contrary to the expectations, no hysteresis was observed in the field sweeps for this probe. The modulation was fully reversible therefore we only show here averages of two half loops for each tunnel condition. The observed I_C modulation was not due to drift of the tip because of the applied magnetic field, as we could confirm by observing the same effect in several locations. To fully prove the magnetic nature of this modulation we have obtained images

of the exact same location for two different polarities of the applied field and obtained the distribution of I_C values for each image, as shown in Figure 7.5d. In this case +80 Oe corresponds to a low collection state and -80 Oe to a high collection state. We associate these states to antiparallel and parallel magnetization of the two magnetic layers of the spin valve in the probe, respectively. By performing a gaussian fit to each I_C distribution we obtained average values for each magnetic state. The resultant magnetocurrent reaches a value of 210 % at a tunnel bias of -1.3 V ($I_C^P = 0.124\,\text{pA}$ and $I_C^{AP} = 0.040\,\text{pA}$). We have observed similar non-hysteretic field sweeps with a modulation of about 200 % for other probes and samples, even on a non-spin-polarized Au surface. Therefore we mainly attribute the effect to the spin valve in the probe alone.

In a few cases we observed hysteresis in I_C during magnetic field sweeps. One such example is shown in Figure 7.6a where a clear hysteresis is present and it is possible to reach well defined parallel and antiparallel states. After setting the spin valve in each magnetic state we have taken energy spectra as shown in Figure 7.6b. Both spectra show similar energy dependence but different magnitude of the collection signal. The magnetocurrent in this case is totally consistent with the previous case of a non-hysteretic probe, reaching about 200 % at -1.3 V ($I_C^P = 0.100\,\text{pA}$ and $I_C^{AP} = 0.034\,\text{pA}$). Even though we observe hysteresis, the magnetic properties of the spin valve on the probe are different than for the case of a planar structure. The field sweep in Figure 7.6a shows that there is only one magnetic reversal event for each sweep direction, at fields of ± 20 Oe. This indicates that only one magnetic layer is switching whereas the other seems to be magnetically pinned. For planar spin valves of similar structure both layers are free to switch their magnetization at relatively low fields. These results using a SF-STM probe coated with a spin valve reinforce the interpretation that the absence of any appreciable magnetocurrent for the case of probes with a single magnetic filter may be due to an inappropriate magnetization direction at the apex of the probes for imaging Co thin films with in-plane magnetization.

We can also use these results to test the validity of the parameters we have considered for the spin filter layers. The total transmission of the spin valve can be evaluated using similar expressions as in Equation 3.1 taking into consideration the presence of two ferromagnetic layers. We have calculated the relative transmission for a spin valve consisting of two magnetic layers of 5 nm and 2 nm with both layers having the same attenuation lengths $\lambda_\uparrow = 3\,\text{nm}$ and $\lambda_\downarrow = 1\,\text{nm}$, as discussed in section 4.1. The calculated magnetocurrent has

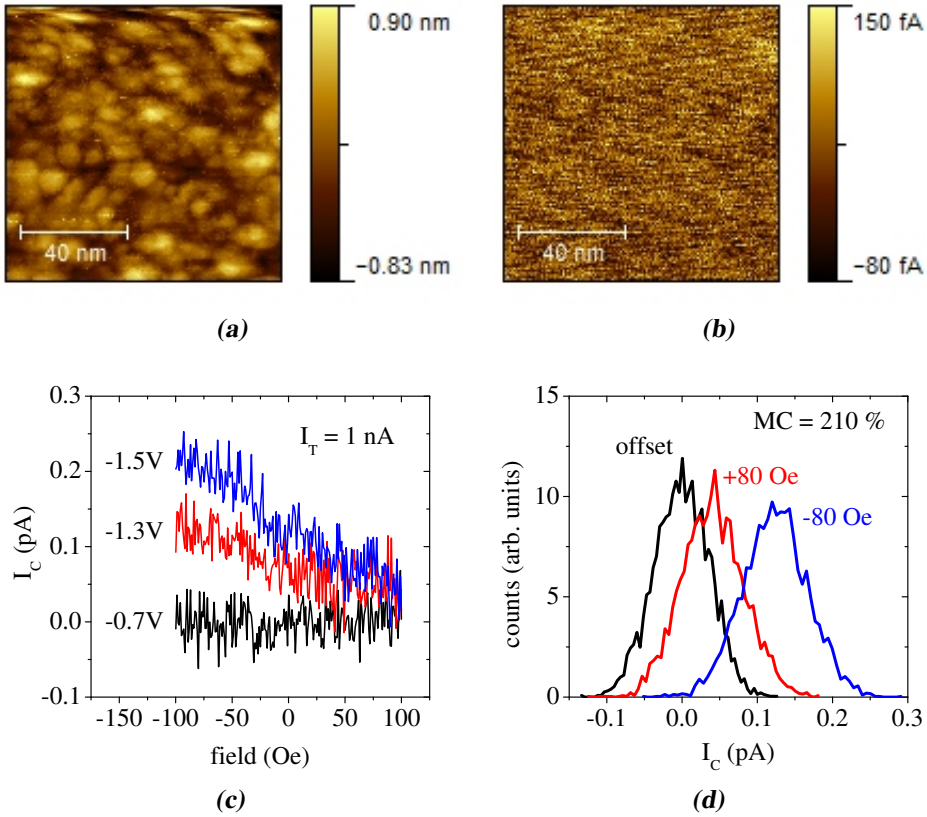

Figure 7.5. *SF-STM with a spin-valve filter in the probe, and a Co sample. (a) Topographic image. (b) Simultaneous probe collector current image. Images acquired at tunneling conditions of -1.3 V, 1 nA and with a +80 Oe magnetic field. (c) Field sweeps at different tunneling bias show a reversible modulation in I_C with field, except at -0.7 V where no collection takes place. (d) I_C distributions for images on same area acquired at similar tunnel conditions as (b), except one for offset current at -0.7 V. The probe was kept at 95 K.*

a value of MC = 237 % that fits very well our observations. Still, we note that similar layer structures but in planar geometry have shown a magnetocurrent of 400 % [30]. The important message is that we have demonstrated the spin-filter effect for electron transmission within our SF-STM probes. This finding allow us to focus on other factors that may be limiting the practical use of the technique.

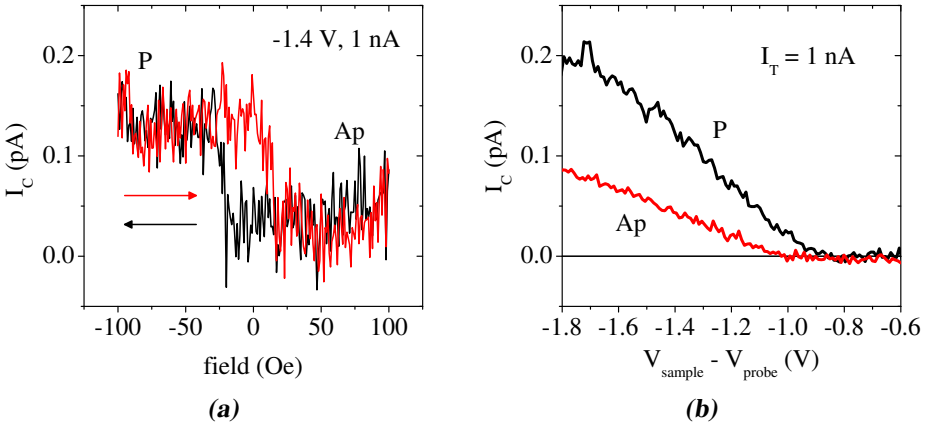

Figure 7.6. *SF-STM with a spin-valve filter in the probe, and a Co sample. (a) Field sweep shows hysteresis in I_C for this probe. (b) Probe collector spectrum for parallel (P) and antiparallel (Ap) states of the spin valve. The probe was kept at 95 K.*

7.3.2 Probes with homogeneous coating

We have identified the magnetization at the apex of the SF-STM probe to be a matter of concern for the reliable determination of spin polarization. Most probes seem to lack hysteresis, probably related to an out-of-plane magnetization that is undesirable from the point of view of our in-plane magnetic field in our STM setup and also for the thin film Co samples. Besides, the experiments with spin-valve structures in the probe (previous subsection) also confirmed this view together with the MFM data (section 6.3). In the following, we present an initial effort to direct the magnetization at the apex of the probe into the proper in-plane orientation.

So far we have used evaporation in a MBE UHV system for the deposition of the metal overlayer. This deposition method is highly directional. In our MBE system the incident beam does not impinge the probes at normal incidence, rather it is at an angle of roughly 20 degrees. The latter, together with the geometry of the pyramidal probes, produces a non-uniform metal coating on the pyramid sidewalls. This is reminiscent to the method used in MFM tips to direct the tip magnetization along the axis of the tip, i.e. covering one or two sides preferentially [31]. Our deposition method might be part of the reason why the probes do not seem to have a well defined in-plane magnetization at the apex. As a first approach to solve this issue we

have included in our deposition procedure the continuous rotation of the chip carrying the probes during the deposition of the metal overlayer. This was not included before because our MBE system does not have such a facility, therefore the user must do this rotation manually while taking care of the rest of the deposition process.

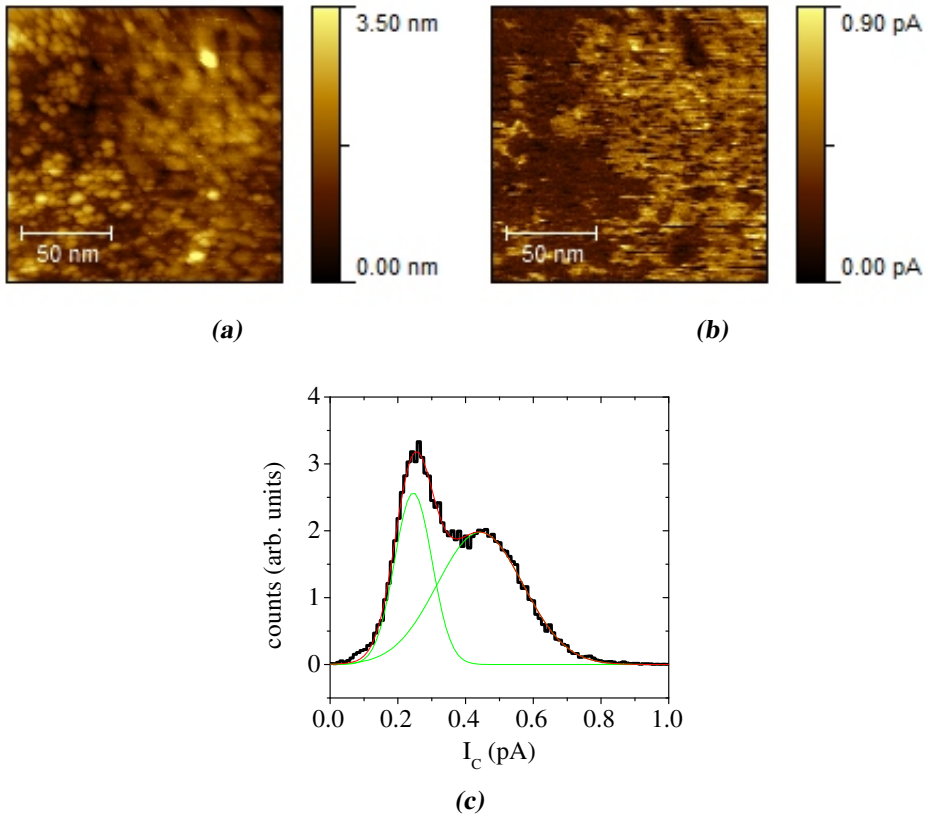

Figure 7.7. *SF-STM with a homogeneously covered Au/$Ni_{80}Fe_{20}$ (4.5 nm)/Au spin filter probe and a Co sample. (a) Topographic image. (b) Simultaneous probe collector current image. (c) Distribution of probe collector current for image (b). Tunneling conditions $V_T = -1.4$ V and $I_T = 1$ nA. The probe was kept at 95 K.*

Using continuous rotation while the incident beam is at 20 degrees indeed improves the homogeneity of the coverage of the metal layers on the pyramidal sidewalls of the probe. We have fabricated a set of such probes and have used them on a fresh Co sample surface as shown in Figure 7.7. From three probes tested, one of them produced a strong contrast in the probe collector current in

Figure 7.7b reminiscent of imaging two adjacent domains. The distribution of the probe collector current is double peaked and can be well fit with two gaussians. The resulting values for low and high collector current are 0.25 pA and 0.44 pA at the tunneling conditions used.

We must be careful while considering this image as being magnetic in origin. We performed magnetic field sweeps in order to see a hysteresis or reproducible modulation of the collector current. Although there were variations in I_C we failed to identify a reproducible modulation with applied field, so we cannot be certain that what we see is magnetic information. If we assume that the contrast is magnetic in origin we can use the results of the fit to extract a magnetocurrent value. Taking the high collector current value (0.44 pA) as that corresponding to the parallel state and the lower value (0.25 pA) to the antiparallel state then we obtain MC = 76 %. For the thickness of the spin filter used and using the numerical results shown in Figure 4.2 this magnetocurrent corresponds to a spin polarization of $P_S = 30\,\%$.

7.4 Perpendicularly magnetized Co/Pt sample

Motivated by the results from the previous section we decided to make modifications on the sample side. If the main reason for the lack of magnetic contrast is that the easy axis for the sample (in-plane) and the probe are orthogonal then using a sample with perpendicular magnetic anisotropy should prove helpful. Currently we are limited in our STM setup to deposit in-situ only one ferromagnetic material and we cannot perform in-situ sample cleaning or treatment (for example in-situ sputtering and annealing). Therefore we looked for a solution that could work with the present experimental setup.

We found a workable solution in preparing a sample outside the STM with perpendicular magnetization and then coating it with a thin ferromagnetic layer inside the STM. As a sample we chose a Co/Pt multilayer: Pt 4 nm + 20*(Co 0.5 nm/ Pt 1 nm). The working protocol was to fabricate the multilayer outside of the STM system in another vacuum system, then expose it to air, load it into the STM chamber and finally cover it by a very thin Co layer in-situ. Co/Pt multilayers can have perpendicular magnetic anisotropy due to interface anisotropy between Co and Pt [32, 33]. We have used them in previous work for the fabrication of magnetic patterned media with perpendicular anisotropy [34]. Furthermore, Pt is a noble metal resistant to oxidation. Exposure to air for short

times results in the oxidation of about one monolayer of Pt [35]. Therefore a Co/Pt multilayer seems as an ideal test sample with out-of-plane magnetization. The last ingredient is the need of a spin-polarized surface. We achieve this by in-situ deposition of about two monolayers of Co on top of the Pt surface of the multilayer after loading it into the STM. Such a thin Co coverage is enough to obtain a spin-polarized surface and at the same time is thin enough so that the magnetization at the surface may remain perpendicularly oriented. We note that another well-known multilayer system involving Co and having perpendicular anisotropy is Co/Au [36, 37].

The result of using SF-STM to scan a Co/Pt sample is presented in Figure 7.8. Besides a slightly rougher surface we observe that there is a clear contrast in the collector current image. The contrast is (partly) correlated to the topography, probably due to the limited resolution of our blunt probes when the surface is not smooth enough. Nevertheless, the contrast shows a distinct pattern that cannot be fully explained by the granular topography of the sample. A statistical analysis of the collector current image yields a broad distribution that seems to be single peaked (see Figure 7.8c). Still, it can be approximated by a double gaussian. The resulting low and high collector current values for the two peaks are 0.29 pA and 0.45 pA. These values are consistent with the average values of the low and high current areas estimated from line cross-sections from the image (see Figure 7.8d). The resulting magnetocurrent is 55 % which for the SF-STM probe used is equivalent to a spin polarization of $P_S = 24\,\%$. The latter is close to the value of $P_S = 30\,\%$ obtained previously for the in-plane Co sample. Therefore the results from both sample magnetization directions seem to be consistent.

We can gain insight into the nature of the contrast by comparing the SF-STM image with MFM on a similar sample. We have processed the SF-STM image shown in Figure 7.8b by applying an averaging filter of 10 pixels (about 40 nm), the result is shown in Figure 7.9a. This filtering serves to artificially reduce the resolution of the SF-STM image and to reduce the noise. Since the resolution of MFM is intrinsically lower than STM this approach is valid to compare both results. The resulting pattern is quite similar to that observed by MFM in Figure 7.9b. We note that the MFM image is not taken in the same area as the SF-STM image. The agreement of contrast pattern among SF-STM and MFM data, together with similar spin polarizations obtained in Co samples with different magnetic anisotropies, is an indication that the last couple of experiments may in fact be the first observation of surface magnetism

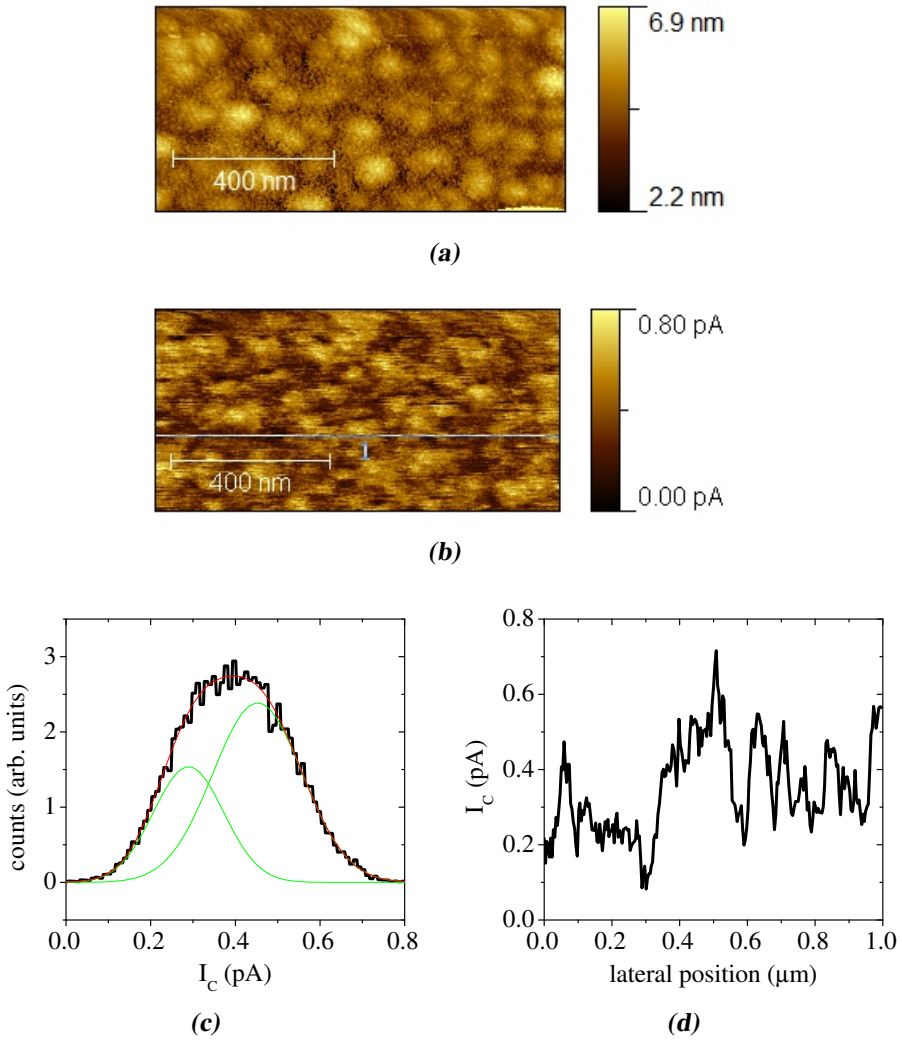

Figure 7.8. *SF-STM with a Au/$Ni_{80}Fe_{20}$ (4.5 nm)/Au spin filter in the probe, and a Co/Pt sample. (a) Topographic image. (b) Simultaneous probe collector current image. (c) Distribution of probe collector current for image (b). (d) I_C Profile along scan line shown in (b). Tunneling conditions of -1.3 V and 1 nA. The probe was kept at 96 K.*

by images acquired with SF-STM. We note that currently we cannot apply out-of-plane magnetic field in order to obtain hysteresis loops of SF-STM images showing explicitly the magnetic field dependence of the probe collector current. Hence, we cannot yet make an unambiguous conclusion about whether or not the observations constitute true SF-STM.

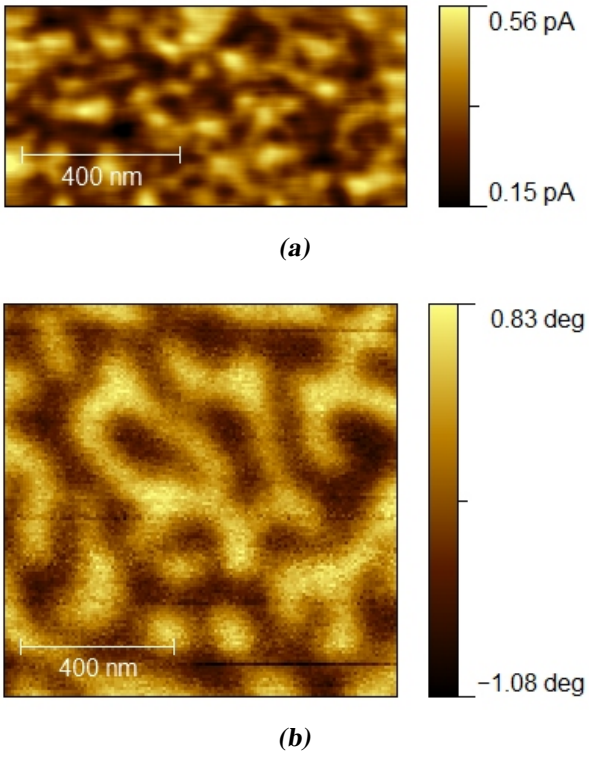

Figure 7.9. *Comparison of magnetic imaging of Co/Pt sample by different methods. (a) Average filtering of Figure 7.8b. (b) MFM image of Co/Pt sample.*

7.5 Discussion and outlook

In previous chapters we have shown that SF-STM probes, which are the cornerstone of SF-STM, can be reliably fabricated such that they fulfill all the geometrical and electrical requirements for SF-STM operation. Nevertheless, the observation of contrast with magnetic origin proved to be challenging. We do know that the probes have spin-filtering properties, as deduced from the experiments using probes with a spin-valve structure. Therefore the initial lack of magnetic contrast in our experiments on Co surfaces pointed to the importance of factors other than the electrical properties and turned our attention to the magnetic properties. Since the MFM and spin-valve data indicate the latter to result in an out-of-plane magnetization of the probe then it is clear that the experimental efforts shown in the last two sections are oriented along a proper path of optimization of the relative magnetization of sample and probe.

A possible concern is the possibility of affecting the sample magnetization by the stray field of a perpendicularly magnetized SF-STM probe. If the sample gets always in parallel magnetic state relative to the probe then no magnetic contrast would be observed. This problem arises especially while imaging samples with low coercivity, as for example the Co films used here. The probe geometry resembles a MFM pyramidal tip, so we consider results from MFM literature. Even for magnetically soft samples a thin enough magnetic probe coating does not have a strong effect on the magnetization of the sample due to the localized nature of the stray field [38]. Still, the generated stray fields can be relatively large [39, 40, 41].

For comparison we can also consider the case of SP-STM tips with ferromagnetic coating. Analysis of SP-STM images have shown that Fe tips caused tip-induced magnetic modifications on the Gd(0001) surface when the Fe thickness was larger than 20 nm [42]. We are using ferromagnetc spin filters of about 5 nm, much thinner than 20 nm. Besides, the presence of minitips made of magnetic material at the apex of SP-STM tips can also produce sizable (though localized) magnetic stray field [43]. The SF-STM probes are partially exempted from the latter problem because the probe surface is not magnetic (Au). There is a bigger chance that any minitip on the probe apex acting as the dominant tunneling tip is just a small Au grain at the surface that will not produce any stray field. The presence of the last Au layer is also acting in our favor because it is a natural limiter of the distance between the probe ferromagnetic filter and the sample. We note that our rounded, blunt, thin film (< 5 nm) probe is a good design for keeping a reasonable level stray field from the tip [44].

We can mention other goals for improving the probe and STM setup besides achieving a better control of the probe magnetization or adding the capability of applying perpendicular magnetic fields in the STM. Improvements on the STM setup would include the modification of the scan head and tip holder to support the use of a two-terminal probe. In this way we would not be forced to use the probe/sample configuration shown in Figure 3.4 leading to more freedom on the type of samples that could be studied. Of course one is also interested in having in-situ facilities for sample treatment and preparation, which would allow for the study of clean and epitaxial samples.

Related to the probe, most improvements are related to the microfabrication process. For a more practical operation of the SF-STM technique one would like to not have to cool down the probe before each measurement. Room

temperature operation (on the probe) can be realized by improving the quality of the isolation oxide edge close to the apex, since a defective edge leads to high leakage currents that can only be avoided by cooling down the probe. The nature of the oxide edge or the diode interface is highly dependent on the microfabrication process. Another fabrication related issue is the properties of the spin filter metallic overlayer. At the moment the metals deposited on the Si apex are polycrystalline. If the probes would have an epitaxial semiconductor/metal heterostructure at the apex then the transmission properties and hence also the probe collector signal could be increased. Larger signals mean less acquisition time. Finally the material at the surface of the SF-STM probe could be different than Au. For example, a probe with a Pt surface could achieve nearly atomic spatial resolution due to the electronic states of Pt atoms or clusters at the apex [45].

Scientific opportunities

We close this work with comments on the scientific opportunities for a technique like SF-STM. A microscopy with the capability of quantifying spin-polarization at high spatial resolution is a strong need for both fundamental materials science and for applications to spintronics. We exhort the reader to consider the influence that scanning probe techniques like MFM or SP-STM have had in shaping modern-day magnetism. In times where the electron spin is entering the field of semiconductor electronics and devices keep getting ever smaller, nanoscale characterization is a must.

From the point of view of materials science, the study of complex surfaces is a rich subject full of possibilities. One can start by considering simple elemental surfaces and aim at determining the tunnel spin polarization for different crystallographic directions. But one may also consider the surface of a magnetic compound where phase separation produces areas with different magnetic and electronic properties at the nanoscale rendering the study by standard x-ray based spectroscopic and diffraction techniques not adequate, like the manganites [46], with the added possibility of phases with 100 % spin polarization [47].

In the intersection between materials science and device application one could focus on the changes of the spin polarization of surfaces due to monolayer coatings by other species. For example, a few layer oxide covering a conducting ferromagnetic surface would be a model system to study the tunnel

spin polarization of the corresponding buried metal/oxide interface. This is an issue relevant for the understanding of fundamental concepts on tunnel spin polarization and simultaneously for the development of magnetic tunnel junctions [48, 49].

Finally, we can look forward to the application of a quantitative technique like SF-STM to study spin transport in nanoelectronic devices. Previous work on cross-sectional imaging of spin-injection structures have demonstrated the power of visualizing the distribution of spin density along a device [50]. For smaller devices optical techniques are insufficient and higher spatial resolution like STM are required. Furthermore, a technique like STM is highly desirable because it probes directly the quantity of interest, namely the electronic properties of the device. A quantitative spin polarization obtained via SF-STM could prove to be the ultimate characterization method of electronic transport for spintronic devices. We note that for spin injection into non-degenerate semiconductors the detection of magnetoresistance either via potentiometric or amperometric means is hampered by the depletion region on a semiconductor surface, whereas the spin polarization of the probed current can indeed have a sizable spin polarization [51]. The latter makes a technique like SF-STM, which is not based in any magnetoresistance effect but on the analysis of the spin polarization after tunneling into the tip, an ideal technique to apply to spin injection devices.

7.6 Conclusions

In this chapter we have applied SF-STM to the study of ferromagnetic surfaces. To this end we have previously proved that the SF-STM probes fulfill all the geometrical and electrical requirements for the realization of this novel technique and we have modified our STM system for the in-situ deposition of clean Co thin films.

Initial imaging experiments demonstrated clean tunneling conditions and homogeneous probe collector current images of Co surfaces, but lacked the observation of contrast in such images. It was possible to observe reproducible contrast only after modifications on the coating method of the metal overlayer on the probes or by using Co samples with a different magnetic anisotropy. We interprete these results as reflecting problems with the magnetic configuration of the probes having a preferred out-of-plane magnetization at the apex that

prevents the observation of magnetic contrast in Co thin films with in-plane magnetization. The spin-filter capabilities of the probes were unambiguously demonstrated by experiments using probes having a spin-valve structure as their metal overlayer. Reproducible modulation of the probe collector current by an applied magnetic field resulted in magnetocurrent effects of 200 % due to the spin-valve effect.

The latest imaging results on Co surfaces where contrast was observed showed a magnetocurrent of 55–76 %, resulting on an equivalent tunnel spin polarization of the Co surface equal to 24–30 %. These results are an indication of the successful implementation of SF-STM. Due to the limitations in our current experimental setup and on the control over the magnetic state of the probe further work is necessary to unequivocally demonstrate the quantitative measurement of tunnel spin polarization by SF-STM. We illustrated the importance of this work by proposing several examples of physical systems where SF-STM has a potential for significant contributions.

References

[1] S. D. Bader. "Colloquium: Opportunities in nanomagnetism". *Reviews of Modern Physics* **78** (1), 1–15 (2006). [Cited on 155]

[2] F. J. Himpsel, K. N. Altmann, G. J. Mankey, J. E. Ortega, and D. Y. Petrovykh. "Electronic states in magnetic nanostructures". *Journal of Magnetism and Magnetic Materials* **200** (1-3), 456–469 (1999). [Cited on 155]

[3] S. A. Wolf, A. Y. Chtchelkanova, and D. M. Treger. "Spintronics - A retrospective and perspective". *IBM Journal of Research and Development* **50** (1), 101–110 (2006). [Cited on 155]

[4] I. Žutić, J. Fabian, and S. D. Sarma. "Spintronics: Fundamentals and applications". *Reviews of Modern Physics* **76** (2), 323 (2004). [Cited on 155]

[5] D. D. Awschalom and M. E. Flatte. "Challenges for semiconductor spintronics". *Nature Physics* **3** (3), 153–159 (2007). [Cited on 156]

[6] A. Thiaville, J. Miltat, and J. M. García. "Magnetic Force Microscopy: Images of Nanostructures and Contrast Modeling". In H. Hopster and H. P. Oepen (eds.), "Magnetic Microscopy of Nanostructures", No. XVIII in NanoScience and Technology, pp. 225–251 (Springer Berlin Heidelberg, 2005), 1st edn. ISBN 978-3-540-40186-5. [Cited on 156]

[7] M. R. Koblischka, U. Hartmann, and T. Sulzbach. "Improving the lateral resolution of the MFM technique to the 10 nm range". *Journal of Magnetism and Magnetic Materials* **272-276** (Part 3), 2138–2140 (2004). [Cited on 156]

[8] L. Abelmann, A. van den Bos, and C. Lodder. "Magnetic Force Microscopy-Towards Higher Resolution". In H. Hopster and H. P. Oepen (eds.), "Magnetic Microscopy of Nanostructures", No. XVIII in NanoScience and Technology, pp. 253–283 (Springer Berlin Heidelberg, 2005), 1st edn. ISBN 978-3-540-40186-5. [Cited on 156]

[9] M. Bode. "Spin-polarized scanning tunnelling microscopy". *Reports on Progress in Physics* **66** (4), 523 (2003). [Cited on 156, 157]

[10] M. Bode and R. Wiesendanger. "Spin-Polarized Scanning Tunneling Spectroscopy". In H. Hopster and H. P. Oepen (eds.), "Magnetic Microscopy of Nanostructures", No. XVIII in NanoScience and Technology, pp. 203–223 (Springer Berlin Heidelberg, 2005), 1st edn. ISBN 978-3-540-40186-5. [Cited on 156]

[11] R. Jansen. "The spin-valve transistor: a review and outlook". *Journal of Physics D: Applied Physics* **36** (19), R289 (2003). [Cited on 156, 164]

[12] J. S. Moodera and G. Mathon. "Spin polarized tunneling in ferromagnetic junctions". *Journal of Magnetism and Magnetic Materials* **200** (1-3), 248–273 (1999). [Cited on 158]

[13] B. G. Park, T. Banerjee, J. C. Lodder, and R. Jansen. "Tunnel Spin Polarization Versus Energy for Clean and Doped Al_2O_3 Barriers". *Physical Review Letters* **99** (21), 217206–4 (2007). [Cited on 158]

[14] J. S. Moodera, E. F. Gallagher, K. Robinson, and J. Nowak. "Optimum tunnel barrier in ferromagnetic–insulator–ferromagnetic tunneling structures". *Applied Physics Letters* **70** (22), 3050 (1997). [Cited on 158]

[15] K. Sin, M. Mao, C. Chien, S. Funada, L. Miloslavsky, H. Tong, and S. Gupta. "Low resistance spin-dependent tunneling junctions with naturally oxidized tunneling barrier". *Magnetics, IEEE Transactions on* **36** (5), 2818–2820 (2000). [Cited on 158]

[16] K. Knechten, P. LeClair, J. T. Kohlhepp, H. J. M. Swagten, B. Koopmans, and W. J. M. de Jonge. "In situ time-resolved optical studies of Al oxidation for magnetic tunnel junctions". *Journal of Applied Physics* **90** (3), 1675–1677 (2001). [Cited on 158]

[17] "Vector Magnetometer Model 10 VSM - ADE Technologies". http://www.microsense.net/products-vsm-model-10.htm. [Cited on 159]

[18] F. Q. Zhu and C. L. Chien. "Determination of multiple easy axes in magnetic multilayers by remanence measurement using a vector magnetometer". *Journal of Applied Physics* **97**, 10J110–3 (2005). [Cited on 159]

[19] S. Entani, M. Kiguchi, S. Ikeda, and K. Saiki. "Magnetic properties of ultrathin cobalt films on SiO2 substrates". *Thin Solid Films* **493** (1-2), 221–225 (2005). [Cited on 160]

[20] T. Kishi, S. Okuno, K. Tanaka, and K. Inomata. "Spin-dependent electronic structure and theoretical SP-STM images for Co(0001) film". *Magnetics, IEEE Transactions on* **36** (5), 2972–2974 (2000). [Cited on 160]

[21] S. N. Okuno, T. Kishi, and K. Tanaka. "Spin-Polarized Tunneling Spectroscopy of Co(0001) Surface States". *Physical Review Letters* **88** (6), 066803 (2002). [Cited on 160]

[22] A. Kubetzka, O. Pietzsch, M. Bode, and R. Wiesendanger. "Determining the spin polarization of surfaces by spin-polarized scanning tunneling spectroscopy". *Applied Physics A: Materials Science & Processing* **76** (6), 873–877 (2003). [Cited on 160]

[23] K. D. Belashchenko, E. Y. Tsymbal, M. van Schilfgaarde, D. A. Stewart, I. I. Oleynik, and S. S. Jaswal. "Effect of interface bonding on spin-dependent tunneling from the oxidized Co surface". *Physical Review B* **69** (17), 174408 (2004). [Cited on 160]

[24] I. I. Oleinik, E. Y. Tsymbal, and D. G. Pettifor. "Structural and electronic properties of Co/Al2O3/Co magnetic tunnel junction from first principles". *Physical Review B* **62** (6), 3952 (2000). [Cited on 160]

[25] K. D. Belashchenko, E. Y. Tsymbal, I. I. Oleynik, and M. van Schilfgaarde. "Positive spin polarization in Co/Al2O3/Co tunnel junctions driven by oxygen adsorption". *Physical Review B* **71** (22), 224422 (2005). [Cited on 160]

[26] E. Y. Tsymbal, I. I. Oleinik, and D. G. Pettifor. "Oxygen-induced positive spin polarization from Fe into the vacuum barrier". *Journal of Applied Physics* **87**, 5230–5232 (2000). [Cited on 160]

[27] M. Sicot, O. Kurnosikov, O. A. O. Adam, H. J. M. Swagten, and B. Koopmans. "STM-induced desorption of hydrogen from Co nanoislands". *Physical Review B (Condensed Matter and Materials Physics)* **77** (3), 035417–7 (2008). [Cited on 160]

[28] G. Binnig, H. Rohrer, C. Gerber, and E. Weibel. "Tunneling through a controllable vacuum gap". *Applied Physics Letters* **40** (2), 178–180 (1982). [Cited on 161]

[29] W. H. Rippard and R. A. Buhrman. "Ballistic electron magnetic microscopy: Imaging magnetic domains with nanometer resolution". *Applied Physics Letters* **75** (7), 1001–1003 (1999). [Cited on 164]

[30] E. Haq, H. Gokcan, T. Banerjee, F. M. Postma, M. H. Siekman, R. Jansen, and J. C. Lodder. "Nanoscale magnetic hysteresis of $Ni_{80}Fe_{20}$/Au/Co trilayers using ballistic electron magnetic microscopy". *Journal of Applied Physics* **95**, 6930–6932 (2004). [Cited on 166]

[31] "SmartTip | Probe Solutions". http://www.smarttip.nl/en/home.php. [Cited on 167]

[32] M. T. Johnson, R. Jungblut, P. J. Kelly, and F. J. A. den Broeder. "Perpendicular magnetic anisotropy of multilayers: recent insights". *Journal of Magnetism and Magnetic Materials* **148** (1-2), 118–124 (1995). [Cited on 169]

[33] N. Nakajima, T. Koide, T. Shidara, H. Miyauchi, H. Fukutani, A. Fujimori, K. Iio, T. Katayama, M. Nývlt, and Y. Suzuki. "Perpendicular Magnetic Anisotropy Caused by Interfacial Hybridization via Enhanced Orbital Moment in Co/Pt Multilayers: Magnetic Circular X-Ray Dichroism Study". *Physical Review Letters* **81** (23), 5229 (1998). [Cited on 169]

[34] I. J. Vera-Marún. "Fabrication of nanomagnets using a hard mask scheme". 3rd report M.Sc. on nanotechnology, University of Twente (2005). [Cited on 169]

[35] H. Y. H. Chan, S. Zou, and M. J. Weaver. "Mechanistic Differences between Electrochemical and Gas-Phase Thermal Oxidation of Platinum-Group Transition Metals As Discerned by Surface-Enhanced Raman Spectroscopy". *The Journal of Physical Chemistry B* **103** (50), 11141–11151 (1999). [Cited on 170]

[36] R. Allenspach, M. Stampanoni, and A. Bischof. "Magnetic domains in thin epitaxial Co/Au(111) films". *Physical Review Letters* **65** (26), 3344 (1990). [Cited on 170]

[37] D. Weller, J. Stöhr, R. Nakajima, A. Carl, M. G. Samant, C. Chappert, R. Mégy, P. Beauvillain, P. Veillet, and G. A. Held. "Microscopic Origin of Magnetic Anisotropy in Au/Co/Au Probed with X-Ray Magnetic Circular Dichroism". *Physical Review Letters* **75** (20), 3752 (1995). [Cited on 170]

[38] J. M. Garcia, A. Thiaville, J. Miltat, K. J. Kirk, J. N. Chapman, and F. Alouges. "Quantitative interpretation of magnetic force microscopy images from soft patterned elements". *Applied Physics Letters* **79** (5), 656–658 (2001). [Cited on 173]

[39] S. McVitie, R. P. Ferrier, J. Scott, G. S. White, and A. Gallagher. "Quantitative field measurements from magnetic force microscope tips and comparison with point and extended charge models". *Journal of Applied Physics* **89** (7), 3656–3661 (2001). [Cited on 173]

[40] H. J. Hug, B. Stiefel, P. J. A. van Schendel, A. Moser, R. Hofer, S. Martin, H. Guntherodt, S. Porthun, L. Abelmann, J. C. Lodder, G. Bochi, and R. C. O'Handley. "Quantitative magnetic force microscopy on perpendicularly magnetized samples". *Journal of Applied Physics* **83** (11), 5609–5620 (1998). [Cited on 173]

[41] P. J. A. van Schendel, H. J. Hug, B. Stiefel, S. Martin, and H. Guntherodt. "A method for the calibration of magnetic force microscopy tips". *Journal of Applied Physics* **88** (1), 435–445 (2000). [Cited on 173]

[42] M. Bode, M. Dreyer, M. Getzlaff, M. Kleiber, A. Wadas, and R. Wiesendanger. "Recent progress in high-resolution magnetic imaging using scanning probe techniques". *Journal of Physics: Condensed Matter* **11** (48), 9387–9402 (1999). [Cited on 173]

[43] A. Kubetzka, M. Bode, O. Pietzsch, and R. Wiesendanger. "Spin-Polarized Scanning Tunneling Microscopy with Antiferromagnetic Probe Tips". *Physical Review Letters* **88** (5), 057201 (2002). [Cited on 173]

[44] A. Wadas and H. J. Hug. "Models for the stray field from magnetic tips used in magnetic force microscopy". *Journal of Applied Physics* **72** (1), 203–206 (1992). [Cited on 173]

[45] C. J. Chen. *Introduction to Scanning Tunneling Microscopy*. No. 64 in Monographs on the Physics and Chemistry of Materials (Oxford University Press, Oxford, 2007), 2nd edn. ISBN 978-0-19-921150-0. [Cited on 174]

[46] C. Renner, G. Aeppli, B. Kim, Y. Soh, and S. Cheong. "Atomic-scale images of charge ordering in a mixed-valence manganite". *Nature* **416** (6880), 518–521 (2002). [Cited on 174]

[47] A. Haghiri-Gosnet and J. Renard. "CMR manganites: physics, thin films and devices". *Journal of Physics D: Applied Physics* **36** (8), R127 (2003). [Cited on 174]

[48] J. M. D. Teresa, A. Barthélémy, A. Fert, J. P. Contour, R. Lyonnet, F. Montaigne, P. Seneor, and A. Vaurès. "Inverse Tunnel Magnetoresistance in Co/SrTiO3/La0.7Sr0.3MnO3: New Ideas on Spin-Polarized Tunneling". *Physical Review Letters* **82** (21), 4288 (1999). [Cited on 175]

[49] J. M. D. Teresa, A. Barthélémy, A. Fert, J. P. Contour, F. Montaigne, and P. Seneor. "Role of Metal-Oxide Interface in Determining the Spin Polarization of Magnetic Tunnel Junctions". *Science* **286** (5439), 507–509 (1999). [Cited on 175]

[50] P. Kotissek, M. Bailleul, M. Sperl, A. Spitzer, D. Schuh, W. Wegscheider, C. H. Back, and G. Bayreuther. "Cross-sectional imaging of spin injection into a semiconductor". *Nature Physics* **3** (12), 872–877 (2007). [Cited on 175]

[51] R. Jansen and B. C. Min. "Detection of a Spin Accumulation in Nondegenerate Semiconductors". *Physical Review Letters* **99** (24), 246604–4 (2007). [Cited on 175]

Summary

This thesis deals with the development of a versatile technique to measure spin polarization with atomic resolution. Such a technique is useful for characterization of magnetic nanostructures, specifically in relation to spin-polarized transport. The progress of our understanding and control of these structures is directly tied to the development of appropriate magnetic microscopy methods. Recent developments in spintronics and data storage systems render the study of electronic spin polarization in nanostructures a major point of interest. Therefore a technique that can measure spin polarization is relevant for characterization of spintronic properties of materials.

In chapter 1 we introduce background information on characterization of nanostructures. In particular, we describe scanning probe microscopies and how they are used to study magnetic materials. Even though magnetic force microscopy (MFM) is the workhorse for imaging magnetic nanostructures, its spatial resolution is limited and it cannot quantify spin polarization. On the other hand, scanning tunneling microscopy (STM) can achieve atomic spatial resolution and it can probe the electronic structure of the sample. Following the considerations above, we pursue in this work the goal of designing and implementing an STM-based technique to study magnetic surfaces. We set three requirements for such a technique. First, a high spatial resolution for magnetic imaging. Second, the ability to quantify the spin polarization near the Fermi

level on the surface of a conducting material. Third, general applicability.

Next, in chapter 2 we present a brief description of tunneling concepts as they evolved from solid state junctions, including spin-dependent tunneling effects. We use these concepts to interpret scanning tunneling microscopy and describe how the most relevant STM-based techniques with spin sensitivity are used to study magnetic samples. Most of these techniques can image nanoscale magnetism but do not offer a reliable measure of sample spin polarization. After a comparative analysis of the relevant techniques, we identify the need for an STM-based technique with practical and quantitative analysis of spin polarization near the Fermi level.

In chapter 3 we introduce our new technique to study magnetic nanostructures: spin-filter scanning tunneling microscopy (SF-STM). We describe the principle of the technique, which is based on spin-polarized tunneling and subsequent analysis of the spin polarization in a multi-terminal semiconductor/ferromagnet probe tip. The spin analysis in the probe relies on the spin-dependent transmission of hot electrons through thin ferromagnetic layers and on the energy-filtering capabilities of semiconductor/metal Schottky barriers. An independent electrical contact to the SF-STM probe offers an information channel decoupled from the tunneling signal, providing a proper separation of magnetic information from topographic or non-spin-polarized electronic contributions. We show that this approach has the ability to yield a quantitative measurement of surface spin polarization near the Fermi level with high spatial resolution and without any strong dependence on the specific electronic structure of the sample. We also describe our modified instrumentation in order to perform this novel STM operation mode.

The design and fabrication of SF-STM probes is described in chapter 4. The behavior of the multi-terminal semiconductor/ferromagnet probes is analyzed in order to find an optimum design for the spin filter within the probe. Considering the materials used in this work, the SF-STM technique is expected to result in a quantitative spin analysis within a range of 5–90 % sample spin polarization. We also devised a microfabrication process for SF-STM probes, based on anisotropic wet etching and local oxidation of silicon. The probes are fabricated in the form of silicon double pyramids terminated with micrometer-sized Schottky diodes, serving as the active elements for tunneling and spin filtering. Through careful monitoring of the fabrication process we obtain a reproducible and well characterized probe geometry.

In chapter 5 we present the electrical characterization of flat semiconduc-

tor/metal diodes formed at the apex of pyramidal structures by a local oxidation of silicon process. These structures serve as an intermediate stage towards the study of SF-STM probes which have a fully rounded apex with a radius of curvature $\lesssim 1\,\mu m$. Ballistic electron emission microscopy is used to study the electron transmission at the semiconductor/metal interface which proved to be sensitive to the details of the fabrication process. Elemental mapping of the heterostructure indicates nitridation of the silicon surface. Optimization of the fabrication process results in the elimination of this oxynitride and in proper electron transmission within the heterostructure. This knowledge is relevant for the fabrication of SF-STM probes.

In chapter 6 we study the properties of SF-STM probes. The probes are used in STM experiments to demonstrate their ability to perform imaging on metallic surfaces. The independent electrical contact to the probe is used to evaluate the energy-filtering and transmission properties of ballistic electrons within the probes, after tunneling has taken place. We have achieved the primary goal of defining a (spin-dependent) energy-filter at the rounded apex of an STM probe. This work satisfies the basic requirements for using the probes for quantitative imaging of spin polarization.

Finally, in chapter 7 we present experiments on imaging of magnetic surfaces with spin-filter scanning tunneling microscopy. The two-terminal probes serve as spin-analyzers for the quantification of tunnel spin polarization. We demonstrate the use of these probes for imaging a ferromagnetic surface and evaluate their spin-filtering capabilities, which are unambiguously demonstrated by experiments using probes having a spin-valve structure. We found that the magnetization at the apex of the probe has a tendency to be oriented along the tip axis, which prevented the observation of magnetic contrast on Co samples with in-plane magnetization. Therefore, tests of magnetic imaging were performed on Co/Pt multilayer samples with out-of-plane magnetization. Further work is necessary to unequivocally demonstrate the quantitative measurement of tunnel spin polarization. These initial imaging results are an indication of the successful implementation of SF-STM.

SF-STM shows the promise of a new and complementary technique to study transport in spintronic materials and devices by offering a quantitative measurement of tunnel spin polarization at high spatial resolution. The operating principle of the technique is widely applicable to any conducting surface with a spin polarization near the Fermi level. This technique will contribute to the development of new systems for spintronics and magnetic data storage.

Samenvatting

Het thema van dit proefschrift is de ontwikkeling van een veelzijdige techniek voor het meten van spin polarisatie met atomaire resolutie. Een dergelijke techniek is geschikt voor karakterisatie van magnetische nanostrukturen, in het bijzonder in relatie tot spin gepolariseerd ladingstransport. De voortschrijding van ons begrip van en controle over deze strukturen staat in directe relatie tot de ontwikkeling van microscopische methoden. Recente ontwikkelingen in spintronica en systemen voor dataopslag zorgen ervoor dat de studie van de spin polarisatie van elektronen in nanostructuren sterk in de belangstelling staat. Daarom is een techniek die deze spin polarisatie kan meten relevant om de voor spintronika geschikte eigenschappen van materialen te kunnen karakteriseren.

In hoofdstuk 1 introduceren we achtergrondinformatie omtrend de karakterisatie van nanostrukturen. Meer specifiek beschrijven we scanning probe microscopie technieken en gaan in op hoe deze gebruikt worden voor de studie van magnetische materialen. Hoewel magnetic force microscopie (MFM) de meest gebruikte techniek is voor het in beeld brengen van magnetische nanostrukturen is de ruimtelijke resolutie beperkt, en is kwantificatie van de spin polarisatie onmogelijk. Scanning tunneling microscopie (STM) kan, aan de andere kant, atomaire resolutie bewerkstelligen en kan de elektronenstruktuur van een sample in kaart brengen. Uitgaande van de bovenstaande beschouwingen,

stelt dit werk tot doel om een op STM gebaseerde techniek te ontwerpen en implementeren voor de studie van magnetische oppervlakken. We definiëren drie criteria voor een dergelijke techniek. Ten eerste, een hoge ruimtelijke resolutie for magnetische afbeeldingen. Ten tweede, de mogelijkheid om de spin polarisatie van de elektronen nabij het Fermi niveau aan het oppervlak van een geleidend materiaal te kwantificeren. Ten derde, algemene toepasbaarheid.

Vervolgens presenteren we in hoofdstuk 2 een korte beschrijving van concepten met betrekking tot tunneling, zoals deze gevormd zijn aan de hand van vaste stof juncties, inclusief effecten van spin afhankelijke tunneling. We gebruiken deze concepten om scanning tunneling microscopie te interpreteren, en beschrijven hoe de meest relevante op STM gebaseerde technieken worden gebruikt om magnetische samples te bestuderen. De meeste van deze technieken zijn in staat om magnetisme op de nanoschaal af te beelden, maar bieden geen betrouwbare meting van de spin polarisatie. Na een vergelijkende analyse van de relevante technieken identificeren we de behoefte aan een op STM gebaseerde techniek voor het op praktische en kwantitatieve wijze analyseren van de spin polarisatie nabij het Fermi niveau.

In hoofdstuk 3 introduceren we onze nieuwe techniek voor de studie van magnetische nanostrukturen: spin-filter scanning tunneling microscopie (ST-STM). We beschrijven het principe van de techniek, die gebaseerd is op tunneling van spin gepolariseerde elektronen en vervolgens analyse van de spin polarisatie in een multi-terminal halfgeleider/ferromagneet STM naald (probe). De spin analyse in de probe is gebaseerd op spin afhankelijke transmissie van hete elektronen door dunne ferromagnetische lagen en op de energie filterende eigenschappen van halfgeleider/metaal Schottky barrières. Een gescheiden elektrisch contact naar de SF-STM probe, ontkoppeld van het tunneling signaal, biedt de mogelijkheid om op geschikte wijze de magnetische informatie te onderscheiden van topografische of andere niet spin gepolariseerde elektronische bijdragen. Er wordt getoond dat deze benadering het mogelijk maakt om een kwantitatieve meting te verrichten van de oppervlakte spin polarisatie nabij het Fermi niveau, met hoge ruimtelijke resolutie en zonder sterkte afhankelijkheid van de elektronenstruktuur van het sample. Tevens is onze gemodificeerde instrumentatie voor het uitvoeren van deze nieuwe vorm van STM beschreven.

Het ontwerp en de fabricage van SF-STM probes wordt beschreven in hoofdstuk 4. Het gedrag van de multi-terminal halfgeleider/ferromagneet probes wordt geanalyseerd om het optimale ontwerp te vinden voor het spin filter in de probe. Uitgaande van de materialen die in dit werk gebruikt

worden, wordt kwantitatieve spin analyse binnen een berijk van 5–90 % spin polarisatie van het sample verwacht voor de SF-STM techniek. We hebben ook een microfabricage proces voor SF-STM probes ontwikkeld, gebaseerd op anisotroop nat etsen en lokale oxidatie van silicium. De probes worden vervaardigd in de vorm van dubbele pyramides van silicium, getermineerd met Schottky diodes met micrometer afmetingen. Die diodes dienen als de actieve componenten voor tunneling en spin filtering. Door het zorgvuldig in kaart brengen van het fabricageproces verkrijgen we een reproduceerbare en goed gekarakteriseerde probe geometrie.

In hoofdstuk 5 presenteren we de elektrische karakterisatie van vlakke halfgeleider/metaal diodes, gevormd aan de apex van pyramide strukturen door een proces gebaseerd op lokale oxidatie van silicium. Deze strukturen dienen als een tussenstation op weg naar de studie van SF-STM probes met een volledig afgeronde apex, en met een kromtestraal van $\lesssim 1\,\mu m$. Ballistic electron emission microscopie wordt gebruikt om de transmissie van elektronen door het halfgeleider/metaal grensvlak te bestuderen, waaruit blijkt dat deze gevoelig is voor de details van het fabricageproces. Het in kaart brengen van de elementenverdeling in de heterostruktuur duidt op nitridatie van het siliciumoppervlak. Optimalisatie van het fabricageproces resulteerd in de eliminatie van het oxynitride en in de juiste transmissie van elektronen door de heterostruktuur. De ontwikkelde kennis is relevant voor de fabricage van de SF-STM probes.

In hoofdstuk 6 bestuderen we de eigenschappen van SF-STM probes. De probes worden gebruikt in STM experimenten om hun geschiktheid om metallische oppervlakken af te beelden aan te tonen. Het gescheiden elektrische contact naar de probe wordt gebruikt om de energieselectie en transmissie van ballistische elektronen in de probes te evalueren, nadat tunneling heeft plaatsgevonden. We hebben het primaire doel, de definitie van een energiefilter aan de afgeronde apex van een STM probe, berijkt. Hiermee is getoond dat aan de randvoorwaarden voor het gebruik van de probes voor het op kwantitatieve wijze in beeld brengen van spin polarisatie voldaan is.

Ten slotte worden in hoofdstuk 7, experimenten met betrekking tot het afbeelden van magnetische oppervlakken met spin-filter scanning tunneling microscopie gepresenteerd. De probes met tweevoudige aansluiting dienen als spin analysator voor de kwantificatie van tunnel spin polarisatie. We demonstreren het gebruik van de probes voor het afbeelden van een ferromagnetisch oppervlak en evalueren hun spin filterende vermogen, dat ondubbelzinnig

naar voren komt in experimenten met probes die een “spin valve” struktuur bevatten. Er is gevonden dat de magnetisatie aan de apex van de probe zich bij voorkeur richt langs de as van de pyramide, hetgeen vooralsnog de observatie van magnetisch contrast in Co dunne films met magnetisatie in het vlak heeft verhinderd. Daarom zijn tests voor het maken van magnetische afbeeldingen uitgevoerd op Co/Pt multilagen met magnetisatie uit het vlak. Verder onderzoek is nodig om kwantitatieve metingen van de tunnel spin polarisatie ontegenzeggelijk te demonstreren. Deze eerste afbeeldingsresultaten vormen een indicatie voor het succesvol implementeren van SF-STM.

SF-STM is veelbelovend als een nieuwe complementaire techniek voor het bestuderen van ladingstransport in materialen en devices voor spintronika, doordat een kwantitatieve meting van de tunnel spin polarisatie mogelijk is met hoge ruimtelijke resolutie. De techniek is breed toepasbaar op ieder geleidend oppervlak met spin polarisatie nabij het Fermi niveau. Deze techniek zal dan ook bijdragen tot de ontwikkeling van nieuwe systemen voor spintronika en magnetische data opslag.

Acknowledgements

This thesis marks the end of a 6 year stay at the University of Twente. Beginning with the master in Nanotechnology and ending with a doctoral degree, I had the opportunity to meet a lot of wonderful people to whom I am truly grateful. In the following I limit myself to mention just a few of them.

I thank my daily supervisor and assistant promoter, Dr. Ron Jansen. From his supervision during two of my master's projects up to this doctoral research he has always aimed towards scientific thoroughness. His careful comments have helped to increase the quality of this work. Ronnie, you helped me with setting a research guideline, while allowing me freedom to explore by myself. I wish you success in your future scientific endeavors.

I thank my promoter Prof. Paul Kelly, whom was also a committee member during my master's final project, for his helpful comments. I would also like to thank the members of my doctoral graduation committee for making time to evaluate this work, specially to those traveling from abroad.

This thesis has benefited from previous work on BEMM performed within the group. I express my gratitude to Ehtsham-ul Haq and Tamalika Banerjee for building the expertise that allowed this project to get off on the right foot. Tamalika you offered a kind support to all students of the group, both scientific and otherwise.

The technical support received at the Nanoelectronics group by Martin

Siekman, Johnny Sanderink, and Thijs Bolhuis, was simply great. Special thanks go to Martin for sharing his broad expertise on scanning probe microscopy and for his improvements to the STM system used in this work. Johnny also helped a big deal with adding the deposition chamber to the STM.

Wabe Koelmans did his master's thesis under my daily supervision. I thank him for his useful contributions to the initial development of the fabrication process presented in Chapter 4. Nowadays Michel Zoontjes is finishing his master's project tackling some open questions from this work.

I am grateful to Michel de Jong for his ultrafast translation of the samenvatting, and to Boudewijn de Jong for further corrections. I would also like to say thanks to my former office mate Tian Gang for being my paranimf.

During my master and PhD I was a member of the former Systems and Materials for Information Storage group (SMI, Prof. Cock Lodder) and the subsequent Nanoelectronics group. Within this environment I learned many things about magnetism and spintronics during the scientific discussions at group meetings and seminars. Much broader subjects led to lengthy discussions at the coffee table. And less than scientific discussions were held during Friday borrels at the Tombe. All in all, my time with the group at Twente has been a delightful one. Thank you all for making of the group a friendly and productive work environment. The group now continues towards new research directions like organic electronics. Dear former colleagues, I wish you all the best.

Fabricating the SF-STM probes would have been impossible without the constant work of the cleanroom personnel to keep all the equipment running, my sincere thanks to all the cleanroom team. I must mention the nice TEM work by Rico Keim. Rico thanks for the challenging sample preparation and imaging of pyramidal structures, I did enjoy the background classical music.

This doctoral work was a direct consequence of the master in Nanotechnology I did at Twente, which was known to me thanks to the outreaching efforts of Prof. María García-Parajó. I would like to say thank you to Prof. Holger Schönherr and Kees van der Werf, for they taught me the fundamentals of scanning probe microscopy and they increased my appreciation for the subject. Furthermore, I thank the MESA$^+$ and the organizers of the master for helping the students with the scholarship program.

Within the university there were friends that offered a helping hand when needed and with whom I shared several celebrations. From those who were there for the full 6 years at Twente I can mention Qi Chen and Juan Manuel Jauregui. I thank you all for making of my stay at Twente a colorful one.

No one has shared with me such a long history of academic life as Maryana. Like you said in your thesis: “after bachelor, master and PhD at the same University, I think this is the end of our academic career together”. Thanks for being always there. My sincere wishes for success in your next step, finally outside academia!

Every time I came back to Venezuela my family and friends offered love and support. To my friends from Puerto La Cruz I say thanks for making me feel every time like we just graduated from high school. My big family (aunts, uncles, cousins...) was always there welcoming me with open arms. Each holyday you gave me the energy to come back and continue the research work far away from home.

Quiero mencionar a mis padres y a mis hermanas. Gracias por darme un hogar lleno de amor en el cual pude encontrar el apoyo necesario para alcanzar nuevas metas. A mis padres debo todo lo que soy. Mamá, gracias por tu amor incondicional. Sé que deseabas compartir este momento conmigo. Te tengo presente ahora y cada día de mi vida.

El apoyo y sacrificio de mi esposa durante esta etapa de mi vida ha sido ejemplar. Ana, tu amor ha traído un balance en mi vida por el cual estaré siempre agradecido. Igualmente tu familia me ha aceptado como un miembro más. Agradezco tu compañía desde el fondo de mi corazón.

Author biography

Iván Jesús Vera Marún was born on October 1, 1980 in Lechería, Venezuela. After graduating from the Italo-Venezuelan School "Angelo de Marta" in Puerto La Cruz in 1997, he went to study Electronics Engineering at the Simón Bolívar University in Caracas. During this period he obtained first place at the III Ibero-American Physics Olympiad, acted as president of the Student Commission of Electronic Engineering, and obtained an honorific mention for his graduation project. He received his undergraduate degree summa cum laude in November 2002. He joined the Master Program in Nanotechnology at the University of Twente in 2003. The program was financed by the MESA$^+$ Institute for Nanotechnology and the Twente Scholarship Program. During this period he worked in four different projects and three research groups, Materials Science and Technology of Polymers (MTP) under the supervision of Dr. Holger Schönherr, Biophysical Engineering (BPE) under the supervision of Dr. Martin Bennink, and Systems and Materials for Information Storage (SMI) under the supervision of Dr. Ron Jansen. He obtained his master degree with distinction. In 2005 he joined the Nanoelectronics group (NE) as a doctoral candidate under the supervision of Dr. Ron Jansen, working on the development of a new microscopy technique to study magnetic nanostructures. During this research he was awarded a poster prize and an invited talk at international conferences. His doctoral research is described in this thesis.

For the things we have to learn before we can do them,
we learn by doing them.

Aristotle